

Non–Analytical Line Profiles in Stellar Atmospheres

For Planetary Host Star Systems

Dissertation
zur Erlangung des Doktorgrades
des Departments Physik
der Universität Hamburg

vorgelegt von
Christine M. S. Johnas
aus Hamburg

Hamburg
2007

Gutachter der Dissertation:

Prof. Dr. P. H. Hauschildt
Prof. Dr. A. P. Hatzes

Gutachter der Disputation:

Prof. Dr. P. H. Hauschildt
Prof. Dr. J. H. M. M. Schmitt

Datum der Disputation:

19. Dezember 2007

Vorsitzender des Prüfungsausschusses:

Prof. Dr. G. Wiedemann

Vorsitzender des Promotionsausschusses:

Prof. Dr. G. Huber

Dekan der Fakultät für Mathematik,
Informatik und Naturwissenschaften:

Prof. Dr. A. Frühwald

Abstract

In this work, non-analytical line profiles for both cool and hot, dense atmospheres are added to the opacity calculations of the multi-purpose stellar atmosphere code PHOENIX. Their influence on model atmospheres and synthetic spectra is studied. Model atmospheres are necessary in order to calculate synthetic spectra and to derive reliable stellar parameters.

For cool, dense atmospheres, i.e., of objects of spectral type similar to and lower than late-type M, van-der-Waals broadening is the most important pressure broadening mechanism. The spectra of these objects below $\sim 1 \mu\text{m}$ are dominated by alkali resonance lines. The profiles of the alkali resonance lines, especially of Na I D and K I, determine mostly the pseudo continuum in this wavelength range. Up to this work, classical analytical impact approximated alkali near line wing profiles perturbed by H₂, He, and H I, which are the dominant perturbing particles, have been applied. In this work, various non-analytical alkali line profiles, including far line wing and near line wing profiles, for Na I D, Li I, K I, and Rb I are included in order to describe the strong alkali absorption features which are characteristic for late-type dwarfs. For the alkali resonance line profiles, different theoretical approaches were used describing the far and near line wings. Non-analytical alkali profiles for the far and near line wings perturbed by H₂ and He are provided in the unified semi-classical theory. Furthermore, He broadened non-analytical near line wing profiles calculated in the fully quantum mechanical theory are included as well as non-analytical near line wing profiles broadened by collisions with H I obtained by the impact approximation. The various alkali line profiles are compared among each other and their influence in synthetic spectra.

For an increased understanding of line formation in cool atmospheres and as application of the van-der-Waals profiles, the influence of two atmospheric dust treatments, DUSTY and DRIFT models, on alkali lines is studied. Dust has in general a larger influence on the line shape than the underlying line profiles. Another application of the alkali profiles is the description of observations. For a sample of Chamaeleon I objects, the Li I doublet is fit and its abundance is determined for the first time. Further comparisons to observations of later spectral type often result in an improved description when using the non-analytical alkali profiles.

Towards atmospheres with higher effective temperatures and densities which are high enough to sustain pressure broadening, Stark broadening is the dominant pressure broadening mechanism. Stark line profiles are significant for stars of spectral type G and earlier, i.e., also for typical host stars of known extrasolar planets. Up to this work, analytical impact approximated near line wing profiles have been considered. Detailed non-analytical Stark near line wing profiles of several atoms and ions are included to the opacity calculations here. The results have been obtained under the assumption that electrons are the most important perturber species. The influence of the Stark profiles on synthetic spectra is shown.

Spectral line profiles do make a difference in synthetic spectra. Non-analytical profiles provide stronger absorption lines than analytical profiles. Their application in synthetic spectra serves as a diagnostic tool in the classification of stellar objects.

Inhaltsangabe

In dieser Arbeit sind nicht-analytische Linienprofile kalter sowie heißer, dichter Atmosphären in die Opazitätsberechnung des Atmosphärenprogramms PHOENIX hinzugefügt worden. Ihr Einfluss auf Modellatmosphären und synthetische Spektren wird untersucht. Modellatmosphären sind notwendig, um synthetische Spektren zu berechnen und um verlässliche stellare Größen abzuleiten. Der dominierende Druckverbreiterungsmechanismus in kalten und dichten Atmosphären (für Objekte des Spektraltyps M oder späteren Spektraltyps) ist die van-der-Waals Verbreiterung. Die Spektren dieser Objekte werden im Wellenlängenbereich kleiner als $1\ \mu\text{m}$ von Alkaliresonanzlinien dominiert. Die Linienprofile von Na I D und K I bestimmen maßgeblich das Pseudokontinuum in diesem Wellenlängenbereich. Bisher sind klassische, analytische Profile verwendet worden, welche den nahen Linienflügel in der Stoßnäherung abschätzen. Dabei sind H_2 , He und HI als wichtigste Störteilchen berücksichtigt worden. In dieser Arbeit sind verschiedene nicht-analytische Profile für die (fernen und nahen) Linienflügel der Alkaliduplette Na I D, Li I, K I und Rb I hinzugefügt worden, um in Spektren signifikante Absorptionsmerkmale dieser Alkali zu beschreiben. Sie sind charakteristisch für späte Zwerge. Es sind verschiedene theoretische Ansätze für die nicht-analytischen Linienprofile verwendet worden. Ferne und nahe Linienflügelprofile unter Berücksichtigung von H_2 und He als Störteilchen sind mit der "vereinten semiklassischen Theorie" bereitgestellt worden. Außerdem sind He verbreiterte Profile der nahen Linienflügel aus der "vollständig quantenmechanischen Theorie" hinzugefügt worden, sowie nahe Linienflügelprofile, welche durch Kollisionen mit HI in der Stoßnäherung verbreitert sind. Die verschiedenen Alkaliliniennprofile werden untereinander und ihr Einfluss auf synthetischen Spektren verglichen. Für ein vertieftes Verständnis der Linienbildung in kalten Atmosphären wird unter Berücksichtigung von den van-der-Waals Profilen der Einfluss von zwei verschiedenen Staubbehandlungen in der Atmosphäre, den DUSTY und DRIFT Modellen, auf Alkaliliniennprofile untersucht. Prinzipiell hat Staub einen größeren Einfluss auf die Linienform als die zugrunde liegenden Alkaliprofile. Für eine Auswahl von Chamaeleon I Objekten wird deren Li I Doublet modelliert und dessen Häufigkeit erstmals bestimmt. Weitere Vergleiche mit Beobachtungen von Objekten späteren Spektraltyps ergeben häufig eine verbesserte Beschreibung bei der Anwendung der nicht-analytischen Linienprofile.

In Atmosphären mit höheren Effektivtemperaturen und Dichten, welche hoch genug sind, um Druckverbreiterung aufrechtzuerhalten, ist die Starkverbreiterung der vorherrschende Druckverbreiterungsmechanismus. Starkprofile sind für Sterne des Spektraltyps G und früheren Spektraltyps, das heißt auch für typische Zentralsterne von bekannten extrasolaren Planeten, von Bedeutung. Bisher sind analytische Profile für die nahen Linienflügel verwendet worden. In dieser Arbeit sind detaillierte, nicht-analytische Starkprofile der nahen Linienflügel verschiedener Atome und Ionen in einer semiklassischen Stoßnäherung der Opazitätsberechnung hinzugefügt und analysiert worden. Hierbei ist angenommen worden, dass Elektronen die wichtigsten Störteilchen sind. Spektrale Linienprofile beeinflussen synthetische Spektren, wobei nicht-analytische Profile stärkere Absorptionslinien als analytische Profile verursachen. Sie dienen als diagnostisches Hilfsmittel bei der Klassifizierung stellarer Objekte.

Contents

Abstract	iii
Inhaltsangabe	iv
1 Introduction	1
1.1 Brown Dwarfs	1
1.2 Extrasolar Systems Hosting Planets	3
1.3 Outline	4
2 Theoretical Background of Spectral Line Broadening	5
2.1 Classical Theory of Collisional Line broadening	7
2.1.1 Impact Approximated Van–Der–Waals Profiles	7
2.1.2 Statistical Approximation	9
2.1.3 Validity of the Impact and Statistical Approximation	10
2.2 The Spectrum of a Quantum Mechanical System and its Autocorrelation Function .	12
2.3 Quantum Theory of Line Broadening	14
2.4 Unified Semi–Classical Theory	18
3 Alkali Line Profiles	23
3.1 Impact Profiles	23
3.2 Profiles in the Unified Semi–Classical Theory	23
3.3 Alkali Broadening through H I	25
3.4 Lorentzian Profiles in the Fully–Quantum Mechanical Theory	28
3.5 Profile Data Discussion	29
4 Stellar Atmospheres Computed with PHOENIX	34
4.1 Basic Physics	34
4.2 Modelling Atmospheres with PHOENIX	39
4.3 The Numerical Evaluation of the Total Line Profile	41
5 Line Profiles in PHOENIX Model Atmospheres and Synthetic Spectra	43
5.1 Legend	43
5.2 Atmospheric Models in PHOENIX	45
5.3 Concentrations of the Most Important Species	46
5.4 Impact, 1 st Generation, and Modern1 Setup	46
5.4.1 Model Atmospheres and Synthetic Spectra	46
5.4.2 The Influence of the Na I D and K I Profiles on the Li I and Rb I Doublets .	50
5.4.3 Satellites	51
5.4.4 The Influence of Stellar Properties on the Line Profile	53

5.4.5	The Dependence on Atmospheric Models	56
5.5	Modern2 and Modern3 Setup	59
5.5.1	Comparison between the Modern1 and Modern2 Setup	59
5.5.2	Comparison between the Modern1 and Modern3 Setup	59
5.5.3	Comparison of φ_λ at 5890 Å of the Modern1, Modern2, and Modern3 Setup	63
5.5.4	Conclusion of the Results of the Modern2 and Modern3 Setup	65
6	The Influence of Dust Formation on Alkali Line Profiles in Spectra of Cool Atmospheres	67
6.1	DRIFT: Consistent Micro-Physics in 1 D Static Model Atmospheres	67
6.2	Influence on Alkali Line Profiles	68
6.3	Conclusion	71
7	The Li I Absorption Line in Cool Atmospheres	73
7.1	Methods for Obtaining the Equivalent Width of Li I	73
7.2	Li I Study on Very Low Mass Objects of Chamaeleon I	75
8	Comparison between the Impact and Modern1 Setup and Selected Observations	87
8.1	Results for Low Resolution Spectra	87
8.2	Results for High Resolution Spectra	89
8.3	Conclusion	97
9	Line Profiles for Stark Broadening	98
9.1	Theoretical Background of Stark Broadening	98
9.1.1	Approximation by Kurucz	99
9.1.2	Theory of Stark Broadening of Isolated Lines in the Impact Approximation	100
9.2	Non-Analytical Stark Profiles by M. S. Dimitrijević and S. Sahal-Bréchet	101
9.3	The Influence of the Stark Profiles in Synthetic Spectra	103
9.4	Conclusion	104
10	Summary and Outlook	107
10.1	Summary	107
10.2	Outlook	109
A	Alkali Profile Data	111
B	Numerical Implementation of the Total Line Profile Calculation	120
C	The Influence of Line Profiles on Models and Spectra II	123
C.1	T-p Structures: Impact, 1 st Generation, and Modern1 Setup	123
C.2	Low Resolution Spectra	125
C.3	Close Up of the Alkali Doublets	130
C.4	T-p Structures: Modern1, Modern2, and Modern3 Setup	133
D	The Na I Doublet in the Impact and Modern1-3 Setup with $\log(g) = 4.5$	135
D.1	The Effects of New Na I D Line Profiles in Cool Atmospheres	135
D.2	Comparison to the Results of Sect. 5.5 with $\log(g) = 5.0$	140

E Numerical Implementation of the Stark Line Profile Calculation	141
Bibliography	142

1 Introduction

Spectral analyses are of fundamental importance for the identification and detailed understanding of the various stellar objects. With the correct interpretation of the observed spectrum, it is possible to determine essential stellar parameters, such as the chemical composition, the element abundances, the effective temperature, the surface gravity, and the spectral type of the stellar object. Therefore, theoretical atmospheric models are required in which the physics of the stellar atmosphere is simulated in order to describe the spectral features of the observed stellar object. In this work, the multi-purpose stellar atmosphere code `PHOENIX` is used in order to address some of the above mentioned topics.

1.1 Brown Dwarfs

The identification of the brown dwarf Gliese 229b by Nakajima et al. (1995) has been a mile stone for the understanding of substellar objects and the modelling of cool atmospheres. Brown dwarfs were first postulated by Kumar (1963b,a) and Hayashi & Nakano (1963). The lower mass limit for hydrogen fusion is 0.072 solar masses (about 75 Jupiter masses) (Basri 2000). Below this limit, the luminosity is solely due to gravitational contraction during which potential energy is transformed to heat. The hydrostatic equilibrium against the gravitational collapse is provided by the electron degeneracy pressure (Chabrier et al. 2005). The masses of brown dwarfs are assumed to be between 13 and 75 Jupiter masses. Chabrier et al. (2005) distinguish between low-mass stars, i.e., objects below one solar mass, and brown dwarfs, i.e., objects below the hydrogen-burning minimum mass. However, there can be some hydrogen burning in the higher mass brown dwarfs (Chabrier & Baraffe 2000). Brown dwarfs heavier than 13 Jupiter masses fuse deuterium and above ~ 65 Jupiter masses, there is also lithium fusion.

In the literature, several names for cool objects in general, such as brown dwarfs, very low mass objects, L and T dwarfs and ultra-/cool dwarfs, can be found. It is more unambiguous when characterizing these objects with their spectral type. Before the identification of the first brown dwarf, the coolest type in the classical stellar sequence was M. Its characteristics are the absorption bands of TiO and VO in the optical wavelength range. New spectral types have been introduced covering the characteristics of the newly found, substellar objects. Note that young brown dwarfs can start with a spectral type of (late) M and cool off with age to an L dwarf (see for example Basri (2000)). With the help of a large observational sample, Kirkpatrick (2005) summarizes the new spectral types, L and T, as following: known L dwarfs have effective temperatures from ~ 2500 K to ~ 1300 K, whereas T dwarfs can be as warm as ~ 1500 K down to ~ 750 K. The overlap of the effective temperature of the two spectral classes indicates the existing theoretical uncertainties. Strong metal hydride lines, for example of CaH and FeH, and alkali resonance lines are prominent in these spectra.

The spectral type L is supposed to cover the low mass end of hydrogen burning stars and substellar objects (brown dwarfs). T dwarfs are believed to be entirely substellar. They have prominent H₂O

and CH₄ bands in the 1–2.5 μm region which can be used for the further spectral classification of T dwarfs (Burgasser et al. 2006).

Furthermore, the presence of dust plays an important role in the atmospheres of L and T dwarfs. For L dwarfs, dust in the photosphere must be taken into account whereas for T dwarf models, it must be already vanished.

Very low mass objects (below ≈ 0.4 solar masses), brown dwarfs, and giant planets are (mostly) fully convective (Chabrier & Baraffe 2000). The lithium test for fully convective objects has been suggested by Rebolo et al. (1992) in order to distinguish between young, very low mass stars and brown dwarfs. Since the evolutionary timescales of these objects are many orders of magnitude larger than the convective timescale, it is possible to assume the core abundances identical with the atmospheric abundances (Chabrier & Baraffe 2000). Usually, young stars, which reach temperatures required for hydrogen fusion, deplete their lithium very quickly whereas the sufficient temperature is not reached in the interior of a brown dwarf. However, there are still uncertainties left. Very young stars could have not yet started their lithium depletion at the time of observation. It is possible for brown dwarfs close to the upper mass limit to deplete their lithium when they are young ($M \gtrsim 65$ Jupiter masses).

It is difficult to distinguish a very low mass brown dwarf from a high mass planet. Due to the increasing number of observations of even lighter brown dwarfs and heavier planets, the theoretical limits were reconsidered, for example, when trying to define them by their orbits, their radius, their mass or their formation mechanisms. Therefore, the working group on extrasolar planets of the IAU has preliminary defined (They are aware that it can be only a temporary definition.):

“(1) Objects with true masses below the limiting mass for thermonuclear fusion of deuterium (currently calculated to be 13 Jupiter masses for objects of solar metallicity) that orbit stars or stellar remnants are “planets” (no matter how they formed). The minimum mass/size required for an extrasolar object to be considered a planet should be the same as that used in our solar system.

(2) Substellar objects with true masses above the limiting mass for thermonuclear fusion of deuterium are “brown dwarfs”, no matter how they formed nor where they are located.

(3) Free-floating objects in young star clusters with masses below the limiting mass for thermonuclear fusion of deuterium are not “planets”, but are “sub-brown dwarfs” (or whatever name is most appropriate)” (position statement on the definition of a “planet”, WGESP, February 28 (2003)).

As mentioned above, the special features of L and T dwarfs are their dominating alkali resonance absorption lines in the optical wavelength range, especially of Na I D and K I. In Fig. 1.1, three observed spectra of a late-type M, early to mid-type L and late-type L dwarfs are shown. The strength of the K I D₁ absorption line (at 7701 Å) increases towards later spectral types. The L8 spectrum is dominated by the strong far line wings of the K I doublet.

These spectra with the strong alkali features could not be described by already existing atmospheric models and synthetic spectra up to 2003. New line profiles had to be calculated and included in stellar atmosphere codes. Van-der-Waals broadening is the dominant pressure broadening mechanism in these atmospheres. For example, Schweitzer et al. (2001) have applied analytical alkali line profiles following the approximation by Unsöld (1968) and concluded that more complete and improved line profiles would improve the description of early- and late-type L dwarfs. In 2003, Burrows & Volobuyev (2003) presented the first non-analytical far line profiles for Na I D and K I doublets in atmospheres of substellar mass objects. In the same year, Allard et al. (2003) published another set of non-analytical Na I D and K I far line wing profiles and applied them to the observation of the T6 methane brown dwarf SDSS 1624. Up to now, more non-analytical alkali profiles have been published, see for example Allard et al. (2005), Allard & Spiegelman (2006),

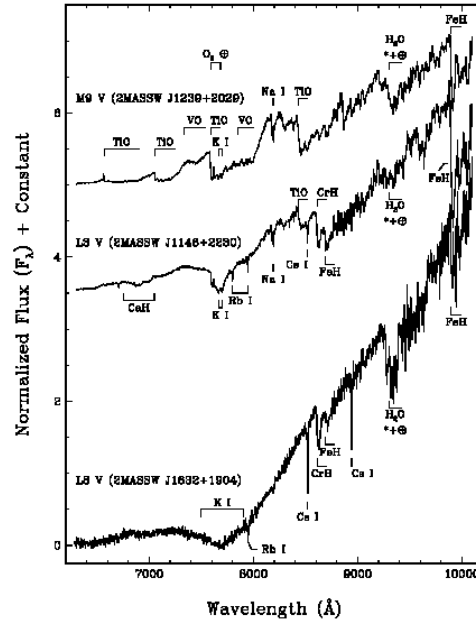


Fig. 1.1: Late-type M, early- to mid-type L, and late-type L dwarfs spectra (Kirkpatrick et al. 1999).

and Allard et al. (2007) covering far line wing and near line profiles, Leo et al. (2000), Peach et al. (2005), Mullamphy et al. (2007) calculating near line wing profiles, Zhu et al. (2005) and Zhu et al. (2006) providing far line wing profiles.

1.2 Extrasolar Systems Hosting Planets

Latham et al. (1989), Wolszczan & Frail (1992), and Mayor & Queloz (1995) were the first who detected planets outside our solar system, so-called extrasolar planets. Currently, 252 candidates of extrasolar planets¹, in short exoplanets, are known. They are objects below 13 Jupiter masses and are orbiting their parent star, the host star. The orbital distances as well as the eccentricities cover a wide parameter range (orbital distance: from ≈ 0.0038 AU to ≈ 5.5 AU, eccentricity: ≈ 0.03 to ≈ 0.9 (Sudarsky et al. 2003)) which is expected to expand with observations with future telescopes and improved detection techniques. Mostly extrasolar giant planets, i.e., with masses close to the upper mass limit, are found whose orbits are close to their host star. These exoplanets are also called hot Jupiters. The host star is mostly a main sequence star of spectral type F7 to M4 (Sudarsky et al. 2003). The detection of smaller extrasolar planets, so-called hot Neptunes, as well as the detection of extrasolar planets orbiting cooler host stars provides still a technical challenge. Recently, Udry et al. (2007) and Gillon et al. (2007) have found those extrasolar planets around M dwarfs. So far, detecting brown dwarfs hosting a planet is very seldom. Chauvin et al. (2005) have found the first system. However in this system, the separation between the planet and the brown dwarf is large (55 AU) whereas in the other systems the separation is only a few AU. This could hint a different formation mechanism. Another candidate system has been found by Caballero et al. (2006). They have detected a probable brown dwarf-exoplanet system. Even the Li I doublet could be observed and its equivalent width could be determined. Charbonneau et al.

¹<http://exoplanet.eu/catalog.php>, considering only objects below 13 Jupiter masses.

(2002) reported first the sodium detection in an atmosphere of an extrasolar planet. The first free floating extrasolar planet, a methane T dwarf, has been detected by Zapatero Osorio et al. (2002), for which van-der-Waals broadening should be considered.

Information about the planetary atmospheres can be obtained when observing the planetary host star system, e.g., taking the spectrum during a transit and subtracting the spectrum of the host star (which can be measured during the secondary transit), and if necessary also subtracting the spectrum of the companion (which could be not only another extrasolar planet but also a brown dwarf). Hence, theoretical models are essential for the interpretation of the observed spectra of these systems. Detailed line profile calculations are necessary in order to provide improved synthetic spectra for the description of special spectral features. Otherwise, it is not possible to distinguish between the stellar, substellar, and planetary spectral characteristics. Thus, spectra and single spectral lines become a diagnostic tool.

If the host star is a main sequence star and if its effective temperature is similar to or larger than 5000 K, Stark broadening is the dominant pressure broadening mechanism. Hence, Stark profiles are important for the detailed description of the spectral lines of the host star. If the host star has a rather low effective temperature, i.e., if it is a late-type M or L dwarf, van-der-Waals broadening is dominating and van-der-Waals profiles are required for an satisfying description of its spectral lines. Van-der-Waals profiles could be also necessary when studying a (well separated so that there is no irradiation) low mass companion of the system. The line strength of the Na I D could be an indicator in order to distinguish between the objects in a planetary host star system. There are suggestions that alkalis may be also an opacity source in extrasolar planet atmospheres (Charbonneau et al. 2002; Zhu et al. 2005).

There are ongoing various radial velocity searches and future space missions, such as CoRoT² (launched December 2006), Kepler³ (launch date 2009), and Darwin⁴ (launch date 2015), searching for extrasolar planetary system. The detailed modelling of the spectral lines is of fundamental importance in order to interpret correctly the spectra of follow-up observations.

1.3 Outline

This thesis is organized as follows: Chap. 2 introduces the theoretical background of pressure broadening with the main emphasis on van-der-Waals broadening. Different theoretical approaches, which were done for alkali line profiles used in this work are outlined. In Chap. 3, the various alkali van-der-Waals profiles are presented and discussed. Chap. 4 gives a brief introduction of stellar atmospheres and their computation with PHOENIX focussing on the opacity calculation with line profiles. The influence of the various van-der-Waals line profiles in stellar atmospheres and synthetic spectra is demonstrated and discussed in Chap. 5. Hereafter, in Chap. 6, the influence of the dust formation on alkali line profiles is briefly outlined. Chaps. 7 and 8 concentrate on the comparison between the synthetic spectra including the alkali line profiles and observations whereas in Chap. 7 the emphasis is on the Li I doublet. Chap. 9 deals with Stark broadening, the inclusion of new, non-analytical Stark profiles in PHOENIX and their influences on synthetic spectra. Finally, a summary is given in Chap. 10 as well as an outlook to future work.

²<http://smc.cnes.fr/COROT/>

³<http://kepler.nasa.gov/>

⁴<http://darwin.esa.int/science-e/www/area/index.cfm?fareaid=28>

2 Theoretical Background of Spectral Line Broadening

In 1895, 100 years before the first identification of a brown dwarf (Nakajima et al. 1995), Michelson (Michelson 1895) assumed that the presence of neighboring particles causes the finite width of spectral lines radiated and absorbed by atoms¹. Furthermore, he considered the two most important reasons for spectral line broadening to be “the change in wavelength due to the Doppler effect of the component of the vibrating atom in the line of sight” and “the limitation of the number of regular vibrations by more or less abrupt changes of phase amplitude or plane of vibration caused by collisions”. Up to now, these statements have been held true. However, in contrast to Michelson’s intuition, that there will be “a complete and satisfactory theory forthcoming in the near future”, many reviews of the subject have appeared still dealing with the complex subject, see for example Peach (1981) and references therein as well as Allard & Kielkopf (1982) (e.g. their Fig. 1) and references therein.

Absorption or emission of electromagnetic radiation is caused by a transition between two states of an atom. The frequency of this transition cannot be described as being purely monochromatic. There is always a distribution in frequency of the emitted respectively absorbed radiation. From the distribution of the radiated power, the line profile of a spectral line is obtained, e.g., Allard et al. (2006).

A spectral line can be broadened by three main processes: natural broadening, Doppler broadening and pressure or collisional broadening. Natural broadening is a consequence of the energy–time–uncertainty relation. It is called natural because it is due to the finite emitting time of an atom without other influences. The time in which an electron in an excited state occupies its orbital is only very brief, so that the energy of the orbit cannot have a precise value, even in the case of motionless, isolated atoms. Therefore, spectral lines cannot be infinitely sharp. However, in the cool stellar objects considered in this work, this kind of line broadening only contributes very little to the width of the overall line profile. The natural broadened line profile has a Lorentzian shape with the full width at half maximum² $\Delta\lambda_L$

$$\varphi(\Delta\lambda) = \frac{\Delta\lambda_L}{2\pi} \frac{1}{\Delta\lambda^2 + \Delta\lambda_L^2/4} \quad (2.1)$$

where $\Delta\lambda_L = (\lambda_0^2/\pi c)\gamma_{nat}$ with γ_{nat} is the half width at half maximum³ of the Lorentzian also known as the natural damping constant

$$2\gamma_{nat} = \frac{8\pi^2 e^2}{3m_e c} \frac{1}{\lambda_0^2} \quad (2.2)$$

¹The following discussion holds for both atoms and molecules.

²FWHM

³HWHM

with $e = 4.803 \cdot 10^{-10} \text{ cm}^{3/2} \text{ g}^{1/2} \text{ s}^{-1}$ being the electric elementary charge in the electrostatic unit system, $m_e = 9.1110 \cdot 10^{-28} \text{ g}$ being the mass of an electron, $c = 2.998 \cdot 10^{10} \text{ cm s}^{-1}$ being the velocity of light, and λ_0 being the central wavelength of the line in cm, see Unsöld (1968) and Aller et al. (1982).

Doppler broadening arises from the thermal velocity of a gas of excited atoms and microturbulences, resulting in a Doppler–shift of the photons emitted or absorbed by the gas atoms. In the local thermal equilibrium, the velocity distribution follows the Maxwell–Boltzmann distribution. The profile of a purely Doppler broadened spectral line is Gaussian

$$\varphi(\Delta\lambda) = \frac{1}{\sqrt{\pi}\Delta\lambda_G} e^{-\Delta\lambda^2/\Delta\lambda_G^2} \quad (2.3)$$

where $\Delta\lambda = \lambda - \lambda_0$ denotes the wavelength distance from the line center and $\Delta\lambda_G$ the Gaussian Doppler width. For a Maxwell-Boltzmann distribution with microturbulences of ξ (2 km s^{-1} is a typical value (Allard & Hauschildt 1995)), the Doppler width can be expressed by

$$\Delta\lambda_G = \frac{\lambda_0}{c} \sqrt{\frac{2kT}{m} + \xi^2} \quad (2.4)$$

with T being the temperature and m the particle mass (Aller et al. 1982). In the visible spectral range, Doppler broadening exceeds natural broadening by approximately two to three orders of magnitude, see e.g. Demtröder (2000) and Carroll & Ostlie (1996).

The final contribution to the line profile is due to pressure or collisional broadening. There are two possible ways of disturbing the state of the atoms: either via collisions with neutral atoms or by close encounters with the electric field of an ion. In the following sections, only the first case is of importance since the electron density is not high enough for taking into account Stark broadening. The shift in frequency of an oscillator A during the passing of a perturber B and hence the phase change due to the collision depends on the interaction potential between the two collision partners A and B , so that the shift can be positive or negative. The line profile is determined mostly by the interaction potential. As a result of elastic and inelastic collisions, the line profile has approximately a Lorentzian shape. The combined line profile due to natural broadening and pressure broadening is referred to as damping profile.

The convolution of the three contributions, the Doppler profile and the two damping profiles, gives the overall line shape, called the Voigt profile

$$\varphi(\Delta\lambda) = \frac{1}{\sqrt{\pi}\Delta\lambda_G} H(\alpha, y) = \frac{1}{\sqrt{\pi}\Delta\lambda_G} \frac{\alpha}{\pi} \int_{-\infty}^{+\infty} \frac{e^{-x^2}}{\alpha^2 + (y-x)^2} dx, \quad (2.5)$$

where $H(\alpha, y)$ is the Voigt function with its damping parameter $\alpha = 2\gamma\lambda_0^2/(4\pi c\Delta\lambda_G)$ with γ as damping constant and $y = \Delta\lambda/\Delta\lambda_G$. In this total line profile, the line core is dominated by the Doppler broadening and hence is Gaussian, whereas the (near) line wings are dominated by the Lorentzian damping profiles.

In the following sections, various calculations of the line profiles will be introduced. First a brief introduction to the classical theory of pressure broadening is given in Sect. 2.1, introducing the analytical approach for line profiles and discussing the various validity ranges of the line profiles. A general quantum–mechanical approach is presented next in Sect. 2.2. Section 2.3 deals with a fully quantum mechanical description of the non–analytical Lorentzian near line wing profiles. In Sect. 2.4, the calculation procedure of the non–analytical line profiles for the far line wing and near line wings via the unified semi–classical theory is presented. The profiles themselves are later introduced in Chap. 3. Only the main assumptions and steps are presented for all methods.

2.1 Classical Theory of Collisional Line broadening

The two basic classical pictures for the interaction of an radiating atom with nearby perturbers are described as well as their validity (see Unsöld (1968) and Mihalas (1970)). General expressions are given with emphasis on the van–der–Waals interaction which is the dominating interaction type in the cool atmospheres considered here. (This is also the case for the Sects. 2.2, 2.3 and 2.4.)

The first theory is based on the impact approximation and is valid for the description of the inner zone of a spectral line for which the interactions of many, more distant particles must be studied in detail. It assumes sudden collisions⁴ which interrupt the radiating wave train with a sudden phase shift or by inducing a transition. The broadened line profile is in this case Lorentzian.

In the alternative approach, the atom is regarded as radiating in the field of an ensemble of perturbers. In this theory, the time dependence of the perturbation is neglected. Instead, the probability of a perturbation in angular frequency is of main interest. Due to this focus this approach is called the statistical approximation, which is valid for the description of the far line wings. Finally, the limits of both approaches are discussed.

2.1.1 Impact Approximated Van–Der–Waals Profiles

The commonly used “simplistic” approach of van–der–Waals broadening in the impact approximation was introduced by Unsöld (1968). It is based on encounters between an emitting atom and perturbing atoms. Consequently, the wave train of the emitter is perturbed in its phase through the collisions. The duration of each collision is assumed to be much shorter than the time in between the collisions (the impact approximation). The probability of an unperturbed flight of an atom between the time t_0 and $t_0 + dt_0$ is

$$e^{-\frac{t_0}{\tau}} \frac{dt_0}{\tau}, \quad (2.6)$$

with τ being the mean time between two encounters. A normalized ($\int_{-\infty}^{+\infty} \varphi(\omega) d\omega = 1$) spectral line profile $\varphi(\omega)$ can be derived, see Unsöld (1968),

$$\varphi(\omega) = \text{const} \int_0^{\infty} \left\{ \frac{\sin \frac{\omega - \omega_0}{2} t_0}{\frac{\omega - \omega_0}{2}} \right\}^2 e^{-\frac{t_0}{\tau}} dt_0 = \frac{1}{\pi\tau} \cdot \frac{1}{(\omega - \omega_0)^2 + (1/\tau)^2}, \quad (2.7)$$

where ω_0 is the unperturbed frequency. The damping constant can be expressed by the mean time τ between two collisions by

$$\gamma = \frac{1}{\tau} = \pi b_0^2 n_P \bar{v}. \quad (2.8)$$

where πb_0^2 is the effective cross section. The mean relative velocity \bar{v} of the emitting and perturbing particles with their molecular weights μ_E and μ_P is given by⁵

$$\bar{v} = \sqrt{\frac{8}{\pi} R_g T \left(\frac{1}{\mu_E} + \frac{1}{\mu_P} \right)} \quad (2.9)$$

with R_g being the gas constant. Simultaneous collisions have been neglected in this derivation and it has been assumed that the mean distance between two perturbing particles is much greater than

⁴This is known as the impact approximation.

⁵This subscript notation for the emitter and perturber properties is valid throughout this work.

b_0 which is discussed in more detail hereafter.

For a description of the interaction between the emitter and perturber, the following approach is used: let the distance between the perturbing particle and the emitter be R . In this case, the shift of the frequency of the spectral line is

$$\Delta\omega = \frac{2\pi C_n}{R^n}, \quad (2.10)$$

where C_n represents a specific interaction constant dependent on the exponent n of the type of interaction.

The Weisskopf Approximation

Already in 1924, Lenz (1924) pointed out that “phase perturbing collisions” also contribute to collisional broadening of a spectral line. Only during such elastic collisions, the energy levels of the emitting atom are slightly shifted so that the frequency of the emitted photon is put out of tune. The energy difference for positive frequency shifts is provided by the kinetic energy of the collision partners. In case of a negative frequency shift, the excess energy is transformed into kinetic energy. Thus the phase change η can be defined by the change $\Delta\omega$ of the unperturbed angular frequency

$$\eta = \int_{-\infty}^{+\infty} \Delta\omega dt. \quad (2.11)$$

Furthermore, it is assumed that the perturber is still treated as a classical particle and moves on a rectilinear trajectory, see Fig. 2.2, with $R(t) = (b^2 + \bar{v}^2 t^2)^{1/2}$ and b being the impact parameter. The interaction is described by Eq. 2.10 and thus Eq. 2.11 becomes

$$\eta = \int_{-\infty}^{+\infty} \frac{2\pi C_n}{R^n(t)} dt. \quad (2.12)$$

The phase shift can be calculated directly when using the angle between R and b as variable of the integration

$$\eta = \frac{2\pi C_n}{\bar{v} b^{n-1}} c_n. \quad (2.13)$$

Since the van-der-Waals interaction is of interest here, the exponent n equals 6 with $c_6 = 3\pi/8$. Lenz (1924, 1933) and Weisskopf (1932) concluded that all encounters with $b \ll b_0$ and $\eta > \eta_0$ have to be considered as impacts, with the arbitrary critical value η_0 . From Eq. 2.13, they have derived the impact radius also known as Weisskopf radius

$$b_0 = \left(\frac{2\pi C_n c_n}{\bar{v} \eta_0} \right)^{\frac{1}{n-1}}. \quad (2.14)$$

This expression for the Weisskopf radius can be in turn set into Eq. 2.8. With b_0 and the Eqs. 2.7–2.9, the damping constant results in

$$2\gamma = \frac{2}{\tau} = 2\pi \left(\frac{2\pi C_n c_n}{\bar{v} \eta_0} \right)^{\frac{2}{n-1}} \bar{v} n_P = \{ (2\pi)^{n+1} c_n^2 \eta_0^{-2} C_n^2 \bar{v}^{n-3} \}^{\frac{1}{n-1}} \cdot n_P. \quad (2.15)$$

If an interaction between neutral unpolarized particles is assumed, which is the van-der-Waals interaction, then as mentioned above $n = 6$. Thus, the Lorentzian damping constant with the phase change $b_0 = 0.61$ (equals a phase change of 35°) is given by

$$2\gamma_6 = 17.0 C_6^{2/5} \bar{v}^{3/5} n_P. \quad (2.16)$$

Perturber	α_P (10^{-24} cm ³)
H	0.666793
H ₂	0.806 ± 0.5 %
He	0.204956

Table 2.1: Polarizabilities of perturbers (Weast 1988).

If hydrogenic perturbers are assumed, C_6 is given by (Unsöld 1968; Mihalas 1970)

$$C_6 = \frac{\alpha_P}{\alpha_H} 1.01 \times 10^{-32} (Z+1)^2 \left[\frac{E_H^2}{(E-E_l)^2} - \frac{E_H^2}{(E-E_u)^2} \right] \quad (2.17)$$

with α_P being the polarizability of the perturber, α_H being the polarizability of hydrogen with $E_H = 13.6$ eV, Z being the charge, E the ionization energy, E_l being the lower energy level and E_u the upper energy level of the absorber. The parameters of the polarizability for the three most important perturbers in cool atmospheres (Weast 1988) are listed in Table 2.1.

2.1.2 Statistical Approximation

The statistical approximation is a conceptually different approach to the impact approximation arising from the work of Holtsmark (1919a,b, 1924) on Stark broadening. For neutral atom pressure broadening, Holtsmark's ideas have been adopted by Margenau (1932) and Kuhn & London (1934). The time dependent development of the perturbations which is characteristic for the theory of collisional broadening is ignored in this approximation. It is assumed that during the collision the emission contributes mostly to the far wing of the line. The unperturbed radiation, i.e., before and after the collision, which is just interrupted by the collision is responsible for the near line wing (Allard & Kielkopf 1982). The basic concept is outlined in the following. The starting point of this approach is an atom radiating in a statistically fluctuating field of perturbers. For the application of the quasi-static approximation, the motions of the perturbers are neglected.

Nearest Neighbor Approximation

It is assumed that the main effect is due to the strongest perturbation at any time so that the shift is due to the impact with the nearest neighbor.

Before starting with the explicit evaluation of the situation above, we discuss the probability $\bar{W}(R)$ that no particle is within the radius R and the probability $\bar{w}(R, dR)$ that there is no particle in the spherical shell with the radius R to $R + dR$. The probability $\bar{W}(R + dR)$ that no particle is found within the radius $R + dR$ can be obtained by a product ansatz

$$\bar{W}(R + dR) = \bar{W}(R) \cdot \bar{w}(R, dR). \quad (2.18)$$

Furthermore, the probability of finding one particle in the spherical shell between R and $R + dR$ is $4\pi R^2 n_P dR$. Thus with

$$\bar{w}(R, dR) + 4\pi R^2 n_P dR = 1 \quad (2.19)$$

Eq. 2.18 becomes⁶

$$\bar{W}(R) + \frac{d\bar{W}(R)}{dR} dR = \bar{W}(R) (1 - 4\pi R^2 n_P dR). \quad (2.20)$$

⁶The left side of Eq. 2.20 is derived from the definition of the partial derivative: $f'(p) = \lim_{h \rightarrow 0} \frac{f(p+h) - f(p)}{h}$.

By integration, an expression for $\bar{W}(R)$ is obtained

$$\bar{W}(R) = e^{-\frac{4\pi}{3}R^3 n_P}. \quad (2.21)$$

Returning to the actual problem, the probability $W(R) dR$ that the nearest perturber has a distance of R from the emitting atom can be calculated as the product of the probability that one particle is within the shell from R to $R + dR$ and the probability that there is no particle within the distance R . Thus, together with the considerations taken above and Eqs. 2.18 and 2.21, the probability $W(R)dR$ is given by

$$W(R)dR = 4\pi R^2 n_P dR e^{-\frac{4\pi}{3}R^3 n_P} = e^{-\left(\frac{R}{r_0}\right)^3} d\left(\frac{R}{r_0}\right)^3, \quad (2.22)$$

if the mean distance r_0 between two perturbers is defined by

$$\frac{4\pi}{3} r_0^3 n_P = 1. \quad (2.23)$$

Applying Eq. 2.23, the “normal” frequency shift when two particles are separated by the mean distance r_0 becomes

$$\Delta\omega_0 = \frac{2\pi C_n}{r_0^n} = 2\pi C_n \left(\frac{4\pi}{3} n_P\right)^{\frac{n}{3}}, \quad (2.24)$$

see Eq. 2.10, so that $\frac{\Delta\omega}{\Delta\omega_0} = \left(\frac{r_0}{R}\right)^n$. The exponent of the van–der–Waals interaction is again $n = 6$ and C_6 is given above. Thus Eq. 2.22 can be rewritten as

$$W(R)dR = e^{-\left(\frac{\Delta\omega_0}{\Delta\omega}\right)^{3/n}} d\left(\frac{\Delta\omega}{\Delta\omega_0}\right)^{3/n}. \quad (2.25)$$

Furthermore, the line profile $\varphi(\Delta\omega)$ (which is the intensity distribution of the spectral line) can be expressed in terms of the probability $W(R)dR$, i.e.

$$\varphi(\Delta\omega) d(\Delta\omega) \propto W(R) \frac{dR}{d(\Delta\omega)} d(\Delta\omega). \quad (2.26)$$

Consequently,

$$\varphi(\Delta\omega) d(\Delta\omega) = \frac{3}{n} \left(\frac{\Delta\omega_0}{\Delta\omega}\right)^{\frac{3}{n}+1} e^{-\left(\frac{\Delta\omega_0}{\Delta\omega}\right)^{3/n}} d\left(\frac{\Delta\omega}{\Delta\omega_0}\right). \quad (2.27)$$

So far, the line profile is assumed to be only the result of the perturbation with the nearest neighbor. However, this theory fails for the description of the near line wing because in this part, the line profile is the result of the perturbations by all particles, especially the more distant ones, and not just by the nearest neighbor. Nevertheless, it is an useful approximation since the nearest neighbor exerts the strongest perturbation.

2.1.3 Validity of the Impact and Statistical Approximation

The basic prerequisite for the validity of the impact approximation is that the collision time $\tau_c \sim b/\bar{v}$ should be small compared to the time τ between the impacts, $\tau_c \ll \tau$. Thus the Weisskopf radius b_0 must be small compared to the mean inter particle distance. There are violations of the criterion for sufficiently high particle densities, i.e., if there is more than one particle within the

Weisskopf radius b_0 , or for sufficiently large values of the impact parameter b , or for slow moving perturbers.

At sufficiently large frequency separations $\Delta\omega$, the statistical approach becomes valid. From the general properties of the Fourier transform, the collision time τ_c can be expressed by the shift of frequency $\Delta\omega$

$$\tau_c \sim \frac{1}{\Delta\omega}. \quad (2.28)$$

However, if the frequency separations $\Delta\omega$ become large, τ_c will be less than the characteristic impact time b/\bar{v} . Thus, the impact approach fails. At such large frequency separations, the radiation is due to collisions with small impact parameters b_c and at the frequency $\omega = \omega_0 + \Delta\omega(b_c)$. Therefore, the line profile will be proportional to the statistical frequency of the collisions at b_c . The statistical approach is valid when all encounters take place within the Weisskopf radius b_0 . Consequently, the total line profile consists of an inner part (near line wing and core) described by the impact theory and the far line wing, which is the result of the statistical theory. Instead of another theory describing the transition region of the two theories, a convolution of these two parts is sufficient. Furthermore, it is assumed that the change between the two regimes is sudden. A boundary frequency $\Delta\omega_b$ can be derived, when assuming that R in Eq. 2.10 is equal the Weisskopf radius b_0 in Eq. 2.14 and $\eta_0 \approx 1$

$$\Delta\omega_b = \left(\frac{\bar{v}^n}{2\pi C_n \cdot c_n^n} \right)^{\frac{1}{n-1}}, \quad (2.29)$$

where n equals 6 for the van-der-Waals interaction. For the Lorentzian impact profile, the intensity distribution is frequency dependent like $1/\Delta\omega^2$, whereas for the statistical profile the frequency dependence is $\sim 1/\Delta\omega^{\frac{3}{n}+1}$, see Eq. 2.27. As long as $n > 3$, the statistical far wing profiles have a slower decay with greater distance from the line center than the impact near line wing profiles.

2.2 The Spectrum of a Quantum Mechanical System and its Autocorrelation Function

In this section, a general quantum mechanical approach of van–der–Waals broadening is given which is used in Sects. 2.3 and 2.4.

An excited atom (emitter) is immersed in a gas of neutral atoms (perturbers). Furthermore, it is assumed that the ratio of emitters to perturbers is very small. Hence, interactions between emitters can be ignored because the average distance between them is large. Therefore, this system can be described as a collection of non–interacting cells each containing one spatially fixed emitter and many moving perturbers. The Hamiltonian of a single cell is given by

$$H = H_E + H_P + V \quad (2.30)$$

where V is the emitter–perturber interaction potential. The probability of a spontaneous dipole transition from an initial state i to a final state f in such a cell is (Schiff 1955; Smith et al. 1969)

$$P_{if} = \frac{4\omega_{if}^3}{3\hbar c^3} |\langle i|\mathbf{d}|f\rangle|^2 \quad (2.31)$$

with $\omega_{if} = (E_i - E_f)/\hbar$ being the frequency and \mathbf{d} the dipole moment of the whole system. $|i\rangle$ and $|f\rangle$ are Hamiltonian eigenstates of the unperturbed Hamiltonian $H_E + H_P$ in Eq. 2.30 and belong to the eigenvalues E_i and E_f . In the following paragraphs, \mathbf{d} describes the dipole moment of the emitter. When starting from Eq. 2.31 and summing over all possible initial and final states of the emitters as well as over all cells with the statistical intrinsic probability ρ_i which is the probability of the atom being in the state $|i\rangle$, the power emitted per unit frequency interval, $P(\omega)$, is obtained by

$$P(\omega) = \frac{4N_E\omega^4}{3c^3} \varphi(\omega) \quad (2.32)$$

with

$$\varphi(\omega) = \sum_{if} \delta(\omega - \omega_{if}) |\langle i|\mathbf{d}|f\rangle|^2 \rho_i \quad (2.33)$$

and N_E being the number of emitters. $\varphi(\omega)$ is still referred to as the line profile function. It is also known as "spectrum" or "line shape" in the literature. In some cases, it is not possible to calculate the profile function as in Eq. 2.33 (Mihalas 1970). Then, it is valuable to use its Fourier transform which results in the autocorrelation function of the light amplitude. The autocorrelation function $\Phi(s)$ describes the average evolution of a wave train⁷ $f(t)$ over a time interval s from an initial time t

$$\Phi(s) = \langle f(t)^* f(t+s) \rangle_t. \quad (2.34)$$

Taking the Fourier transform of Eq. 2.33, the following expression is obtained for the autocorrelation function

$$\Phi(s) = \int_{-\infty}^{+\infty} e^{-i\omega s} \varphi(\omega) d\omega = \sum_{if} e^{-i\omega_{if}s} \rho_i |\langle i|\mathbf{d}|f\rangle|^2. \quad (2.35)$$

Since $\varphi(\omega)$ must be real, the autocorrelation function must be only computed for positive s . Eq. 2.35 satisfies

$$\Phi(-s) = [\Phi(s)]^* \quad (2.36)$$

⁷* is used for complex conjugate.

and $\varphi(\omega)$ can be calculated from the real part \Re of the inverse Fourier transform

$$\varphi(\omega) = \frac{1}{\pi} \Re \left\{ \int_0^{\infty} e^{i\omega s} \Phi(s) ds \right\}. \quad (2.37)$$

2.3 Quantum Theory of Line Broadening

This section gives a short introduction of quantum mechanical line broadening as described in Mullaamphy et al. (2007) and references therein. The derivation of the theoretical background presented here closely follows the approach of Mullaamphy (2002) and Cooper (1968). The general impact theory of pressure broadening by Baranger (1958c), in which the fully quantum mechanical scattering problem is treated, is discussed. This is Baranger's third part of his pressure broadening theory and based on Baranger (1958a) and Baranger (1958b). The quantum mechanical line profile is derived briefly including the main assumptions. It is expressed in a form so that the width and shift can be extracted for the Lorentzian describing the near line wing of the perturbed spectral line.

The Spectrum

The δ function in Eq. 2.33 represents the spectrum as a number of infinite spikes at discrete values of ω . Considering radiation damping, a natural line width can be introduced by replacing the δ function in Eq. 2.37 by a Lorentzian with a half width γ_{if} . Hence, the line profile including a shift η_{if} becomes

$$\varphi(\omega) = \sum_{if} \frac{\gamma_{if}/\pi}{(\omega - \omega_{if} - \eta_{if})^2 + \gamma_{if}^2} \rho_i |\langle i | \mathbf{d} | f \rangle|^2. \quad (2.38)$$

The autocorrelation function in Eq. 2.35 can be equivalently written in terms of the time evolution operator $\mathcal{U}(s, 0)$ which transforms a state at a time 0 into a state at a time s

$$|\Psi(s)\rangle = \mathcal{U}(s, 0)|\Psi(0)\rangle \quad (2.39)$$

so that

$$\Phi(s) = \sum_n \langle n | \mathbf{d} \mathcal{U}^\dagger(s, 0) \rho \mathbf{d} \mathcal{U}(s, 0) | n \rangle \quad (2.40)$$

and since H is time independent in Eq. 2.30, $\mathcal{U}(s, 0)$ is given in the Schrödinger representation

$$\mathcal{U}(s, 0) = e^{-iHs/\hbar}. \quad (2.41)$$

In Eq. 2.40, the density operator of the entire system reads

$$\rho = \sum_m |m\rangle \rho_m \langle m| \propto e^{-H/kT} \quad (2.42)$$

with k being Boltzmann's constant and T the gas temperature. Furthermore, Eq. 2.40 is in the form of a trace and can be rewritten with the trace operator Tr which acts over all states of the entire system of the radiating atom and the assembly of perturbers as

$$\Phi(s) = Tr[\rho \mathbf{d}(0) \mathbf{d}(s)], \quad (2.43)$$

where

$$\mathbf{d}(0) = \mathbf{d} \quad \text{and} \quad \mathbf{d}(s) = \mathcal{U}^\dagger(s, 0) \mathbf{d}(0) \mathcal{U}(s, 0) \quad (2.44)$$

are the dipole operators of the emitter in the Heisenberg representation at the time 0 and s . The right hand side in Eq. 2.43 represents the weighted average over the statistical mixture of states and can be written therefore as

$$\Phi(s) = \langle \mathbf{d}(0) \mathbf{d}(s) \rangle_{AV}. \quad (2.45)$$

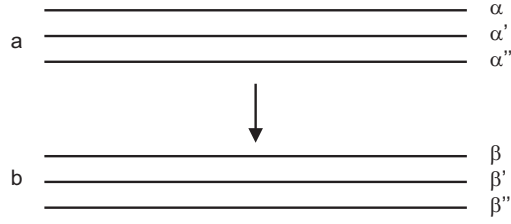


Fig. 2.1: Transition between the fine structure levels (Mullamphy 2002).

Weak Coupling Approximation

Using Eq. 2.30 in Eq. 2.42 and assuming that the average interaction in each cell between the emitter and the perturbers is negligible (i.e. $V \ll kT$), then the term representing the emitter-perturber interaction in Eq. 2.30 tends to be zero and the density operator results in

$$\rho \sim e^{-(H_E+H_P)/kT} \sim \rho_E \rho_P. \quad (2.46)$$

Consequently, there is no correlation between the initial emitter and perturber states. Equation 2.46 represents the weak coupling approximation. It is valid if the energy splitting between the atomic levels satisfy the condition $\hbar\Delta\omega \ll kT$ (Smith et al. 1969). Furthermore introducing the evolution operator $\mathcal{U}_E(s, 0)$ via⁸

$$\mathcal{U}(s, 0) = e^{-iH_P s/\hbar} \mathcal{U}_E(s, 0) \quad (2.47)$$

and separating the states of the total system into the product of emitter and perturber states, the autocorrelation function can be expressed as

$$\Phi(s) = Tr_N \left[\mathbf{d} \langle \mathcal{U}_E^\dagger(s, 0) \mathbf{d} \mathcal{U}_E(s, 0) \rangle_{AV} \rho_E \right], \quad (2.48)$$

where the trace is performed over N perturber states.

Impact Approximation

In the impact approximation, it is assumed that the time between the collisions is large compared to the duration of the collision. Therefore, each collision represents an independent event since it is effectively complete before the next collision starts. But because of the low importance of each independent event, the average over a large number of collisions is taken. Consequently, it means that the average collision is weak.

In Fig. 2.1, a transition between the fine structure levels is depicted. The transition between the two sets of well separated fine structure levels (labelled a and b) yield the emitted radiation. Each level is divided into Zeeman substates (labelled with α, α', \dots and β, β', \dots). Furthermore, the assumption is made that the collisions cause transitions between the substates and not between the fine structure levels.

In the following, the emitter density ρ_E is considered constant for the initial states because the energy difference between the fine structure levels is much greater than the Zeeman splitting. Hence, Eq. 2.48 can be reformulated to

$$\Phi(s) = \rho_E \sum_{\alpha\alpha'\beta\beta'} \mathbf{d}_{\alpha\beta} \left\{ \langle \beta | \mathcal{U}_E^\dagger(s, 0) | \beta' \rangle \langle \alpha' | \mathcal{U}_E(s, 0) | \alpha \rangle \right\}_{AV} \mathbf{d}_{\alpha'\beta'} \quad (2.49)$$

⁸It is the solution of $i\hbar \frac{d}{ds} \mathcal{U}_E(s, 0) = (H_E + e^{iH_P s/\hbar} V e^{-iH_P s/\hbar}) \mathcal{U}_E(s, 0)$.

where

$$\mathbf{d}_{\alpha\beta} = \langle \alpha | \mathbf{d} | \beta \rangle. \quad (2.50)$$

For a perturbation solution, the interaction picture is used via the evolution operator⁹

$$U(s, 0) = e^{iH_E s/\hbar} \mathcal{U}_E(s, 0). \quad (2.51)$$

Applying Eqs. 2.49 and 2.51 and dropping ρ_E now (since $\Phi(s)$ will be normalized later) the auto-correlation function reads

$$\begin{aligned} \Phi(s) &= \sum_{\alpha\alpha'\beta\beta'} \mathbf{d}_{\alpha\beta} \{ \langle \beta | U^\dagger(s, 0) e^{iH_E s/\hbar} | \beta' \rangle \langle \alpha' | e^{-iH_E s/\hbar} U(s, 0) | \alpha \rangle \}_{AV} \mathbf{d}_{\alpha\beta}^* \\ &= \sum_{\alpha\alpha'\beta\beta'} e^{-i(E_{\alpha'} - E_{\beta'})s/\hbar} \mathbf{d}_{\alpha\beta} \{ \langle \alpha' | U^\dagger(s, 0) | \alpha \rangle \langle \beta | U(s, 0) | \beta' \rangle \}_{AV} \mathbf{d}_{\alpha'\beta'}^*. \end{aligned} \quad (2.52)$$

In order to find the solution of Eq. 2.52, the average must be determined. Therefore a small time interval Δt is considered. With the impact approximation, the problem can be converted into a differential equation which can be solved. Additionally, the notation of the ‘‘doubled atom’’ (Baranger 1958b) is introduced in order to make the two–state case similar to an one–state case. Baranger considered a new function space. It is the direct product of the function space of the atom by itself, i.e., each state of the ‘‘doubled’’ system is associated with two states of the atom with an initial state and a complex conjugate of the final state. Hence, the autocorrelation function is given by

$$\Phi(s) = \sum_{\alpha\alpha'\beta\beta'} \mathbf{d}_{\alpha\beta} \langle \langle \alpha\beta | \exp \left[\frac{-i(H_a - H_b)s}{\hbar} + \Phi_{ab}s \right] | \alpha'\beta' \rangle \rangle \mathbf{d}_{\alpha'\beta'}^* \quad (2.53)$$

with

$$\Phi_{ab} \equiv \frac{1}{\Delta t} \{ U_b^\dagger(\Delta t, 0) U_a(\Delta t, 0) - 1 \}_{AV}, \quad (2.54)$$

where $U_{a(b)}$ acts only on the states $|\alpha\rangle(|\beta\rangle)$ respectively. The resulting line profile can be written as following

$$\varphi(\omega) = \frac{1}{\pi} \Re \left\{ \sum_{\alpha\alpha'\beta\beta'} \mathbf{d}_{\alpha\beta} \langle \langle \alpha\beta | \exp \left[i\omega s - \frac{i(H_a - H_b)s}{\hbar} + \Phi_{ab}s \right] | \alpha'\beta' \rangle \rangle \mathbf{d}_{\alpha'\beta'}^* \right\}. \quad (2.55)$$

The derivation of the results above is restricted to the following validity criteria:

$$\tau \gg \tau_c \quad \text{and} \quad \Phi_{ab}\tau \ll 1. \quad (2.56)$$

These criteria originate from the introduction of a differential equation and the limitation of the duration τ_c of a collision which must be smaller than the time τ between the collisions. With the combination of the two restrictions the validity criterion under the impact approximation is obtained

$$\Phi_{ab}\tau_c \ll 1. \quad (2.57)$$

Mullamphy (2002) found that Φ_{ab} is of the same order as the line width so that the impact approximation is valid for their analyzed transitions.

⁹It satisfies $i\hbar \frac{d}{ds} U(s, 0) = V(s)U(s, 0)$ where $V(s) = e^{i(H_E + H_P)s/\hbar} V e^{-i(H_E + H_P)s/\hbar}$.

Because of the assumption of completed collisions within the time τ under the impact approximation, the time evolution operator $U(\tau, 0)$ is replaced by the scattering operator S in the interaction pictures for a single collision

$$U(+\infty, -\infty) = S. \quad (2.58)$$

The time of closest approach for the colliding atom happens at $t = 0$. With Eq. 2.58, Eq. 2.54 can be rewritten in terms of the scattering matrix S

$$\Phi_{ab} = \frac{1}{\tau} \left\{ S_b^\dagger S_a - 1 \right\}_{AV}. \quad (2.59)$$

Spectral Line Profiles

The application of Baranger's quantum mechanical theory (Baranger 1958c) for non-overlapping isolated spectral lines results in the line width and line shift of a Lorentzian profile. Considering a spectral line with the transition between an initial $|j_i\rangle$ and a final emitter state $|j_f\rangle$ of total angular momentum $\mathbf{j} = \mathbf{L} + \mathbf{S}$ for which the quantum numbers (n, L, S) are suppressed for convenience, the Lorentzian half width γ and shift η is given by¹⁰

$$\gamma + i\eta = n_P \int_0^\infty f(E) S(E) dE, \quad (2.60)$$

where $f(E)$ is the normalized Maxwellian perturber energy distribution

$$f(E) = \frac{2\pi}{(\pi kT)^{3/2}} \sqrt{E} e^{-\frac{E}{kT}}, \quad (2.61)$$

n_P the perturber number density and

$$S(E) = \frac{\hbar^2 \pi}{M^2} \sqrt{\frac{M}{2E}} \sum_{l'} \sum_{J_i J_f} (2J_i + 1)(2J_f + 1) (-1)^{l+l'} \left\{ \begin{matrix} J_f & J_i & 1 \\ j_i & j_f & l \end{matrix} \right\} \left\{ \begin{matrix} J_f & J_i & 1 \\ j_i & j_f & l' \end{matrix} \right\} \\ [\delta_{ll'} - \langle j_i l' J_i | S | j_i l J_i \rangle \langle j_f l' J_f | S | j_f l J_f \rangle^*]. \quad (2.62)$$

The 6-j symbols represent a summation over Clebsch–Gordan coefficients for elastic and inelastic contributions. The scattering matrix of the lower and upper states of the transition has to be determined. The procedure for obtaining these elements is discussed in Mullamphy et al. (2007) and references therein.

¹⁰The detailed derivation of the following expressions can be found in Mullamphy (2002).

2.4 Unified Semi–Classical Theory

There are two types of theories which are discussed in the literature for the case of pressure broadening in cool atmospheres. For the near line wing of a spectral line, the impact approximation can be applied, see Sects. 2.1.1 and 2.3, and for the far line wing of the line, the statistical approximation, see Sect. 2.1.2, is applicable (Unsöld 1968). With the unified semi–classical theory, it is possible to compute an overall line profile. The perturbers are treated classically and it is assumed that they follow rectilinear trajectories. The emitters are treated quantum mechanically. Two terms describe the total line profile. The first term corresponds to the impact near line wing and the second to the far line wing in the one–perturber approximation. The far line wing is convoluted with the impact near line wing. An expansion in powers of the perturber density is made. Higher order terms represent successive convolution powers of the far line wing into the near line wing. The detailed derivations are found in Anderson (1952), Baranger (1958a,b), and Royer (1971, 1978, 1980). The two theories are combined in a modern detailed approach in Allard & Kielkopf (1982) and Allard et al. (1994, 1999, 2003, 2005). Nicole Allard’s approach is outlined in the following paragraphs, and the expansion in powers of perturber density of the line profile has been done up to the third order.

Basic Concepts

As before, the starting point is an atom, the emitter, immersed in a gas with other atoms, the perturbers. There are N_P perturbers in a volume V . Considering the following assumptions when calculating $\Phi(s)$:

- the radiator is stationary in space
- the perturbers are mutually independent
- the interaction potentials between the emitter and perturbers are scalarly additive
- the dipole moment d_{if} is supposed to be slowly varying with the interatomic distance and can be factored out as constant.

Furthermore, in order to include degeneracy of atomic levels, the adiabatic assumption¹¹ is considered, i.e., the total wave function is a product of electronic χ_e and nuclear $\phi_{e,n}$ components (Royer 1978) in Baranger’s quantum theory of spectral line shapes (Baranger 1958a,b). With these simplifying assumptions, the total spectral line profile $\varphi(\omega)$, i.e., when all N_P perturbers interact, can be expressed as the Fourier transformation (FT) of the N_P^{th} power of the autocorrelation function $\phi_1(s)$ of a unique atom–perturber pair at a time s . Then the total autocorrelation function $\Phi(s)$ reads (Royer 1971)

$$\Phi(s) = (\phi_1(s))^{N_P} |d_{if}|. \quad (2.63)$$

Since d_{if} is assumed to be constant it is neglected until otherwise mentioned.

Thus, for a fixed number density of perturbers n_P (the ratio of the number of perturbers and their occupied volume) and a large volume, the autocorrelation function can be written as

$$\Phi(s) = e^{-n_P g(s)} \quad (2.64)$$

¹¹or equivalently the Born–Oppenheimer approximation in the case where the translational motion of the atom is treated quantum mechanically (Royer 1971).

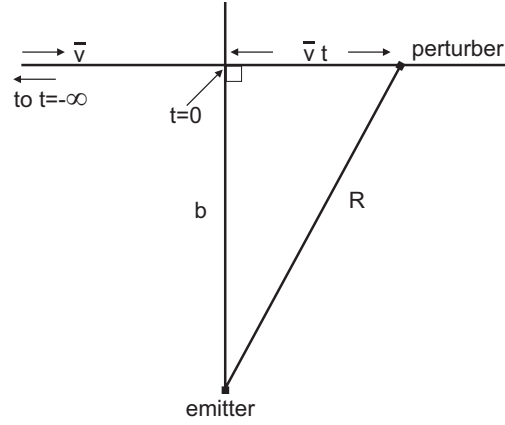


Fig. 2.2: Time dependence of the perturbation of the emitter via the perturber. It is the geometry of a classical emitter-perturber collision (Peach 1981).

with

$$g(s) = \int_0^{+\infty} v f(v) dv \int_0^{+\infty} 2\pi b db \int_{-\infty}^{+\infty} (1 - e^{i\eta(t,s)}) dt, \quad (2.65)$$

where b is the impact parameter of the perturber trajectory, v the relative velocity, $f(v)$ the Maxwellian velocity distribution, and $\eta(t,s)$ the phase shift calculated along a classical path

$$\eta(t,s) = \int_t^{t+s} \Delta V(t') dt'. \quad (2.66)$$

The phase shift is evaluated in terms of the potential ΔV between the electronic energies of the transition.

However, the electric-dipole moment is not constant as assumed earlier and in Allard et al. (1999) the *modulated* dipole moment in dependence of the internuclear distance $R(s)$ at a time s is introduced. Each perturber follows a rectilinear trajectory, since the classical path approximation is assumed, see Fig. 2.2, and the separation of the emitter and perturber $R(s)$ is

$$R(s) = [b^2 + (x + \bar{v}s)^2]^{1/2} \quad (2.67)$$

with x as the position of the perturber along its trajectory at a time $t = 0$ for a single mean velocity $\bar{v} = (8kT/\pi\mu)^{1/2}$, where μ is the reduced mass of the atoms. The interacting atoms approach the initial and final atomic states of the transition as $R \rightarrow \infty$ at different energy surfaces e and e' (e belongs to the initial and e' to the final states). Furthermore, the radiative dipole transition moment $d_{ee'}$ of each component of the line changes during the collision due to its dependence of $R(s)$. For a state e the potential energy is

$$V_e[R(s)] = E_e[R(s)] - E_e^\infty \quad (2.68)$$

with E_e^∞ being the initial energy for $R \rightarrow \infty$ and the difference potential, which is the difference between the potential energies of the states e' and e , is

$$\Delta V(R) \equiv V_{e'e}[R(s)] = V_{e'}[R(s)] - V_e[R(s)]. \quad (2.69)$$

With Eq. 2.69 the *modulated* dipole moment is defined by

$$\tilde{d}_{ee'}[R(s)] = d_{ee'}[R(s)] e^{-\frac{\beta}{2} V_e[R(s)]}, \quad (2.70)$$

with $\beta = 1/(kT)$. For consistency with the straight trajectory approximation, the Boltzmann factor $e^{-\beta V_e(R)}$ should be dropped but it is kept because of an improvement of the results in the line wings (Allard et al. 2005). For a transition $\alpha = (i, f)$ from an initial state i to a final state f , Eq. 2.65 has to be rewritten as

$$g_\alpha(s) = \frac{1}{\sum_{e,e'}^{(\alpha)} |d_{ee'}|^2} \sum_{e,e'}^{(\alpha)} \int_0^{+\infty} 2\pi b db \int_{-\infty}^{+\infty} dx \tilde{d}_{ee'}[R(0)] \times \left[\exp \left\{ \frac{i}{\hbar} \int_0^s dt V_{e'e}[R(t)] \right\} \tilde{d}_{ee'}^*[R(s)] - \tilde{d}_{ee'}[R(0)] \right]. \quad (2.71)$$

The phase shift $\eta(s)$ along a classical path can be written in an analogous form to Eq. 2.66

$$\eta(s) = \frac{i}{\hbar} \int_0^s V_{e'e}[R(t)] dt. \quad (2.72)$$

Low Density Approximation

At densities found in cool stellar atmospheres, the evaluation of the autocorrelation function can be done by the expansion in powers of the perturber density

$$\Phi(s) = 1 - n_P g(s) + \frac{n_P^2}{2!} g(s)^2 + \dots \quad (2.73)$$

At the same time, the many-perturber effects are uniquely recognizable and only the term by term Fourier transform would have to be done in order to obtain the total line profile function. But for large s , the Fourier transform diverges as $\omega \rightarrow 0$ because $g(s)$ is unbounded near the line center in this approximation. Therefore, the autocorrelation function has to be factored so that the expansion converges. One needs a "locally averaged part" of $g(s)$ which gives the impact near line wing and an oscillating part of $g(s)$ which gives the far line wing.

In the following, the calculations for the near line wing as described in Baranger (1958a,b) are introduced. The main assumption is the impact approximation. Consequently, for large s the exponent $g(s)$ is described by a "locally averaged" part g_{av} by convolving¹² $g(s)$ from Eq. 2.71 into a Gaussian $A(s)$

$$g_{av}(s) = A(s) * g(s). \quad (2.74)$$

g_{av} becomes linear in time

$$g_{av}(s) = (\alpha_0 + i\beta_0) + (\alpha_1 + i\beta_1)s. \quad (2.75)$$

The resulting profile function has a Lorentzian shape

$$\varphi(\omega) = e^{-n_P \alpha_0} \left[\cos(n_P \beta_0) \frac{\gamma/\pi}{(\omega - \eta)^2 + \gamma^2} + \sin(n_P \beta_0) \frac{(\omega - \eta)/\pi}{(\omega - \eta)^2 + \gamma^2} \right] \quad (2.76)$$

with the HWHM being $\gamma = n_P \alpha_1$ and the line shift being $\eta = n_P \beta_1$ as characteristic parameters. There are different possible expressions for the HWHM and shift (Allard & Kielkopf 1982). If the interatomic forces are scalar and additive then the Anderson–Talman theory (Anderson & Talman 1956) is valid. Alternatively, the Lorentzian parameters can be expressed in Baranger's theory. In the case of spherically symmetric interactions in the adiabatic approximation, the results are

¹²In the following, * symbolizes a convolution.

equivalent. In Eqs. 2.74 and 2.75, α_0 , β_0 , α_1 , and β_1 are complex constants. In the unified theory, for a difference potential $\Delta V(R)$ and with the already mentioned average velocity \bar{v} , the following expressions can be derived

$$\xi = \int_{-\infty}^{+\infty} dt \Delta V [(b^2 + \bar{v}^2 t^2)^{1/2}] / \hbar \quad (2.77)$$

$$\gamma = n_P \bar{v} \int_0^{\infty} 2\pi b db [1 - \cos \xi], \quad (2.78)$$

$$\eta = n_P \bar{v} \int_0^{\infty} 2\pi b db \sin \xi. \quad (2.79)$$

More details can be found in (Allard & Kielkopf 1982).

Detailed calculations considering the far line wing in the case of van-der-Waals pressure broadening have been made by Royer (1971). Contributions to the far line wing occur when one or several perturbers are close to the radiator and thus contribute part of the transition energy during the radiative transitions. The collisions alter $g(s)$ so that now an ‘‘oscillating’’ function g_{osc} for the exponent $g(s)$ is necessary. Furthermore, the one-perturber assumption is applied which states that there is hardly more than one perturber close the radiator at low densities. For obtaining such an expression $g(s)$, defined by Eq. 2.71, has to be subtracted by the impact limit described in Eq. 2.74:

$$g_{osc}(s) = g(s) - g_{av}(s). \quad (2.80)$$

Since large s are considered, the expansion of the autocorrelation function in powers of the perturber density in Eq. 2.73 is possible

$$\Phi(s) = 1 - n_P g_{osc}(s) + \frac{n_P^2}{2!} g_{osc}^2(s) + \dots \quad (2.81)$$

By combining Eqs. 2.74 and 2.80, Eq. 2.64 becomes

$$\Phi(s) = e^{-n_P g_{av}} \left[1 - n_P g_{osc}(s) + \frac{n_P^2}{2!} g_{osc}^2 + \dots \right]. \quad (2.82)$$

Because of the splitting of the exponent $g(s)$ into two parts, the problem with the unbounded $g(s)$ vanishes. The complete profile function is given by the term by term FT of Eq. 2.82

$$\varphi(\omega) = \varphi_{nw}(\omega) * \left[\delta(\omega) - n_P \varphi_{fw}(\omega) + \frac{n_P^2}{2!} \varphi_{fw}(\omega) * \varphi_{fw}(\omega) + \dots \right] \quad (2.83)$$

and results in the convolution of the profile functions of the far line wing, for which $\varphi_{fw} = \text{FT}[g_{osc}(s)]$, into the near line wing for which $\varphi_{nw} = \text{FT}[e^{-n_P g_{av}(s)}]$. Under pressure variation the far line wing is broadened and shifted in the same way as the near line wing and line core (Royer 1971), which is in agreement with experimental observations from Ch'en and his coworkers (Ch'en & Wilson 1961; Ch'en & Fountain 1964; Ch'en & Garrett 1966; Garrett & Ch'en 1966; Ch'en et al. 1967; Garrett et al. 1967; Ch'en et al. 1969). The line profiles are calculated up to the third order of the density expansion.

The results obtained via this method agree with the Fourier transformation of the general autocorrelation function (without density expansion) at higher densities. At densities dealt with in this work, multiple perturber effects, so called satellites, are seen in the far line wing, which are discussed in the next paragraph.

Satellites

Satellite features appear in the far line wings of the line profile. They are local maxima in $\varphi(\omega)$ and can be either sharp or resemble rather a shoulder (Allard & Kielkopf 1982). Slow collisions between the emitter and perturber can cause transient quasi-molecules whose “finger prints” are the satellites. During these slow collisions, the emitter and perturber are close to each other. The relative motion of the two nuclei has to be much slower than the orbiting velocity of the electrons. Consequently, the interaction between the two atomic particles can be viewed as that of a quasi-molecule. In the calculations introduced in Sect. 2.4, satellites are present at the extrema of the difference potential of a transition. Then a relatively wide range of internuclear distances is responsible for the same spectral frequency which results in the local maximum in the far line wing. In the unified theory, satellites are predicted to be centered periodically at frequencies corresponding to the extrema of the difference potential $\Delta V(R)$ between the upper and the lower states, $\Delta\hbar\omega = k\Delta V_{ext}$ with $k = 1, 2, 3 \dots$ (Royer 1978; Allard 1978). If $k > 1$, there is a series of satellites which is due to many-body interactions. Hence the k^{th} satellite corresponds to k perturbers in the interaction volume. There is a direct correlation between the interaction volume and the potential energy curves and hence the atomic transition levels (Allard & Kielkopf 1982; Allard et al. 1998). Therefore, when simulating satellite features, the applied interaction potential is crucial. Satellites in molecular hydrogen broadened potassium line profiles are discussed in Allard et al. (2007).

3 Alkali Line Profiles

This chapter presents an overview of the raw data of the line profiles for which the theoretical background has been introduced in Chap. 2. Alkali line profiles are necessary for an improved description of the alkali absorption lines, especially of their line wings, in observations of cool substellar objects. As introduced in the previous chapters, so far there have been various line profile function calculations done. The line profiles are presented in chronological order, as they have been included in PHOENIX. There are profile functions for the Na I D, Li I, K I, Rb I, and Cs I doublets. The transitions can be found in Table 3.1. At first, the already established, analytical impact approximated van-der-Waals profiles (Schweitzer 1995; Schweitzer et al. 1996) are briefly discussed in Sect. 3.1 without going into details since the emphasis in this work refers to the new, non-analytical profiles. The far and near line wing profiles obtained by the unified semi-classical theory, see Sect. 2.4, are calculated with the perturbers H₂ in the two symmetries C_{2v} and C_{∞v} as well as He perturbers and are presented in Sect. 3.2. In Sect. 3.3, H I as an additional perturber is motivated and the near line wing profile background by Leininger et al. (2000) is briefly introduced. Details of the He broadened near line profiles done by Mullanphy et al. (2007), see Sect. 2.3, are given in Sect. 3.4. The comparison and discussion of the various line profiles follows in Sect. 3.5.

3.1 Impact Profiles

The first analytical approach of alkali profiles used in PHOENIX has been the impact approximated van-der-Waals profiles (Schweitzer 1995; Schweitzer et al. 1996), see Sect. 2.1.1. This approximation has been made for all atoms and molecules, in particular for the resonance alkali doublets: Na I D, Li I, K I, Rb I, and Cs I. Throughout this work, the label of the doublet lines is D₂ for the shorter wavelength and D₁ for the longer wavelength line¹. The collisions take place with the perturbers H₂, He, and H I. These perturbers represent the species with the highest concentrations in cool atmospheres and hence collisions with them are most likely. Note that these Lorentzian profiles describe only the near line wing.

3.2 Profiles in the Unified Semi-Classical Theory

A first version of non-analytical profiles (1st generation) calculated in the unified semi-classical theory, see Sect. 2.4, was introduced in 2003 (Allard et al. 2003). When referring to these profiles, their label in the figures is “Allard et al. 2003”. These profiles together with the profiles by Burrows & Volobuyev (2003) have been the first detailed alkali line profiles beyond the impact approximation for the improved description of brown dwarf spectra. They were calculated by Nicole Allard for various gas temperatures and with the perturber densities $n_{H_2} = n_{H_2C_{2v}} = n_{H_2C_{\infty v}} = n_{He} = 10^{19} \text{ atom cm}^{-3}$ which is within the range of values found in cool atmospheres². The far line wing

¹The numeration of the doublet lines originates from the lines appearing in frequencies.

²So far, there is no weighting of the perturber species. This is taken into account in PHOENIX.

Alkali Line	Transition	Central Wavelength (Å in air)
NaID ₂	3p ² P _{3/2} – 3s ² S _{1/2}	5890.0
NaID ₁	3p ² P _{1/2} – 3s ² S _{1/2}	5895.9
LiID ₂	2p ² P _{3/2} – 2s ² S _{1/2}	6707.8
LiID ₁	2p ² P _{1/2} – 2s ² S _{1/2}	6707.9
KID ₂	4p ² P _{3/2} – 4s ² S _{1/2}	7664.9
KID ₁	4p ² P _{1/2} – 4s ² S _{1/2}	7699.0
RbID ₂	5p ² P _{3/2} – 5s ² S _{1/2}	7800.0
RbID ₁	5p ² P _{1/2} – 5s ² S _{1/2}	7947.6
CsID ₂	6p ² P _{3/2} – 6s ² S _{1/2}	8521.1
CsID ₁	6p ² P _{1/2} – 6s ² S _{1/2}	8943.5

Table 3.1: Transitions of the resonance alkali doublets (Ralchenko et al. 2007).

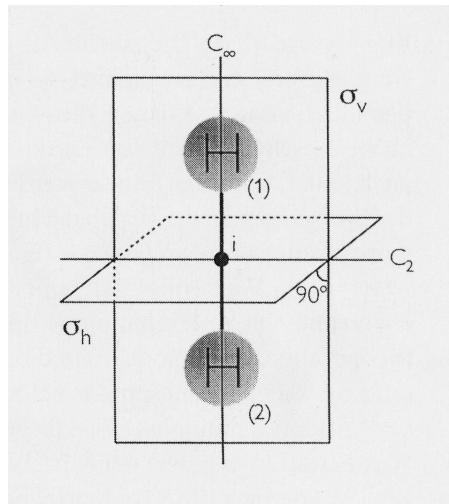


Fig. 3.1: Symmetries of the H₂ molecule (Wedler 2005).

data is supplied per perturbing particle ($\text{cm}^{-1} \text{cm}^3 \text{atom}^{-1}$). For a better interpolation, the far line wing profiles are split each into a blue and red far line wing³ separately for each temperature and an initial wavelength grid given in Å. They are saved logarithmically (to the base 10). Furthermore, the Lorentzian damping constant, the HWHM, and the line shift are supplied. They are provided again in the units of the inverse wavelength per perturbing particle in $\text{cm}^{-1} \text{cm}^3 \text{atom}^{-1}$. A tabulated overview of the existing data can be found in Table A.1 in Appendix A. For the line profile calculations, H₂ including its two symmetries and He have been considered as perturber species. Rossi's and Pascale's alkali–H₂ molecular potentials (Rossi & Pascale 1985) have been applied in the profile evaluations. They have considered the two symmetries: C_{2v} for which the orientation of the H₂ axis is perpendicular to the inter particle line between H₂ and the alkali and C_{∞v} for which the orientation of the involved axes is collinear. These symmetries are displayed schematically in Fig. 3.1.

The potential calculations of the interaction with He have been performed by Pascale (1983). No

³Blue means smaller wavelengths than the central wavelengths and red larger ones.

fine structure has been taken into account so that no distinction between the D₁ and D₂ lines had been possible in the earliest calculations except for the far line wing profiles of the Rb I and Cs I doublets.

However, this work concentrates on more recent alkali line profiles calculated with the unified semi-classical theory, introduced in Allard et al. (2005), Allard & Spiegelman (2006), and Johnas et al. (2006). Throughout this chapter, these results are labelled with “Allard et al. new”. Their calculation is similar to the one of the 1st generation profiles. For the light alkalis such as Na I D, Li I, and K I doublets, the fine structure has been included in order to distinguish between the D₁ and D₂ lines of the doublets. Rb I and Cs I belong to the heavy alkalis. For these the spin-orbit coupling of the alkali has been included. In an analogous approach to the one by Cohen & Schneider (1974), an atom-in-molecule intermediate spin-orbit coupling scheme is used. Therefore, the degeneracy is split partially by the spin-orbit coupling and the differentiation between the results of D₁ and D₂ implying the different spin states. The availability of the alkali profile data is listed in Table 3.2. The symbol “√” denotes that there is a far *and* a near line wing profile, contrary to “-” which means that there is no profile. In the case of Li I and Rb I perturbed by H₂, the resulting profiles for both symmetries have already been convolved by N. Allard. So far, only H₂ C_{2v}, H₂ C_{∞v}, and He as perturber types have been considered in PHOENIX. Hence a new type of perturber, the combined H₂ symmetry, has been introduced in the profile computation in PHOENIX⁴.

The far wing profiles have been smoothed because of numerical noise in the blue satellite region and at the blue and red wavelength end of the profiles (Allard 2004).

For Cs I, no complete set of profiles exists so far, so that in the following the profile of the 1st generation is used. Consequently, there is no discussion of Cs I profiles possible.

3.3 Alkali Broadening through H I

Motivation of H I Broadened Alkali Profiles

In Johnas et al. (2006), the necessity of including H I as third perturber species has been motivated which was before only considered in the classical impact profiles. The motivation is outlined in the following.

The concentrations (P/P_{gas}) of the three most important perturber species (H₂, He, and H I) in cool atmospheres change with depth and the effective temperature, see Fig. 3.2. While He remains basically at its cosmic abundance in all parts of the atmosphere, almost all hydrogen is distributed between H₂ and H I according to the dissociation equilibrium. At low effective temperatures such as $T_{eff} = 1000$ K, H₂ is the perturber species with the highest concentration, followed by He. Only in the innermost part of the atmosphere, H I forms in appreciable amounts. However, towards higher effective temperatures, the concentration of H I increases drastically. At $T_{eff} = 3000$ K, even in the outer part of the atmosphere, the concentration of H I is strongly increased compared to the concentration at $T_{eff} = 1100$ K. Now, H I represents the most important species followed by H₂ from $\tau_{std} \approx 1.0$ on inwards where τ_{std} is the continuum optical depth τ at a wavelength of 1.2 μm . Furthermore, the intensity contribution function \mathcal{C}_I is defined as

$$\mathcal{C}_I(\log \tau_{std}) = \mu^{-1} \log \tau_{std} \frac{\kappa_\lambda}{\kappa_{std}} S_\lambda e^{-\tau/\mu},$$

⁴see *cas_update_n.f* in Appendix B

H_2C_{2v}					$H_2C_{\infty v}$					He				
T_{gas}	NaID	K I	Li I	Rb I	T_{gas}	NaID	K I	Li I	Rb I	T_{gas}	NaID	K I	Li I	Rb I
500 K	✓	✓	✓	✓	500 K	✓	✓	✓	✓	500 K	✓	✓	✓	✓
650 K	✓	-	-	-	650 K	✓/near	-	-	-	650 K	✓	✓	-	-
1000 K	✓	✓	✓	✓	1000 K	✓	✓	✓	✓	1000 K	✓	✓	✓	✓
1500 K	✓	✓	✓	✓	1500 K	✓	✓	✓	✓	1500 K	✓	✓	✓	✓
2000 K	✓	✓	✓	✓	2000 K	✓	✓	✓	✓	2000 K	✓	✓	✓	✓
2500 K	✓	✓	✓	✓	2500 K	✓	✓	✓	✓	2500 K	✓	✓	✓	✓
3000 K	✓	✓	✓	✓	3000 K	✓	✓	✓	✓	3000 K	✓	✓	✓	✓
4000 K	-	✓	-	-	4000 K	-	✓	-	-	4000 K	-	-	-	-
5000 K	-	✓	-	-	5000 K	-	✓	-	-	5000 K	-	-	-	-
6000 K	-	✓	-	-	6000 K	-	✓	-	-	6000 K	-	-	-	-

Table 3.2: Overview of the far and near line wing profiles of NaID, K I, Li I, and Rb I doublets perturbed by H_2C_{2v} , $H_2C_{\infty v}$, and He for temperatures from 500 K to 6000 K. “✓” stands for existent profiles and “-” for the nonexistent ones. In the case of NaID perturbed by $H_2C_{\infty v}$ for 650 K only the calculation for the near line wing profile exists but not for the far line wing. The profiles of the two symmetries of H_2 are already convolved for Li I and Rb I by N. Allard.

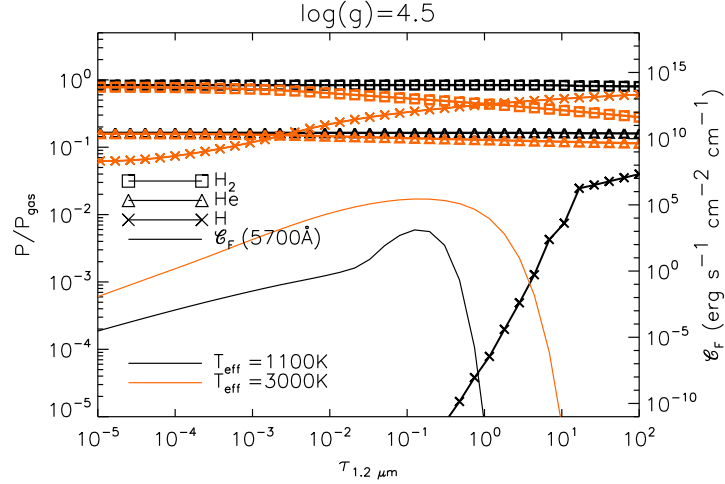


Fig. 3.2: Concentrations of H₂, He and HI in the atmosphere at $T_{\text{eff}} = 1100$ K and 3000 K with $\log(g) = 4.5$ and solar composition (left ordinate). In addition, the flux contribution functions of impact profiles in synthetic spectra with $\log(g) = 4.5$ and solar composition at a wavelength of 5700 Å for $T_{\text{eff}} = 1100$ K and 3000 K are depicted (right ordinate).

with S_λ being the source function at a given wavelength, κ_λ the absorption coefficient at this wavelength, κ_{std} the absorption coefficient at $\lambda_{\text{std}} = 1.2 \mu\text{m}$, and $\mu = \cos \theta$ the angle between the considered direction and the normal onto the surface. For a better approximation of the contribution function of the entire star, the flux contribution function \mathcal{C}_F has to be calculated by integrating \mathcal{C}_I over all angles. This approximation is legitimate for strong lines (Magain 1986) and has been implemented in PHOENIX (Fuhrmeister et al. 2006). In order to determine the region in the atmosphere in which the absorption lines are formed and hence which perturber influences need to be taken into account, we use the formation of the line wing of Na I D₂ as an example. The flux contribution functions \mathcal{C}_F for $T_{\text{eff}} = 1100$ K and 3000 K at a wavelength of 5700 Å are displayed in Fig. 3.2 (right ordinate) next to the concentrations. Its maxima mark the location of the formation of the line in the atmosphere at the specific wavelength. For $T_{\text{eff}} = 1100$ K, the maximum of \mathcal{C}_F is not located close to regions of significant HI concentration. This changes towards higher effective temperatures. At $T_{\text{eff}} = 3000$ K, the regions in the atmosphere where HI becomes dominant and the line wing forms are very close together. Hence, towards higher effective temperatures (≥ 2000 K), it will be more important to consider also collisional broadening due to HI in order to obtain a more accurate line profile.

As theoretically expected, studies show, that the far line wings of spectral lines form deeper inside the atmosphere than the near line wings and the cores of the line, see Chap. 4. Consequently, the contribution of HI to the far line wing profile in the deep layers of the atmosphere is of great importance. This is also true for the near line wings since in the atmospheric layers, in which they form, HI represents still the perturber species with the second highest concentration.

HI broadening Na I D Profile in the Classical Impact Approximation

Leininger et al. (2000) have calculated non-analytically the Lorentzian damping constants of HI broadened Na I D with the impact approximation. They have assumed classical rectilinear perturber paths (classical path approximation). They derive the following expression for the

Alkali Line	a	b
NaID ₁	0.02011	0.4270
NaID ₂	0.02918	0.3866
KID ₁	0.01385	0.4886
KID ₂	0.03173	0.4136
LiID ₁	0.02461	0.4042
LiID ₂	0.02533	0.3998

Table 3.3: Fit parameters a and b of the power law fit $\gamma(T) = aT^b$ for the Lorentzian HWHM (in units of $10^{-21}\text{MHz m}^3 \text{atom}^{-1}$) of the alkali doublets Na I, K I and Li I broadened by He (Mullamphy et al. 2007).

Lorentzian parameters, the HWHM γ and the shift η ,

$$\gamma(T) + i\eta(T) = \langle 2\pi v \int b \Pi(b, v) db \rangle \quad (3.1)$$

where T denotes the gas temperature, b the impact parameter, v the relative velocity and Π a detailed expression for the opacity in terms of the scattering matrix S given by Roueff (1974). Furthermore on the right side of Eq. 3.1, $\langle \rangle$ indicates the average over a Maxwellian distribution with relative speeds at temperature T . The Lorentzian parameters are given in angular frequencies. The damping constants for both Na I D resonance lines are approximated for temperatures between 300 K and 10 000 K by

$$\gamma(T) = 1.10 \cdot 10^{-8} \left(\frac{T}{5000 \text{ K}} \right)^{0.4} \frac{\text{cm}^3}{\text{atom} \cdot \text{s}}. \quad (3.2)$$

In Eq. 3.2, the damping constant is given in the units of the angular frequency per perturbing H I atom ($\text{cm}^3 \text{atom}^{-1} \text{s}^{-1}$). For this work, these Lorentzian widths have been evaluated for the temperatures for which the majority of the profile by N. Allard are calculated: 500 K, 650 K, 1000 K, 1500 K, 2000 K, 2500 K, and 3000 K. The conversion into the units of the inverse wavelength per perturbing particle is $1/\lambda = \omega/(2\pi c)$ with ω being the angular frequency and c the speed of light ($2.997925 \cdot 10^{10} \text{ cm s}^{-1}$). HI represents again a new perturber type in the detailed profile calculations in PHOENIX and has been introduced as fifth perturber type⁵, see Chap. 4.

Note that the data from Leininger et al. (2000) has been the only available data of alkalis perturbed by HI in literature during this work.

3.4 Lorentzian Profiles in the Fully–Quantum Mechanical Theory

For the light alkali doublets, Na I D, K I, and Li I, perturbed by He, Mullamphy et al. (2007) provide an alternative source of the Lorentzian damping constants for temperatures from 70 K to 3000 K⁶ which are calculated non–analytically. They are calculated in the fully–quantum mechanical theory, see Sect. 2.3, and are given in the units of frequency per perturbing He atom

⁵The fourth perturber type in PHOENIX represents collisions with electrons which have to be considered for Stark broadening.

⁶The results for the K I doublet apply only for temperatures between 500 K and 3000 K.

(10^{-21} MHz m³ atom⁻¹). The HWHM is fitted with a power law: $\gamma(T) = aT^b$ with the coefficients a and b listed in Table 3.3.

The conversion into the units needed for PHOENIX, cm⁻¹ cm³ atom⁻¹, is done via $1/\lambda = \nu/c$ where ν is the frequency. The HWHMs for the alkalis listed above have been generated for the temperatures: 500 K, 650 K, 1000 K, 1500 K, 2000 K, 2500 K, and 3000 K.

3.5 Profile Data Discussion

For clarity, the far line wing data by N. Allard and the various Lorentzian near line wing data are discussed separately. Only the damping constants of the Lorentzians will be discussed since there is not enough shift data available. The comparison is between the various data sets: the first data set refers to “Allard et al. 2003”, the new one to “Allard et al. new”, and the other data sets are cited as needed. Only the results for NaID will be plotted here in Figs. 3.3–3.6 as an example. The complete set of figures can be found in Appendix A, Figs. A.1–A.9.

The far line wing profiles calculated in the unified semi-classical theory, see Sect. 3.2 are plotted in Fig. 3.3 and Figs. A.1–A.3. The differences in shape between the old and new far line wing profiles are so severe that the relative changes are extremely large. The results of Allard et al. (2003) have to be considered as preliminary results (Allard 2004). An asymmetry is noticeable. All D₁ far line wings have no contribution to their blue wings, so that the effect of the profiles in synthetic spectra is due to the red part of the D₂ far line wing profile. It is important to mention that the new data sets are complete for the four perturber types, H₂, H₂ C_{2v}, H₂ C_{∞v}, and He, and also are calculated with smaller step sizes in temperature which will improve the quality of the temperature interpolation. As discussed in Sects. 2.4 and 3.2, satellites in the blue far wings of the D₂ lines are visible. Only blue satellites are predicted by the theory. On the one hand their positions depend on the interaction potential and on the other hand their strengths depend on the radiative dipole moments (Allard et al. 2007) and the temperature.

In general, the magnitude of the damping constants increases with rising temperatures. In Figs. 3.4 and A.4, the Lorentzian damping constants for NaID perturbed by H₂ and HI are shown. There are large differences in the H₂ broadened NaID HWHMs for both symmetries between the data from Allard et al. new and Allard et al. 2003. The relative changes between these data sets for the NaID₁ and D₂ lines are depicted in Figs. 3.5 and A.5. The relative changes of the HWHMs of NaID₁ perturbed by H₂ C_{2v} by Allard et al. 2003 and Allard et al. new vary with the temperature. There is no monotonic change. The relative change between the new data set and the one from 2003 ranges between 18.6 % and -5.2 %. The Allard et al. 2003 data set of this line with H₂ C_{∞v} as perturber has been generally larger than the Allard et al. new data set, up to 46.1% for 2000 K.

For the NaID₂ HWHMs, the relative change behaves differently, especially with H₂ C_{2v} as perturber. The Allard et al. new H₂ C_{2v} data set is always larger by at least 120%. The maximum relative change is at 1000 K with 125.7%. For NaID₂ perturbed by H₂ C_{∞v}, the largest change is at 2000 K, for which the data set from 2003 is up to 17.3% larger, otherwise the relative changes are only in the range of a few percent.

The HWHMs of NaID perturbed by HI by Leininger et al. (2000) are in a similar range in their magnitudes as the other NaID data with H₂ as perturber.

Comparing the HWHMs of Li I and KI broadened by H₂, there are again differences. The discussion is resumed analogous in Appendix A.

The results of the perturbations with He of the alkalis, NaID, Li I, KI, and Rb I, are summarized

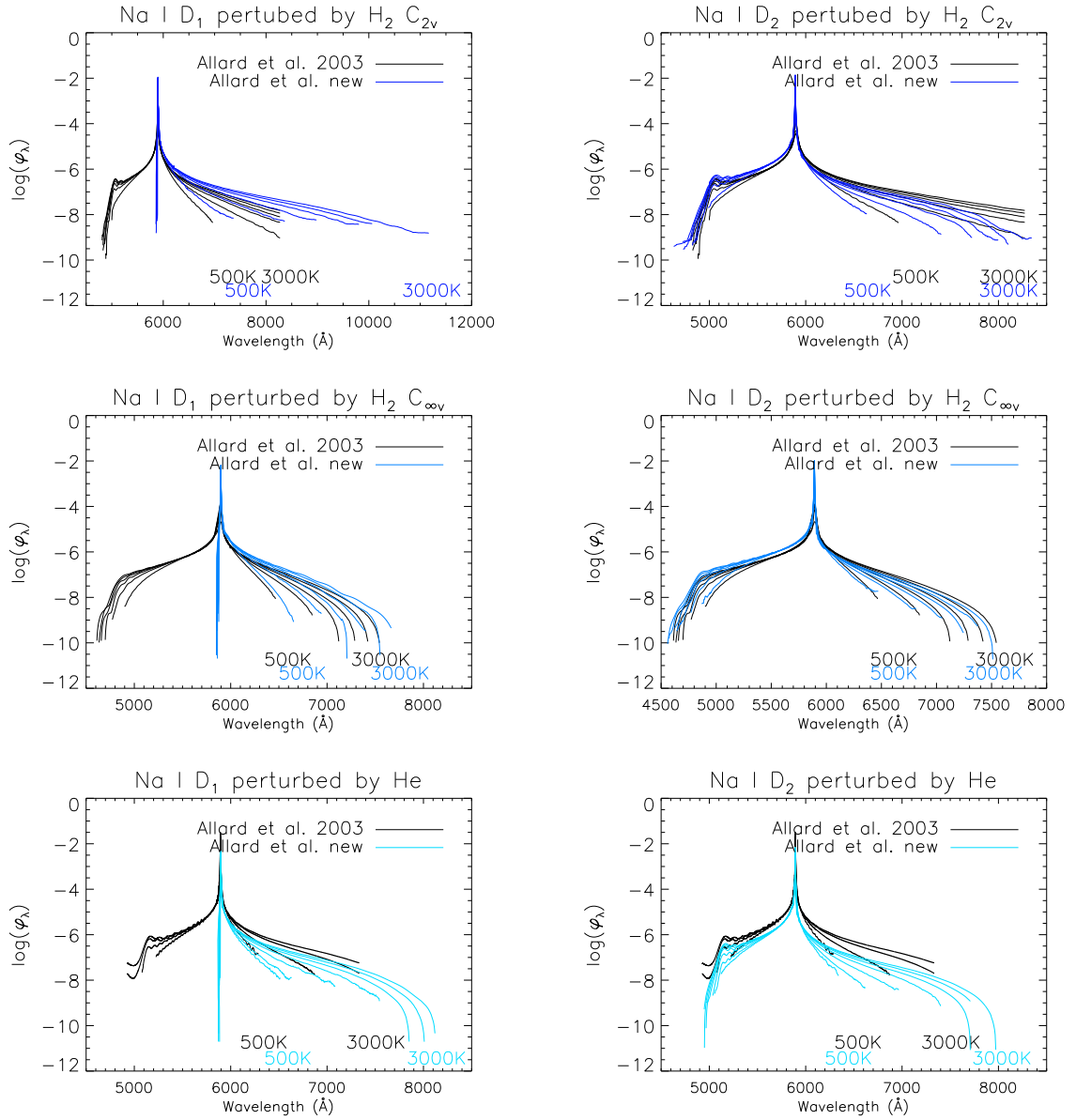


Fig. 3.3: The far line wing profiles of Na I D₁ and D₂ perturbed by H₂ C_{2v}, H₂ C _{∞ v}, and He by Allard et al. (2003) and Allard et al. new, see Sect. 3.2, with larger temperature giving broader profiles. The profile function of the far wing ϕ_λ per perturbing particle is displayed for an perturber density $n_p = 10^{19} \text{ cm}^{-3} \text{ atom}^{-1}$ in the units of $\text{cm}^{-1} \text{ cm}^3 \text{ atom}^{-1}$.

in Figs. 3.4 and A.8. The existing Allard et al. 2003 D_1 HWHMs are larger than the new D_1 data by N. Allard, see Fig. 3.6. Furthermore, the HWHMs supplied by Mullamphy et al. (2007) for Na I D, Li I, and K I are larger than the new damping constants by N. Allard. For the D_2 lines, it is the opposite: the new damping constants by N. Allard are larger than the old ones and the data from Mullamphy et al. (2007).

In more detail, the new Na I D_1 damping constants by N. Allard perturbed by He are between 25.3% (3000 K) and 38.0% (500 K) smaller than the ones from 2003. The damping constants from Mullamphy et al. (2007) are between 12.7% (500 K) and 15.7% (3000 K) larger than the new ones by N. Allard. The relative changes between the new and the HWHMs from 2003 by N. Allard for the Na I D_2 line are between 50.1% (1000 K) and 54.3% (3000 K). Comparing the new results by N. Allard and those by Mullamphy et al. (2007), one finds that the Allard et al. new data set is between 18.1% (650 K) and 21.5% (3000 K) larger.

The comparison of the HWHMs of the Li I, K I and Rb I doublets perturbed by He is again similar and described in detail in Appendix A.

These differences in the profile data are expected to be visible in synthetic spectra, see Chap. 5.

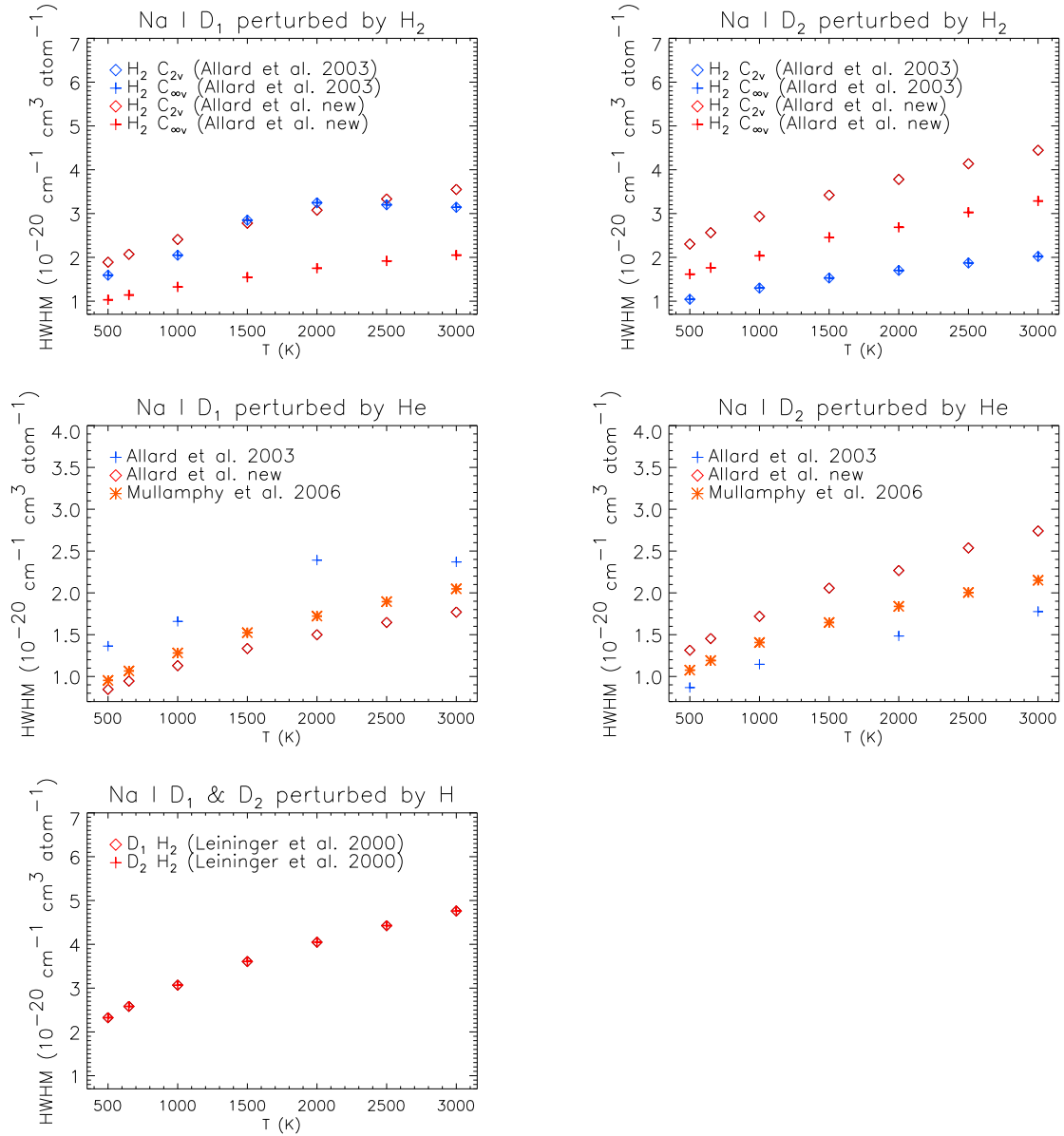


Fig. 3.4: The Lorentzian damping constants for the Na I D doublet perturbed by H₂ in the two symmetries C_{2v} and C_{∞v} by Allard et al. 2003 and Allard et al. new (top panels), introduced in Sect. 3.2. In the middle panels, the HWHMs perturbed by N. Allard and by Mullamphy et al. 2006, see Sect. 3.4, are shown and Na I D HWHMs perturbed by HI (lower panel) (Leininger et al. 2000), see Sect. 3.3.

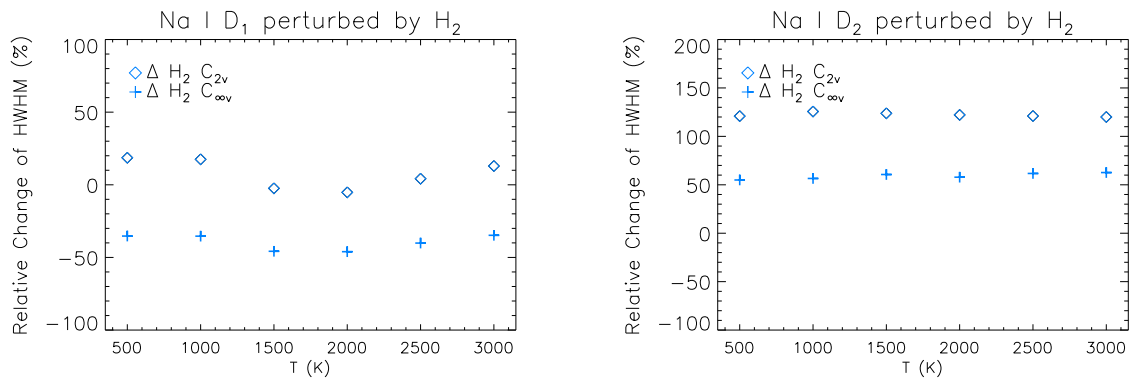


Fig. 3.5: The relative change of the Lorentzian damping constants by Allard et al. new and Allard et al. (2003), shown in Fig. 3.4, for the Na I D doublet perturbed by H₂ in the two symmetries C_{2v} and C_{∞v}.

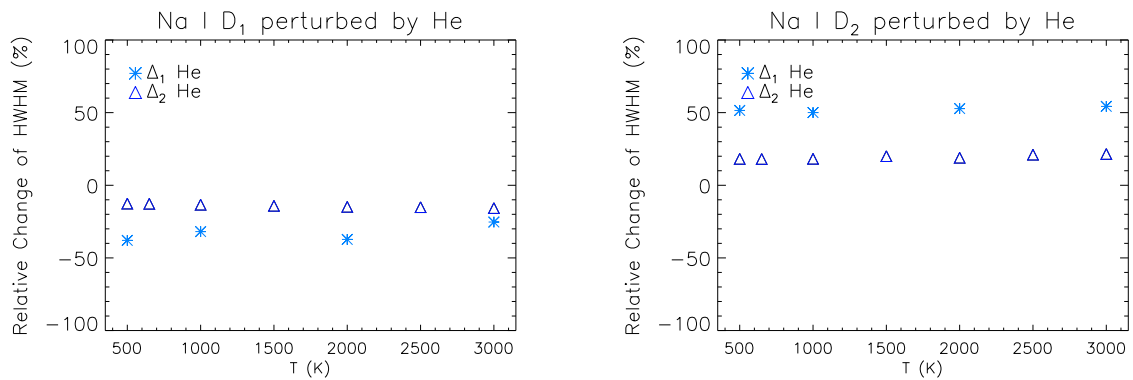


Fig. 3.6: Δ₁: The relative change of the Lorentzian damping constants by Allard et al. new and Allard et al. 2003, shown in Fig. 3.4, for the Na I D doublet perturbed by He. Δ₂: The relative change of the Lorentzian damping constants by Allard et al. new and Mullamphy et al. 2006 for the Na I D doublet perturbed by He, see also Fig. 3.4.

4 Stellar Atmospheres Computed with PHOENIX

In order to understand stellar atmospheres, detailed atomic physics must be taken into account. Theoretical stellar atmospheres are indispensable for a description and prediction of observational characteristics. It is necessary to simulate stellar atmospheres numerically. The goal of the theory of stellar atmospheres is the description of the energy flow through the outermost layers of a stellar object. In this work, the multi-purpose stellar atmosphere code PHOENIX is used for studies of stellar atmospheres and in order to provide synthetic spectra for comparisons with observations. In Sect. 4.1, the basic physics necessary for stellar atmosphere modelling is introduced. A short introduction about the modelling of a stellar atmosphere is given in Sect. 4.2. The background of the numerical evaluation of the total line profile is briefly introduced in Sect. 4.3. The details of stellar atmospheres in general can be found in classical textbooks, e.g., Mihalas (1970) and Rutten (2003). The specifics of the atmosphere code PHOENIX can be found, e.g., in Hauschildt (1992), Hauschildt & Baron (1999), and Hauschildt & Murdin (2001).

4.1 Basic Physics

Two equations play a fundamental role in the description of stellar atmospheres: (a) the hydrostatic equation and (b) the energy conservation. It is possible to provide an unambiguous characterization of a stellar atmosphere by the parameters of these two equations. Both equations are here time independent (though not in general) but are not independent of each other. For the calculation of a self-consistent stellar atmosphere the radiative transport equation must be solved and the underlying atmospheric structure must be determined via the hydrostatic equation. Based on the consistent stellar atmosphere, a synthetic spectrum can be obtained which can be used for high resolution studies. The theoretical background is briefly introduced in the next paragraphs.

Radiative Transport

If not mentioned otherwise in this work, the atmospheres are assumed to be static and spherically symmetric. No fast stellar rotation or stellar winds have to be regarded for the stellar objects dealt with in this work. Hence, the static, spherically symmetric equation of transfer in spherical polar coordinates¹ is given by

$$\frac{\partial I_\nu}{\partial s} = \mu \frac{\partial I_\nu}{\partial r} + \frac{1 - \mu^2}{r} \frac{\partial}{\partial \mu} I_\nu = j_\nu - \chi_\nu I_\nu, \quad (4.1)$$

where $I_\nu(r, \nu, \mu)$ is the monochromatic specific intensity and s is the geometrical depth. In Eq. 4.1, $\mu = \cos \theta$ is the angle of a beam of radiation with the specific intensity I_ν to the radially outward

¹with $dr = \cos \theta ds$ and $r d\theta = -\sin \theta ds$ and no azimuthal intensity variations

direction. $j_\nu = j_\lambda(r, \nu)$ is referred to as monochromatic emissivity and $\chi_\nu = \kappa_\nu(r) + \sigma_\nu(r)$ is the monochromatic extinction coefficient or total opacity which is the sum of the monochromatic absorption coefficient κ_ν and the monochromatic scattering coefficient σ_ν . They depend on the spatial position and hence depend on the optical depth τ_ν at a given frequency and geometrical depth s

$$d\tau_\nu = -\chi_\nu \rho ds \quad (4.2)$$

with ρ being the density. Note that the optical depth is measured from the outside to the inside, whereas the geometrical depth is measured in the opposite direction. The ratio of emissivity and opacity is defined as the source function S_ν

$$S_\nu = \frac{j_\nu}{\chi_\nu}. \quad (4.3)$$

With Eq. 4.3, Eq. 4.1 becomes

$$\frac{\mu}{\chi_\nu} \frac{\partial I_\nu}{\partial r} + \frac{1 - \mu^2}{\chi_\nu r} \frac{\partial}{\partial \mu} I_\nu = S_\nu - I_\nu. \quad (4.4)$$

It is possible to give a formal solution of Eq. 4.1, respectively of Eq. 4.4 for a given S_ν and $I_\nu(\tau_0)$:

$$I_\nu(\tau) = I_\nu(\tau_0) e^{\tau_0 - \tau} + \int_{\tau_0}^{\tau} S_\nu(\tau') e^{\tau' - \tau} d\tau'. \quad (4.5)$$

τ labels the optical depth.

The basic problem is that the source function S_ν depends on the mean intensity J_ν and therefore also depends on I_ν . A general form of the source function S_ν for the simple case of a two-level atom without continuum and background absorption or scattering is

$$S_\nu = (1 - \varepsilon_\nu) \bar{J}_\nu + \varepsilon_\nu B_\nu, \quad (4.6)$$

where $\varepsilon_\nu = \kappa_\nu / (\kappa_\nu + \sigma_\nu)$ denotes the monochromatic thermal coupling parameter also known as photon destruction parameter. \bar{J}_ν is the mean intensity averaged over the line profile

$$\bar{J}_\nu = \int \varphi(\nu) J_\nu d\nu, \quad (4.7)$$

where J_ν is the mean intensity and the average of I_ν over all solid angles

$$J_\nu = \frac{1}{4\pi} \oint I_\nu d\Omega \quad (4.8)$$

with the solid angle $d\Omega = \sin \vartheta d\vartheta d\varphi$ being dependent on direction angles ϑ and φ . $\varphi(\nu)$ is the profile function of a spectral line. In Eq. 4.6, B_ν is Planck's function

$$B_\nu(T) = \frac{2h\nu^3}{c^2} \frac{1}{e^{\frac{h\nu}{kT}} - 1} \quad (4.9)$$

with c being the speed of light.

With Eq. 4.5, I_ν and thus J_ν depends on S_ν . Thus, Eqs. 4.1 and 4.4 are integro-differential equations. A general form of the solution of Eq. 4.1 with Eqs. 4.5 through 4.9 can be expressed through an operator Λ

$$J_\nu = \Lambda S_\nu. \quad (4.10)$$

Equations 4.10 and 4.6 are vector equations dependent on the optical depth and frequency and Λ is a matrix. A simple Λ -iteration method in the form of Eq. 4.10 fails for small ε_ν , i.e., when scattering becomes dominant and at large optical depths.

It was shown (Canon 1973; Scharmer 1981) that an operator splitting method, also known as approximated or accelerated lambda iteration, improves the slow convergence of the Λ -iteration and makes the solution of the scattering problem feasible in time and computing power. The operator is split as $\Lambda = \Lambda^* + (\Lambda - \Lambda^*)$. An appropriate Λ^* operator must be determined in terms of its construction time, its convergence rate, its inversion time, and the computer architecture, see Hauschildt (1992) and Hauschildt & Baron (1999) for details.

The opacity plays a major role when modelling stellar atmospheres, e.g., see Eq. 4.1. The main emphasis of this work is the contribution of the absorption line profiles for which the theoretical background has been introduced in Chap. 2 and which have been presented in Chap. 3. For the derivation of the absorption coefficient κ_ν , the following assumptions are made: an atom in an upward transition between two bound states absorbs radiation. The lower state i has a statistical weight g_i and the upper state j has a statistical weight g_j . Einstein's rate R_{ij} from the state i to the state j for direct absorption in bound-bound transitions is

$$n_i(\nu)R_{ij}\frac{d\Omega}{4\pi} = n_i(\nu)B_{ij}I_\nu\frac{d\Omega}{4\pi}, \quad (4.11)$$

where $n_i(\nu)$ is the number density of atoms in the state i for which absorption at frequencies from ν to $\nu + d\nu$ is possible. B_{ij} denotes Einstein's absorption probability for a transition $i \rightarrow j$. As mentioned already in Chap. 2, the spectral line corresponding to this transition is not sharp. Due to the perturbations with nearby atoms, ions, and molecules and due to the finite lifetime of the upper state j , a spread in frequency is observable which is described by the normalized absorption profile function $\varphi(\nu)$, see Chap. 2. The total line profile in PHOENIX is a convolution of a Gauss core, a Lorentzian near line wing profile, and a far line wing profile. The Gauss core corresponds to a Doppler profile which represents the thermal micro turbulent velocity of the absorbing atoms. It is described by the Maxwell-Boltzmann velocity distribution. Thus with the total number of atoms per unit cell in the state i being n_i , the number of atoms per unit cell which can absorb radiation at the frequency ν is

$$n_i(\nu) = n_i\varphi(\nu). \quad (4.12)$$

With Eq. 4.11, the absorption coefficient and hence the opacity for the transition from i to j at frequency ν is directly dependent on the line profile

$$\kappa_{\nu,i \rightarrow j} = \frac{h\nu_{ij}}{4\pi}B_{ij}n_i\varphi(\nu), \quad (4.13)$$

where $h\nu_{ij} = E_j - E_i$ is the energy of the photons absorbed by the atoms when the transition from level i to j is made.

Eddington-Barbier Approximation in LTE

The purpose of the Eddington-Barbier approximation is the determination of the atmospheric layer, which contributes most to the emergent intensity at the stellar surface at a certain frequency ν . A short derivation is presented here, following Rutten (2003) and Unsöld & Baschek (2005). The emergent intensity at the stellar surface with $\tau_\nu = 0$ and $\mu = \cos \theta > 0$ is given by

$$I_\nu^+(\tau_\nu = 0, \mu) = \int_0^\infty S_\nu(\tau_\nu)e^{-\tau_\nu/\mu}d\tau_\nu/\mu. \quad (4.14)$$

Then S_V is substituted by

$$S_V(\tau_V) = \sum_{n=0}^{\infty} a_n \tau_V^n = a_0 + a_1 \tau_V + a_2 \tau_V^2 + \dots + a_n \tau_V^n. \quad (4.15)$$

With Eq. 4.15 and use of $\int_0^{\infty} x^n e^{-x} dx = n!$, Eq. 4.14 becomes

$$I_V^+(\tau_V = 0, \mu) = a_0 + a_1 \mu + 2a_2 \mu^2 + \dots + n! a_n \mu^n. \quad (4.16)$$

Considering only the first two terms of the expansions in Eqs. 4.15 and 4.16 results in the Eddington–Barbier approximation

$$I_V^+(\tau_V = 0, \mu) \approx S_V(\tau_V = \mu), \quad (4.17)$$

which is exact if S_V varies linearly with τ_V . Furthermore, the following approximation of the radiative flux $F_V(\tau_V = 0)$ at the surface is valid

$$F_V(\tau_V = 0) = 2\pi \int_0^{\pi/2} I_V(\tau_V = 0, \mu) \cos \theta \sin \theta d\theta \simeq \pi S_V(\tau_V = 2/3). \quad (4.18)$$

In the local thermal equilibrium (LTE), the flux at a certain frequency corresponds to a local temperature at an optical depth of $2/3$.

The optical depth depends on the opacity. If a geometrical depth s is given, the optical depth differs for the central wavelength of an absorption line and its far line wing / continuum. The optical depth in the line core τ_{core} is given by

$$\tau_{core}(s) = \int_{-\infty}^s \chi_{core}(s') \rho ds' \quad (4.19)$$

and the optical depth in the far line wing τ_f

$$\tau_f(s) = \int_{-\infty}^s \chi_f(s') \rho ds'. \quad (4.20)$$

Since $\chi_{core} \gg \chi_f$ and the average optical depth in which it is possible to “view” into the star is $2/3$, the flux of the absorption line center originates from a smaller geometrical depth than the flux of the far line wing. In Fig. 4.1, this is visualized with the flux contribution function of several wavelengths in the line wing of the Na I D_2 absorption line in the classical impact approximation.

The Stellar Atmosphere

A characterization of a stellar atmosphere is possible with: the gravitational acceleration at the surface g or $\log(g)$, the effective temperature T_{eff} , luminosities, abundances, g is used in the hydrostatic equation and T_{eff} in the energy conservation. The hydrostatic equation is given by

$$\frac{dP}{d\tau_V} = \frac{dP_{gas}}{d\tau_V} + \frac{dP_{rad}}{d\tau_V} + \frac{dP_{micro}}{d\tau_V} = \frac{g}{\chi_V} \quad (4.21)$$

with P being the total pressure consisting of the gas pressure P_{gas} , the radiative pressure P_{rad} , and the pressure caused by micro turbulences P_{micro} . For very low mass objects, $P = P_{gas}$, since they are assumed to be fully convective and the micro turbulence is assumed to be 2 km s^{-1}

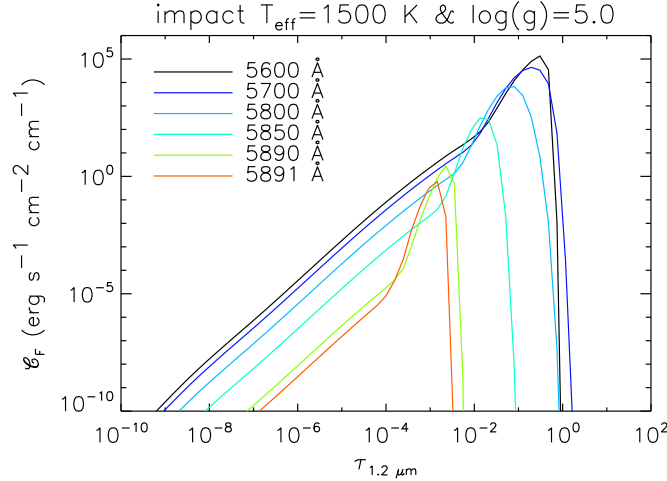


Fig. 4.1: Flux contribution function of wavelengths in the wing of the Na ID₂ line in the impact setup at $T_{\text{eff}} = 1500$ K and $\log(g) = 5.0$.

(Allard et al. 2001). The gravitational acceleration at the surface g depends on the constant of gravitation G , the stellar mass M and the stellar radius R , $g = GM/R^2$.

The energy conservation is expressed by

$$F_{\text{rad}} + F_{\text{conv}} = \text{const} \equiv \sigma T_{\text{eff}}^4, \quad (4.22)$$

with

$$F_{\text{rad}} = \int_0^\infty F_\nu d\nu \quad (4.23)$$

where F_{conv} is the convective flux and F_{rad} the radiative flux. The flux F_ν is defined as

$$F_\nu = \oint I_\nu \cos \theta d\Omega \quad (4.24)$$

with $d\Omega$ being the solid angle. In Eq. 4.22, the effective temperature T_{eff} does not represent a temperature somewhere in the atmosphere but helps to characterize an atmosphere since it yields the actual flux in the stellar atmosphere; $\sigma = 5.67 \cdot 10^{-5} \text{ erg s}^{-1} \text{ cm}^{-2} \text{ K}^{-4}$ is the Stefan–Boltzmann constant. The convection and radiation are predominately responsible for the energy transport in the atmosphere.

In cool atmospheres, an outer radiative zone in which convection is negligible and an inner convective zone can be found. The depth of the convection zone in brown dwarf atmospheres is dependent on the mass of the (sub)stellar object (Chabrier & Baraffe 2000). For $M \leq 0.5M_\odot$, the convective zone covers the range from the optical thin layers of the atmosphere to the center of the star, so that there is only a very thin outer radiative zone. Very low mass objects are “fully convective”. Convection appears when the radiative temperature gradient exceeds the adiabatic one (Schwarzschildt instability criterion). The convection in PHOENIX is described by the mixing–length theory. It assumes the following picture: “bubbles” or turbulent elements move up and down in the surrounding environment. However, up and down moving bubbles have different thermal energies. There is an excess of thermal energy over the surrounding material for up moving bubbles and a deficit for down moving bubbles. After a characteristic length, the mixing–length (for M dwarfs about twice

the local pressure scale height of the atmosphere), it is assumed that the turbulent elements dissolve into the surrounding material and thus deliver their excess energy or absorb any deficit. A transport of energy takes place.

The temperature structure of the stellar atmosphere is determined by the conservation of energy in Eq. 4.22. This dependence couples the radiative transport to the physical structure. The energy conservation requires the knowledge of the radiative flux and the radiation field requires the knowledge of the temperature structure. In PHOENIX, it is solved iteratively providing a starting model with an effective temperature, which is necessary for the energy conservation, and a model structure. The iterations are continued until the physical structure is consistent with the radiation field.

A possible (simplistic) way to characterize the chemical composition of an atmosphere which influences its density and opacity, is with the metallicity Z . It is defined by the ratio of the abundances of metals M and hydrogen H relative to the corresponding values in the sun

$$Z = \frac{[M]}{[H]} = \log \left(\frac{M/H}{M_{\odot}/H_{\odot}} \right). \quad (4.25)$$

Throughout this work the assumption of the local thermal equilibrium (LTE) is made. All level populations, i.e. atomic, molecular, and ionic, are given by the Saha–Boltzmann distribution and are thus determined by the local temperature T and electron density n_e . LTE is a local theory and does not describe any coupling between the radiation field and the state of the gas.

4.2 Modelling Atmospheres with PHOENIX

The flow chart in Fig. 4.2 gives an overview of the general iteration scheme of PHOENIX for a LTE stellar atmosphere calculation. At first, given temperature and density structures are used as starting guesses for the atmosphere. Due to the assumption of LTE, the properties such as the opacity, determined by occupation numbers, and the total pressure (for late dwarfs the gas pressure) depend only on the gas temperature and electron density. Via the integration of the hydrostatic equation a new atmospheric structure is calculated. Then a line selection follows in order to decrease the number of lines taken into account². This is necessary for the speed up of the computation of the line opacity since the line lists in PHOENIX contain several hundred million lines. With the knowledge of the new pressure and density distribution and the evaluated line profiles, the new opacities are calculated. Then the transfer equation can be solved using these opacities. From the solution of the radiative transfer equation, the mean intensity and the flux are obtained so that the energy conservation can be checked. The calculation of the opacity with the previous evaluation of the line profile function and the following solution of the radiative transport is done for each wavelength. If the (arbitrarily) chosen temperature distribution from the beginning does not yield a solution which satisfies the energy conservation, another temperature structure must be found in order to conserve the energy. With this new temperature structure, the process is repeated until the requirement of energy conservation is achieved and the new atmospheric model is converged to the prescribed accuracy.

²The weakest lines are neglected.

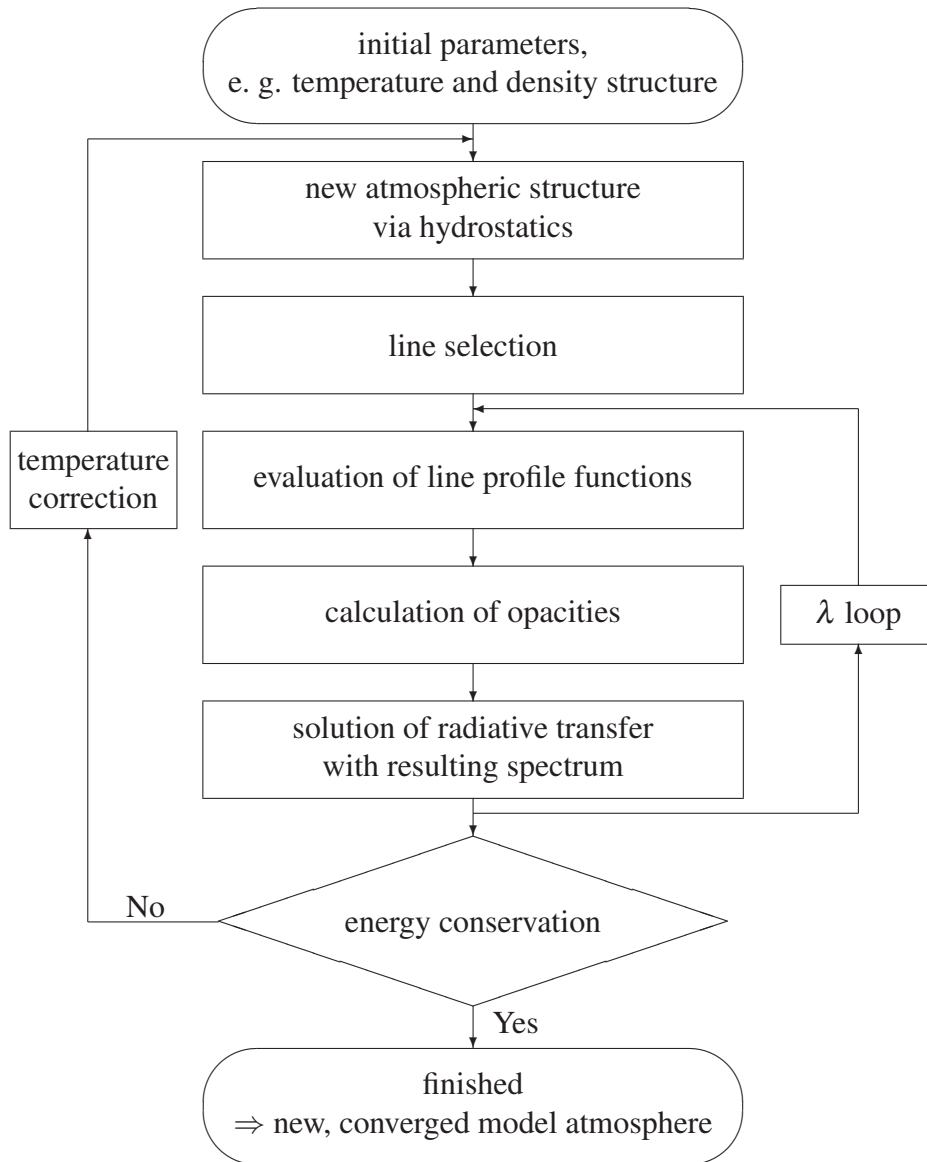


Fig. 4.2: The iteration scheme for a LTE model atmosphere in PHOENIX.

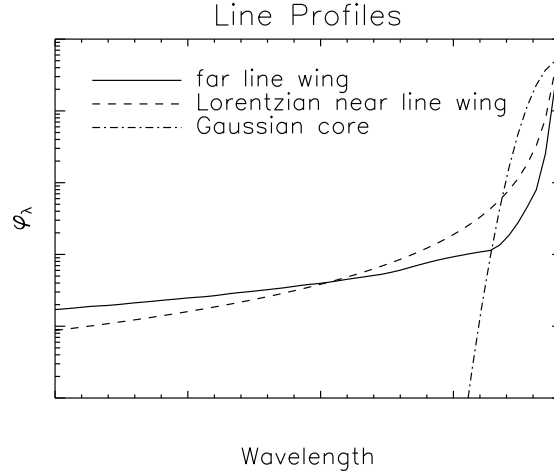


Fig. 4.3: Sketch of the far line wing, Lorentzian near line wing, and Gaussian core contribution of the total line profile function in PHOENIX.

4.3 The Numerical Evaluation of the Total Line Profile

Line profiles of the alkali absorption lines are indispensable for the opacity calculations of very low mass objects in general (objects of spectral type late-type M to T). As mentioned above, for the numerical evaluation of the opacity, each alkali resonance line (in this work the doublets of Na I D, Li I, K I, and Rb I are considered) is broken down in three regions: the far line wing, the near line wing and the core. In Fig. 4.3, a sketch of the three profiles is shown. It is for illustration purposes only in order to give an overview of the line profile contributions.

For the far and near line wings, the profiles introduced in Chap. 3 are used. They are temperature as well as perturber specie dependent. Five perturber types, H_2 (already convolved $H_2 C_{2v}$ and $H_2 C_{\infty v}$ perturbation contributions), $H_2 C_{2v}$, $H_2 C_{\infty v}$, He, and HI, need to be considered in the further calculations with the profiles. Furthermore, there are alternatives for a profile, e.g., for Na I D, Li I, and K I perturbed by He.

The near line wing and the core profiles are merged to a Voigt profile. The approximations for the numerical evaluation of the Voigt function are (Aller et al. 1982): for $\alpha \rightarrow \infty$

$$H(\alpha, y) = \frac{\alpha}{\sqrt{\pi}} \frac{1}{\alpha^2 + y^2}; \quad (4.26)$$

otherwise

$$H(\alpha, y) \simeq \begin{cases} e^{-y^2} + \alpha y^{-2} \sum_{j=0}^6 c_j y^{2j} + \alpha^2 (1 - 2y^2) e^{-y^2} & (\text{for } \alpha \leq 10^{-3}, y \geq 2.5) \\ \Re \left\{ \frac{\sum_{j=0}^6 a_j (\alpha - iy)^j}{(\alpha - iy)^7 + \sum_{j=0}^6 b_j (\alpha - iy)^j} \right\} & (\text{otherwise}) \end{cases} \quad (4.27)$$

where the coefficients of a , b , and c are listed in Table 4.1. The first term in Eq. 4.27, e^{-y^2} , represents the limit of the Voigt function when $\alpha \rightarrow 0$.

In each atmospheric layer, the physical conditions are different, such as the temperature and the perturber density. Hence, for each wavelength point, the partial profiles have not only to be convolved in order to give a profile for the entire spectral line but also have to be evaluated for each atmospheric layer. Moreover, they have to be interpolated onto the internal wavelength grid in PHOENIX. The details of the actual numerical implementation can be found in Appendix B.

j	a	b	c
0	122.607931777104326	122.607931773875350	0.5641641
1	214.382388694706425	352.730625110963558	0.8718681
2	181.928533092181549	457.334478783897737	1.474395
3	93.155580458138441	348.703917719495792	-19.57862
4	30.180142196210589	170.354001821091472	802.4513
5	5.912626209773153	53.992906912940207	-4850.316
6	0.564189583562615	10.479857114260399	8031.468

Table 4.1: Coefficients of the approximated Voigt function in Eq. 4.27 (Aller et al. 1982).

5 Line Profiles in PHOENIX Model Atmospheres and Synthetic Spectra

In the following sections, model atmospheres and synthetic spectra calculated with the PHOENIX code package (version 15) are presented in order to demonstrate the influence of the alkali line profiles on them. The analysis is done for effective temperatures of 1100 K, 1500 K, 2000 K, 2500 K, and 3000 K. Within this large effective temperature range, the influence of alkali line profiles shall be visualized over a large spectral range of late-type M to T dwarfs. For a better demonstration of the effects of the line profiles on models and spectra, “COND” models and spectra are used. In the atmospheric COND approximation, it is assumed that dust has already formed and dust grains have moved below the atmosphere. The opacity provided by the dust is not taken into account (see Sect. 5.2). Model atmospheres and synthetic spectra with this approximation are discussed throughout this chapter. Representative for the stellar properties of very low mass objects and brown dwarfs, $\log(g) = 5.0$, solar composition, and $M = 0.1 M_{\odot}$ are chosen. Note that although the models are computed in spherical symmetry, they are close to the limit of a plane parallel object. Hence, the mass of the object has no significant effect on the resulting synthetic spectrum, which is shown in Fig. 5.1.

Abbreviations for the use of the various alkali line profiles are introduced in Sect. 5.1. In Sect. 5.2, different model types of PHOENIX, which were used in this work, are explained. The concentrations of the most important species, especially of Na I and K I, are briefly discussed in Sect. 5.3. Hereafter, the influence of alkali line profiles on synthetic spectra is discussed in Sects. 5.4 and 5.5. Special details concerning the other effective temperatures will be mentioned.

When discussing relative changes between two quantities (A and B) in Sects. 5.4 and 5.5 (and throughout this work), it is abbreviated with “norm. $\Delta(A,B)$ ” which implies $(A - B)/A \cdot 100$, see for example Fig. 5.1.

5.1 Legend

Various line profiles have been added in PHOENIX in order to study their effects in model atmospheres and synthetic spectra. For a better overview, the following abbreviations for the various setups will be used throughout this work if not mentioned otherwise.

Impact Setup

In this setup, analytical, impact approximated van-der-Waals profiles have been considered in the calculations of model atmospheres and synthetic spectra, see Sects. 2.1.1 and 3.1.

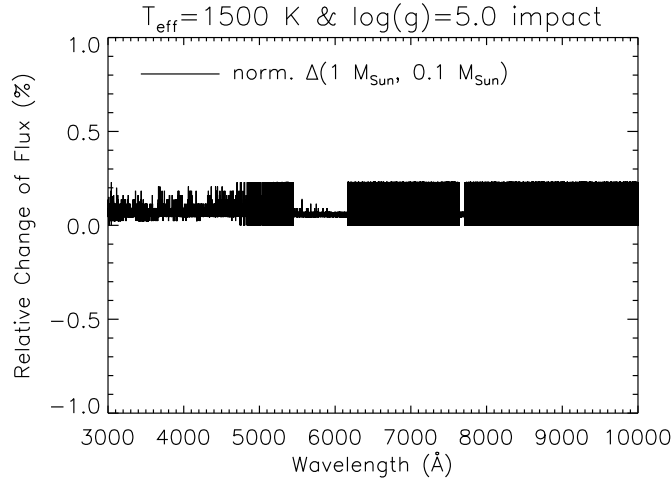


Fig. 5.1: Relative change of the flux of a synthetic spectrum computed with $M = 1 M_{\odot}$ and $0.1 M_{\odot}$ and $T_{\text{eff}} = 1500 \text{ K}$, $\log(g) = 5.0$, and solar composition.

1st Generation Setup

This setup implies model calculations with the 1st generation of non-analytical alkali profiles (Allard et al. 2003) for the Na I D, Li I, K I, Rb I, and Cs I doublets which are calculated in the unified semi-classical theory, see Sects. 2.4 and 3.2.

Modern1 Setup

The modern1 setup is similar to the 1st generation setup except that now newly introduced non-analytical profiles for the Na I D, Li I, K I, and Rb I absorption lines, see Sect. 3.2, are included in the atmosphere calculations. They are also calculated in the unified semi-classical theory but in a new, more detailed approach.

Modern2 Setup

The modern2 setup is an extension of the modern1 setup. In the Na I D profiles, HI broadened Lorentzian data by (Leininger et al. 2000) has been included, which has been also obtained non-analytically, see Sect. 3.3.

Modern3 Setup

The Lorentzian HWHMs for the Na I D, Li I, and K I doublets perturbed by He in the modern1 and modern2 setup have been substituted with the non-analytical line profiles by Mullanphy et al. (2007). They have been calculated in the fully quantum mechanical theory, see Sect. 2.3, and have been introduced in Sect. 3.4. The Lorentzian profiles of Na I D perturbed by HI are still included here (see the modern2 setup).

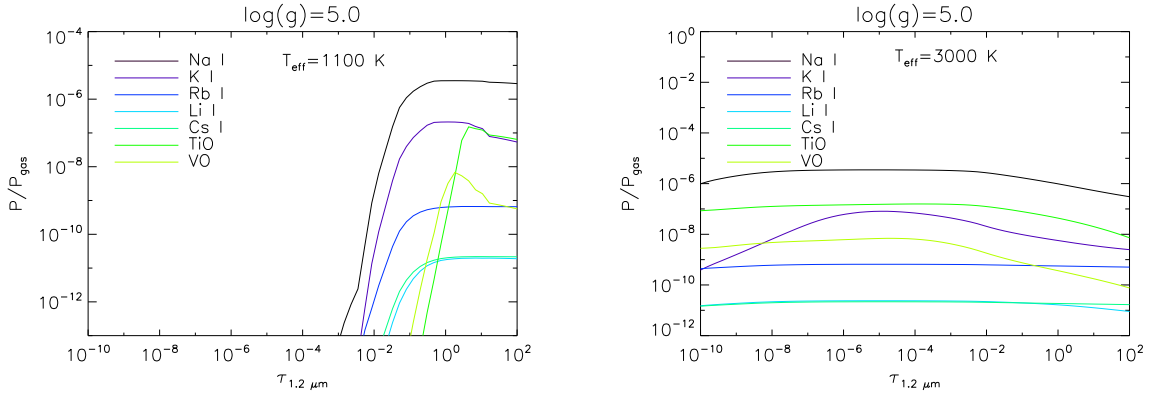


Fig. 5.2: Concentrations of the alkalis, TiO, and VO for an atmosphere at $T_{\text{eff}} = 1100$ K (left) and 3000 K (right), $\log(g) = 5.0$ and solar composition.

5.2 Atmospheric Models in PHOENIX

In order to take into account the existence of dust in cool stellar atmospheres, two limiting cases have been introduced to PHOENIX (Allard et al. 2001): COND and DUSTY models. For completeness, a third alternative, DRIFT models, is briefly mentioned here.

COND Models

The COND approximation considers dust in chemical equilibrium. The dust opacities are ignored because it is assumed that after dust grains have formed, they sink down completely. This scenario is applicable for atmospheres in which sedimentation, i.e., dust settling below the photosphere, takes place. It is typically the case for T_{eff} lower than 1800 K. Throughout this chapter, COND models have been used.

DUSTY Models

After dust has formed in the atmosphere in chemical equilibrium, it remains at its place and a respective amount of dust grains is subtracted from the gas phase. No dust settling is taken into account. The dust grains are assumed to be spherical with a homogeneous size distribution in order to calculate the dust opacities. No DUSTY models are presented in this chapter. Details to these models can be found in Chap. 6.

DRIFT Models

There is an alternative more sophisticated approach of the dust treatment compared to DUSTY models in PHOENIX, the DRIFT models, (Dehn 2007; Helling et al. 2007; Helling & Woitke 2006; Woitke & Helling 2004, 2003). It includes a self consistent dust treatment in phase non-equilibrium which is coupled to PHOENIX. DRIFT models will be introduced in more detail in Chap. 6.

5.3 Concentrations of the Most Important Species

Kirkpatrick et al. (1999) pointed out the increase in the width of the KI resonance doublet towards later spectral types. Furthermore, they have argued that this unique behavior is due to the extraordinary high concentration of KI. This is also valid for Na I, since it is the alkali with the highest concentration, followed by KI. In decreasing concentration order, the alkalis Rb I, Li I, and Cs I have a (much) smaller concentration compared to Na I and KI. In Fig. 5.2, for atmospheres at $T_{\text{eff}} = 1100$ K and 3000 K with $\log(g) = 5.0$ and solar composition, the concentrations of the alkali species and of TiO and VO are displayed. As mentioned in Chap. 1, molecular bands of TiO and VO in the optical wavelength range are characteristic for M-type and later-type dwarfs which is due to their high concentrations, see Fig. 5.2. The dominance of Na I and KI is easily visible. This is the reason why the far line wings of these two alkalis belong next to the absorption bands of TiO and VO to the main contributors of the pseudo continuum in these spectra, see also Sect. 5.4.2. Therefore, it is most important to model these two lines as good as possible.

5.4 Impact, 1st Generation, and Modern1 Setup

In order to narrow down the number of comparisons of the various setups, the discussion in Sect. 5.4.1 is focused on $T_{\text{eff}} = 1500$ K, $\log(g) = 5.0$, and solar composition¹ (Grevesse & Noels 1993). The results for all other effective temperatures can be found in Appendix C.2, Figs. C.6–C.15. The discussion is similarly valid for the other effective temperatures, if not mentioned otherwise. In Sect. 5.4.1, there is a discussion of the influence of the impact, 1st generation, and modern1 setup on their temperature–pressure structure and their synthetic spectra. In Sect. 5.4.2, the influence of the Na I D and KI profiles on Li I and Rb I is discussed. Satellites in synthetic spectra are shown and discussed in Sect. 5.4.3. The influence of the stellar parameters on the synthetic spectra is illustrated in Sect. 5.4.4. A brief analysis on the influence of the model atmosphere on synthetic spectra is given in Sect. 5.4.5. Some aspects of the upcoming discussion have been already presented in Johnas et al. (2006).

5.4.1 Model Atmospheres and Synthetic Spectra

The temperature–pressure (T–p) structure of impact, 1st generation, and modern1 models and the relative changes in the gas temperature are presented in Fig. 5.3, see also Figs. C.1–C.5 in Appendix C.1. The alkali line profiles cause no significant changes in the T–p structure. The random behavior of the T–p structures in the innermost layers (left panel of Fig. 5.3) is due to an under-sampling and can be reduced if the number of atmospheric layers is increased. The relative change of the T–p structures is mostly below $\pm 1\%$ except for the innermost layers in which the convection zone becomes dominant. Except for the T–p structure at $T_{\text{eff}} = 1100$ K, see Fig. C.1, the changes of the temperature of the other effective temperatures are within the range of $\pm 1\%$ and are negligible. Models at and below $T_{\text{eff}} = 1100$ K are computed at the limits of the current physical background and have to be taken with caution. They represent only preliminary results.

Consequently, the effects in the atmospheric models and synthetic spectra, which are discussed here, are due to the opacities provided by the line profiles and not because of a change in the T–p structure.

¹If not mentioned otherwise, solar composition is assumed throughout this work.

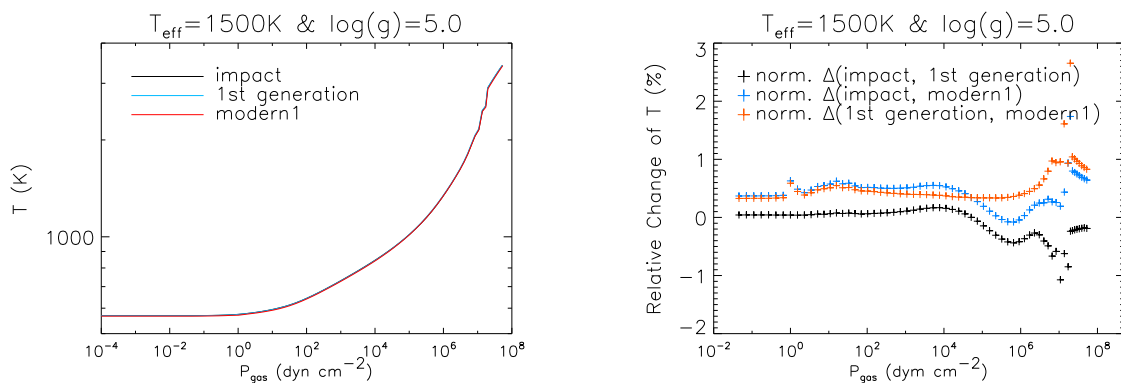


Fig. 5.3: Left: T-p structures of the impact, 1st generation, and modern1 atmospheres in Fig. 5.4. Right: relative change of the gas temperature between the three setups.

In Fig. 5.4, low resolution spectra with the impact, 1st generation, and modern1 setup with $T_{\text{eff}} = 1500 \text{ K}$ and $\log(g) = 5.0$ as well as the relative change of the flux between the various setups are shown. These spectra are computed with a 2 \AA resolution in the optical and near infrared wavelength ranges². The differences of the fluxes in these spectra are significant. Up to approximately $1 \mu\text{m}$, the impact spectrum has more flux, see also Allard et al. (2003), than the 1st generation and modern1 spectra. There has been a shift towards higher fluxes so that the modern1 spectra carry less opacity than in the 1st generation setup but more than in the impact setup. A more detailed overview (with a resolution of $\Delta\lambda = 0.02 \text{ \AA}$) of the changes in the alkali doublets is shown in Fig. 5.5. Since the differences in the alkali doublets are of importance, these close-ups are shown for the other effective temperatures in Figs. C.6–C.10 in Appendix C.2 (with a resolution of $\Delta\lambda = 2 \text{ \AA}$). The artificial edge in the 1st generation and modern1 high resolution spectra in the top panel of Fig. 5.5 around 5000 \AA is due to the supplied Na I D far line wing profiles which influences vanish there so that there is a drop off in the profile functions and an increase of the flux. The presence of this edge stresses the importance of expanding the profile calculations of the Na I D₂ far line wing and at the same time, expanding the profile calculations to atoms appearing at wavelengths smaller than 5000 \AA , e.g., for Fe I and Ca I.

Details of the alkali doublets in the impact, 1st generation, and modern1 setup are shown with a resolution of 0.02 \AA in Fig. 5.6 and in Figs. C.11–C.15 for the other effective temperatures in Appendix C.3. The Na I D line wings of the 1st generation and modern1 setup cross on each side of the doublet. The stronger line broadening effect in the modern1 Na I D near line wings compared to those in the 1st generation setup is due to the larger damping constants of Na I D₂ by the profiles of the modern1 setup. The crossing could be due to the weaker far line wing profiles with He as perturber provided by Allard et al. new (profiles of the modern1 setup). The asymmetry of the far line wing profiles which is due to the very different potentials used for the D₁ and D₂ lines (see Sect. 3.5) is also noticeable in the synthetic spectra in between the line centers of the resonance doublets, especially for K I. The K I doublet has much more flux in the modern1 setup than in the 1st generation setup. It has less than in the impact setup.

The overall change of flux in the alkali absorption lines with lower concentrations, i.e. Li I and Rb I, between the 1st generation and modern1 setup can be explained by the overlapping far line wings of Na I D and K I, see Sect. 5.4.2 for details.

²The sampling rate in the optical wavelength range of each low resolution spectrum is 2 \AA in this work.

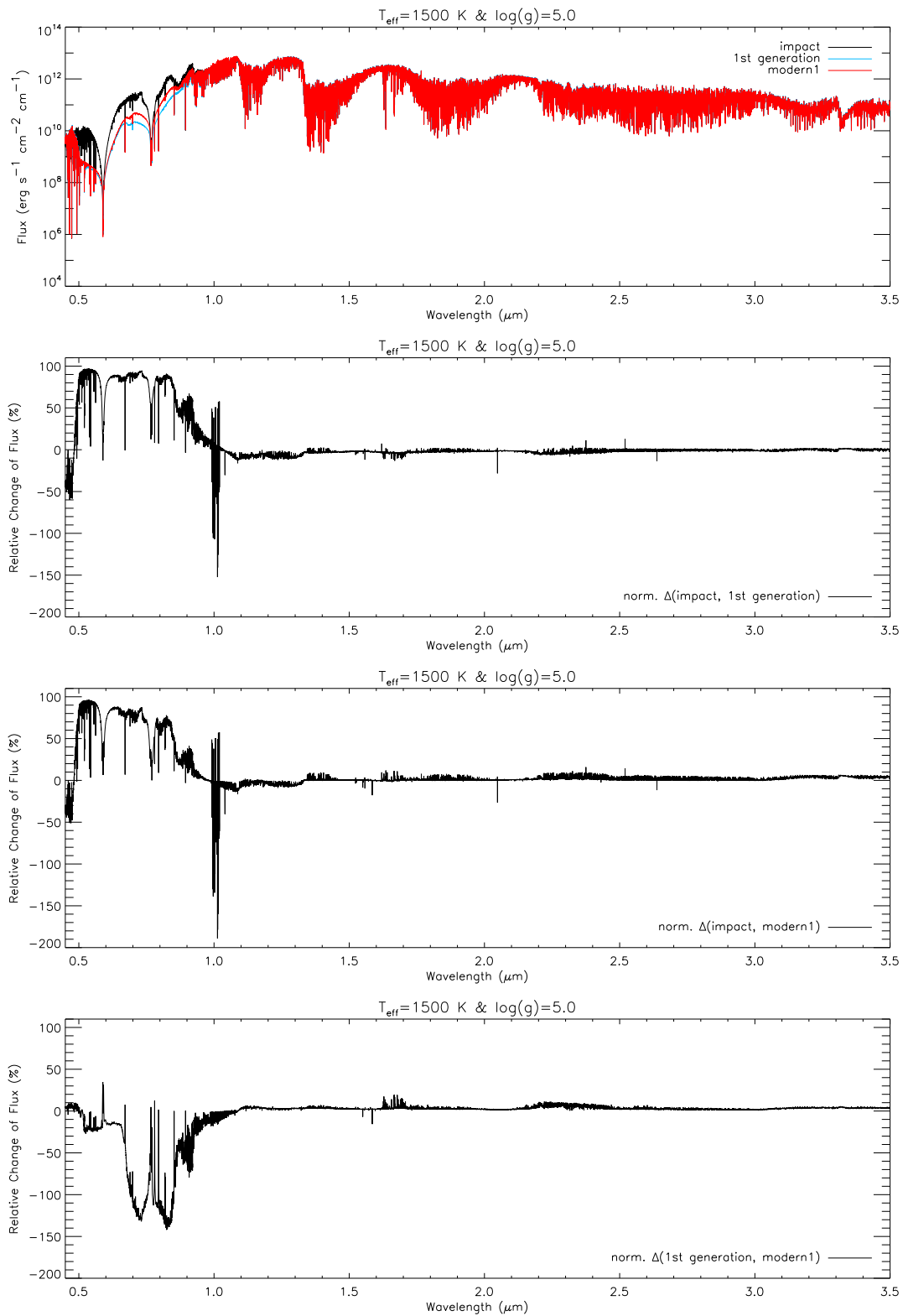


Fig. 5.4: Upper panel: atmospheric model spectra with $T_{\text{eff}} = 1500 \text{ K}$, $\log(g) = 5.0$, and solar composition computed with the impact, 1st generation, and modern1 setup. In the three lower panels, the relative changes of the flux between the various setups are shown.

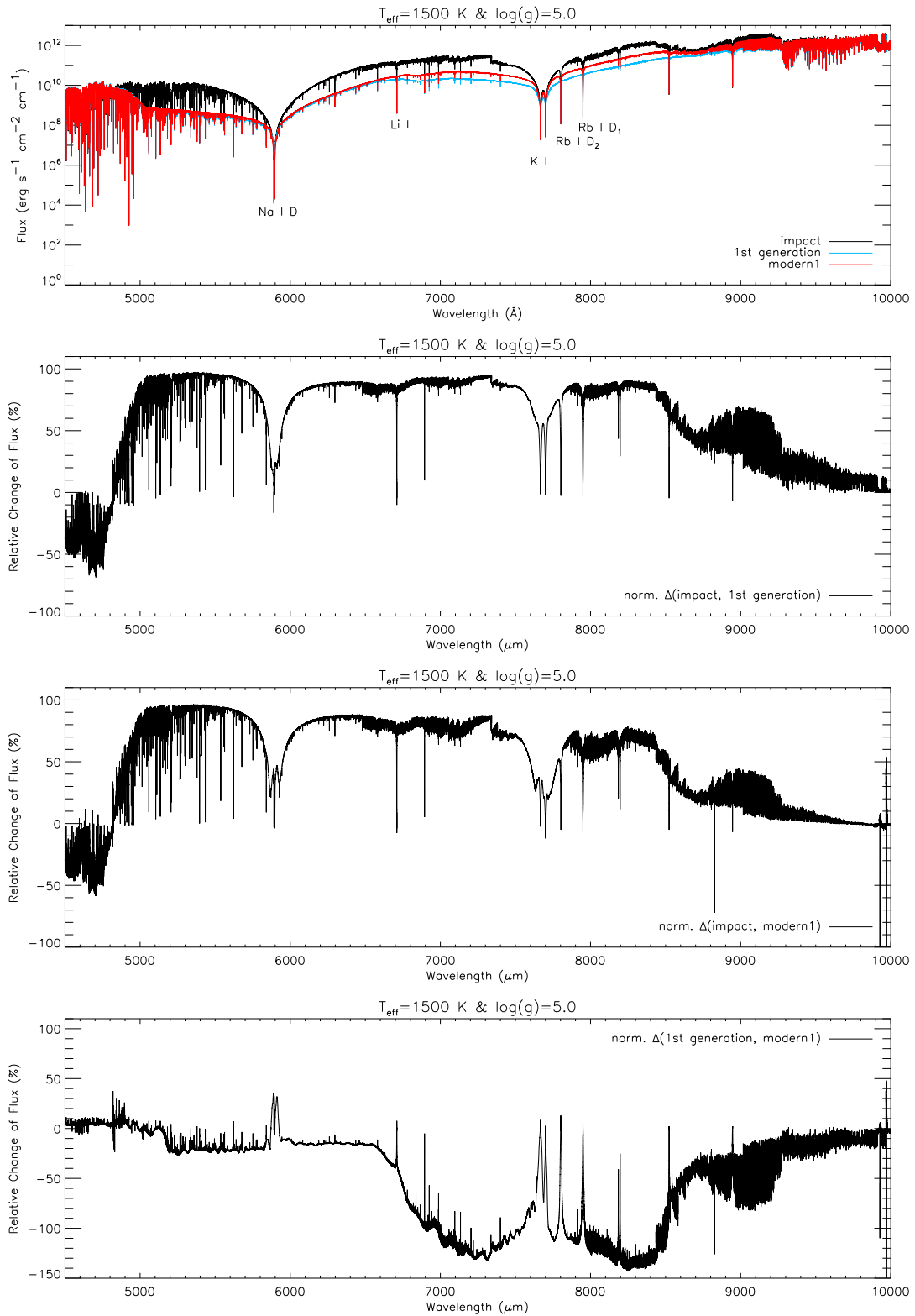


Fig. 5.5: Upper panel: high resolution spectra with $T_{\text{eff}} = 1500 \text{ K}$, $\log(g) = 5.0$, and solar composition computed with the impact, 1st generation, and modern1 setup. In the three lower panels, the relative changes of the flux between the various setups are shown.

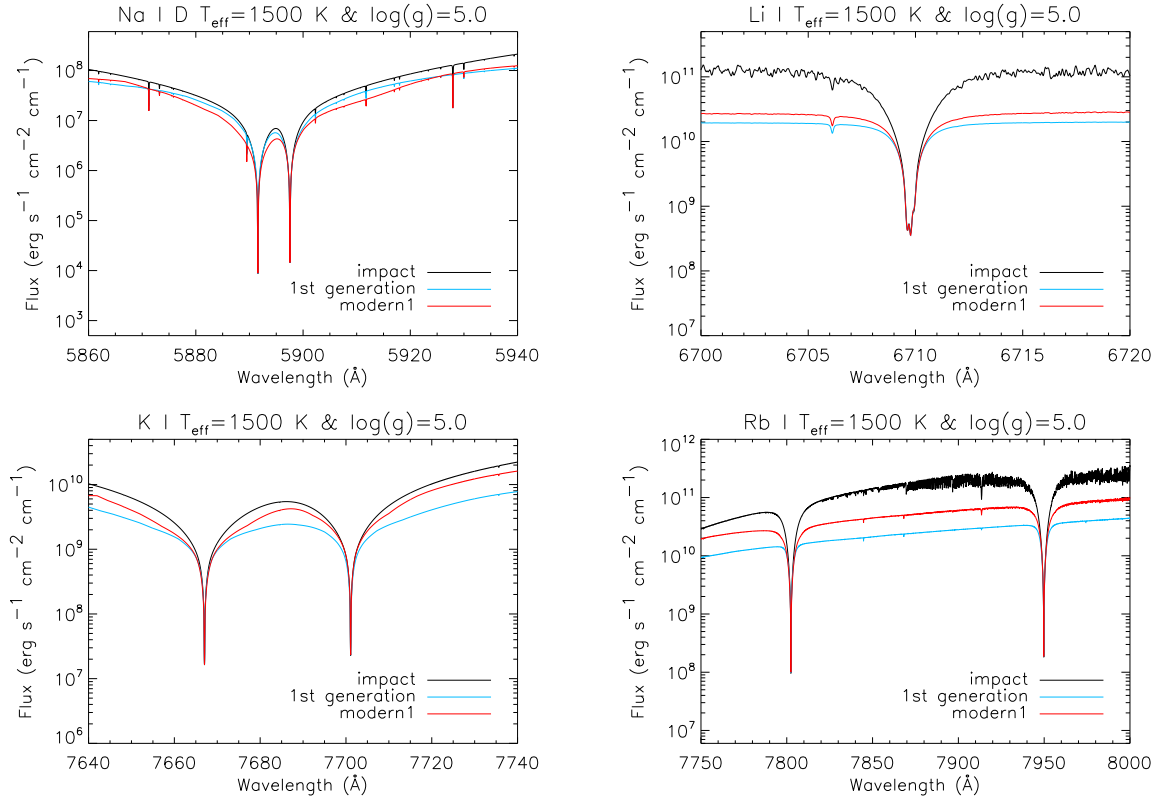


Fig. 5.6: Close-up of the high resolution spectra of Fig. 5.5 of the Na I D, Li I, K I, and Rb I doublets.

Since the modern1 setup represents an improvement over the 1st generation setup in the line profile calculation and differences are visible, the results obtained with the 1st generation setup will be omitted in further discussions (Allard 2006).

5.4.2 The Influence of the Na I D and K I Profiles on the Li I and Rb I Doublets

There have been advances in the precision especially in the description of the Li I and Rb I absorption lines due to the more detailed and completed line profiles of the modern1 setup, see Chap. 3. Hence, the influence of these line profiles in synthetic spectra is studied in more detail here.

In the close-ups of the Li I and Rb I lines in Fig. 5.6, the strength of the modern1 (and 1st generation) profiles is noticeable. In the impact setup, there is still some visible influence of the TiO and CaH bands, which mask the Li I lines. The Rb I doublet is overlapped by a slightly stronger TiO band. These molecular features are suppressed in the synthetic spectra computed with the modern1 (and 1st generation) setup due to the dominance of the alkali line profiles.

In order to demonstrate the influence of the Na I D and K I modern1 profiles, the Li I and Rb I absorption lines in a modern1 synthetic spectrum and a “reduced” modern1 synthetic spectrum (considering the modern1 setup for Na I D and K I and the impact setup for the Li I and Rb I doublets) are shown in Fig. 5.7. Except for the considered alkali profiles, the two spectra have been obtained with the same settings. There are differences only in the closest vicinity of the central wavelengths of the Li I and Rb I doublets visible, which implies the overlap of the Na I D and K I far line wings. The relative change of the flux, which is displayed in the lower panels in Fig. 5.7,

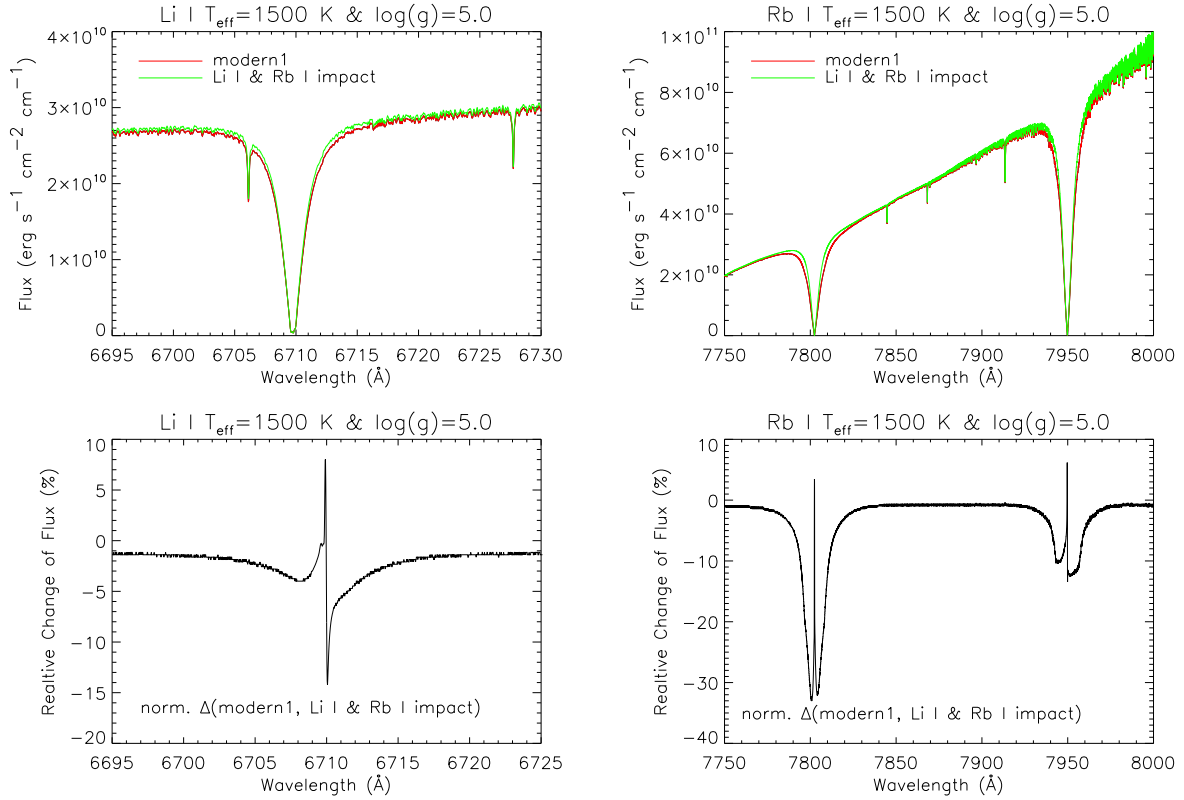


Fig. 5.7: Close-up of the Li I (left) and Rb I (right) doublet, where Na I D, Li I, KI, and Rb I are computed with the modern1 setup, and where only Na I D and KI are computed with the modern1 setup and Li I and Rb I in the impact setup. The relative changes of the flux between these two settings are shown for the Li I and Rb I doublets in the two panels at the bottom.

is larger for Rb I than for Li I which is due to the higher concentration of Rb I than of Li I. Furthermore, the Rb I doublet is purely masked by the KI far line wings whereas the Li I doublet is overlapped by the far line wings of Na I D and KI.

The far line wing profiles of Li I and Rb I play a minor role for the computation of these alkali resonance lines. This gives evidence that the far line wings of Na I D and KI provide the pseudo-continuum. They overlap with the other alkalis of lower concentrations. For later applications in regard to the description of observations, very high resolution observations with a good signal-to-noise ratio are necessary in order to test the profiles of the alkalis with a lower concentrations. Nevertheless, the good simulation of the Na I D and KI absorption doublets is most crucial for the description of those alkalis. Especially the good description of the Li I doublet is important for the identification of brown dwarfs (Rebolo et al. 1992), see Chap. 7.

5.4.3 Satellites

The satellites in the modern1 far line wing profiles have already been discussed in Sect. 3.5. Now, their influence on synthetic spectra needs to be tested. Satellites appear always very far-off the central wavelengths. Due to the strong presence of molecular bands, they are less noticeable in synthetic spectra for $T_{\text{eff}} \geq 2000$ K. If at all, only the outermost satellite of the two alkalis with the highest concentrations can be resolved in synthetic spectra.

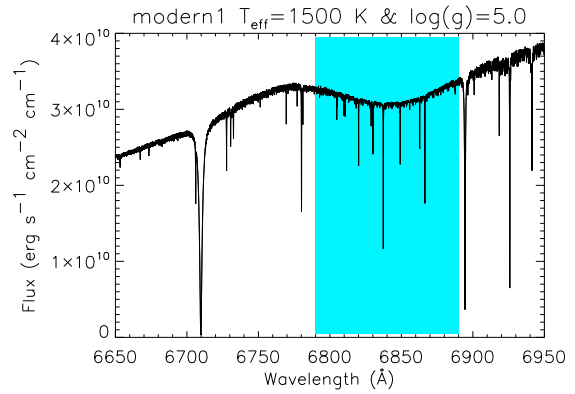
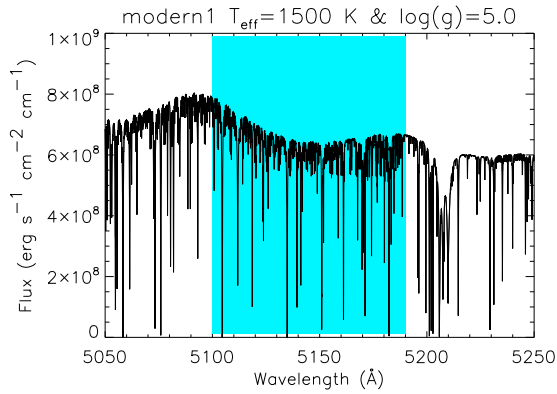
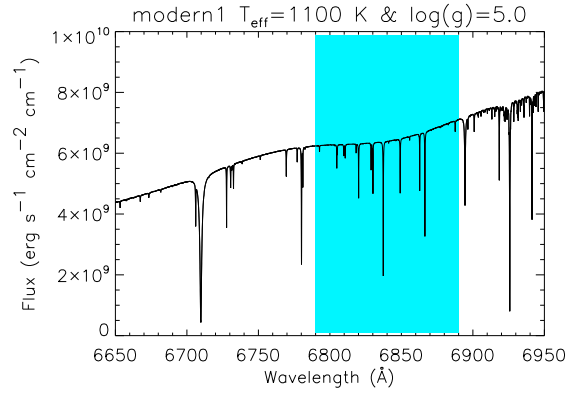
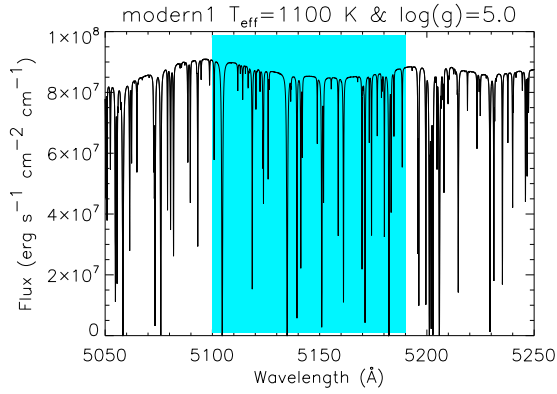


Fig. 5.8: NaID₂ satellite in synthetic spectra with $T_{\text{eff}} = 1100$ K and 1500 K and $\log(g) = 5.0$.

Fig. 5.9: KID₂ satellite in synthetic spectra with $T_{\text{eff}} = 1100$ K and 1500 K and $\log(g) = 5.0$.

The line profiles for NaID₂ only show relatively weak satellites, which is why these features are hardly noticeable in the synthetic spectra, see Fig. 5.8. The satellite, i.e., the broad absorption feature, between approximately 5100 \AA and 5190 \AA is better visible for $T_{\text{eff}} = 1500$ K than for $T_{\text{eff}} = 1100$ K. The NaID₂ far line wing profiles, see Chap. 3, show only significant satellites when perturbed by H₂ C_{2v} or He. Due to the higher concentration of H₂ than of He, the satellite is mostly due to the perturbations with H₂. Molecular bands and atomic lines are predominant at these short wavelengths so that the satellite is masked by them. It seems unlikely to be observable in the near future in observations due to the difficulty in measuring such low flux levels and flux differences. (Observing the Na I D doublet in a (very) high resolution provides already a challenge for the spectroscopy.)

In Fig. 5.9, the KID₂ satellite for $T_{\text{eff}} = 1100$ K and 1500 K between approximately 6790 \AA and 6890 \AA is easier recognizable due to fewer molecular features. The perturbations with H₂ C_{2v} contribute most to this line satellite. Again, it is stronger for $T_{\text{eff}} = 1500$ K and due to the increasing dominance of molecular bands no longer noticeable for $T_{\text{eff}} \geq 2000$ K. It is close to the Li I doublet. Also the observation of this satellite provides a challenge due to the required very good resolution and extremely good signal-to-noise ratio. However, such an observation would be a very good proof for the theoretical predictions. The position of the K–H₂ satellite is in competition with a CaH system molecule band, see Burgasser et al. (2003) and Allard et al. (2007). Furthermore, there is also a TiO band present in the satellite, which weakens the strength of the satellite.

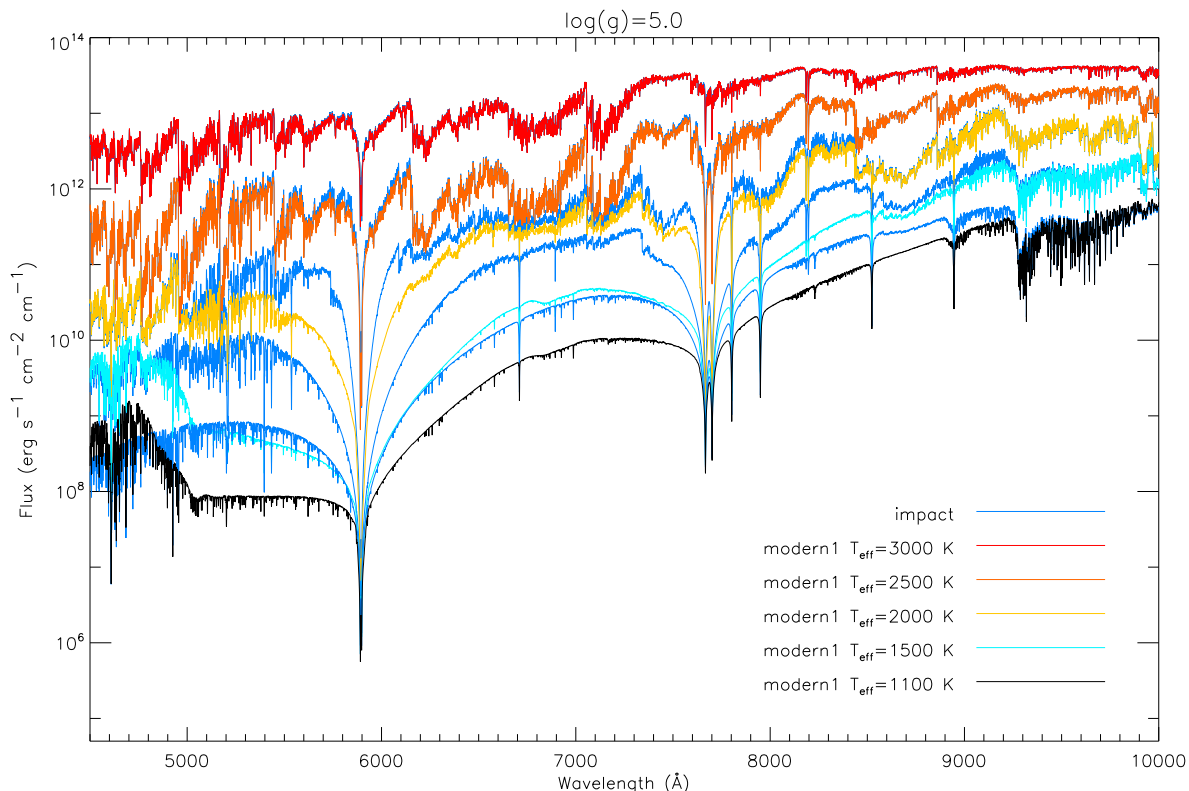


Fig. 5.10: Synthetic spectra with a resolution $\lambda/\Delta\lambda$ of 10 000 in the impact (blue) and modern1 (colored) setup for $T_{\text{eff}} = 1100$ K to 3000 K with $\log(g) = 5.0$ and solar composition.

5.4.4 The Influence of Stellar Properties on the Line Profile

The stellar properties, such as the effective temperature, the surface gravity, and the metallicity, can change the perturber densities in the model atmospheres.

The Influence of the Effective Temperature

Synthetic spectra computed in the impact and modern1 setup for effective temperatures from 1100 K to 3000 K with $\log(g) = 5.0$ and solar composition are displayed in Fig. 5.10. A close-up of Fig. 5.10 is presented in Fig. 5.11 showing the NaID₂ line for $T_{\text{eff}} = 1100$ K, 2000 K, and 3000 K. As it is also shown in Figs. C.6–C.15, the influence of the alkali absorption lines increases towards decreasing effective temperatures, so that at $T_{\text{eff}} = 1100$ K the spectrum is dominated by the alkali absorption lines and their broad far line wings. However, the line profiles themselves become broader towards higher gas temperatures, see Sect. 3, which seems to imply the opposite effective temperature dependence.

However, the gas pressure over the atmospheric layers increases towards lower effective temperatures, as depicted in Fig. 5.12. The lower the effective temperature is, the higher is the gas density and hence more collisions occur. The line broadening effect is increased.

Furthermore, for high effective temperatures, molecular bands (especially between $T_{\text{eff}} = 2500$ K and 3000 K), e.g., of TiO and VO, provide the background opacity. Only the cores of the alkali absorption lines are visible, see Figs. 5.10 and 5.11. The molecular bands gradually disappear towards lower effective temperatures due to the condensation of related species, see also Allard

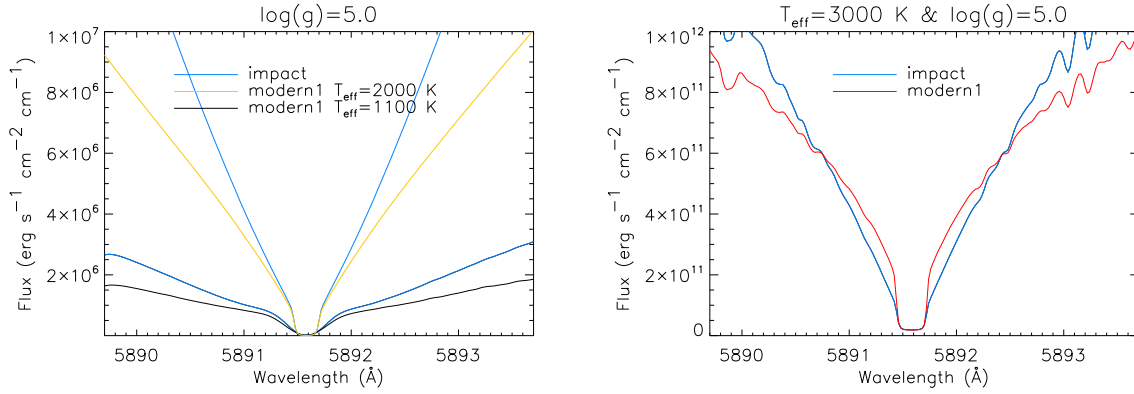


Fig. 5.11: Close-up of Fig. 5.10 in the Na I D₂ line for $T_{\text{eff}} = 1100$ K, 2000 K, and 3000 K.

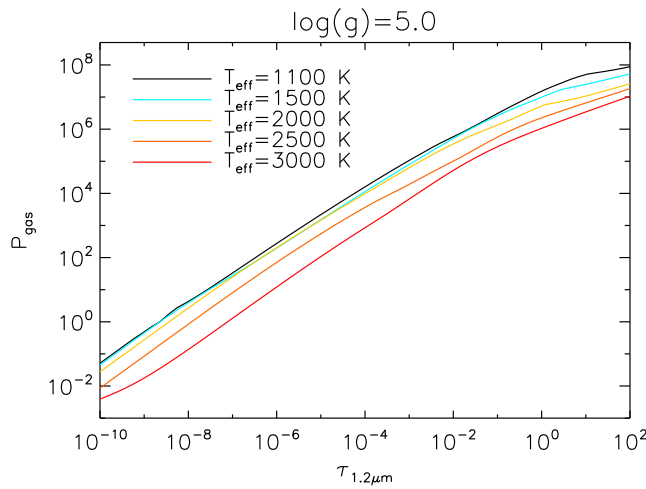


Fig. 5.12: The gas pressure found in model atmospheres for $T_{\text{eff}} = 1100$ K to 3000 K with $\log(g) = 5.0$ and solar composition.

et al. (2001).

Thus, the alkali doublets are strengthened towards lower effective temperatures due to the higher collision rate at lower effective temperatures and less background opacity from molecular bands.

The Influence of the Surface Gravity

The surface gravity has a direct influence on the gas pressure in the atmosphere. The higher $\log(g)$ is, the larger is the gas pressure and the stronger is the line broadening effect. The $\log(g)$ dependence is illustrated in Fig. 5.13 for $\log(g) = 4.0$ and 5.0 and $T_{\text{eff}} = 1100$ K, 2000 K, and 3000 K.

In Figs. 5.14 and 5.15, a close-up of the KI doublet for $T_{\text{eff}} = 3000$ K and 1100 K is shown. At $T_{\text{eff}} = 3000$ K, the expected relationship between $\log(g)$ and the line width is easily visible. However, towards lower effective temperatures, the effect is not unambiguously visible anymore. At first sight, it seems as if for both setups the opposite is true, see Fig. 5.15, i.e., the line broadening increases towards smaller $\log(g)$. Since the effect is observable in both setups, it is not a feature due to more sophisticated line profiles. It is only due to the different flux ranges in the spectra. When

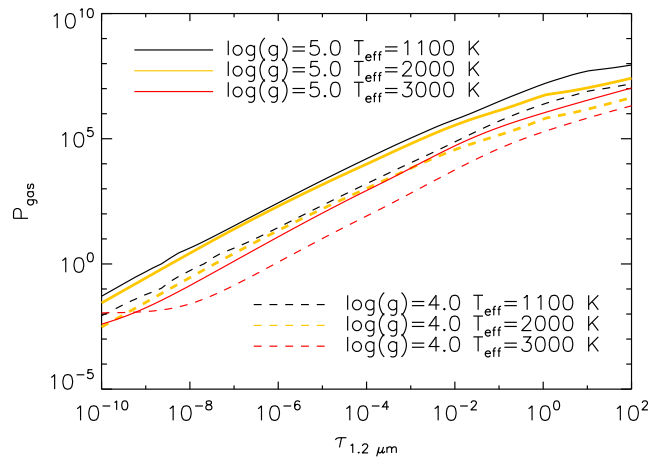


Fig. 5.13: The gas pressure found in model atmospheres for $T_{\text{eff}} = 1100$ K, 2000 K, and 3000 K with $\log(g) = 4.0$ and 5.0 and solar composition.

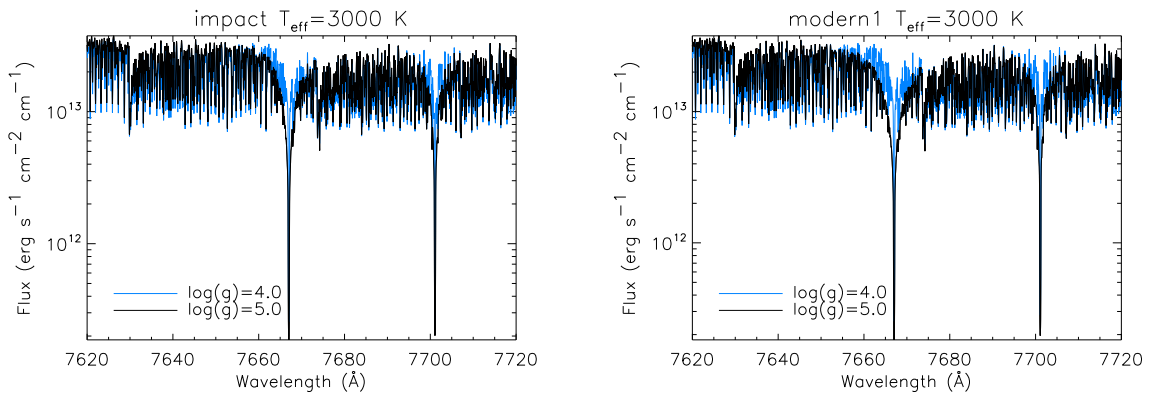


Fig. 5.14: Close-up of the KI doublet in the impact (left) and modern1 (right) setup for $T_{\text{eff}} = 3000$ K with $\log(g) = 4.0$ and 5.0 and solar composition.

scaling the spectra with $\log(g) = 4.0$ to the maximum flux between the central wavelengths, the expected increased line broadness towards higher values of $\log(g)$ is again visible, see Fig. 5.16. This is true for each alkali doublet.

The Influence of the Metallicity

With decreasing metallicity Z , the overall opacity decreases in the model atmospheres. Thus, it is possible to “view” into deeper layers of the atmosphere which is shown for the impact and modern1 setup for $Z = -2.0$ and $+0.0$, $T_{\text{eff}} = 1100$ K and 3000 K, and $\log(g) = 5.0$ with the flux contribution function in Fig. 5.17. At the same optical depth, hotter and deeper layers with higher gas pressures are visible, see Fig. 5.18. Hence, more collisions occur in the line forming regions and the alkali absorption line width increases. The influence of the metallicity in synthetic spectra is shown for the KI doublet in Figs. 5.19 and 5.20. Note that the effect is much smaller in synthetic spectra towards higher effective temperatures, due to the larger background opacity and lower gas pressure, and for the impact setup, due to the different near line wing profiles and the lack of far line wing profiles in this setup.

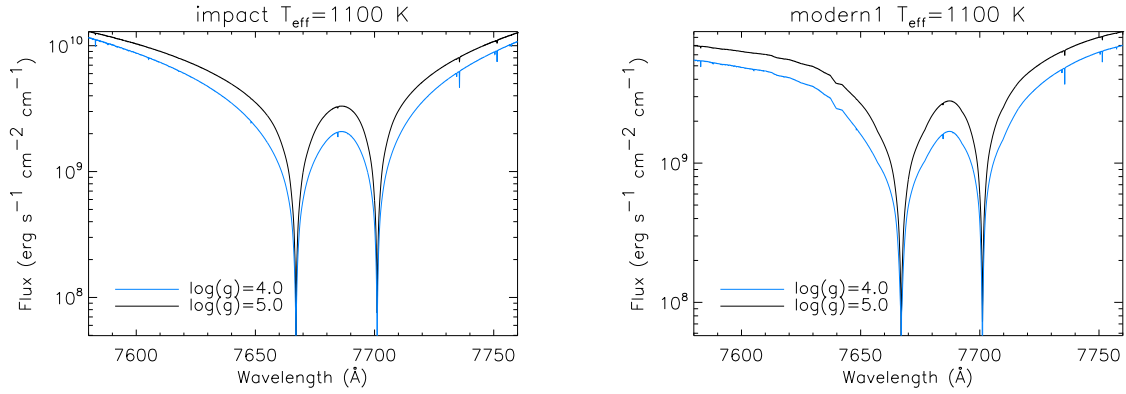


Fig. 5.15: Same as Fig. 5.14, but for $T_{\text{eff}} = 1100$ K.

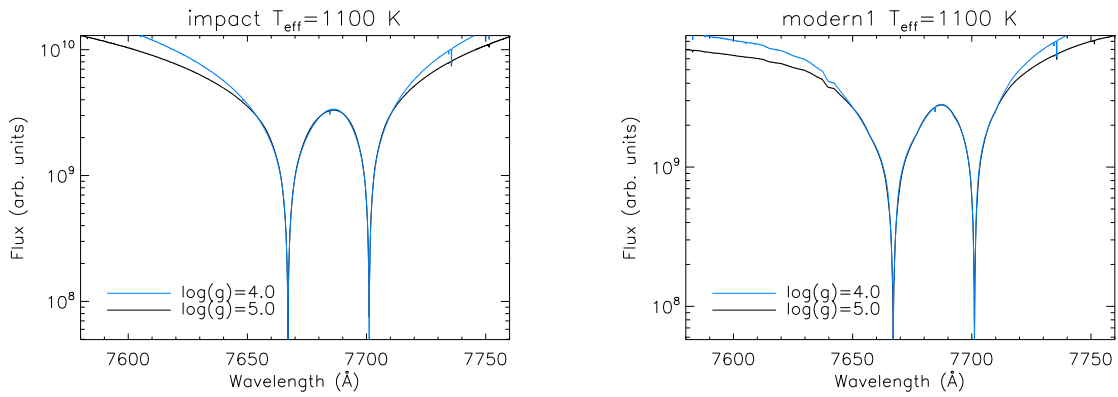


Fig. 5.16: Scaled $\log(g) = 4.0$ spectra to the maximum flux between the line centers of Fig. 5.15 for the impact (left) and modern1 (right) setup.

5.4.5 The Dependence on Atmospheric Models

It is possible to compute the synthetic spectrum in the modern1 (and modern2 and modern3) setup with a computational shortcut by computing a modern1 synthetic spectrum with an impact model instead of converging a modern1 atmosphere before. This could seem reasonable due to the negligible differences in the T - p structures between the various setups. However, there are differences in the details especially of the alkali doublets. This is of special importance when dealing with the modern2 and modern3 setups, which are discussed in the next sections.

A comparison between two modern1 synthetic spectra is shown in Fig. 5.21, displaying a modern1 synthetic spectrum based on a modern1 model atmosphere (setting 1) and another modern1 synthetic spectrum based on an impact model atmosphere (setting 2). The changes concerning the alkali lines, especially the ones of Na I D and K I are not extremely large, about $\pm 3\%$. However, these changes can increase. Keeping in mind the significant differences in the models and synthetic spectra between, e.g., the impact and modern1 setup, a complete set of a converged model atmosphere and a resulting synthetic spectrum provides a reliable result.

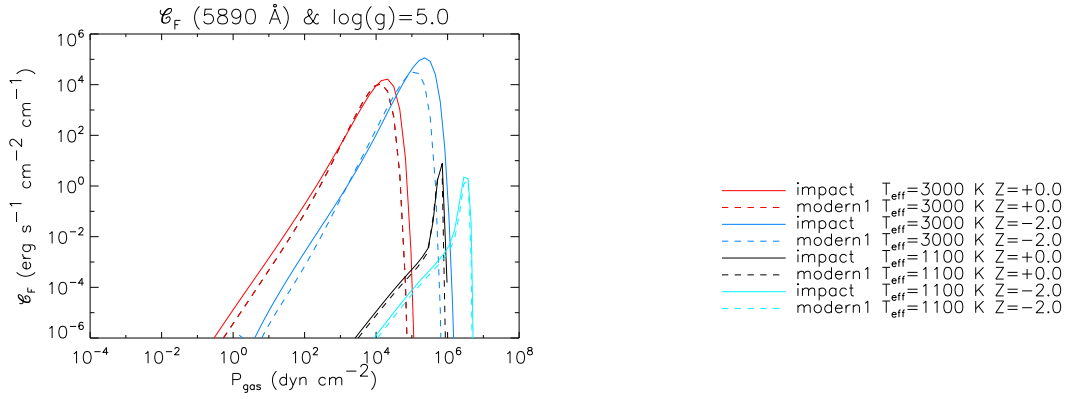


Fig. 5.17: Flux contribution functions of the impact and modern1 setup at 5890 Å for $Z = -2.0$ and $+0.0$, $T_{\text{eff}} = 1100$ K and 3000 K, and $\log(g) = 5.0$.

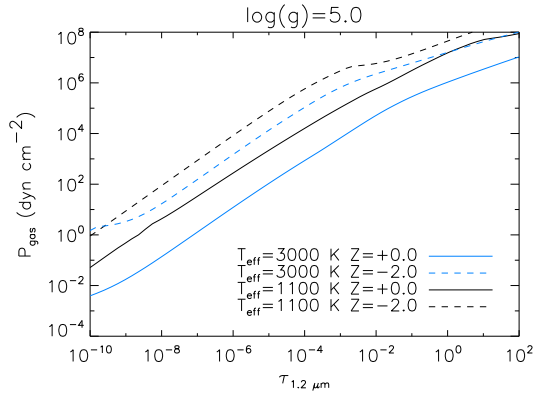


Fig. 5.18: Gas pressure at $Z = -2.0$ and $+0.0$, $T_{\text{eff}} = 1100$ K and 3000 K, and $\log(g) = 5.0$.

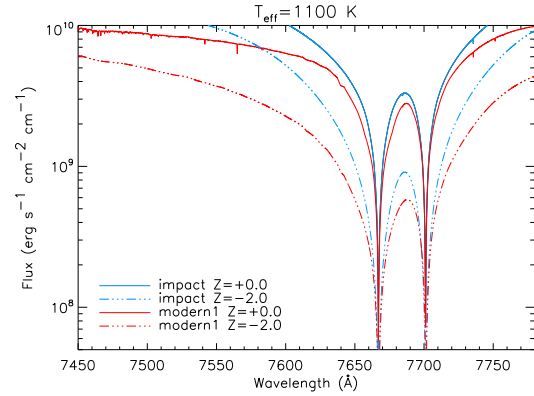


Fig. 5.19: Same as Fig. 5.20, but for $T_{\text{eff}} = 1100$ K.

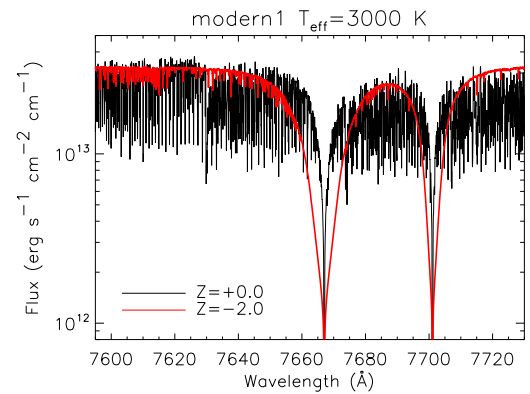
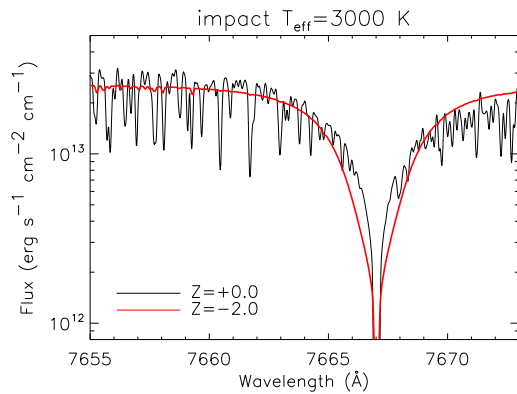


Fig. 5.20: Close-up of the KI doublet in synthetic spectra in the impact (left) and modern1 (right) setup for $T_{\text{eff}} = 3000$ K and $\log(g) = 5.0$ with $Z = -2.0$ and $+0.0$.

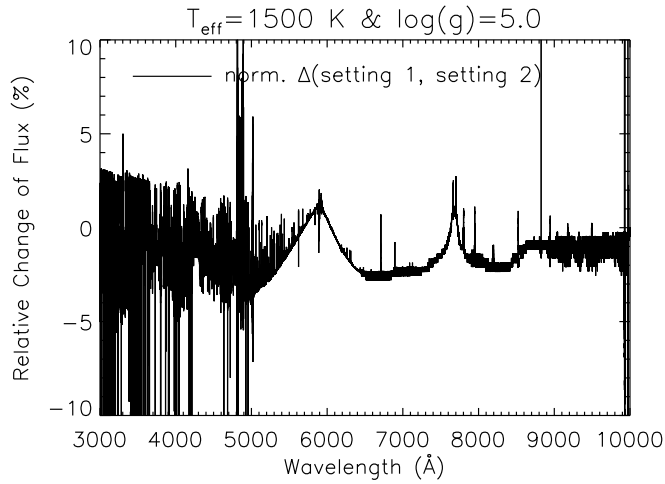


Fig. 5.21: The relative change of the flux of two synthetic spectra computed with the same settings for the modern1 setup, $T_{\text{eff}} = 1500$ K, $\log(g) = 5.0$, and solar composition. Setting 1 relies on a converged modern1 model atmosphere and the setting 2 on a converged impact model atmosphere.

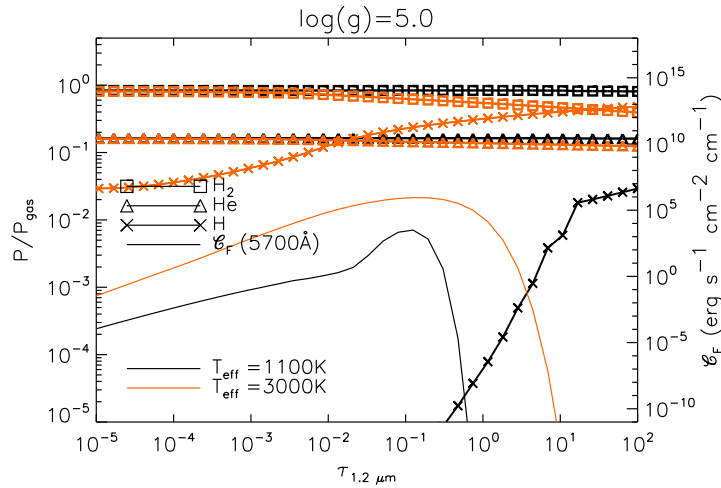


Fig. 5.22: Concentration of H_2 , He, and HI in the atmosphere at $T_{\text{eff}} = 1100$ K and 3000 K with $\log(g) = 5.0$ and solar composition (left ordinate). Besides the flux contribution functions of impact synthetic spectra with $\log(g) = 5.0$ and solar composition at a wavelength of 5700 \AA for $T_{\text{eff}} = 1100$ K and 3000 K are depicted (right ordinate).

5.5 Modern2 and Modern3 Setup

A similar comparison as in Sect. 5.4.1 is done in this section, only some Lorentzian profiles have been added, respectively exchanged, in the models and synthetic spectra. The difference between the modern2 and modern1 setup is just the inclusion of Lorentzian near line wing profiles of Na I D perturbed by HI (Leininger et al. 2000). In the modern3 setup, the Lorentzian profiles of Na I D, Li I, and KI perturbed by He in the unified semi-classical theory have been exchanged with the profiles obtained by the fully quantum-mechanical theory (Mullamphy et al. 2007) (compared to the modern2 setup). The analyses are done for the effective temperature range from 1100 K to 3000 K, $\log(g) = 5.0$, and solar composition. Since the differences in the setups concern only Lorentzian profiles, flux changes are expected only in the near line wings of the considered alkalis. In order to demonstrate the significance of the perturber species H₂, He, and HI in model atmospheres with $\log(g) = 5.0$, the concentrations as well as the flux contribution functions at 5700 Å at $T_{\text{eff}} = 1100$ K and 3000 K are shown in Fig. 5.22.

A similar analysis for the Na I D absorption doublet has been done for $\log(g) = 4.5$ in Johnas et al. (2007a) and Johnas et al. (2007b) and is presented in Appendix D. There, slightly different settings had been used. The general statements about the influences of the modern2 and modern3 setups are similar.

First, the comparison between the modern1 and modern2 setup is presented in Sect. 5.5.1. In Sect. 5.5.2, there is the comparison between the modern1 and modern3 setup and the influence by the He profiles is shown. The differences are traced back to the total profile functions in PHOENIX and discussed in Sect. 5.5.3. Finally in Sect. 5.5.4, the results of the comparisons of the various setups are summed up and the final conclusions made.

5.5.1 Comparison between the Modern1 and Modern2 Setup

Figure 5.23 shows the flux change between the modern1 and modern2 spectra for each effective temperature. Neither here nor in Sect. 5.5.2, the differences would be easily visible in the synthetic spectra which is why only the relative changes of the flux are presented. Changes in the near line wings of the Na I D doublet between the modern1 and modern2 setup appear at $T_{\text{eff}} = 2500$ K and 3000 K. They are in the range of 3% and thus hardly measurable. Only at these effective temperatures, HI is present in appreciable amounts in the regions where the line wings form and becomes an important perturber species, see Fig. 5.22. The opacity in the modern2 Na I D doublet is larger than in the modern1 setup.

As expected, the relative changes in the T-p structures are even less than for the comparison of the impact, 1st generation, and modern1 setup. They are below $\pm 5\%$, see Figs. C.16–C.20 in Appendix C.4.

5.5.2 Comparison between the Modern1 and Modern3 Setup

Results of similar size compared to the ones presented in Sect. 5.5.1 are found, when comparing modern1 synthetic spectra and modern3 synthetic spectra, see Fig. 5.24. This time, the details of the Na I D, Li I, and KI doublets are of interest. For a better overview, they are highlighted in Fig. 5.24. In general, the effects are very small (in the range of a few percent) for each of the three alkalis and again only present in each near line wing region. However, they are noticeable in the entire effective temperature range. Due to the low concentration of Li I, the relative changes of the

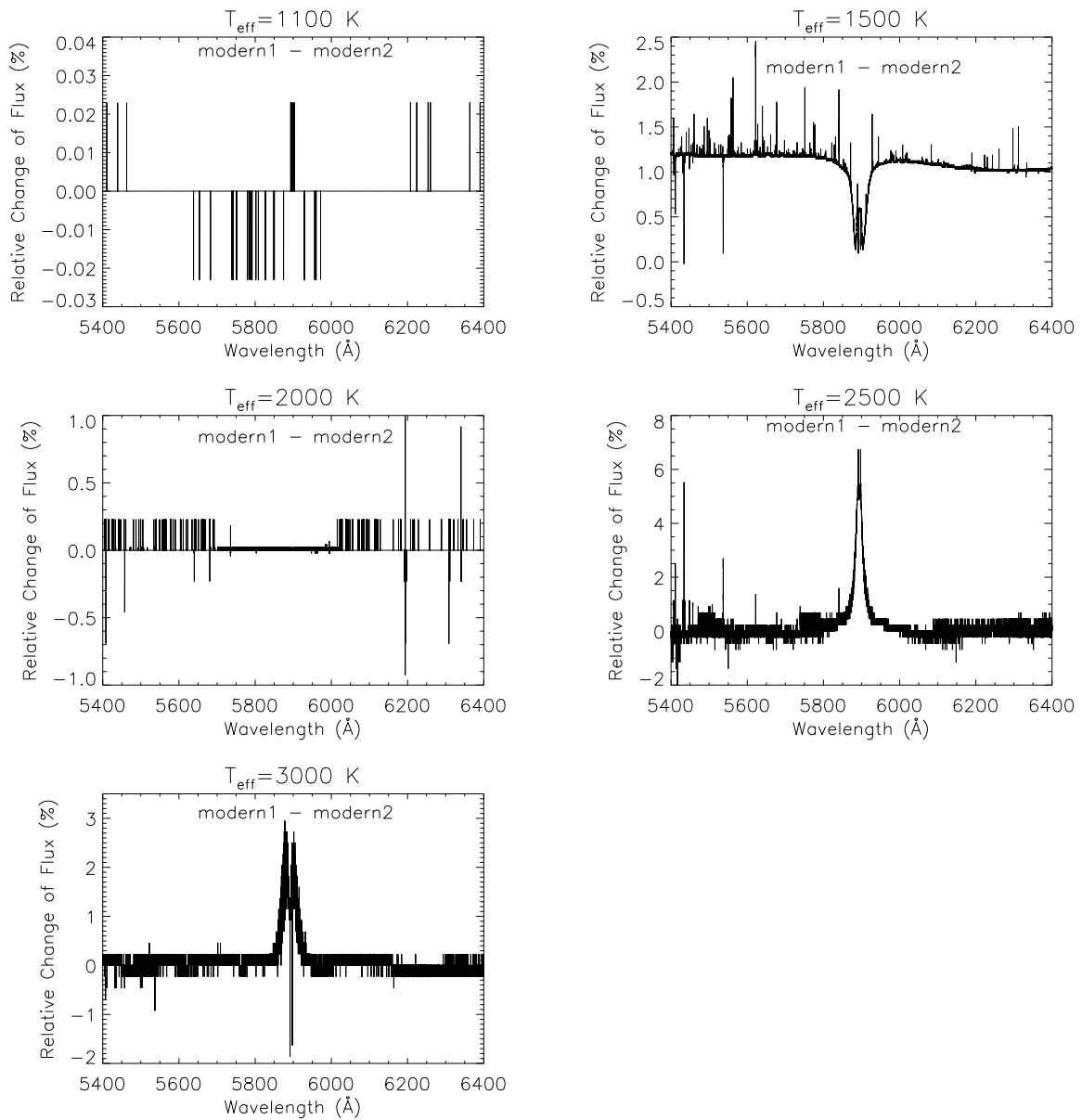


Fig. 5.23: Relative change of the flux for the NaID doublet when comparing modern1 with modern2 synthetic spectra for effective temperatures from 1100 K to 3000 K.

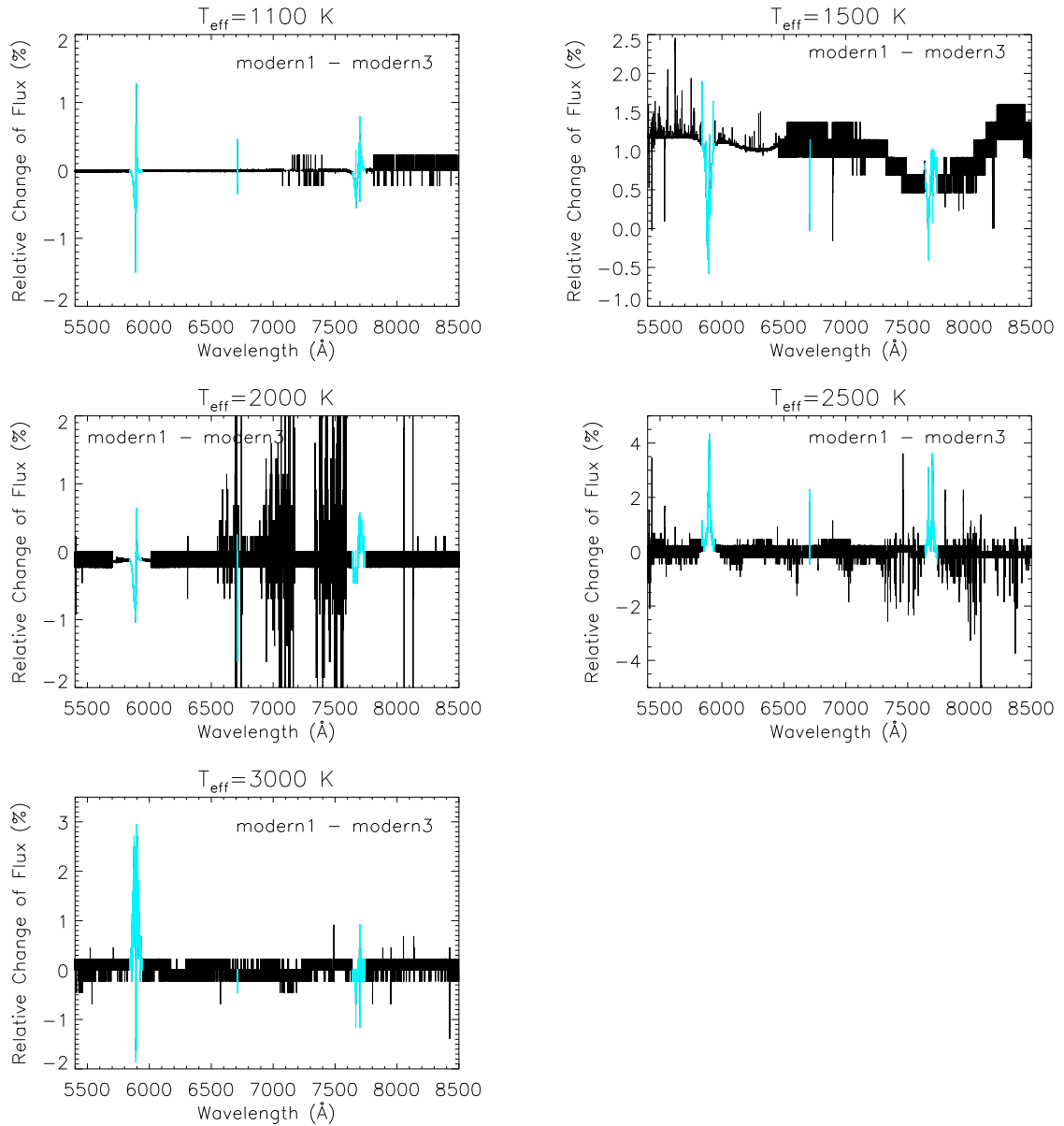


Fig. 5.24: Relative change of the flux when comparing modern1 with modern3 synthetic spectra for effective temperatures from 1100 K to 3000 K. The NaID, LiI, and KI doublets are highlighted.

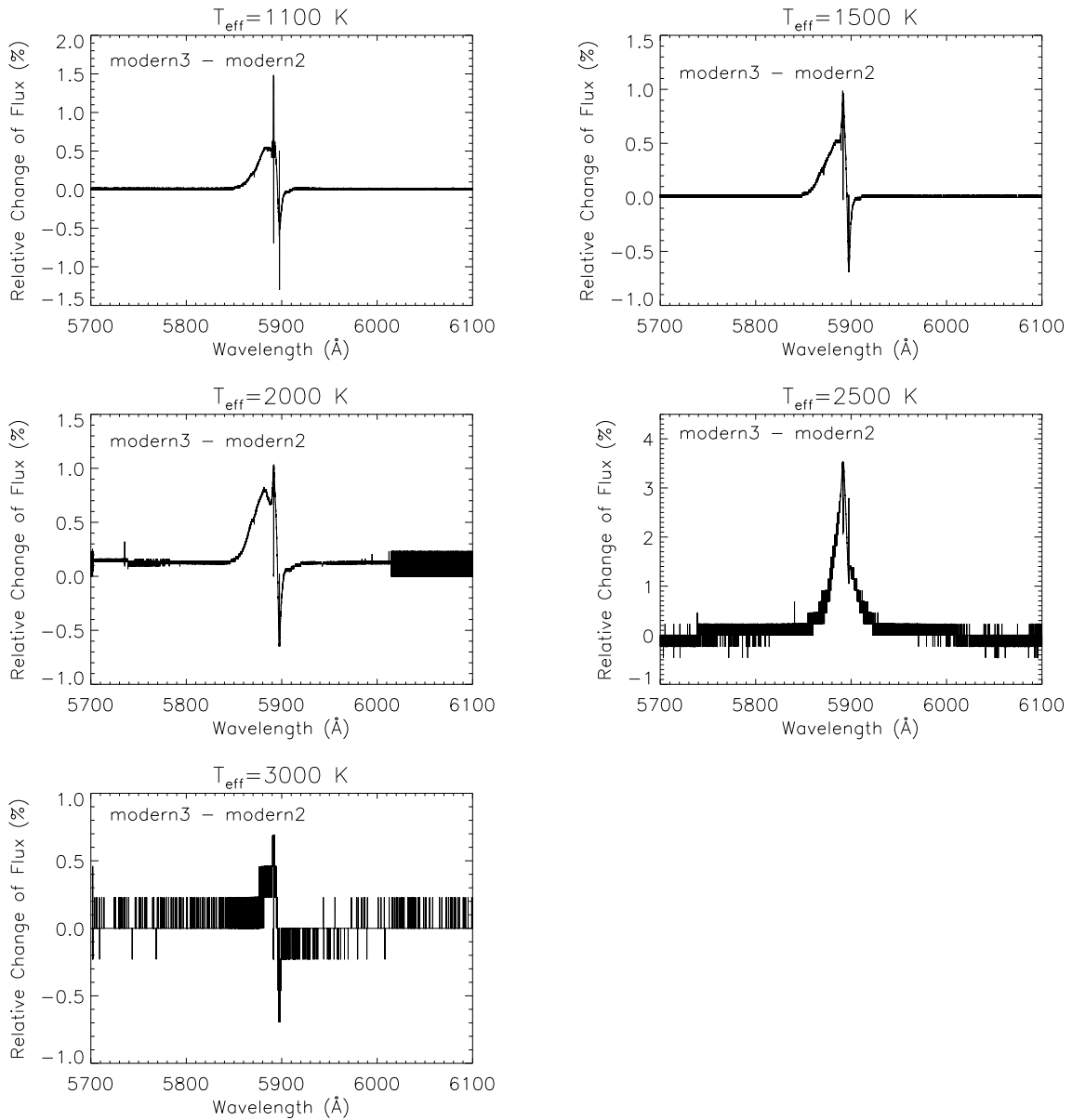


Fig. 5.25: Relative change of the flux when comparing the modern3 with modern2 Na I D doublet in synthetic spectra for effective temperatures from 1100 K to 3000 K.

flux are especially small for the Li I doublet. The effect of its profiles is masked by the overlapping TiO band at higher effective temperatures. The asymmetry in the relative change of flux can be explained by the damping constants with He as perturber of the modern1 and modern3 setup, see Sect. 3.5. The fully quantum mechanically calculated D_1 damping constants are smaller than the D_1 damping constants from the unified semi-classical theory. Thus, the relative change is positive. It is the opposite for the D_2 damping constants which explains the negative change of flux. For the Na I D doublet at $T_{\text{eff}} = 3000$ K, the largest relative change is visible. However, this is due the high concentration of H I.

The pure effect of He as perturber on Na I D for the various effective temperatures is shown in Fig. 5.25. Due to the high concentrations of He in all parts of the atmosphere and for the entire effective temperature range, its influence is always noticeable. It is of similar small size as the effects on the Li I and K I doublets. At $T_{\text{eff}} = 2500$ K, there is the largest difference between the influence of the two He profiles. The collisional broadened Na I D₂ line dominates in the doublet. The He D₂ damping constants by Mullamphy et al. (2007) (modern3 setup) are smaller and hence produce less line broadening. Thus a higher flux is obtained. However, this is in an effective temperature regime in which dust plays an important role so that the He effect will be probably decreased when considering dust in other approximations than COND. The differences in the T-p structures between the modern1 and modern3 setups are still negligible, see Figs. C.16–C.20 in Appendix C.4.

5.5.3 Comparison of φ_λ at 5890 Å of the Modern1, Modern2, and Modern3 Setup

The differences between the modern1, modern2, and modern3 setups are due to the total (convolved) profile function φ_λ used in PHOENIX. Therefore, a discussion of φ_λ at 5890 Å follows. This wavelength has been chosen because it is in the near line wing of Na I D₂, for which the influences of the modern2 and modern3 setups are observable if present. In Fig. 5.26, the relative changes of the profile functions are displayed as well as the flux contribution function \mathcal{C}_F at this wavelength, see also Fig. 5.27.

In Fig. 5.26 for $T_{\text{eff}} = 1100$ K to 2500 K, the relative changes between the profile functions of the modern1 and modern2 setups and respectively the modern3 setup are mostly constant except for the innermost regions which are convective and in which the line wing is not formed. (Except for $T_{\text{eff}} = 3000$ K, for which the large changes are in the outer- and innermost atmospheric layers.) As already seen in Fig. 5.23, the influence of H I broadened Na I D vanishes mostly except for the effective temperatures of 2500 K and 3000 K.

In the atmospheric region, where the near line wing at 5890 Å is formed, the relative changes between the modern1 φ_λ and modern2 φ_λ are always larger than 1 % and than the relative changes between the modern1 φ_λ and modern3 φ_λ except for the case at $T_{\text{eff}} = 3000$ K. Both, the modern2 φ_λ and modern3 φ_λ are larger than the modern1 φ_λ which implies a higher opacity in the modern2 and modern3 setups. This exception at $T_{\text{eff}} = 3000$ K can be explained by the very much increased H I concentration and hence by the increased number of collisions with H I atoms. The influence of H I perturbing Na I D has been already indicated in Fig. 5.23 showing a larger opacity. The unusual behavior of φ_λ of the modern2 and modern3 setup compared to modern1 setup at $T_{\text{eff}} = 3000$ K in the outermost atmospheric layers is not that critical since the maximum of \mathcal{C}_F is located where the changes of φ_λ are still in the range of -5%. Furthermore, the total opacity is also influenced by the strong presence of molecular bands at this “upper” effective temperature limit of the importance

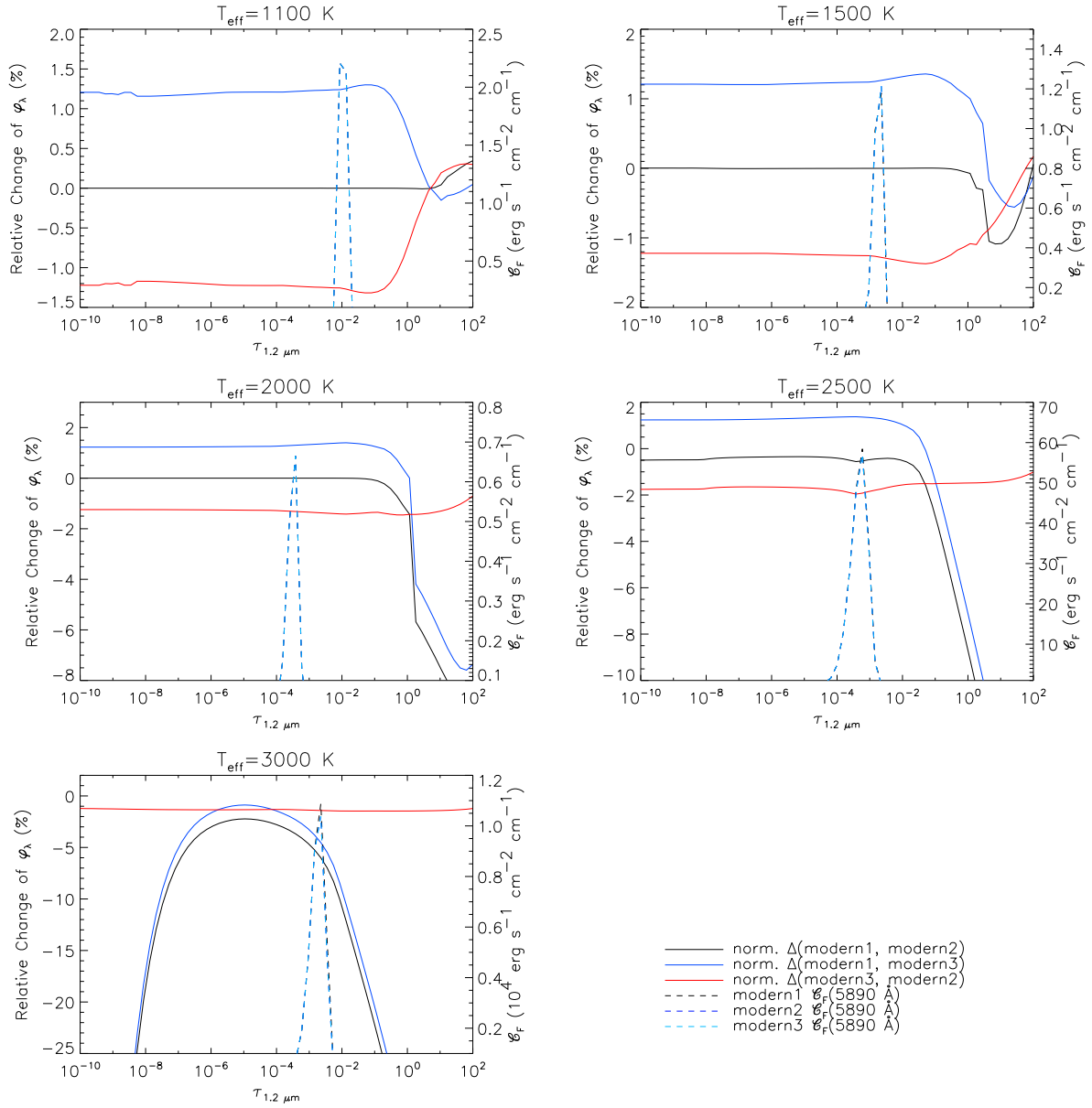


Fig. 5.26: For different T_{eff} , the relative change of φ_λ at 5890 Å of the modern1 and modern2 and the modern1 and modern3 setup is shown (left ordinate). Furthermore, the flux contribution function \mathcal{C}_F at 5890 Å which is displayed as dashed line is shown (right ordinate). The legend is valid for each panel of this figure.

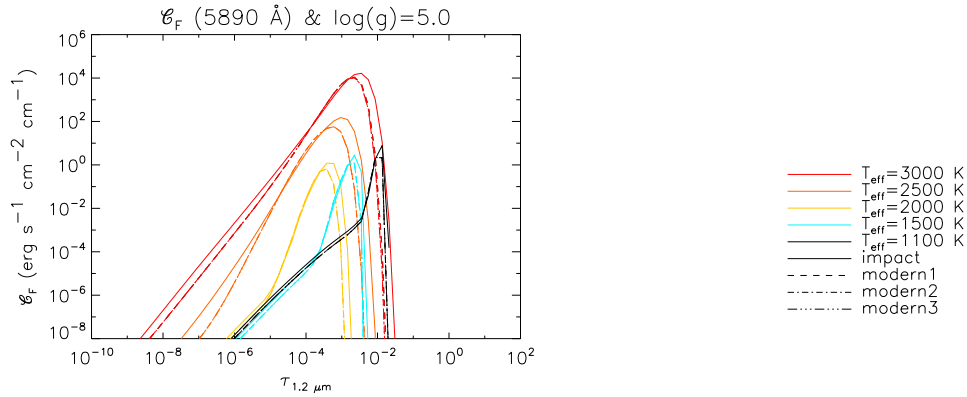


Fig. 5.27: Flux contribution functions at 5890 Å of the impact, modern1, modern2, and modern3 setup for effective temperatures from 3000 K to 1100 K, $\log(g) = 5.0$, and solar composition.

of line profiles.

With \mathcal{C}_F , it is easier to see in which regions the relative change of the profile functions is important for the line formation. All line wings of the modern1-3 setups form in very similar atmospheric regions at each effective temperature. A better overview of the wing forming regions is given in Fig. 5.27 for each effective temperature and each setup. The position of the maxima of the modern1-3 \mathcal{C}_F for each effective temperature is very similar and still close to the maxima of the impact setup. Hence, similar atmospheric conditions are valid for each setup.

5.5.4 Conclusion of the Results of the Modern2 and Modern3 Setup

The results from the modern2 setup confirm that the modern1 setup without considering HI as perturber in the near wings is an appropriate approximation, especially for effective temperatures below 2500 K. Furthermore, the unified semi-classical theory, applied in the modern1 setup, and the fully quantum mechanical theory, applied in the modern3 setup, with He as perturber yield very similar results although there are larger differences in the profile data, see Sect. 3.5. Thus, the He broadening is confirmed through these two approaches.

The influence of the stellar parameters is analogous to the one in Sect. 5.4.4. Due to the small differences between the modern2 and modern3 setup compared to the modern1 setup, it has not been repeated here.

This is only a study concerning the near line wings. Larger changes in the synthetic spectra are expected if there would be a comparison including far line wing profiles calculated in each approach. Therefore, the inclusion of HI as perturber species in the line profile calculations is still important, also for the KI doublet, due to its increasing influence towards higher effective temperatures.

The effects shown above of the modern2 and modern3 setup are presented for synthetic spectra with a 0.02 Å resolution. (They are also recognizable in low resolution spectra with a resolution of 2 Å.) Consequently, in order to observe such small changes in late-type M to T dwarfs, a signal-to-noise ratio of at least 20 to 50 is necessary, as well as a resolution $\lambda/\Delta\lambda$ of at least 3000 for low resolution observations and of at least 300 000 for high resolution studies for wavelengths between 5000 Å and 8000 Å. This combination of technical requirements still provides a challenge especially towards the shorter wavelengths of the optical regime and objects of later spectral types but should be feasible with future telescopes, e. g., the ESO project E-ELT (European Extremely

Large Telescope³) and the American project TMT (Thirty Meter Telescope⁴).

³see <http://www.eso.org/projects/e-elt/>

⁴see <http://www.tmt.org/>

6 The Influence of Dust Formation on Alkali Line Profiles in Spectra of Cool Atmospheres

In the work by Dehn (2007), a non-equilibrium treatment of chemically heterogeneous dust clouds (DRIFT) by Christiane Helling and Peter Woitke has been coupled to PHOENIX. Since there are only very small changes between the modern2 and the modern3 setup compared to the modern1 setup, see Sect. 5.5, only the modern1 setup, representing the modern profiles, is studied together with the impact setup. In Sect. 6.1, a short introduction of the dust treatment of DRIFT is given, for a brief description of DUSTY atmospheres see Sect. 5.2. Hereafter, DRIFT and DUSTY atmospheric models and synthetic spectra are compared and presented in Sect. 6.2, concentrating on the coupling of alkali line profiles and the dust treatment. Conclusions are given in Sect. 6.3. A summary of this chapter is published in Johnas et al. (2007d).

6.1 DRIFT: Consistent Micro-Physics in 1 D Static Model Atmospheres

The complete derivation of the modelling of dust formation (DRIFT) is provided in Woitke & Helling (2003), Woitke & Helling (2004), Helling & Woitke (2006), Helling et al. (2007), and Dehn (2007) as well as in references therein. Generally, the time-dependent dust formation is treated as a stationary process inside a static model described by PHOENIX (plane parallel atmospheric structure, 256 layers). The formation of seed particles (nucleation), their growth and evaporation, gravitational settling, and convective up-mixing consistently coupled to element conservation is modelled in DRIFT. Furthermore, the grain size distribution, the material composition of the dust, and the remaining gas-phase element abundances are provided and serve as input for the opacity calculation in PHOENIX (see Chap. 4).

In Fig. 6.1, the dust formation process with gravitational settling and convective up-mixing is illustrated. Due to the thermodynamics in the outer and hence cooler layers of the atmosphere, the atmosphere is in pure gas phase and thus $0 < S \ll 1$. S is the supersaturation ratio and is defined as $S = n_{gas}kT/P_{vap}$ with n_{gas} being the gas density, k Boltzmann's constant, T the gas temperature, and P_{vap} the vapor pressure of the gas component.

In order to have dust formation, phase non-equilibrium is needed. This is a conceptually totally different approach than used in DUSTY models. For efficient dust nucleation, $S \gg 1$ is necessary otherwise the newly formed dust seed particles could be destroyed through evaporation. In this model, TiO_2 is chosen as a seed particle. It has stable monomers in the gas phase and homogenous nucleation can take place by the addition of TiO_2 molecules to the $(TiO_2)_N$ system (Jeong 2000). In cool atmospheres, dust seeds do not need to exist a priori, thus spontaneous nucleation is as-

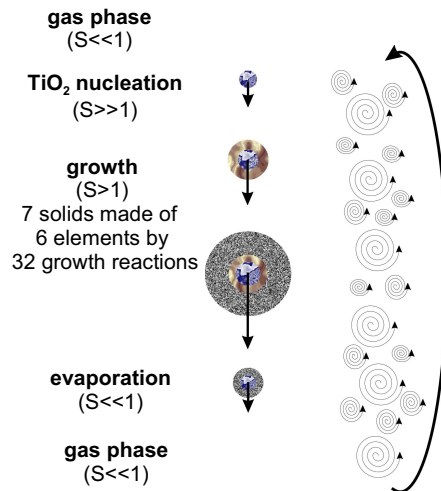


Fig. 6.1: Dust formation with gravitational settling and convective up-mixing (Johnas et al. 2007d).

sumed. Other solids can be already thermally stable in the atmosphere¹ which can grow on the surface of the TiO₂ seeds.

The conditions in deeper atmospheric layers do not allow the new formation of dust grains, e.g., because of the increased temperature. However due to gravitational settling, the dust, which grains were formed in higher atmospheric layers, falls into deeper layers. During the gravitational settling, dust material in the atmosphere condensates onto the dust grain surface and causes it to grow further. In this work, 7 dust species made of 6 elements have been considered: SiO₂, Al₂O₃, Fe, MgO, MgSiO₃, Mg₂SiO₄, and TiO₂. For detailed information about the 32 growth reactions see Appendix 2.2 in Dehn (2007). The growth continues until the dust grains evaporate into their molecules and/or atoms. The region in the atmosphere, in which the evaporation of the dust particles starts, depends on the composition of the dust particle.

Very low mass stars and brown dwarfs have a convective inner atmosphere. Due to the convective up-mixing, the gas, which is enriched by the elements of the evaporated dust particles, is transported in higher, cooler regions of the atmosphere, in which it can support again the formation of new dust particles.

6.2 Influence on Alkali Line Profiles

The results when considering a DRIFT and a DUSTY model atmosphere and synthetic spectra, each computed with the impact and modern1 setup for $T_{\text{eff}} = 2000$ K, $\log(g) = 5.0$, and solar composition, are presented in the following. The DRIFT and DUSTY models have been computed with the same setup except for the dust treatment. The chosen effective temperature is within the effective temperature range for which the presence of dust has to be taken into account. Hauschildt & Baron (2005) state that, based on observational evidence, for $T_{\text{eff}} \geq 1800$ K additional opacity due to dust particles has to be considered.

The DRIFT and DUSTY T-p structures differ by up to 30 %, see Fig. 6.2, whereas the relative differences of the temperature between the impact and modern1 setup of each dust setup are negligible

¹but with the gas not being supersaturated.

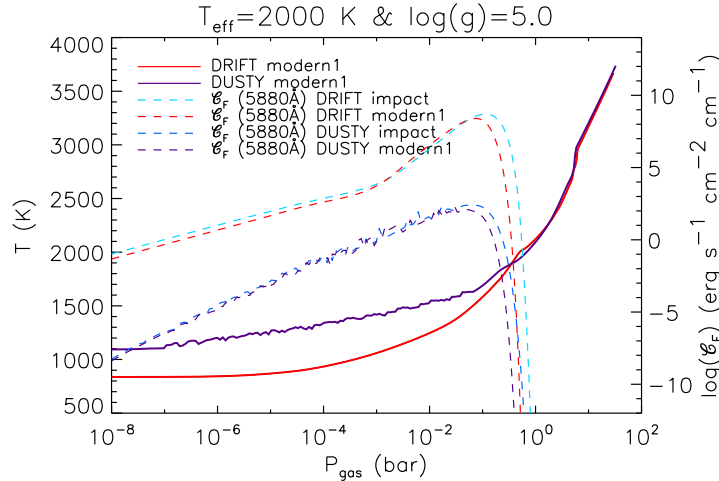


Fig. 6.2: Left ordinate: T–p structures of DUSTY and DRIFT models with the modern1 setup. Right ordinate: flux contribution function at 5880 Å of the four different model setups (DRIFT, DUSTY, impact setup, modern1 setup).

(see Chap. 5 for a similar result with COND models). Note that the non-monotonic temperature run of the DUSTY model is due to numerical problems. The DRIFT temperature gradient is much steeper than the DUSTY one. The large differences in the T–p structures of the DUSTY and DRIFT models, which are due to the different dust treatment and hence the provided dust opacities, cause large differences in the flux magnitude of the synthetic spectra, see Figs. 6.4 and 6.5.

In addition to the T–p structures in Fig. 6.2, the flux contribution function \mathcal{C}_F of each dust approximation with the impact and modern1 setup at 5880 Å is shown. This wavelength is in the line wing of the Na I D₂ resonance line, for which differences in the synthetic spectra of the various models are visible, see Fig. 6.5. The Na I D₂ line wings at 5880 Å form at similar gas pressures and temperatures in the atmospheres.

In Figs. 6.3 and 6.4, the influences on low resolution spectra of the various dust and profile setups up to 2.5 μm are shown. The influence of the DRIFT–modern1 setup compared to the DRIFT–impact setup is recognizable up to ≈1.3 μm, see Fig. 6.3, whereas in COND spectra (Chap. 5), the flux difference between impact and modern1 spectra reaches only up to ≈1.05 μm.

When comparing DRIFT and DUSTY spectra with the modern1 setup, the DRIFT spectra show more flux from the optical wavelength range up to ≈1.3 μm than the DUSTY spectra, see Figs. 6.4. In Fig. 6.5, relatively weak DUSTY Na I D and K I doublets are shown compared to the much stronger doublets in DRIFT. Due to the different dust opacities provided, the T–p structures are very different which has a large influence on the line strength and shape. The line shape depends more on the model structure than on the line profile setup. As a theoretical comparison (since the effective temperature of 2000 K exceeds the application of COND models), the influence of the line profile setup is larger in COND models, see Fig. 6.6. There are large differences in the line shape of the Na I D doublet visible because only the dust formation is included in COND models but not the dust opacity.

The dust properties of DRIFT using the impact and the modern1 setup are displayed in Figs. 6.7–6.9. With the nucleation rate, the number of dust particles in the cloud is determined. These dust particles grow to a certain size (the mean grain size). As expected, the differences in the dust properties are as small as the differences in the alkali lines in the spectra.

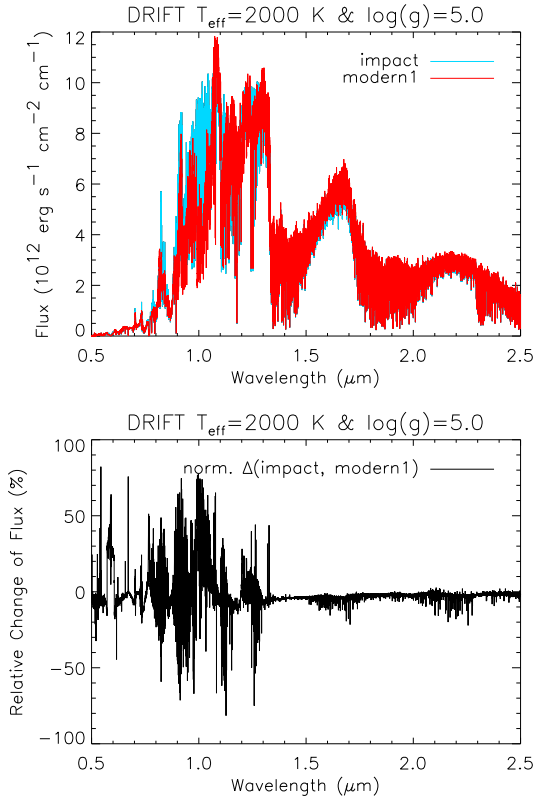


Fig. 6.3: Top panel: DRIFT model atmospheres computed with the impact and modern1 setup. Bottom panel: relative change of flux of the two setups.

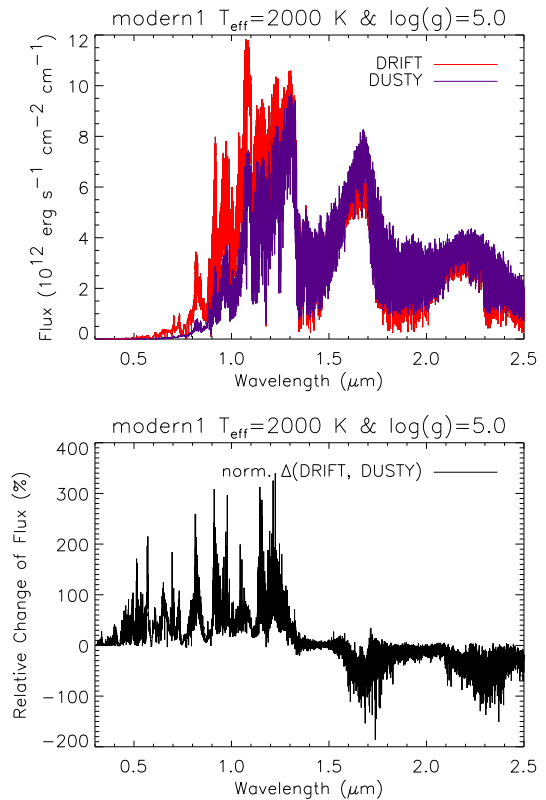


Fig. 6.4: Top panel: DUSTY and DRIFT model atmospheres computed with the modern1 setup. Bottom panel: relative change of flux of the two models.

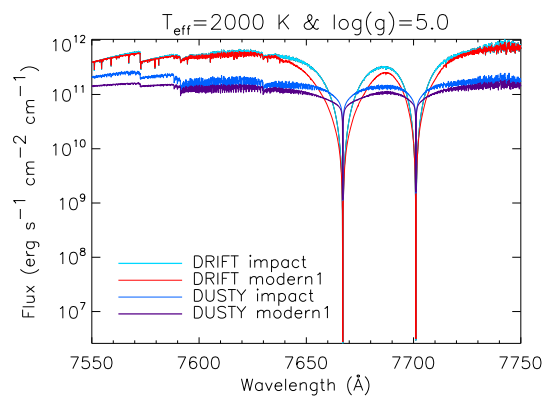
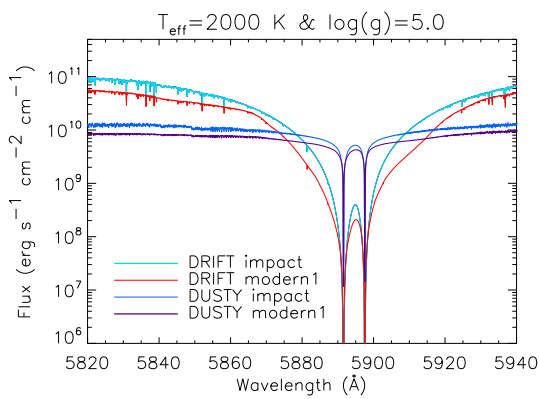


Fig. 6.5: Synthetic spectra displaying the alkali species with the highest concentration in cool atmospheres, the NaID (left) and KI (right) doublets, computed with DUSTY and DRIFT models in the impact and modern1 setup.

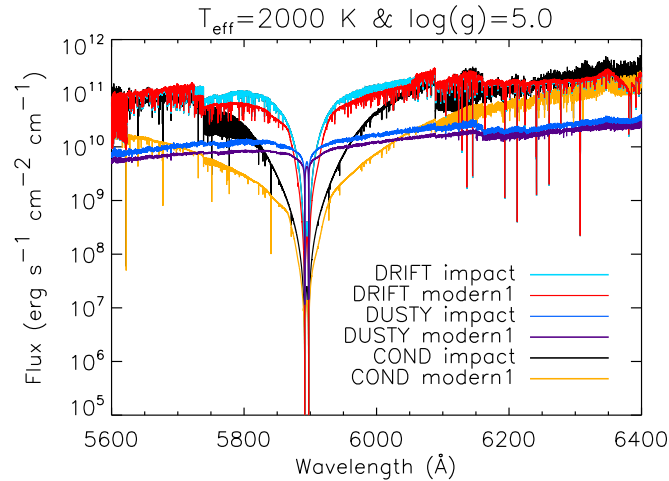


Fig. 6.6: The NaID doublet computed with the impact and modern1 setups and the DRIFT, DUSTY, and COND model approximation.

6.3 Conclusion

DRIFT and DUSTY models have very different T–p structures. The dust treatment shows a significant influence on the spectrum, especially on the alkali resonance lines. They are much stronger in DRIFT spectra than in DUSTY spectra. The alkali line profiles of the modern1 setup cause no significant changes in the dust properties which is due to the negligible differences in the T–p structures between the impact and modern1 setup.

Presumably, dust in general has a larger influence on the line shape than the line profiles, which has been already assumed in Schweitzer et al. (2001).

DRIFT–impact and modern1 spectra need to be tested on observations of late M and L dwarfs, as well as on extreme extrasolar planets. First tests on observations show an improved fit with DRIFT spectra (Dehn 2007).

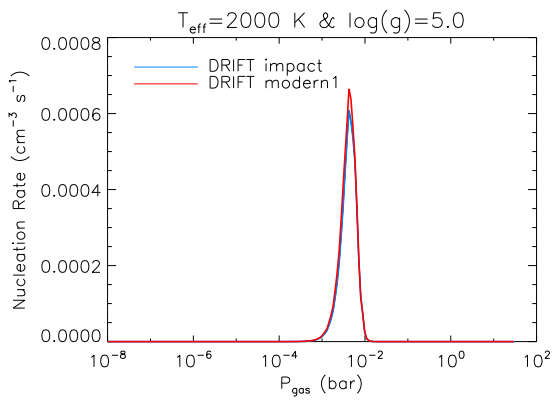


Fig. 6.7: DRIFT nucleation rate with the impact and modern1 setup.

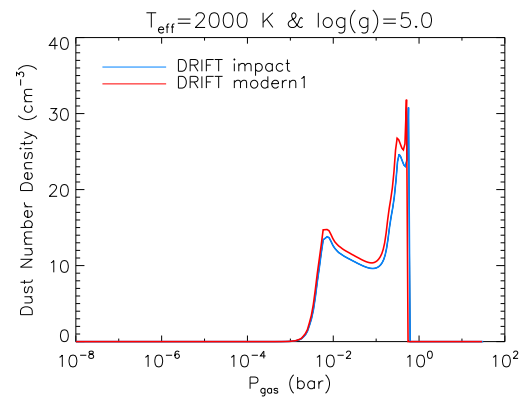


Fig. 6.8: DRIFT dust number density with the impact and modern1 setup.

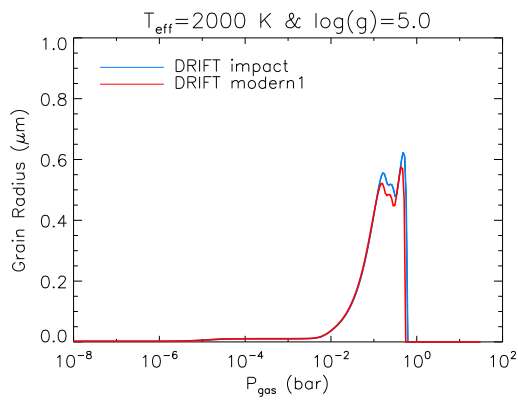


Fig. 6.9: Mean grain radius in DRIFT of the impact and modern1 setup as a function of the gas pressure.

7 The Li I Absorption Line in Cool Atmospheres

The Li I abundance is used as a diagnostic tool in order to distinguish between young stars and substellar objects, i.e., whether Li I depletion has already started or not. First, the problem of obtaining reliable equivalent widths (EWs) is discussed in Sect. 7.1. Then, the Li I abundance study on low mass members of the Chamaeleon I association is presented in Sect. 7.2; this study is accepted by A&A and is in press (Johnas et al. 2007c).

7.1 Methods for Obtaining the Equivalent Width of Li I

It is common to derive any element abundance from a measured EW of the observation and then compare it with a theoretical curve of growth. However in observations of objects of spectral type late M to T, the EW is strongly dependent on the continuum which is the main source of error. Furthermore, there is no true continuum due to the multitude on molecular bands and atomic lines in these spectra. Hence, it is impossible to locate the exact beginning and end of the absorption line with its line wings.

Four different methods for obtaining the EW have been tested on synthetic spectra, here for the Li I abundances $\log(\epsilon)$ from 0.0 to 3.5 in steps of 0.5. (Note that a logarithmic Li I abundance of 0.0 does not imply that there is no Li I.) For the first method, an artificial pseudo continuum has been calculated by assuming that Li I is completely depleted. After taking the difference between this pseudo continuum and the synthetic spectrum, the remaining area is normalized over the mean flux between the D₁ and D₂ line of Li I. Hereafter, the method is named “pseudo continuum”.

In the second method, the simplistic approach of taking the median in a wavelength range shortly before the blue Li I line wing has been assumed to be the pseudo continuum. The difference between the closest interception points of the synthetic spectrum and the median in respect to the line center has been taken. After the integration of this area, it has been normalized by the median, which results in the EW. In the following, this method is referred to as “median”.

The third method is a modification of the second. The mean of the eight prior determined medians, for each Li I abundance, has been assumed to represent the pseudo continuum in order to decrease the systematic error. All following steps are the same as described above and this method is called “mean median”.

In order to have a link to observations and EWs obtained from observed lines, the IRAF¹ package (sbands) has been tested, too. However, this has not provided any more insight because this package is not meant to work with such continua, i.e., with many molecular bands (when talking about observations, the low signal-to-noise ratios is the problem). This package fails: randomly totally wrong EW estimates are produced, such as negative values. It only works reliably with “flat” continua, e.g., the ones found in stars of earlier spectral type. This is the reason why no further results

¹The Image Reduction and Analysis Facility, provided by the National Optical Astronomy Observatories (NOAO).

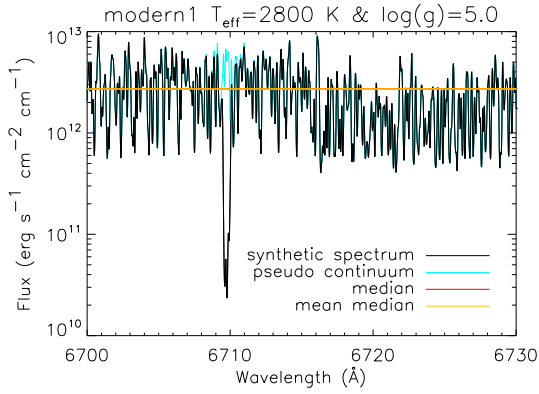


Fig. 7.1: Synthetic modern1 Li I absorption line (with $\log(\epsilon) = 2.0$) and the three different pseudo continua: synthetic pseudo continuum, median, and mean median.

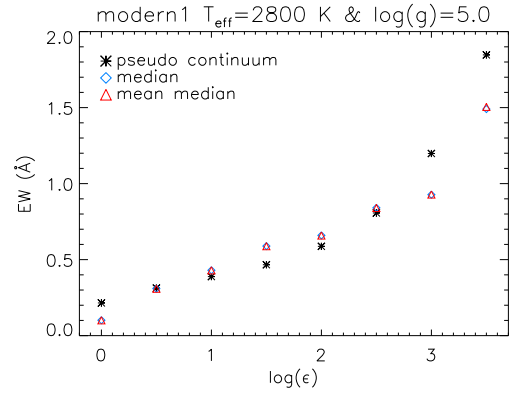


Fig. 7.2: EWs of modern1 synthetic spectra with $T_{\text{eff}} = 2800$ K and $\log(g) = 5.0$ obtained with the three methods: pseudo continuum, median, and mean median.

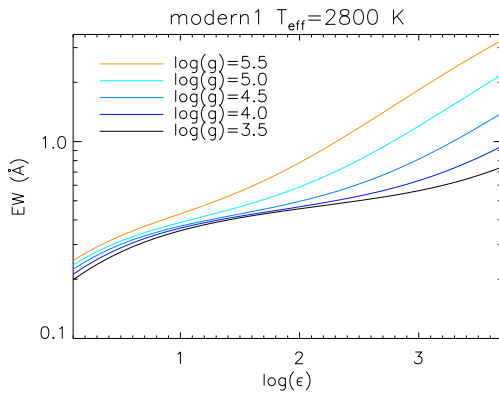


Fig. 7.3: Theoretical curves of growth of the modern1 setup derived by the pseudo continuum method for $T_{\text{eff}} = 2800$ K and various values of $\log(g)$.

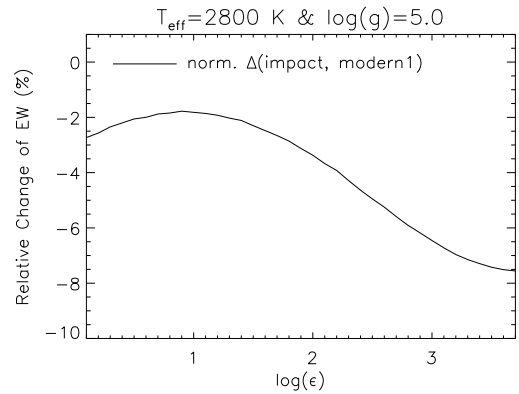


Fig. 7.4: Relative change of the EWs of the impact and modern1 setup for $T_{\text{eff}} = 2800$ K and $\log(g) = 5.0$.

obtained by this method are presented here and it is strongly recommended not to use this package for the determination of EWs of observations of cool objects showing no unambiguous continuum. In Fig. 7.1, exemplarily the Li I line with $\log(\epsilon) = 2.0$ in the COND modern1 setup with $T_{\text{eff}} = 2800$ K, $\log(g) = 5.0$, and solar composition is shown together with the three types of continuum described above. (Note that larger effects would be visible for lower effective temperatures but this discussion is preparatory for Sect. 7.2.) It is already visible that there is no large difference between the median and mean median continuum. The results are analogous for the impact and modern3 setups as well as for DUSTY and DRIFT atmospheres. As expected, the EWs obtained by the three methods differ, see Fig. 7.2. The variation is only small between the median and mean median method which can be already derived from Fig. 7.1. Note that the Li I EWs depend also on the Na I D and K I doublets in the various setups since the far line wings of these two alkalis and also molecular bands, such as of TiO, mask the Li I doublet, see Sect. 5.4.2.

Nevertheless, these methods can only provide theoretical EWs obtained by synthetic spectra and pseudo continua. Additionally, one must be aware of the fact that a perfect match of a synthetic

spectrum and an observation is unlikely, e.g., due to uncertainties in the models, a bad signal-to-noise ratio, setting limitations of the spectrograph (only a limited wavelength range of the Li I absorption line is covered in the band). Being aware of the existing error-proneness, the first method, calculating a synthetic pseudo continuum, is judged to be the most reliable one, since there are no subjective boundary conditions to set. A direct comparison of the observation with synthetic spectra with varied Li I abundances is recommended in order to avoid this error source. In Fig. 7.3, theoretical curves of growth of the modern1 setup derived by the pseudo continuum method for $T_{\text{eff}} = 2800$ K and $\log(g) = 5.0$ are shown. The influence of $\log(g)$, as discussed in Sect. 5.4.4, is visible, i.e., the lines become stronger with higher values of $\log(g)$ and hence the EWs, too. Since the differences between the Li I absorption line of the modern3 and modern1 setup are not possible to detect in observations, only the input of the impact and modern1 setup will be discussed in Sect. 7.2. Although Li I is an alkali with only a lower concentration, differences between the two setups still exist and the EWs are dependent on the setup, see Fig. 7.4 and Sect. 5.4, so that the simulation of the Li I doublet is still a good tool to test the setups on observations which is done in Sect. 7.2.

7.2 Li I Study on Very Low Mass Objects of Chamaeleon I

The following study is accepted for publication in A&A (2007). Section 2 of the paper has been contributed by Eike W. Guenther and Viki Joergens who have also done the data reduction. In Sect. 4, the paragraphs about spots on the surface of the studied objects and the discussion if veiling is present are mainly composed by Eike W. Guenther.

Lithium abundances of very low mass members of Chamaeleon I

★

C. M. S. Johnas¹, E. W. Guenther², V. Joergens³, A. Schweitzer¹, and P. H. Hauschildt¹¹ Hamburger Sternwarte, Gojenbergsweg 112, D-21029 Hamburg, Germany
e-mail: cjohnas@hs.uni-hamburg.de² Thüringer Landessternwarte Tautenburg, D-07778 Tautenburg, Germany³ Max-Planck-Institut für Astronomie, Königstuhl 17, D-69117 Heidelberg, Germany

Received 27 March 2007; accepted 6 August 2007

ABSTRACT

Aims. We present the first study of the lithium abundances of very low mass objects in Chamaeleon I close to the hydrogen burning mass limit based on atmospheric models and high-resolution spectroscopic observations. The studied objects, Cha H α 2, 3, 4, 5, 6 and 8, are very young brown dwarf candidates and very low mass stars on the verge of lithium depletion.

Methods. For this analysis, we have computed a new “GAIA-cond” class model grid over effective temperatures from 2600 K to 3100 K, surface gravities from $\log(g) = 3.5$ to 5.5, and lithium abundances from $\log \epsilon = 0.0$ to 3.7, for two different line profile setups introduced in previous work. Calculated synthetic spectra are compared with high-resolution UVES/VLT echelle spectra of the objects.

Results. We find good descriptions of the lithium resonance doublet lines at 6708 Å and of the surrounding pseudo-continuum and determine a consistent set of lithium abundances ($\log(\epsilon) = 1.55$). However, the derived lithium abundances are lower than the meteoritic one ($\log(\epsilon) = 3.31$) and that of higher mass stars in Cha I ($\log(\epsilon) = 3.1/3.4$ for LTE-/non-LTE-calculations). By modeling the TiO-line, we demonstrate that veiling does not make the lithium lines appear weaker. We can also rule out that the results are spoiled by the presence of spots.

Conclusions. A possible explanation for these results would be that the objects are either more massive, or much older, than previously thought, so that the lithium depletion has already started. Although the uncertainties of the masses and ages are large, they are not large enough as to explain the observed lithium depletion. Therefore, the most likely explanation is either a lack of understanding of the details of the formation of the lithium line, or a lack of understanding of the internal structure of the very young low-mass objects.

Key words. Stars: atmospheres – Line: profiles – Stars: low-mass, brown dwarfs – Stars: individual: Cha H α 2, Cha H α 3, Cha H α 4, Cha H α 5, Cha H α 6, Cha H α 8

1. Introduction

Brown dwarfs (BDs) are objects that are not massive enough to sustain thermonuclear fusion of hydrogen at their centers but are distinguished from gas-giant planets by their ability to burn deuterium. Thermonuclear fusion reactions in young stars do not only include the burning of hydrogen but also of heavier elements, for example Li I, above very similar mass limits. Since lithium is quickly depleted in young stars, the presence of an original amount of Li I in a number of old, very low-mass objects, together with the assumption of fully convective interiors in this mass regime, has been used as an argument that these objects fuse neither lithium nor hydrogen and are thus BDs. Therefore, the Li I abundance is a very important diagnostic for identifying old BDs (‘Lithium-test’) (Rebolo et al. 1992; Basri

2000). The application of this substellar test is more complicated for very massive BDs and very young stars (ages of a few millions years). Massive BDs (above $0.06 M_{\odot}$) burn lithium: they can even burn hydrogen, however not at a rate sufficient to fully compensate radiative losses. Young stars with an age of about one Myr or less also show a substantial amount of Li I in their spectra because they are too young to have burned their initial lithium, i. e., their central temperature has not yet reached the lithium burning limit. In order to better understand the Li I depletion in young objects, it is required to study the abundance of Li I in very young (a few Myr) objects at the boundary between stars and BDs, and to compare it with the Li I abundance of higher mass stars of similar age.

The determination of element abundances from spectroscopic observations of such low-mass and, hence, cool objects, such as BDs, is hampered by the large number of absorption lines in their spectra leading to the fact that there is essentially no continuum in the optical regime. It is therefore impossible to completely identify the Li I resonance absorption line from

Send offprint requests to: C. M. S. Johnas

* based on observations obtained at the European Southern Observatory at Paranal, Chile in program 65.L-0629(A,B) and 65.L-0011(A)

observations alone (this is valid for any other spectral line of objects in this effective temperature regime). A way out is to calculate synthetic spectra of the objects, including all spectral lines, and fit them to observed spectra by varying the abundance of Li I. This requires a sophisticated modeling of the (sub)stellar atmosphere. We have generated a grid of model atmospheres and spectra with varied lithium abundances with the general purpose stellar atmosphere code PHOENIX (Hauschildt & Baron 1999) using two different setups for the lithium absorption line profile treatment (Johnas et al. 2006). In addition to work by members of the PHOENIX group, synthetic spectra of BDs that aim at an improved description of the lithium resonance lines have also been calculated previously by Pavlenko et al. (2000) and Tsuji (2001).

Current observational studies of lithium in BD atmospheres have been performed by means of measurements of the equivalent width (EW) of Li I based on high-resolution spectra by Tinney (1998), Joergens & Guenther (2001), and Pavlenko (2005), based on intermediate-resolution spectra by Kenyon et al. (2005) and Neuhäuser & Comerón (1999), and based on low-resolution spectra by Zapatero Osorio et al. (2002).

However, as mentioned before, due to the large number of densely spaced spectral lines in BD and very low-mass star (VLMS) spectra and the missing continuum, the determination of the lithium abundances via a derived EW and comparison with theoretical curves of growth implicates large uncertainties and should be considered with care. Of course, the missing continuum also has an influence on the determination of the rotational broadening. The approximation of the continuum influences the results of the EWs. In standard methods the continuum is approximated by a straight line, which is not sufficient and does not provide reliable values of the derived EWs. It is important to have a description of the continuum as close as possible, e. g., synthetic pseudo continua. Exemplarily, a theoretical series of synthetic spectra of Setup2, see Sect. 3, in a representative combination of the stellar parameters, $T_{\text{eff}} = 3000$ K and $\log(g) = 4.0$, showing the Li I line is presented in Fig. 1, in which the challenges mentioned above are visible. In all previous studies of these objects, the EWs and the rotational broadening were determined by fitting a continuum to the data. Since we model the entire spectrum in this work, we avoid the problems associated with continuum fitting and methods using EWs and curves of growth. Thus, the new values of the EWs and rotational broadening differ from the older ones. In this work we present the results of a Li I abundance study of very low mass members of the Chamaeleon I star forming region. The aim of this work is to better understand the Li I depletion in young objects close to the boundary between stars and BDs. Detailed studies have led to the identification of a number of BDs and VLMSs in the Chamaeleon I region (Comerón et al. 1999, 2000; Luhman 2004). Among them are the BD candidates Cha H α 2, 3, 6 and 8 (spectral type M6.5–M7) (Comerón et al. 2000) and the VLMSs Cha H α 4 and 5 (M6) (Comerón et al. 2000), for which high-resolution spectra have been taken by Joergens & Guenther (2001) and Joergens (2006), and whose Li I abundances will be discussed in detail in this work. An overview of the derived stellar properties from Comerón et al. (1999, 2000) and Luhman (2004) can

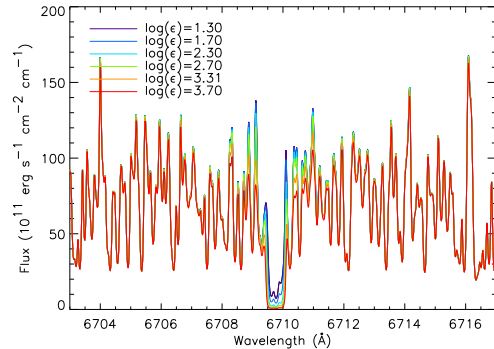


Fig. 1. Synthetic spectra of Setup2 for a $T_{\text{eff}} = 3000$ K and $\log(g) = 4.0$ displaying the Li I with varied abundances from $\log(\epsilon) = 1.3$ to 3.7.

be found in Table 1. The varying values in the tables represent the uncertainties in the stellar properties when studying these objects. These objects cannot currently be identified unambiguously as either young stars or BDs. Note that due to differences in the calibrations Neuhäuser & Comerón (1999) considered Cha H α 3 and 6 as bona fide BDs. Comerón et al. (2000) derived masses for Cha H α 2, 3, 4, 5, 6 and 8 between $0.05 M_{\odot}$ and $0.11 M_{\odot}$, and ages between <2 and 3 Myr based on evolutionary models of Baraffe et al. (1998). These age estimates are in agreement with a determination of the mean age of the Chamaeleon I association (3 Myr) by López Martí et al. (2004). The determination of the effective temperature and luminosity of the objects is crucial when applying evolutionary track calculations in order to give an estimate of the mass and age of the objects. Applying different sets of evolutionary tracks leads to (slightly) different masses and ages, see Table 1. For example, in Comerón et al. (2000), evolutionary models by Burrows et al. (1997) yield slightly higher masses and a factor of two greater ages compared to the predictions by track calculations from Baraffe et al. (1998). These discrepancies are due to uncertainties in evolutionary models for such small ages and masses, e.g., due to the fact that these objects are still contracting, missing calibrations of the models with observations, and the difficulty of setting the initial conditions of the models. Nevertheless, the cores of these objects either never reach the lithium burning temperature (when considering the models of Baraffe et al. 1998) or are only on the verge of reaching it (when considering the results of the Burrows et al. 1997 models) (Chabrier & Baraffe 2000).

2. Observations

We use two sets of observations in this paper. First, there are high-resolution spectroscopic observations of the BDs/VLMSs Cha H α 2, 3, 4, 5, 6 and 8, which have been carried out with the Uv-Visual Echelle Spectrograph (UVES) at the VLT Unit telescope 2 (KUEYEN) by Joergens & Guenther (2001). They have been subjected to an improved data reduction by Joergens

Table 1. Stellar properties of Cha H α objects.

Object	Sp. type	T_{eff} (K)	$\log(L/L_{\odot})$	Luhman (2004)		Baraffe et al. (1998)	
				Age (Myr)	Mass (M_{\odot})	Age (Myr)	Mass (M_{\odot})
Cha H α 2	M 5.25	3091	-0.92	< 3	0.2	< 2	> 0.1
Cha H α 3	M 5.5	3058	-1.11	< 3	0.1<M<0.2	< 2	> 0.1
Cha H α 4	M 5.5	3058	-1.17	3<a<10	0.1<M<0.2	2	0.1<M<0.2
Cha H α 5	M 5.5	3058	-1.00	< 3	0.1<M<0.2	< 2	> 0.1
Cha H α 6	M 5.75	3024	-1.13	3<a<10	0.1<M<0.2	< 2	> 0.1
Cha H α 8	M 5.75	3024	-1.35	3<a<10	0.1<M<0.2	2<a< 5	> 0.1

Object	Sp. Type	T_{eff} (K)	$\log(L/L_{\odot})$	Comerón et al. (2000)		Baraffe et al. (1998)	
				Age (Myr)	Mass (M_{\odot})	Age (Myr)	Mass (M_{\odot})
Cha H α 2	M 6.5	2910	-1.47	4.5	0.08	2	0.07
Cha H α 3	M 7	2840	-1.46	2	0.07	<2	0.06
Cha H α 4	M 6	2980	-1.25	3.5	0.11	2	0.1
Cha H α 5	M 6	2980	-1.31	3.5	0.11	2	0.1
Cha H α 6	M 7	2840	-1.57	4	0.07	<2	0.05
Cha H α 8	M 6.5	2910	-1.65	5.5	0.08	3	0.07

object	Sp. type	T_{eff} (K)	$\log(L/L_{\odot})$	Comerón et al. (1999)		D’Antona & Mazzitelli (1997)	
				age (Myr)	mass (M_{\odot})	age (Myr)	mass (M_{\odot})
Cha H α 2	M 6	2831	-1.16	0.4	0.08	1	0.10
Cha H α 3	M 6	2824	-1.27	0.5	0.075	1.5	0.09
Cha H α 4	M 6.5	2781	-1.31	0.5	0.065	1	0.08
Cha H α 5	M 6	2816	-1.06	0.4	0.09	0.5	0.10
Cha H α 6	M6	2815	-1.57	2	0.06	3	0.08
Cha H α 8	–	–	–	–	–	–	–

(2006), which is consistent for the lithium resonance line with the previous method. The IRAF Echelle package was used to subtract the bias, flat-field and extract the spectra, remove the scattered light, cosmic rays and the sky background, and finally to wavelength calibrate the spectra. Details of the reduction and wavelength calibration can be found in the given references. We note here only that no rebinning of the spectra was done in order to avoid any changes of the line profiles. In this work, we use between 1 and 7 individual spectra for each object depending on availability and signal-to-noise ratio. We label the spectra of each Cha I object with the modified Julian day (MJD) of its observation, as defined by $\text{MJD} = \text{JD} - 2\,400\,000.5$. The obtained spectra cover simultaneously the wavelength regions from 6700 Å to 8545 Å and 8640 Å to 10400 Å, at a resolution of $R = 40\,000$. The Li I doublet line at 6708 Å is in the last order of the echelle spectrum, which is only partly covered by the detector. Nevertheless, it is possible to extract the line and the continuum red-wards of it.

In the second set of observations, we use spectra of Cha H α 2, 3, 5 and 6, which have been published by Natta et al. (2004). They were also obtained with UVES at the same resolution of 40000 but with a different wavelength range (479-679 nm) covering both wings of the Li I doublet.

3. Models and Methods

We have generated a model atmosphere grid with two different line profile setups: Setup1 corresponds to synthetic spectra with impact approximated van der Waals alkali line profiles (Schweitzer et al. 1996), whereas Setup2 represents synthetic spectra with more sophisticated line profile calculations (Johnas et al. 2006; Allard et al. 2006, 2005). For both setups, models are calculated using varied lithium abundances. For each line profile setup, a model atmosphere is calculated and converged before generating the synthetic spectrum. “GAIA-cond” settings are applied for $T_{\text{eff}} = 2600$ K to 3100 K in steps of 100 K. This temperature range covers the effective temperatures of the studied BDs/VLMSs as determined by Comerón et al. (2000) from spectral types. The “GAIA-cond” approximations consider fully “rained-out” condensed dust in chemical equilibrium, see Allard et al. (2001) for details. At these effective temperatures, dust is not important and the Cond-approximation can be applied. For calculating the model atmospheres, we have to assume a value for the surface gravity $\log(g)$. Since the masses are required in order to estimate the $\log(g)$ -values, we have to use evolutionary tracks for the estimation. Using the table in Chabrier et al. (2000) for objects with an age of 1 and 5 Myr, and the luminosities of the objects derived by Luhman (2004) (see Table 1), we find $\log(g)$ -values

between 3.5 and ≥ 4 . For the luminosities derived by Comerón et al. (2000), we find values between 3.48 and 3.6 for an age of 1 Myr, and larger than 4 for an age of 5 Myr. Nevertheless, we want to stress that the luminosities in Table 1 also include the disk and accretion, which is why the luminosity of only the VLMS/BD is expected to be lower, and thus the values of $\log(g)$ higher. If we use the effective temperature instead of the luminosity, the masses of the objects are in general slightly higher and hence the $\log(g)$ -values a bit larger. For this reason, we varied the surface gravity $\log(g)$ between 3.5 and 5.5 in steps of 0.5. The lithium abundance is varied from $\log(\epsilon) = 0.0$ to 3.7 in steps of 0.1 dex. For comparison, in standard spectra the meteoritic lithium abundance of $\log(\epsilon) = 3.31$ is used. Every spectrum is calculated at a spectral resolution of 670 000 for the wavelength range around the lithium resonance doublet. In the model atmosphere and synthetic spectra, we assume a microturbulence of 2.0 km/s, which is a typical value used in M dwarf modeling (Allard & Hauschildt 1995). A χ^2 -technique is applied to quantify the differences between observations and models, as described in Schweitzer et al. (2001). The synthetic spectra are first convolved down to the resolution of the observations ($R = 40\,000$). For the rotational broadening, a standard limb darkening coefficient is used (Gray 1992; Eqs. 17.11 and 17.12).

The results of the fits are presented in Table 2 for the observations by Joergens & Guenther (2001) and in Table 3 for the observations by Natta et al. (2004). The first row for each observation of each section is the fit over all dimensions of the parameter range. In order to limit the number of free parameters, the effective temperatures derived by Comerón et al. (2000) are used for a second fit. Results for this second fit are presented for each observation in the second row of Table 2.

The quality of the fit is very sensitive to the selected wavelength range. Therefore, we use the same range, from 6707 Å to 6717 Å, in all our fits of the observations by Joergens & Guenther (2001). The lower limit here is set by the wavelength range of the observations, which starts just shortward of 6707 Å. The small lithium EWs obtained by Joergens & Guenther (2001) justify the chosen range in wavelength. With the fit parameters obtained by this wavelength range, a satisfying description is also provided towards the redder part of the observations.

Although the $v \sin i$ -values used for the modeling are in general agreement with the values given in Joergens & Guenther (2001), there are noticeable differences in some cases. Notable differences occur when the EWs are determined by fitting a continuum to the spectral region close to the lithium line. Because of the large number of spectral lines in very late-type objects (see Fig. 1), this approach is problematic. Setting the continuum right is especially difficult for observations of relative low signal-to-noise ratio, especially those of Cha H α 2, 3 and 8. Another difference in the two determinations of the $v \sin i$ is that in the old data, the spectra were deconvolved with the point-spread-function (PSF) of the spectrograph, which was determined from the telluric lines. Given the differences in the two approaches, it is not surprising that the $v \sin i$ -values obtained are slightly different from the older ones. Altogether, our empirical error estimate for $\log(\epsilon)$ is 0.4 dex. It is derived

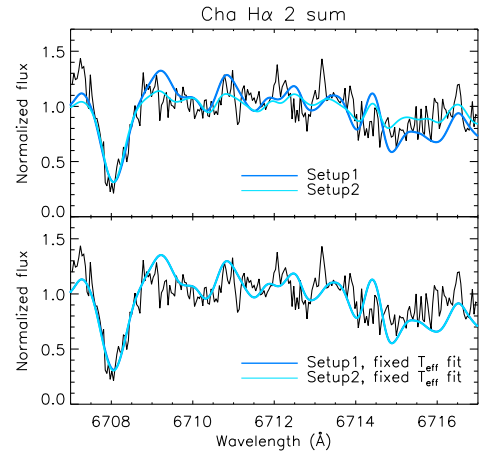


Fig. 2. High-resolution UVES spectrum of Cha H α 2 covering the lithium line at 6708 Å (Joergens & Guenther 2001; Joergens 2006) fitted with synthetic GAIA-cond models using 2 different line profile setups as described in Table 2. *Upper panel:* observation with free fit (first row of each observation in Table 2) and *lower panel:* observation with “effective temperature fixed fit” (second row of each observation in Table 2).

from studying the changes due to the variation of the free parameters.

In Table 2 we also list the values of the lithium EWs. The most crucial step when determining the EW is identifying the continuum in the spectrum; this is the main source of error, see the discussion in Sect. 1. The “true” continuum (ignoring the effects of all atomic and molecular lines in the spectrum) is at much higher flux levels than the observed pseudo-continuum. Therefore, we construct a pseudo-continuum in the wavelength range from 6700 Å to 6720 Å by calculating a spectrum without the lithium lines. After taking the difference between this pseudo continuum and the synthetic spectrum, the remaining area is normalized over the mean flux between the D₁ and D₂ line of Li I, resulting in the theoretical/synthetic EWs, which are also listed in Tables 2 and 3.

4. Results

The results are listed in Table 2 and are presented graphically in Figs. 2–7. For most objects more than one observed spectrum has been fitted. Figures 2–7 display for each object the model fit to one observation as an example. The upper panels in the figures show the fit over all free parameters, while the lower panels show the fit with fixed effective temperature. The relatively low signal-to-noise ratio of the observations limits the fit quality, in particular when applying the first fitting method with more free parameters. This is less severe for the case of Cha H α 4, for which the obtained spectra have a higher signal-

Table 2. Physical parameters of BDs/VLMs in Chamaeleon I derived from a comparison of synthetic GAIa-cond models and high-resolution UVES spectra using different line profile setups: (from left to right) effective temperature, surface gravity, lithium abundance and EW of lithium. The given results are for (i) a fit to the full range of free model parameters: T_{eff} , $\log(g)$, $\log(\epsilon)$, radial velocity and rotational velocity (first row of each observation) and (ii) for a fit with fixed effective temperature as determined by Comerón et al. (2000) (second row).

Object	T_{eff} (K)					$\log(g)$					$\log(\epsilon)$					EW_{Li} (Å)				
	Setup 1					Setup 2					Setup 1					Setup 2				
Cha H α 2, MJD = 51638.087	3100	4.5	0.9	0.33		3000	5.5	1.3	0.38		3100	4.5	0.9	0.33		3000	5.5	1.3	0.38	
	2900	3.5	1.0	0.34		2900	3.5	0.9	0.33		2900	3.5	0.9	0.33		2900	3.5	0.9	0.33	
Cha H α 2, MJD = 51658.096	3100	4.0	1.5	0.40		3000	5.5	1.6	0.45		3100	4.0	1.5	0.40		3000	5.5	1.6	0.45	
	2900	3.5	1.6	0.41		2900	3.5	1.6	0.41		2900	3.5	1.6	0.41		2900	3.5	1.6	0.41	
Cha H α 2 sum	3100	4.0	1.4	0.39		3000	5.5	1.6	0.45		3100	4.0	1.4	0.39		3000	5.5	1.6	0.45	
	2900	3.5	1.4	0.39		2900	3.5	1.4	0.39		2900	3.5	1.4	0.39		2900	3.5	1.4	0.39	
Cha H α 3, MJD = 51638.987	3100	4.0	1.0	0.34		3000	5.5	1.3	0.38		3100	4.0	1.0	0.34		3000	5.5	1.3	0.38	
	2800	3.5	1.0	0.35		2800	3.5	1.0	0.35		2800	3.5	1.0	0.35		2800	3.5	1.0	0.35	
Cha H α 3, MJD = 51658.113	3100	4.0	1.5	0.40		3100	4.0	1.5	0.40		3100	4.0	1.5	0.40		3100	4.0	1.5	0.40	
	2800	3.5	1.5	0.41		2800	3.5	1.5	0.41		2800	3.5	1.5	0.41		2800	3.5	1.5	0.41	
Cha H α 3 sum	3100	4.0	1.4	0.39		3100	4.0	1.4	0.39		3100	4.0	1.4	0.39		3100	4.0	1.4	0.39	
	2800	3.5	1.3	0.39		2800	3.5	1.3	0.39		2800	3.5	1.3	0.39		2800	3.5	1.3	0.39	
Cha H α 4, MJD = 51617.210	3100	4.0	1.8	0.44		3000	5.5	1.9	0.54		3100	4.0	1.8	0.44		3000	5.5	1.9	0.54	
	3000	3.5	1.8	0.43		3000	3.5	1.8	0.43		3000	3.5	1.8	0.43		3000	3.5	1.8	0.43	
Cha H α 4, MJD = 51617.236	3100	4.0	1.8	0.44		3000	5.5	1.9	0.54		3100	4.0	1.8	0.44		3000	5.5	1.9	0.54	
	3000	3.5	1.8	0.43		3000	3.5	1.8	0.43		3000	3.5	1.8	0.43		3000	3.5	1.8	0.43	
Cha H α 4, MJD = 51627.277	3100	4.0	1.4	0.39		3000	5.5	1.7	0.48		3100	4.0	1.4	0.39		3000	5.5	1.7	0.48	
	3000	3.5	1.5	0.40		3000	3.5	1.5	0.40		3000	3.5	1.5	0.40		3000	3.5	1.5	0.40	
Cha H α 4, MJD = 51627.303	3100	4.0	1.4	0.39		3000	5.5	1.6	0.45		3100	4.0	1.4	0.39		3000	5.5	1.6	0.45	
	3000	3.5	1.4	0.39		3000	3.5	1.4	0.39		3000	3.5	1.4	0.39		3000	3.5	1.4	0.39	
Cha H α 4, MJD = 51634.997	3100	4.0	1.5	0.40		3000	5.5	1.7	0.48		3100	4.0	1.5	0.40		3000	5.5	1.7	0.48	
	3000	3.5	1.6	0.41		3000	3.5	1.6	0.41		3000	3.5	1.6	0.41		3000	3.5	1.6	0.41	
Cha H α 4, MJD = 51635.023	3100	4.0	1.6	0.41		3000	5.5	1.7	0.48		3100	4.0	1.6	0.41		3000	5.5	1.7	0.48	
	3000	3.5	1.6	0.41		3000	3.5	1.6	0.41		3000	3.5	1.6	0.41		3000	3.5	1.6	0.41	
Cha H α 4, MJD = 51657.994	3100	4.0	1.6	0.41		3000	5.5	1.6	0.45		3100	4.0	1.6	0.41		3000	5.5	1.6	0.45	
	3000	3.5	1.6	0.41		3000	3.5	1.6	0.41		3000	3.5	1.6	0.41		3000	3.5	1.6	0.41	
Cha H α 4 sum	3100	4.0	1.6	0.41		3000	5.5	1.7	0.48		3100	4.0	1.6	0.41		3000	5.5	1.7	0.48	
	3000	3.5	1.6	0.41		3000	3.5	1.6	0.41		3000	3.5	1.6	0.41		3000	3.5	1.6	0.41	
Cha H α 5, MJD = 51639.009	3100	4.5	1.6	0.43		3000	5.5	1.8	0.51		3100	4.5	1.6	0.43		3000	5.5	1.8	0.51	
	3000	3.5	1.8	0.43		3000	3.5	1.8	0.43		3000	3.5	1.8	0.43		3000	3.5	1.8	0.43	
Cha H α 5, MJD = 51658.128	3100	4.0	1.5	0.40		3000	5.5	1.6	0.45		3100	4.0	1.5	0.40		3000	5.5	1.6	0.45	
	3000	3.5	1.5	0.40		3000	3.5	1.5	0.40		3000	3.5	1.5	0.40		3000	3.5	1.5	0.40	
Cha H α 6, MJD = 51658.143	3100	4.0	1.8	0.44		3000	5.5	1.9	0.54		3100	4.0	1.8	0.44		3000	5.5	1.9	0.54	
	2800	3.5	1.8	0.43		2800	3.5	1.8	0.43		2800	3.5	1.8	0.43		2800	3.5	1.8	0.43	
Cha H α 8, MJD = 51639.100	3100	4.0	1.5	0.40		3000	5.5	1.6	0.45		3100	4.0	1.5	0.40		3000	5.5	1.6	0.45	
	2900	3.5	1.5	0.40		2900	3.5	1.5	0.40		2900	3.5	1.5	0.40		2900	3.5	1.5	0.40	
Cha H α 8, MJD = 51658.215	3100	4.0	1.6	0.41		3000	5.5	1.7	0.48		3100	4.0	1.6	0.41		3000	5.5	1.7	0.48	
	2900	3.5	1.7	0.42		2900	3.5	1.7	0.42		2900	3.5	1.7	0.42		2900	3.5	1.7	0.42	

Table 3. Physical parameters of BDs/VLMs in Chamaeleon I derived from a comparison of synthetic GAIA-cond models and high-resolution by Natta et al. (2004) using different line profile setups: (from left to right) effective temperature, surface gravity, lithium abundance and EW of lithium. The given results are for (i) a fit to the full range of free model parameters: T_{eff} , $\log(g)$, $\log(\epsilon)$, radial velocity and rotational velocity (first row of each observation) and (ii) for a fit with fixed effective temperature as determined by Comerón et al. (2000) (second row).

Object	T_{eff} (K)	$\log(g)$	$\log(\epsilon)$	EW_{Li} (Å)	T_{eff} (K)	$\log(g)$	$\log(\epsilon)$	EW_{Li} (Å)
<i>Setup1</i>					<i>Setup2</i>			
Cha H α 2	3100	4.0	1.2	0.37	3000	5.5	1.5	0.43
	2900	3.5	1.2	0.37	2900	3.5	1.3	0.38
Cha H α 3	3100	4.0	1.3	0.38	3000	5.5	1.6	0.45
	2800	3.5	1.3	0.38	2800	3.5	1.3	0.39
Cha H α 5	3100	4.0	1.5	0.40	3000	5.5	1.7	0.48
	3000	3.5	1.5	0.40	3000	5.5	1.7	0.48
Cha H α 6	3100	4.0	1.6	0.41	3000	5.5	1.7	0.48
	2800	3.5	1.5	0.41	2900	3.5	1.5	0.41

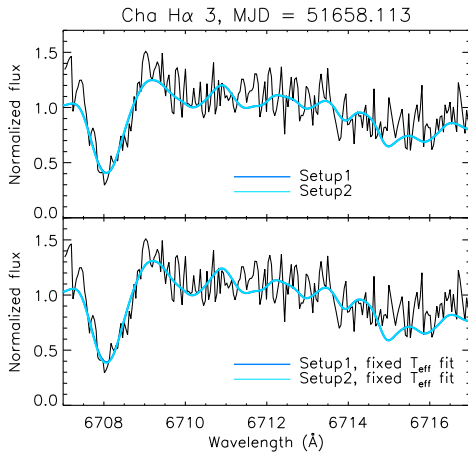


Fig. 3. The same as in Fig. 2 for the observation of Cha H α 3.

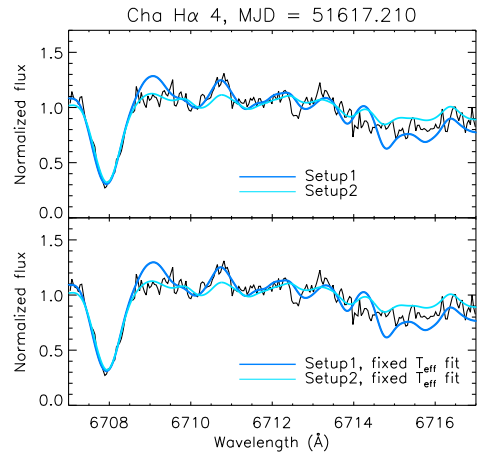


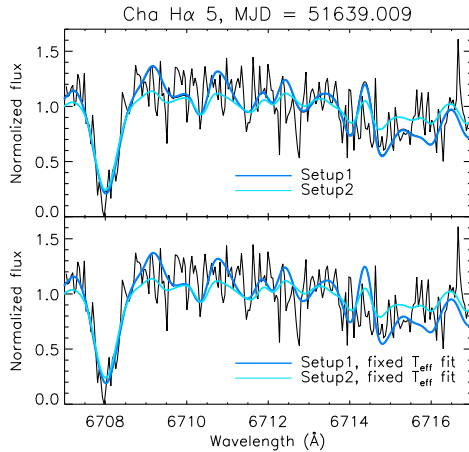
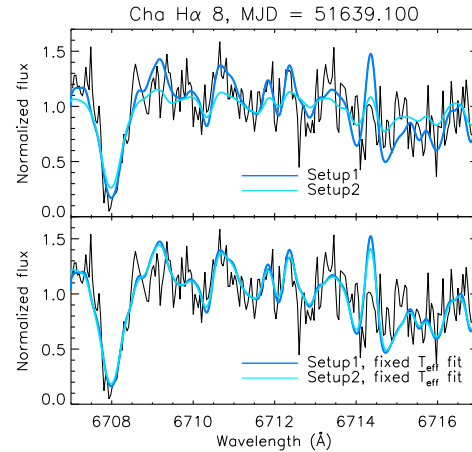
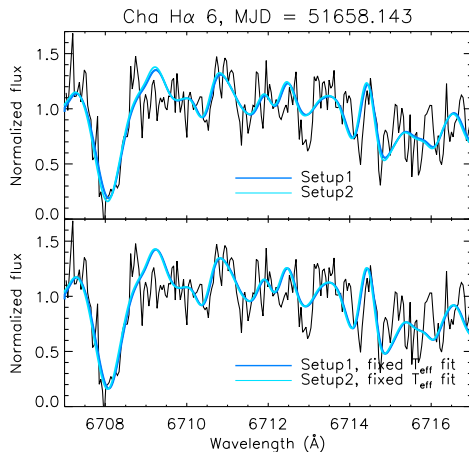
Fig. 4. The same as in Fig. 2 for the observation of Cha H α 4.

to-noise ratio. In the following, we give details for the fits to the individual observations.

Due to the relatively low signal-to-noise ratios in the observations of Cha H α 2 and 3 (Fig. 3), we have added the two spectra of each of the objects (labeled with “sum”). An improved fitting with these spectra is possible. The fit results are consistent with the two methods and hint towards the higher lithium abundance. The description of Cha H α 2 is mostly satisfying, as depicted in Fig. 2. The blue and the red part of the lithium absorption line, as well as the red wing, are nicely delineated. However, there is a feature from approximately 6714.4 Å to 6716 Å in the synthetic spectra that cannot be identified through the observations. We assume that this feature is due to the TiO bands in the synthetic spectra, which cover this wavelength range. The red wing of the Li I line of Cha H α 3 is described fairly well by the setups, in contrast, the

fitting of the blue wing is unsatisfactory. This could be due to the very limited range of the observation at the shorter wavelengths.

The observations of Cha H α 4 have the best signal-to-noise ratio, therefore, a more detailed description is possible, as shown in Fig. 4. Both setups provide a good representation of the absorption core. The fits of Setup1 tend to show a feature at the beginning of the red wing, at approximately 6709 Å, contrary to the observations. Note the existence of a similar feature in the observation shown in Fig. 2, in which this feature is described by the synthetic spectra. The lack of this feature appears to be characteristic for Cha H α 4. The feature at approximately 6710.7 Å is well described. The fits of Setup2 provide a better description at 6709 Å, but an insufficient one at 6710.7 Å, compared to the fit with Setup1. From Table 2 it can be seen that both fits result in an equal, or very similar,


 Fig. 5. The same as in Fig. 2 for the observation of Cha H α 5.

 Fig. 7. The same as in Fig. 2 for the observation of Cha H α 8.

 Fig. 6. The same as in Fig. 2 for the observation of Cha H α 6.

lithium abundance estimate for each setup. In particular, the fits for the synthetic spectra of Setup2 give the same effective temperature and surface gravity, except for one case, which is very close.

We consider in the following the effect of surface activity on the measured lithium abundances. The fluctuations in the derived lithium abundances (Table 2) for the different observations of Cha H α 4 are well within the estimated error of 0.4 dex in $\log(\epsilon)$. Studies of the variability of Cha H α 4, based on radial velocity monitoring (Joergens 2006; partly the very same spectra as evaluated here) and quasi-simultaneous photometric monitoring (Joergens et al. 2003) on the time scale of its rotational period (Joergens & Guenther 2001), indicate a very small

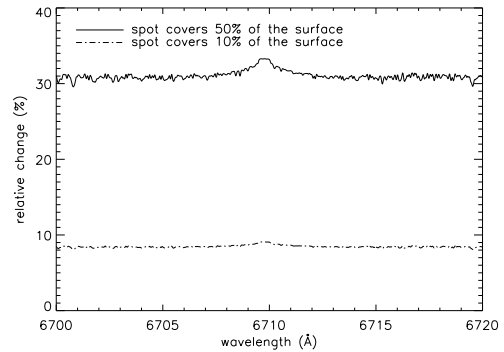


Fig. 8. Relative change in the spectrum, when assuming a 500 K cooler spot with a spatial coverage of 10% and 50% respectively.

surface activity level for Cha H α 4. The determined photometric peak-to-peak amplitudes in the Bessel R and Gunn i filters ($\Delta R < 0.03$ mag, $\Delta i < 0.03$ mag) and the radial velocity peak-to-peak amplitude ($\Delta RV < 0.2$ km/s) allow us to estimate that if caused by a spot or spots 500 K cooler than the surrounding atmosphere, these cover less than 1% of its surface. However, for general interest, we consider here the influence of spots on the lithium abundance measurements. The problem with spots in G and K stars is that their contribution to the continuum is very small, so that T_{eff} essentially comes from the spot free region since the Li I line becomes stronger in cooler atmospheres. Hence to a large part, the Li I absorption line would originate from the cool spot. Thus, the atmospheric model that is used to determine the abundance and EW of the Li I line would have a wrong temperature. Such effects have been observed in very

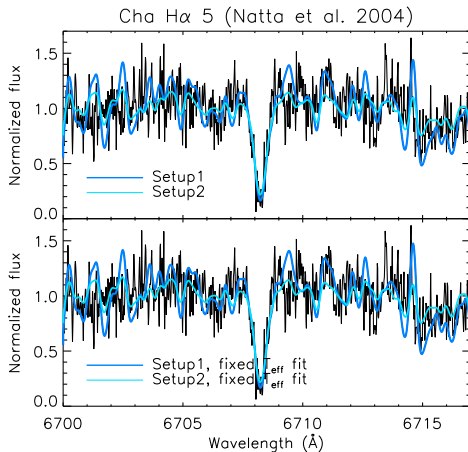


Fig. 9. The same as in Fig. 2 for the observation of Cha H α 5 using the spectra obtained by Natta et al. (2004).

active G and K stars, like EK Draconis (König et al. 2005). For objects of spectral type M or later this effect should not play a role, because these objects are so cool that the Li I originates mainly from the photosphere. In order to demonstrate this, we assume a spot with an effective temperature which is 500 K cooler than a given effective temperature of the object, which is assumed to be 3100 K. Furthermore, we assume that the spot coverage is 10% of the object. Although this is quite a substantial spot for such an object, the depth of the Li I line in the spectrum only changes by approximately a seven-tenth of a percent (dashed-dotted line in Fig. 8). Even when increasing the spot area to 50%, the relative change is just 2.4% (solid line in Fig. 8), so that the effect of spots at the surface has a small effect on the spectrum of the lithium lines. We thus conclude that even very large spots have essentially no influence on the abundance in objects of spectral type M.

In Figs. 5 and 7 the results of the fitting procedure are displayed for Cha H α 5 and 8. With the fits of Setup1 and the “effective temperature fixed fits” for Setup2, a satisfactory fit quality is reached. The free fit of Setup2 underestimates the flux especially towards the blue wing, but nevertheless gives a reasonable description of the pseudo-continuum. For Cha H α 6, all three setups are in agreement and provide a sufficient description, see Fig. 6.

When fitting the observations of Cha H α 2, 3, 5 and 6 by Natta et al. (2004) similar results to the previous ones are obtained. Their observations have the same resolution but a better coverage of the Li I absorption line. The same fitting procedure was applied to these observations. In Table 3, the results are summarized. In Fig. 9, representing Cha H α 5, the results with the free fit and “fixed effective temperature fit” are shown. The fits have been performed for both the wavelength range that has been used before and additionally the one from 6700 Å to 6717 Å. The fit results are not wavelength range depen-

dent. For Cha H α 2, 3 and 5 good fits were possible, however the Li I line core of Cha H α 6 could be fitted only very poorly. Nevertheless, the line wing and pseudo continuum can be described satisfactorily, also for Cha H α 6.

The effective temperatures for Cha H α 4 and Cha H α 5 (plus Cha H α 2 for Setup2 and Cha H α 8 MJD = 51639.100 for Setup2) derived from our model fits are consistent within the error estimate of ± 100 K in both setups with the effective temperatures from Comerón et al. (2000), as can be seen in Table 2. For the other objects there is a greater deviation of an additional 100 K - 200 K (we assume improvements after narrowing down the free fit parameters in future work). When comparing the derived effective temperatures in Table 2 with those of Luhman (2004), the agreement is very good for all objects fitted with every setup, since he provides slightly higher effective temperatures. The values of the derived surface gravities depend strongly on the used setup. The fit with Setup2 provides higher surface gravities, often at the upper limit. When applying Setup1, the free fit provides a surface gravity within its range, whereas the “effective temperature fixed fit” always results in the lowest surface gravity value. Chabrier & Baraffe (2000) predict for substellar objects of ages between one Myr and 10 Myr a $\log(g)$ around 3.5 and 4.0. Hence, these low values of $\log(g)$ also imply the relatively young age of Chamaeleon I. Consequently, we want to stress that no final statement about the surface gravity can be made yet by fitting the Li I absorption line. Further studies for obtaining the surface gravity are necessary and will be performed in future work. Nevertheless, both fit possibilities, the “effective temperature fixed fit” and the free fit, yield very similar values of the lithium abundance, independent of the effective temperature. When comparing the lithium abundance results between the two setups there is just a small visible discrepancy, which is consistent with the results within the estimated errors (Sect. 3). The mean values of the derived lithium abundances is 1.5 for Setup1 and 1.6 for Setup2. However, our tests show that the derived parameters provide a good description of the overall continuum of the observations, e. g., the continuum characteristic and the TiO bands. These bands are shown in Fig. 10, 11, 12 and 13, representing Cha H α 4, MJD = 51617.210, and Cha H α 6, MJD = 51658.143. The fits have been normalized via their medians in this wavelength range and do not show large differences between the two fitting procedures. When comparing the EWs derived by Joergens & Guenther (2001) with those presented in Table 2, we find that they are mostly in agreement, within their error range. For Cha H α 2 only the values of the first spectrum are in agreement. Generally our EWs of Cha H α 3 and 6 are greater (or at the upper limit within the error bars of Joergens & Guenther 2001). The values of Cha H α 4, 5 and 8 are consistent with the ones of Joergens & Guenther (2001). The reason for this slight discrepancy is due to the different methods with which the EWs are obtained, see the discussion in Sect. 1 about the difficulties when trying to obtain the EWs.

The Li I line in the first data set is in the last order close to the edge of our spectra range. Using a different setting, Natta et al. (2004) have obtained spectra of Cha H α 2, 3, 5 and 6 using a setting in which the Li I line is in the middle of the spectrum.

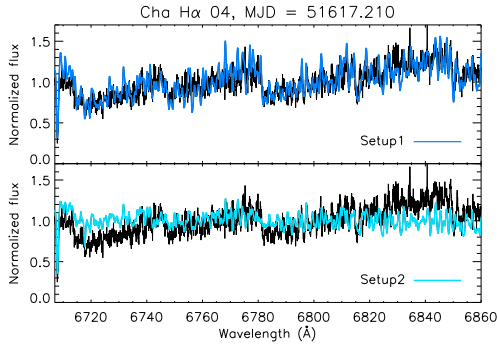


Fig. 10. The TiO bands are depicted for Cha H α 4, MJD = 51617.210 with the free fit with both setups.

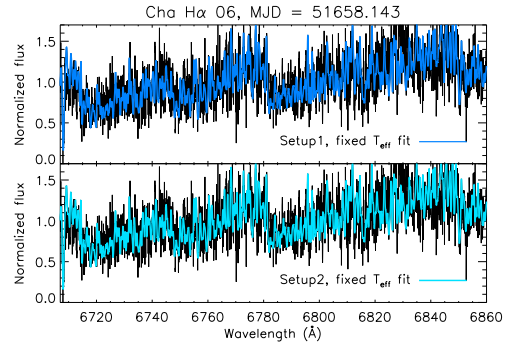


Fig. 13. The TiO bands are depicted for Cha H α 6, MJD = 51658.143 with the “fixed effective temperature” fit.

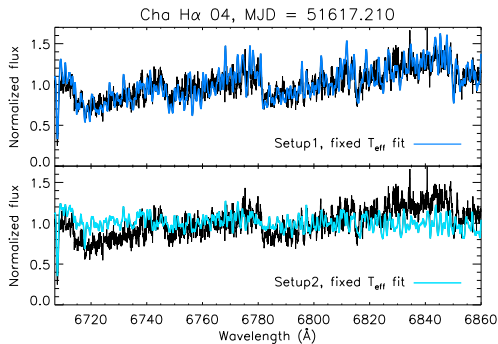


Fig. 11. The TiO bands are depicted for Cha H α 4, MJD = 51617.210 with the “fixed effective temperature” setups.

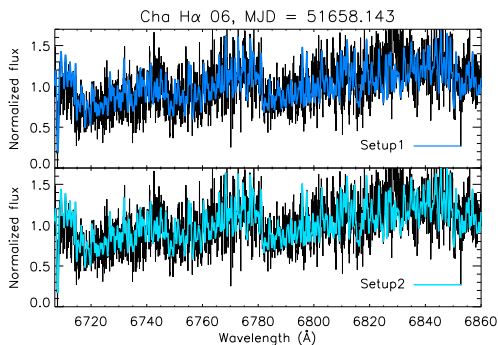


Fig. 12. The TiO bands are depicted for Cha H α 6, MJD = 51658.143 with the free fit with both setups.

We have analyzed both data sets and have basically found the same low lithium abundances in both cases, see Tables 2 and 3 for details.

We compare the here derived lithium abundances for objects close to the substellar border (M6-M7) with those of higher mass Chamaeleon I members (Sz 19, Sz 6, Sz 24, Sz 3, Sz 5 and Sz 9) determined by Magazzu et al. (1992). Magazzu et al. (1992) classify them as classical T Tauri stars of spectral type G2, K2, and M0. They are relatively young, below 0.3 to 1.3 Myr, which confirms the discussion regarding the young age of these cloud members given in the introduction. Moreover, it is assumed that there is no lithium depletion in the sample of the classical T Tauri stars.

Magazzu and colleagues derive the lithium abundances via curves of growth obtained from LTE- and non-LTE-calculations and compare them to observed EWs after correcting for veiling. For the six classical T Tauri stars mentioned above they obtain a mean $\log(\epsilon)$ of 3.1 from LTE-calculations and 3.4 from non-LTE-calculations, which are values much closer to the meteorite lithium abundance.

Classical T Tauri stars show a strong infrared-excess due to the presence of an accretion disk. In addition to the infrared-excess, classical T Tauri stars often have photospheric absorption lines, which have smaller EWs than main sequence stars of similar spectral types. This is generally attributed to the presence of an additional continuum and perhaps an emission line source, which is interpreted as the signature of the accretion shock on the surface of the stars (see Hessman & Guenther 1997 for details). Since young BDs are also known to have accretion disks (Natta et al. 2004; Mohanty et al. 2005), it is possible that our spectra of the young BDs are affected by such a veiling continuum. Jayawardhana et al. (2003) have in fact detected an L-band excess for our Cha H α objects and estimate a disk fraction of 40–60% for objects in Chamaeleon. In addition, Persi et al. (2000) have observed 108 stars and BDs in Chamaeleon at 6.7 and 14.3 μm , of which 82 sources show infrared-excess. Although most of these objects are classical T Tauri stars, some are BDs. The largest excess of a BD was

found in Cha H α 2. It can thus be concluded that disks are also common amongst the low-mass objects studied in this work. Hence the question arises as to whether low-mass objects could also have a veiling continuum, in analogy to the T Tauri stars. The veiling continuum of T Tauri stars originates from an accretion shock on the surface of the star, which forms because of a gap between the disk and the star. One would expect that the temperature of the shock in objects of lower mass would be correspondingly lower. Whether objects of very low-mass have shocks of sufficiently high temperature to veil the optical continuum is an open question that can only be addressed observationally. White & Basri (2003) studied three very low-mass objects of spectral type M7 in Taurus, and conclude that while these objects do show clear signs of disks and accretion, there is no detectable veiling continuum. Using our spectra, we also investigated whether the spectra are veiled or not by using the TiO-lines. If the spectra are veiled, TiO-lines in the model would have to be stronger than the observed ones. As shown in Figs. 10, 11, 12 and 13, this is not the case, as we are able to fit the TiO-lines with the $\log(g)$ and T_{eff} -values listed in Table 2 without assuming the presence of a veiling continuum. We therefore conclude that the veiling continuum is not very prominent in these objects.

An explanation for the discrepancies in the derived lithium abundances between the BDs/VLMSs studied here at the substellar boundary and higher mass T Tauri stars studied by Magazzu et al. (1992), could be an error in the estimate of age and mass, not only because of the uncertainties in the evolutionary track predictions below 10 Myr, but also because of uncertainties in the measurement of the luminosity and effective temperatures, which have been used in the comparison with the evolutionary tracks, see Table 1. The critical question is whether the observed large depletion of the lithium can be explained by the objects being either older or more massive than assumed. This is possible because the uncertainties in the determination of the ages of these objects are in fact large (see Table 1). For example, Comerón et al. (1999) finds a mean age of roughly 0.5 Myrs for our objects, whereas Comerón et al. (2000) gives ages between 2 and 5.5 Myrs. However, these age estimates for Cha H α BD candidates and VLMSs are still in general agreement with the young age of the Cha I association, as indicated by the presence of classical T Tauri stars. When using the effective temperatures and luminosities derived by Luhman (2004), with the evolutionary tracks used by Comerón et al. (2000), the age and mass estimates again differ from the previous results. In order to test this hypothesis, we determined the ages and masses that the objects should have to show a lithium depletion like the one observed. According to Chabrier & Baraffe (2000), the minimum age for the lithium depletion is 10 Myr for an object of $0.1 M_{\odot}$. At younger ages the core temperatures are too low for the depletion of lithium. For objects of even lower masses, for example $0.07 M_{\odot}$, the age would have to be larger than $10^{7.7}$ yrs. For objects of higher mass, the lithium depletion starts at an earlier age. For example, at $0.3 M_{\odot}$ the depletion sets in at $10^{6.7}$ yrs. Thus, if the objects studied here had such a high mass, the observed lithium abundance would be explained. However, all evolutionary track calculations (Burrows et al. 1997; D'Antona & Mazzitelli 1997;

Baraffe et al. 1998) give much lower masses for our objects. Although the ages of the objects are uncertain, in none of the cases are the masses and ages sufficiently high to explain the lithium depletion when using the evolutionary tracks (Chabrier & Baraffe 2000), regardless of whether we use the masses and ages from Comerón et al. (1999), Comerón et al. (2000), or Luhman (2004).

In summary, as possible explanations for the observed lithium depletion we can rule out the presence of a veiling continuum, the effects of spots, and that the objects are more massive or much older than previously thought. We are therefore left with two possible explanations: one is just a general lack of the understanding of the details of the formation of the lithium line, and the other is that the internal structure of the object differs from the internal structure of the evolutionary tracks predicted. This is possible because the objects are quite young and the evolutionary tracks may not have fully forgotten the initial conditions with which they were started. This could also be the case for the classical T Tauri stars from Magazzu et al. (1992), which could no longer be fully convective. As a result, they could have already started the destruction of lithium without displaying any evidence at the surface.

5. Conclusions

The lithium resonance lines in high-resolution spectroscopic observations of very young BDs and VLMSs in Cha I are fairly well described by the synthetic spectra calculated with the GAIA-cond atmosphere model using different model setups. The same is valid for the red pseudo-continua in the observations. We present the first study of the lithium abundance of these objects. The results of the lithium abundance obtained by the observations of Natta et al. (2004) confirm those observed by Joergens & Guenther (2001). The synthetic spectra lead to similar results for the different line profile setups. However, there are small differences in the derived lithium abundance, as expected. The lithium abundances using Setup2 are generally the largest. In some cases, Setup1 provides a better description than Setup2, although Setup2 includes the detailed physics. However, next to the low resolution, the effective temperature range of our observed objects is near the upper limit for which the effect of pressure broadening described with van der Waals broadening is observable. A stronger statement is expected in an analysis of objects with later spectral type. Nevertheless, the results give a consistent picture and are within the estimated errors. Note that the EWs presented here are synthetic ones. The choice of continuum has a large influence on their values. We have used pseudo synthetic continua assuming total lithium depletion.

Despite the young age of the studied BDs and VLMSs in Chamaeleon I and the assumption that lithium depletion has not yet started, the lithium abundances show an unexpected underabundance compared to meteoritic lithium abundance. We do not expect veiling to be an important effect for our objects. Observations with a higher resolution in the optical wavelength regime are important and needed for improved insight into the physics, including, e. g., the description of the more abundant alkalis, such as sodium and potassium, and the presence of

satellites. Furthermore, a consistent set of observations of objects with spectral type G to M in Cha I is desirable for an improved study with consistent model atmospheres and synthetic spectra.

More detailed theoretical models are necessary to evaluate if lithium depletion has already started in these objects, although this is a very difficult task.

Acknowledgements. We thank G. Torres for providing the estimate of the spot coverage for Cha H α 4 based on our photometric and radial velocity data. Furthermore, we thank A. Natta and S. Randich for making the spectra available.

References

- Allard, F. & Hauschildt, P. H. 1995, *ApJ*, 445, 433
- Allard, F., Hauschildt, P. H., Alexander, D. R., Tamanai, A., & Schweitzer, A. 2001, *ApJ*, 556, 357
- Allard, N. F., Allard, F., Johnas, C. M. S., & Kielkopf, J. F. 2006, *A&A*, submitted
- Allard, N. F., Allard, F., & Kielkopf, J. F. 2005, *A&A*, 440, 1195
- Baraffe, I., Chabrier, G., Allard, F., & Hauschildt, P. H. 1998, *A&A*, 337, 403
- Basri, G. 2000, *ARA&A*, 38, 485
- Burrows, A., Marley, M., Hubbard, W. B., et al. 1997, *ApJ*, 491, 856
- Chabrier, G. & Baraffe, I. 2000, *Ann. Rev. Astron. Astrophys.*, 38, 337
- Chabrier, G., Baraffe, I., Allard, F., & Hauschildt, P. H. 2000, *ApJ*, 542, 464
- Comerón, F., Neuhäuser, R., & Kaas, A. A. 2000, *A&A*, 359, 269
- Comerón, F., Rieke, G. H., & Neuhäuser, R. 1999, *A&A*, 343, 477
- D'Antona, F. & Mazzitelli, I. 1997, *Memorie della Societa Astronomica Italiana*, 68, 807
- Gray, D. F. 1992, *Science*, 257, 1978
- Hauschildt, P. H. & Baron, E. 1999, *JCAM*, 109, 41
- Hessman, F. V. & Guenther, E. W. 1997, *A&A*, 321, 497
- Jayawardhana, R., Ardila, D. R., Stelzer, B., & Haisch, Jr., K. E. 2003, *AJ*, 126, 1515
- Joergens, V. 2006, *A&A*, 446, 1165
- Joergens, V., Fernández, M., Carpenter, J. M., & Neuhäuser, R. 2003, *ApJ*, 594, 971
- Joergens, V. & Guenther, E. 2001, *A&A*, 379, L9
- Johnas, C. M. S., Allard, N. F., Homeier, D., Allard, F., & Hauschildt, P. H. 2006, *AIP Conf. Proc.*, 874, 354
- Kenyon, M. J., Jeffries, R. D., Oliveira, J. M., & Maxted, P. F. L. 2005, *MNRAS*, 356, 89
- König, B., Guenther, E. W., Woitas, J., & Hatzes, A. P. 2005, *A&A*, 435, 215
- López Martí, B., Eislöffel, J., Scholz, A., & Mundt, R. 2004, *A&A*, 416, 555
- Luhman, K. L. 2004, *ApJ*, 602, 816
- Magazzu, A., Rebolo, R., & Pavlenko, I. V. 1992, *ApJ*, 392, 159
- Mohanty, S., Jayawardhana, R., & Basri, G. 2005, *ApJ*, 626, 498
- Natta, A., Testi, L., Muzerolle, J., et al. 2004, *A&A*, 424, 603
- Neuhäuser, R. & Comerón, F. 1999, *A&A*, 350, 612
- Pavlenko, Y., Zapatero Osorio, M. R., & Rebolo, R. 2000, *ã*, 355, 245
- Pavlenko, Y. V. 2005, *Astronomische Nachrichten*, 326, 934
- Persi, P., Marenzi, A. R., Olofsson, G., et al. 2000, *A&A*, 357, 219
- Rebolo, R., Martin, E. L., & Magazzu, A. 1992, *ApJ*, 389, L83
- Schweitzer, A., Gizis, J. E., Hauschildt, P. H., Allard, F., & Reid, I. N. 2001, *ApJ*, 555, 368
- Schweitzer, A., Hauschildt, P. H., Allard, F., & Basri, G. 1996, *MNRAS*, 283, 821
- Tinney, C. G. 1998, *MNRAS*, 296, L42
- Tsuji, T. 2001, in *Ultracool Dwarfs: New Spectral Types L and T*, ed. H. R. A. Jones & I. A. Steele, 9–+
- White, R. J. & Basri, G. 2003, *ApJ*, 582, 1109
- Zapatero Osorio, M. R., Béjar, V. J. S., Martín, E. L., et al. 2002, *ApJ*, 578, 536

8 Comparison between the Impact and Modern1 Setup and Selected Observations

In Chap. 5, it is explained that the influence of the alkali line profiles increases towards lower effective temperatures. There has been a Li I study with observations of relatively “hot” cool objects but with a relatively high resolution and decent signal-to-noise ratio in Sect. 7.2. It is very important to study the Na I D and K I doublets. However, the very low flux towards smaller optical wavelengths is still a challenge when observing objects of (very) late spectral type.

It is best to test the setups with observations of (very) late objects. Therefore, observations with low and high resolution of very low mass objects and a good signal-to-noise ratio is required. The influence of the far line wings of the alkalis can be reasonably studied on low resolution observations. In order to test the alkali absorption lines in detail, (very) high resolution observations are necessary.

Impact and modern1 fits of selected observations of very low mass objects are presented here. Since there are only small differences between the modern1, modern2, and modern3 setup, the comparison has been done with the modern1 setup. Nevertheless, the following discussion is valid for any “modern” setup. The aim is to compare the fitting quality of the impact and the modern1 setups and not to provide reliable stellar parameters. A detailed analysis on the stellar parameters will be done in future work. Tests on low resolution observations are presented in Sect. 8.1. They focus on the K I D₁ line with its far line wing. In Sect. 8.2, comparisons for selected resonance alkali lines to observations with higher resolution are shown. A conclusion about the application of the two setups is given in Sect. 8.3.

8.1 Results for Low Resolution Spectra

The sample of low resolution observations of L dwarfs in Figs. 8.1–8.6 is provided by Schweitzer et al. (2002). These observations have a resolution $\lambda/\Delta\lambda$ of less than 1000. In Fig. 8.7, the observation of the T6 dwarf SDSS 162414+0029 is provided by Sandy Leggett for the work in Allard et al. (2003). It has a resolution of $\lambda/\Delta\lambda = 5000$. For the impact and modern1 fit, synthetic COND spectra with the standard resolution $\Delta\lambda$ of 2 Å have been used. (Tests with synthetic spectra with a resolution of $\Delta\lambda = 0.02$ Å provide the same results; synthetic spectra with this higher resolution have been reduced to the resolution of 5000 for the fits of SDSS 162414+0029.) The fits in Figs. 8.1–8.7 were obtained with the χ^2 -method introduced in Sect. 7.2 (The fits are again scaled with their medians.). For the impact and modern1 setup, a grid with T_{eff} from 1400 K to 1800 K with 100 K step size, $\log(g)$ from 4.5 to 6.0 with a 0.5 dex step size, and solar composition has been used. $T_{\text{eff}} = 1800$ K has been chosen as upper limit for the COND spectra because for higher effective temperatures dust opacities need to be taken into account. The stellar parameters

Name	Spectral Type	Impact Setup		Modern1 Setup		Fig.
		T_{eff} (K)	$\log(g)$	T_{eff} (K)	$\log(g)$	
2MASSI J0850359+105716	L6	1400	6.0	1800	5.5	8.1
2MASSI J0825197+211552	L7.5	1400	6.0	1800	5.5	8.2
2MASSW J0929336+342953	L8	1400	6.0	1800	5.5	8.3
2MASSI J0328427+230205	L8	1800	5.5	1800	5.5	8.4
2MASSW J1632291+190441	L8	1400	6.0	1800	5.5	8.5
2MASSW J1523226+301456	L8	1400	6.0	1800	6.0	8.6
SDSS 162414+0029	T6	1000	5.5	1000	5.5	8.7

Table 8.1: Low resolution sample with derived stellar parameters.

derived by the fitting as well as the spectral type taken from Schweitzer et al. (2002) and Allard et al. (2003) are listed in Table 8.1. The error bars of the effective temperature are estimated to ± 100 K and of the surface gravity to ± 0.5 dex.

The derived effective temperatures do not correlate with the spectral type independent of the setup, see also Schweitzer et al. (2001). Comparing the derived effective temperatures with those determined in Schweitzer et al. (2002), the impact setup provides too low effective temperatures for the L6 to L7.5 objects but the derived effective temperatures for the L8 objects agree with the expected effective temperatures, see Kirkpatrick (2005). Generally, the effective temperatures derived by the modern1 setup are 400 K higher than the ones derived by the impact setup. These effective temperatures correspond to values obtained by the K_S band fitting by Schweitzer et al. (2002). However, the modern1 effective temperatures are overestimated for the L8 dwarfs. The effect that higher effective temperatures are derived with the modern1 setup has already been noted in Sect. 7.2. In Figs. 8.1–8.6, the upper boundary of the wavelength range has been restricted to 9000 \AA in order to avoid the problematic FeH band. The mismatch of the FeH band is still recognizable in the fits of both setups, which implies a systematic problem in the description of the FeH band. In the modern1 setup, the mismatch is decreased with increasing effective temperature which explains the high derived values of T_{eff} . However, it has not been the aim of these synthetic spectra to describe this molecular band but to study the effect of the resonance alkali lines.

Kirkpatrick (2005) has studied observationally whether the spectral sequence is a T_{eff} sequence. Depending on the wavelength range of the observational data, he has found a rather monotonic, decreasing dependence for the optical range (except for early T dwarfs) and for the near infrared data, a plateau for mid-type L to mid-type T dwarfs. Furthermore, there is large variety of T_{eff} , from 1200 K to 1750 K of the L8 dwarfs in the optical sample by Kirkpatrick (2005). This could be the reason for the multiple possible T_{eff} describing the L8 dwarfs satisfactorily.

The high values of $\log(g)$ in Table 8.1 confirm that the objects in the sample are not young and are well contracted (Schweitzer et al. 2002). Nevertheless, the main purpose of the fitting has been the evaluation of the fitting quality of the two setups and not the derivation of the exact stellar parameters.

Often, there is an improvement in the descriptions of the observations in Figs. 8.1–8.6, when using the modern1 setup. Spectra with the impact setup show generally less flux in the KID_1 far line wing, see Figs. 8.1, 8.2, and 8.4–8.6. Also, between 8400 \AA and 9000 \AA , the impact spectra show a strong absorption feature in flux which does not match with the observations, see Figs. 8.2–8.6. This feature is not (if at all much weaker) present in the modern1 spectra. Synthetic, spectral

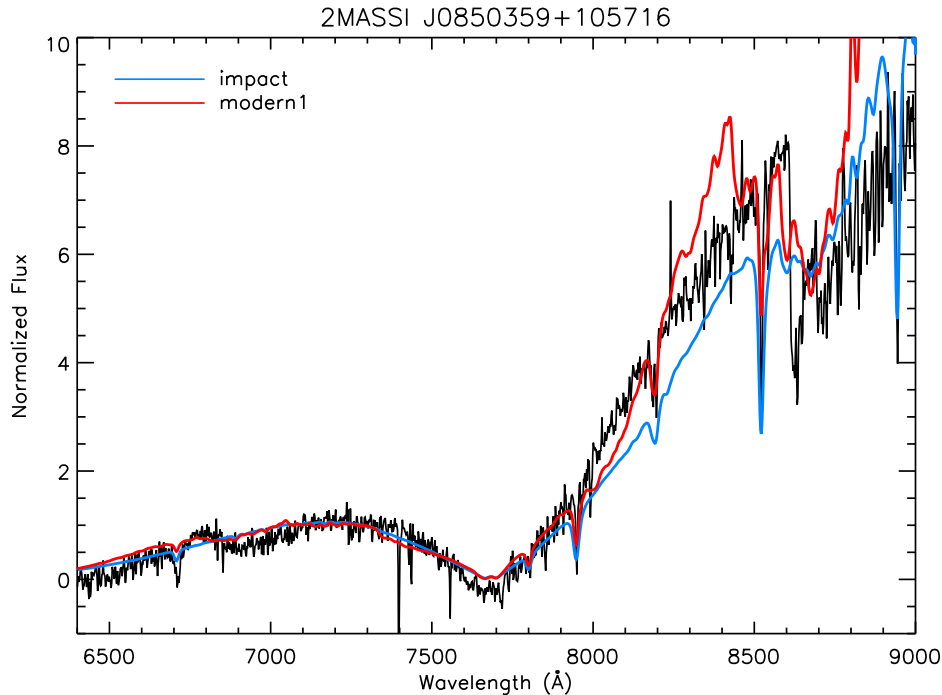


Fig. 8.1: Fits with the impact and modern1 setup to the optical spectrum of 2MASS J0850359+105716 (black line). See Table 8.1 for parameters.

features between the central wavelengths of the K I doublet can be observed when using the impact setup (especially towards $T_{\text{eff}} \geq 1400$ K) which are not present in the spectra of modern1 setup and which do not correspond with the observations, see Fig. 8.4 and also Schweitzer et al. (2002). With the modern1 spectra, a much smoother fit of K I and its D₁ far line wing is possible. A very good description of 2MASSW J0929336+342953 in Fig. 8.3 is obtained with the impact setup.

For SDSS 162414+0029, the fit done in Allard et al. (2003) has been repeated with the same stellar parameters, see Table 8.1. Liebert et al. (2000) have used similar parameters: $T_{\text{eff}} = 1100$ K and $\log(g) = 5.0$. In Fig. 8.7, the KID₁ line and its far line wing of the T6 dwarf is shown. The modern1 setup fits the observation of SDSS 162414+0029 extremely well whereas the impact setup provides only a poor description.

8.2 Results for High Resolution Spectra

The stellar parameters of a sample with a resolution of $\lambda/\Delta\lambda = 30000$ are listed in Table 8.2. It is a sample of late-type M and early-type L dwarfs provided by A. Reiners and G. Basri. Only selected observed alkali lines of each observation are presented. The focus is still on the test of the setups and not on the derivation of the stellar parameters. A grid of DUSTY spectra of each setup for $T_{\text{eff}} = 1800$ K to 2300 K with a step size of 100 K and $\log(g) = 4.5$ to 5.5 with a 0.5 dex step size has been used. The fits are done with the χ^2 -method, which is already used in Sects. 7.2 and 8.1. They are shown in Figs. 8.8–8.16. T_{eff} and $\log(g)$ depend on the setup and on the alkali line. As already mentioned in Sect. 8.1, the derived effective temperatures do not correlate with the spectral type, see also Schweitzer et al. (2001). The error bars are the same as before. There are deviations between the derived stellar parameters for the various alkali lines of an observation.

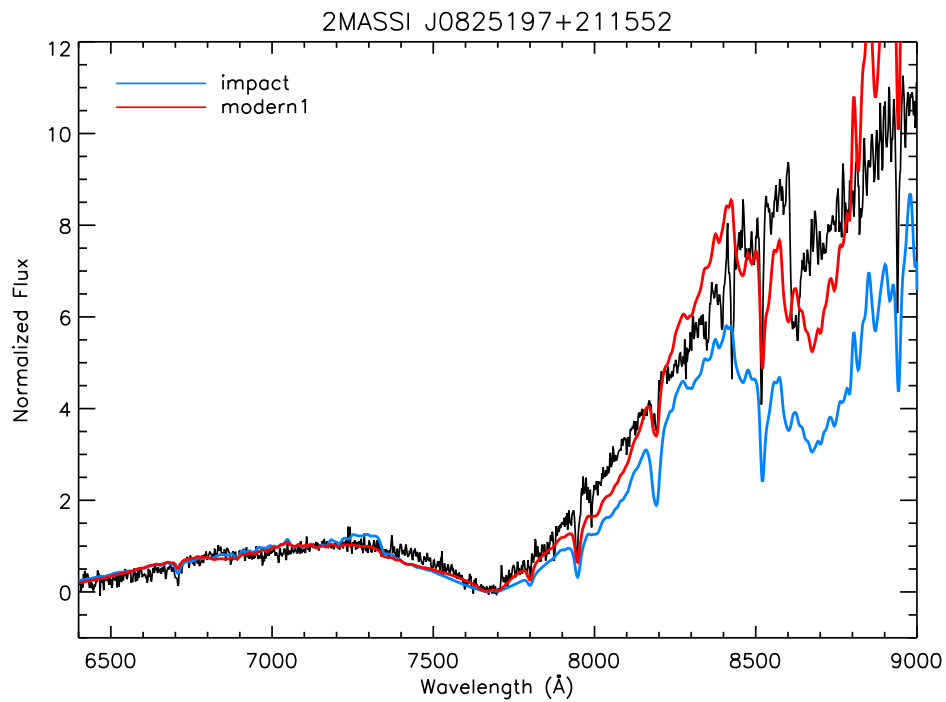


Fig. 8.2: Same as Fig. 8.1, but for 2MASS J0825197+211552.

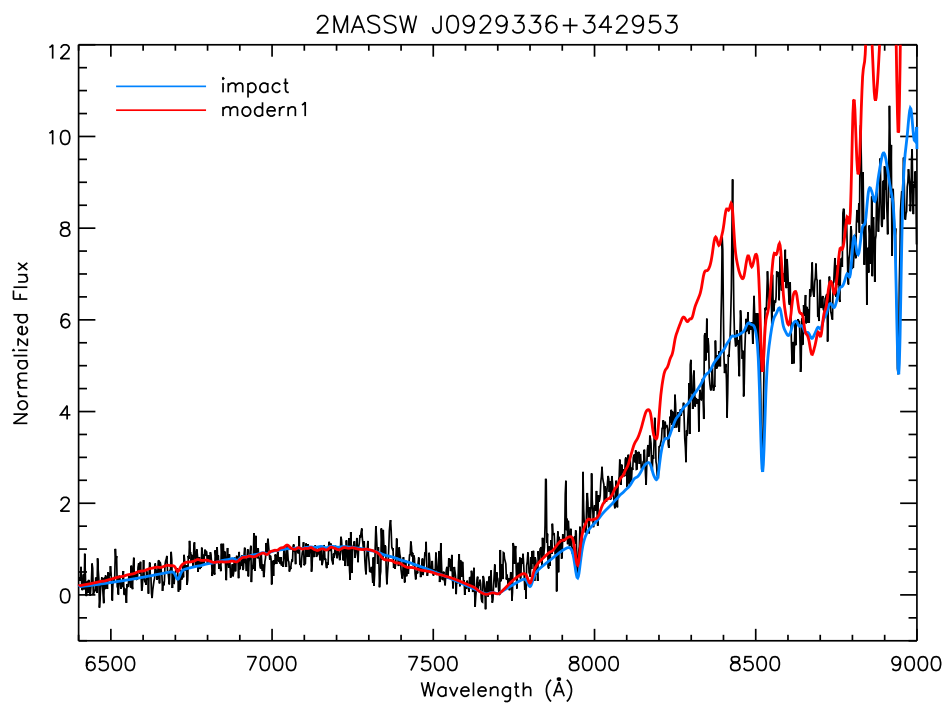


Fig. 8.3: Same as Fig. 8.1, but for 2MASSW J0929336+342953.

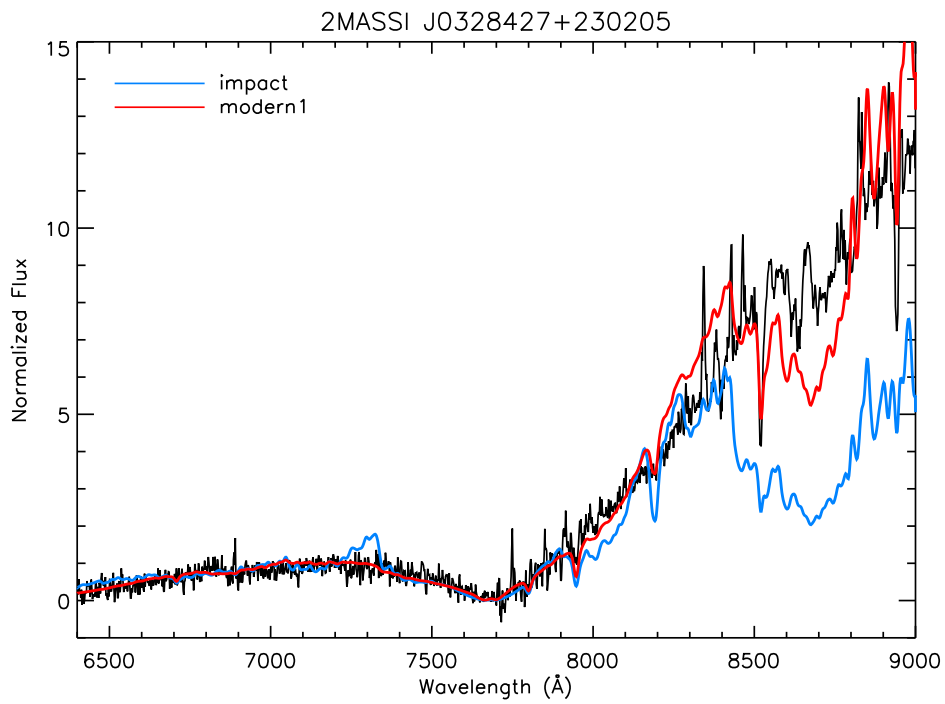


Fig. 8.4: Same as Fig. 8.1, but for 2MASS J0328427+230205.

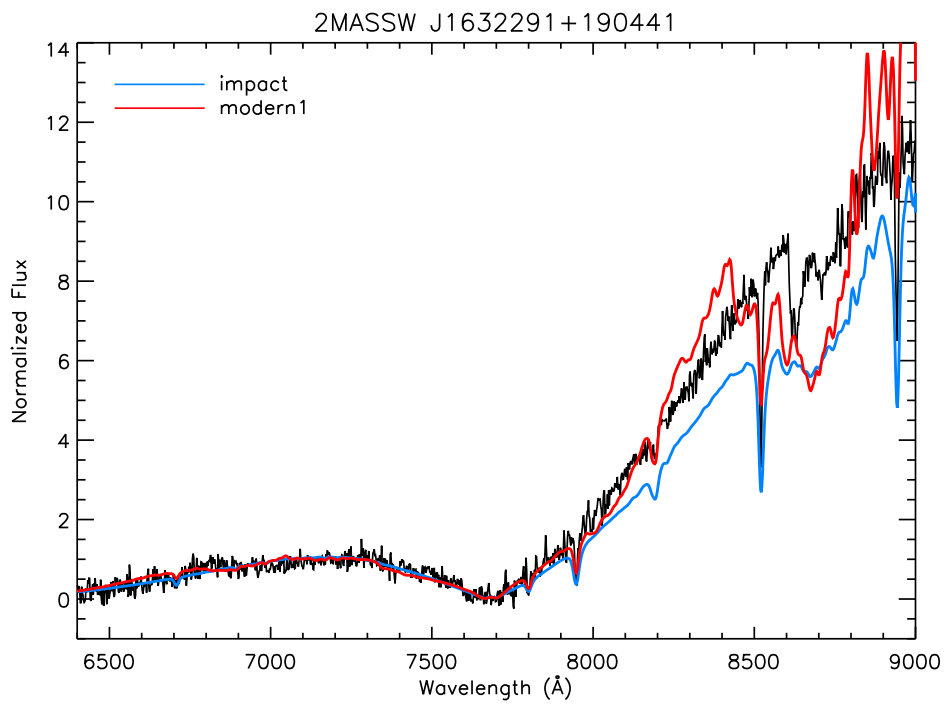


Fig. 8.5: Same as Fig. 8.1, but for 2MASSW J1632291+190441.

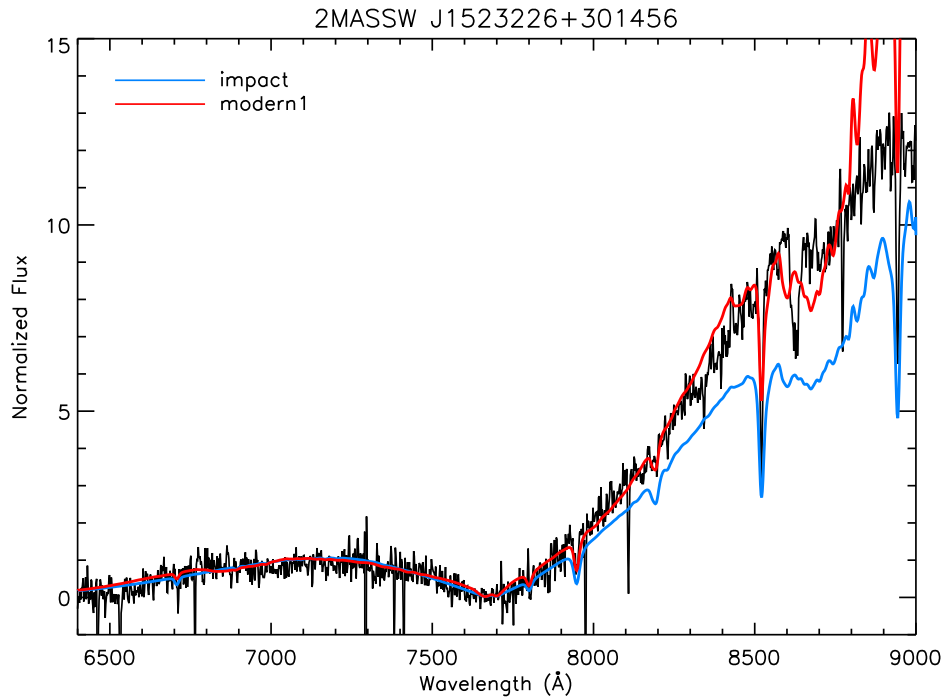


Fig. 8.6: Same as Fig. 8.1, but for 2MASSW J1523226+301456.

Name	Alkali Line	Spectral Type	Impact Setup		Modern1 Setup		Fig.
			T_{eff} (K)	$\log(g)$	T_{eff} (K)	$\log(g)$	
LP 944-20	Li I	M9 ^a	2200	5.5	2200	5.5	8.8
LP 944-20	K I	M9	2000	5.5	2000	5.5	8.9
LP 944-20	Rb ID ₁	M9	1800	4.5	1900	5.0	8.10
DENIS-P J033411-495333	K I	M9 ^b	2200	4.5	2200	4.5	8.11
2MASS J23515044-2537367 ^c	K I	M9 ^d	2000	5.0	1900	4.5	8.12
2MASS J2351-25	Rb ID ₂	M9	2000	5.5	2100	5.5	8.13
2MASS J2351-25	Rb ID ₁	M9	2000	5.5	2000	5.5	8.14
2MASS J14392836+1929149	Rb ID ₂	L1 ^e	2200	5.5	2200	5.5	8.15
2MASS J14392836+1929149	Rb ID ₁	L1	2200	5.5	2200	5.5	8.16

^aTinney (1998); Basri et al. (2000); Reiners (2006)

^bPhan-Bao et al. (2006); Reiners (2006)

^calso known as SSSPM J2352-2538.

^dLodieu et al. (2005); Reiners (2006)

^eBasri et al. (2000); Golimowski et al. (2004); Reiners (2006)

Table 8.2: High resolution sample with derived stellar parameters.

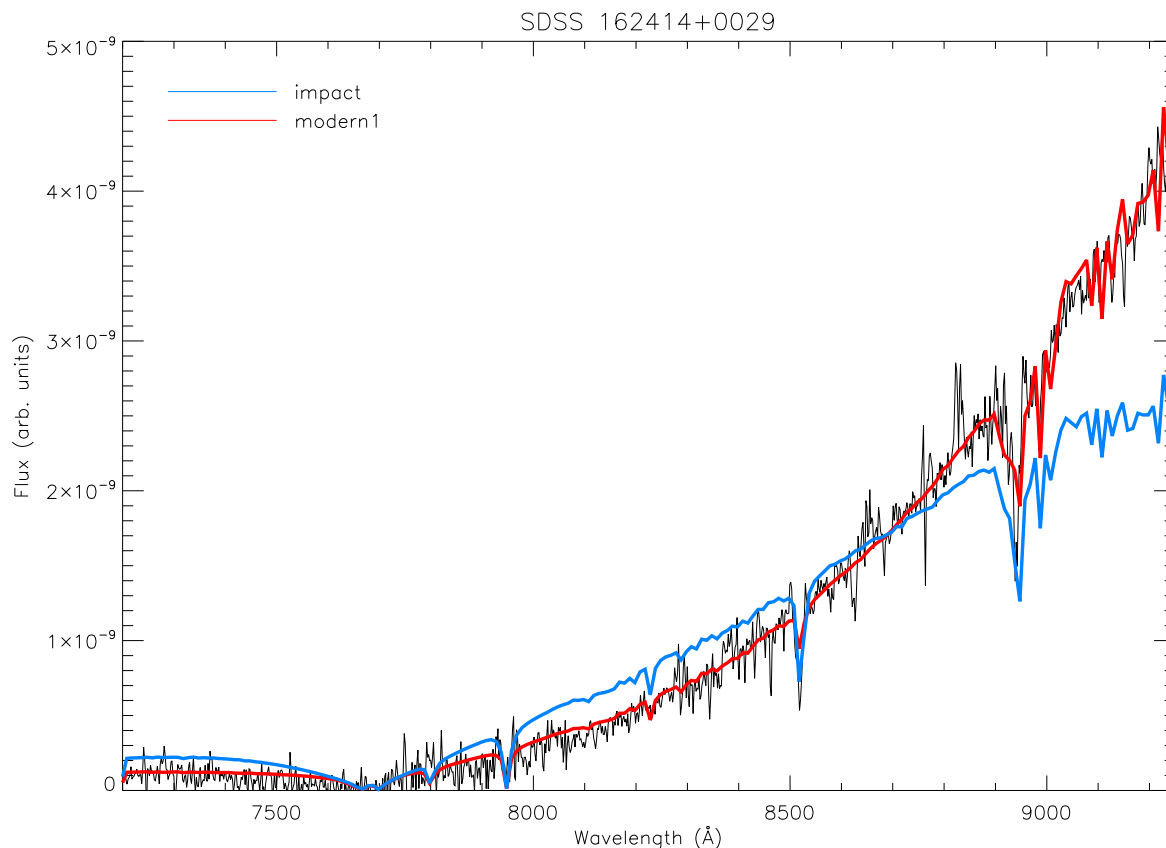


Fig. 8.7: Same as Fig. 8.1, but for SDSS 162414+0029 with a resolution $\lambda/\Delta\lambda$ of 5000.

Schweitzer et al. (2001) report the same problem.

LP 944-20 shows the Li I doublet. Previous analyses have been done studying its abundance. In Fig. 8.8–8.10, fits for LP 944-20 are shown. The Li I doublet has been fitted with a lithium abundance of $\log(\epsilon) = 1.7$. Note that Tinney (1998) found $\log(\epsilon) = 0.5$ and Pavlenko et al. (2007) obtained $\log(\epsilon) = 3.25$, so that there is a large spread in its Li I abundance in the literature. The modern1 Li I doublet is slightly deeper than the one with the impact setup and hence describes it slightly better. Also, the modern1 fit provides an improved description of the K I D₁ far line wing compared to the impact fit due to the stronger opacity provided by the K I profiles of the modern1 setup. Both setups fit the Rb D₁ of LP 944-20 line satisfactorily.

In general in Figs. 8.10–8.16, the fits with the impact and modern1 setup are of similar good quality. There are only small differences in details but mostly in favor for the modern1 setup. Nevertheless, the good description of the Li I and Rb I lines is not surprising since they are alkalis with relatively low concentrations. Only their line cores are visible so that their absorption features are not as characteristic as of the Na I D and K I doublets. The K I D₁ lines in Figs. 8.11 and 8.12 are provided only very limited in their wavelength range so that the complete D₂ line and the D₁ far line wing are missing. In this small wavelength range, considering also the relatively low signal-to-noise ratio of the observation of 2MASS J2351-25, the descriptions with the fits are satisfying.

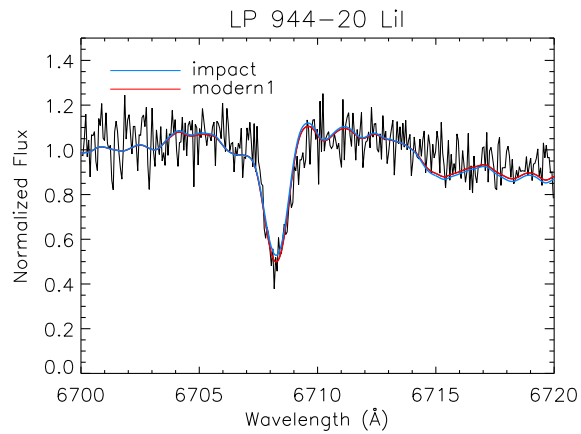


Fig. 8.8: Fits (with a Li I abundance of $\log(\epsilon) = 1.7$) with the impact and modern1 setup of the Li I doublet of LP 944-20 (black line). See Table 8.2 for parameters.

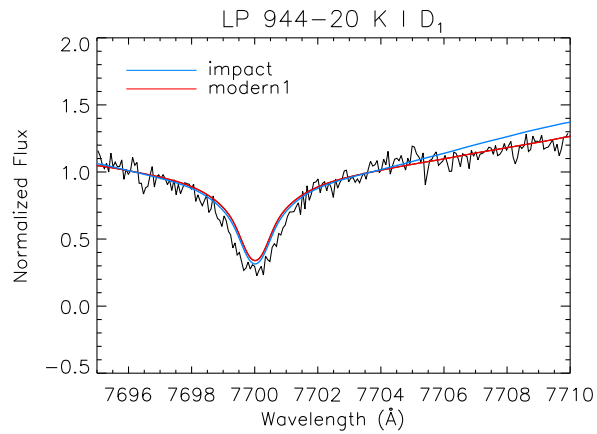


Fig. 8.9: Same as Fig. 8.8, but for the K I D₁ line of LP 944-20.

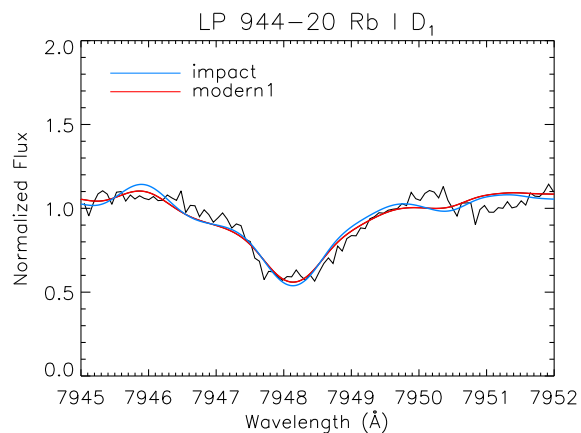


Fig. 8.10: Same as Fig. 8.8, but for the Rb I D₁ line of LP 944-20.

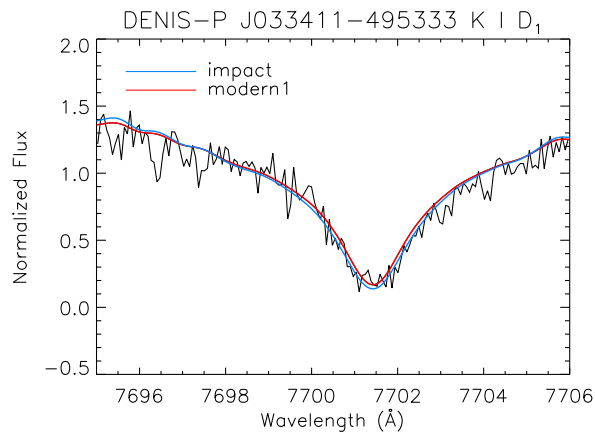


Fig. 8.11: Same as Fig. 8.8, but for the K I D₁ line of DENIS-P J033411-495333.

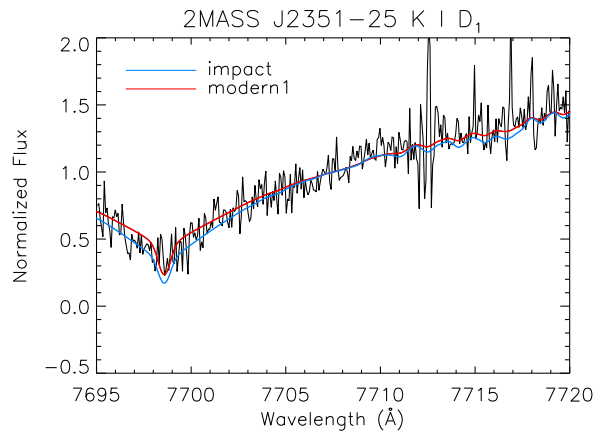


Fig. 8.12: Same as Fig. 8.8, but for the K I D₁ line of 2MASS J2351-25.

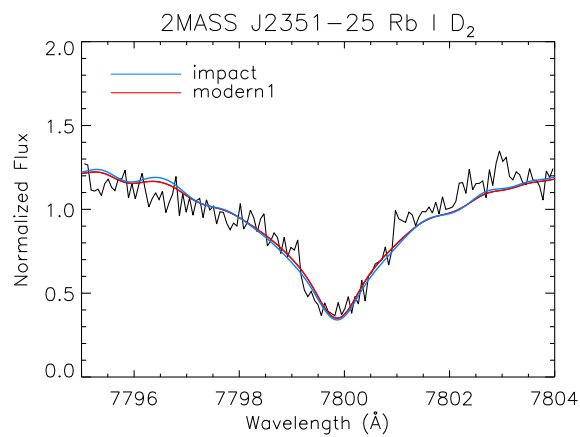


Fig. 8.13: Same as Fig. 8.8, but for the Rb I D₂ line of 2MASS J2351-25.

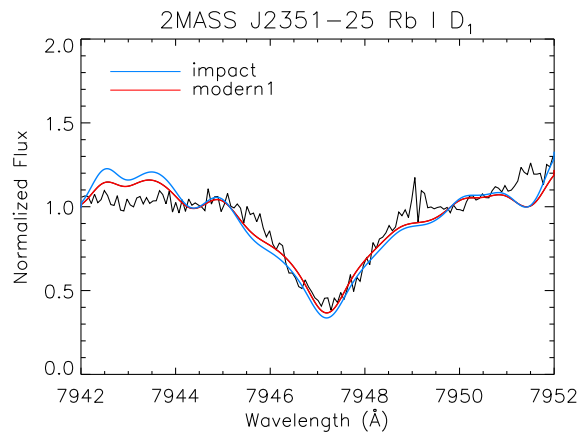


Fig. 8.14: Same as Fig. 8.8 but for the Rb I D₁ line of 2MASS J2351-25.

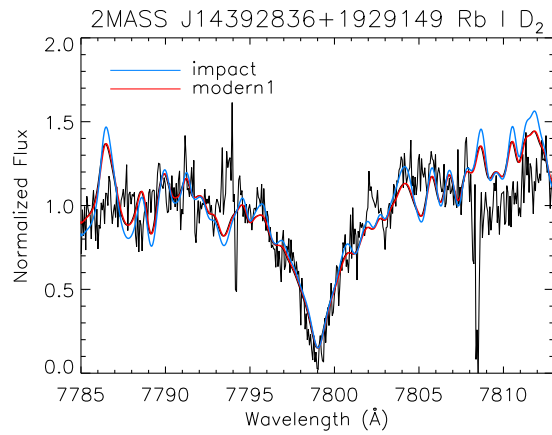


Fig. 8.15: Same as Fig. 8.8, but for the Rb I D₂ line of 2MASS J14392836+1929149.

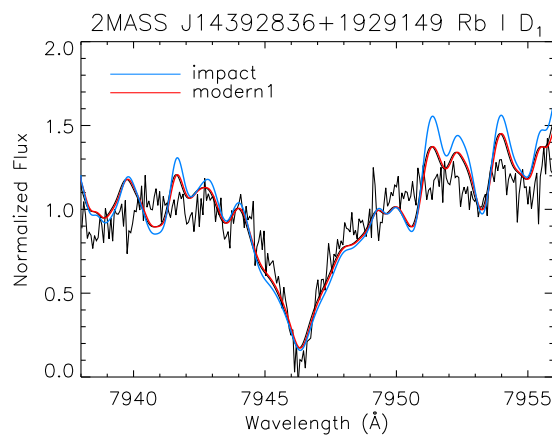


Fig. 8.16: Same as Fig. 8.8, but for the Rb I D₁ line of 2MASS J14392836+1929149.

8.3 Conclusion

With regard to an improved description of observations, the impact setup and modern1 setup have been tested. The results obtained with the modern1 setup represent the results for any “modern” setup. As already implied in Sect. 7.2 and shown in Sect. 8.2 for the alkalis with lower concentration, i.e., Li I and Rb I, the impact setup is a very good approximation in the cool dwarf regime. Their far line wings are masked by the Na I D and K I far line wings and by molecular bands so that only their line cores are showing through the atmosphere. The modern setup works very well, too. However, the availability of the non-analytical profiles, also in terms of the various perturber species, is restricted to the presence in the literature. Nevertheless, details in the Li I and Rb I lines are often described better by the modern setup.

The usage of the modern setup becomes important for the K I doublet and its D₁ far line wing, especially towards later spectral types, see Sect. 8.1. This implies that it is also very important for the Na I D doublet. It is best visible for the T6 dwarf in Fig. 8.7. Hence the cooler the objects and the higher the concentration of the alkalis are, the more important becomes the application of the modern setup.

There is a spread in the derived effective temperatures between the impact and modern1 setup. The correlation between the derived effective temperatures and the spectral type must be improved. Furthermore, the modern1 setup implies higher effective temperatures. This must be studied in more detail by more comparisons to observations in future work. Another future aspect is the test of DRIFT models, see Chap. 6, on the low resolution observations.

9 Line Profiles for Stark Broadening

In the previous chapters, pressure broadening is represented by van-der-Waals broadening which is the main broadening process in cool, dense atmospheres. Towards higher effective temperatures, matter in the stellar atmosphere is mostly ionized. As long as the densities are high enough to sustain pressure broadening, Stark broadening is the dominant pressure broadening mechanism and plays a non-negligible role in the calculation of opacities. It is the main broadening mechanism for stars of the spectral type G and earlier. Charged particles close to an absorbing atom or ion can broaden the lines in the spectrum. In the laboratory, this has been found first by Johannes Stark: “One can broaden spectral lines without raising the temperature by increasing the density of the luminous vapor. This type of spectral line broadening does not arise from the conditions of the Doppler effect, but probably through a force which deforms the emitting atom or ion, hence altering the period of the emitted spectral lines” (Stark 1906b,a). Especially for main sequence stars with $T_{\text{eff}} \gtrsim 5000$ K, Stark broadening with electrons is predominant because hydrogen is increasingly ionized and the density of free electrons is strongly increased. They are the dominant perturber species.

M. S. Dimitrijević and S. Sahal-Bréchet have calculated non-analytical Lorentzian Stark profiles for atoms and ions broadened by collisions with charged particles, i.e., with electrons, protons, He III and sometimes also other ions. A semi-classical perturbation approach developed by Sahal-Bréchet (1969a,b) has been applied for the profile calculations of isolated lines. The densities of free electrons and protons outweigh the density of the other perturber species in atmospheres for which Stark broadening has to be considered. The results with electrons as perturbers are of interest here since they are the dominant collision partners. Due to the higher mass of protons, their velocity is smaller and hence less collisions with them as perturbing particles occur. Non-analytical Stark profiles with Lorentzian FWHMs and shifts are provided for various temperatures and electron densities.

Sect. 9.1 gives a short introduction of the theoretical background of Stark broadening. In Sect. 9.1.1, the analytical approximation, which has been used for Stark broadening in PHOENIX so far, is briefly described. The theoretical background of the new Stark profiles provided by M. S. Dimitrijević and S. Sahal-Bréchet is outlined in Sect. 9.1.2. In Sect. 9.2, the new, non-analytical Stark profiles are introduced. The influence of the Stark profiles in synthetic spectra on the example of Ca I is shown in Sect. 9.3. A conclusion is given in Sect. 9.4.

9.1 Theoretical Background of Stark Broadening

Stark broadening is another type of pressure broadening. It describes the broadening mechanism of atomic / ionic transitions due to the Coulomb interaction of the particles in a plasma.

Stark broadening can be explained with two limiting cases (Spitzer 1940; Büscher 2000). If the velocities of the perturbers are large, the impact approximation resulting in a Lorentzian profile can be applied, see Chap. 2.

This is the case when considering free electrons as perturbing particles. They have a much smaller mass and thus have higher velocities at the same energy than ions. Therefore, for perturbations with free electrons, the impact approximation is used. It is valid for weak collisions, see Sect. 2.1.3.

The second limiting case is for sufficiently small perturber velocities, so that the quasi-static approximation gives the line profile (Holtzmark 1919a). If the quasi-static approximation is made, the Stark splitting of the considered line has to be calculated. In hydrogenic atoms, it is due to the linear Stark effect, in other atoms, it is due to the quadratic Stark effect for small fields and because of the linear Stark effect for large ones (Baranger 1962)¹. Furthermore, the electric field distribution must be known, which has been calculated for example by Holtzmark (1919a).

Ions are much heavier than electrons which results in much smaller velocities. Thus the quasi-static approximation is used for the broadening by ions. However, the validity of the quasi-static approximation, considering ions as perturbing particles, is not always granted (Baranger 1962), e.g., the motion of an ion can only be neglected if the line splitting of the emitting particle caused by the electric field of the perturbing ion is much larger than the inverse of the ion collision time, otherwise Fourier components are introduced into the line shape (Spitzer 1940; Holstein 1950). Baranger (1962) concluded that as soon as the line splitting is larger than the inverse ion collision time, the quasi-static approximation is at least valid in the (far) line wings. Note, that if the line is emitted by an ion, the interaction between the emitting ion and perturbing ion needs to be taken into account (Lewis & Margenau 19598). Thus, the wings of the ion line are cut down by the Coulomb repulsion. For nonhydrogenic atoms broadened by ions, it can happen that for the line center neither the quasi-static nor the impact limit is valid for the perturbations by ions. For these atoms, the Stark splitting is smaller than in hydrogen. Here, the ion broadening is weaker than the electron broadening. An approximation following Griem et al. (1962) and Baranger (1962) can be made. Nevertheless for the nonhydrogenic atoms broadened by ions, the overall effect is small.

Summing up, the domain of the quasi-static approximation is the (far) line wing and the domain of the collisions with free electrons is the near line wing and line core (Cowley 1970). In the following sections, only Stark broadening by collisions with electrons is discussed, concerning the near line wing.

9.1.1 Approximation by Kurucz

Up to this work, internal, analytical Lorentzian Stark profiles have been considered in PHOENIX. They are derived by an approximation done by Kurucz (1979) following Peytremann who has done a fit to detailed calculations by Sahal-Br  chot & Segre (1971). The Lorentzian Stark damping constant, the HWHM, reads

$$\gamma_S = 10^{-8} n_{\text{eff}}^5 \cdot n_e, \quad (9.1)$$

where n_{eff} is the effective quantum number of the upper energy level and n_e the electron density. n_{eff} can be expressed by

$$n_{\text{eff}}^2 = \frac{\chi(\text{HI})}{E_{\text{ion}} - E_{\text{upp}}} Z^2, \quad (9.2)$$

¹There are two Stark effects: the linear and the quadratic Stark effect. Note that the magnetic analogue to the electric Stark effect is the Zeeman effect. Excited states of an atom being degenerated result in the linear Stark effect. The atom in the electric field has a permanent electric dipole moment. The energy of the dipole moment is proportional to the electric field strength and the shift in energy is proportional to R^{-2} .

The quadratic Stark effect causes a shift of the energy levels proportional to the square of the electric field strength and proportional to R^{-4} . The external electric field induces an electrical dipole moment due to reversed displacement of the atomic protons and electrons.

with $\chi(\text{HI})$ being the ionization or Rydberg energy of HI, E_{ion} the ionization energy of the ion, E_{upp} the energy of the upper level, and Z the charge of the ion. The derivation of this expression originates from the energy difference caused by the change of orbits during a transition.

Equation 9.1 is not valid for hydrogen like species.

9.1.2 Theory of Stark Broadening of Isolated Lines in the Impact Approximation

Only the principal ideas of the Stark broadening in the impact approximation by Sahal-Br echot (1969a,b) are outlined here, following Dimitrijevi c & Sahal-Br echot (1984). These profiles describe the near line wings. The complete calculation procedure is described in Sahal-Br echot (1969a,b). The quantum mechanical considerations done in Sect. 2.2 were also applied there. A semi-classical perturbation approach is used with the following approximations:

(a) the interaction potential of the perturbing electron is the electrostatic interaction potential between the perturbing electron, the active atomic electron and the atomic nucleus.

(b) The perturber is a classical particle. Its coordinates are known and time dependent. The perturber trajectory is not perturbed by the collisions. If the emitter is neutral, the perturber trajectory is rectilinear and if the emitter is ionized, the trajectory is hyperbolic. The perturbers do not interact with each other.

(c) The scattering matrix elements are developed up to the second order of perturbation theory.

Only if most of the collisions taken into account are weak², this semi-classical approach including the impact approximation is valid. That means that close (or strong) collision can be neglected. The validity criterion is $\Delta E/kT \ll 1$ (Sahal-Br echot 1969b), where ΔE is the energy difference between the interacting levels of the emitting atom and T is the temperature. The application of the impact approximation leads to a Lorentzian profile. The Lorentzian parameters, the FWHM $2\gamma_S$ and the shift η_S , are given by

$$2\gamma_S = N \int_0^\infty v f(v) dv \left(\sum_{j \neq i} \sigma_{ij}(v) + \sum_{j' \neq f} \sigma_{fj'}(v) + \sigma_{el} \right), \quad (9.3)$$

$$\eta_S = \int_0^\infty v f(v) dv \int_{R_3}^{R_d} 2\pi b db \sin 2\Phi_p, \quad (9.4)$$

where v is the relative velocity, $f(v)$ the Maxwellian velocity distribution, and b is the impact parameter of the perturber trajectory. i and f denote, respectively, the initial and final levels and j and j' the corresponding perturbing levels. $\sigma_{ij}(v)$ is the inelastic cross-section and is described by the impact parameter and the transition probability P_{ij}

$$\sum_{j \neq i} \sigma_{ij}(v) = \frac{1}{2} \pi R_1^2 + \int_{R_1}^{R_d} 2\pi b db \sum_{j \neq i} P_{ij}(b, v). \quad (9.5)$$

The elastic cross-section reads

$$\sigma_{el} = 2\pi R_2^2 + \int_{R_2}^{R_d} 8\pi b db \sin^2 \delta, \quad (9.6)$$

$$\text{with } \delta = (\Phi_p^2 + \Phi_q^2)^{1/2}, \quad (9.7)$$

$$\text{with } \Phi_p = \sum_{j \neq i} \Phi_{ij} - \sum_{j' \neq f} \Phi_{fj'}. \quad (9.8)$$

²The duration of a collision is small compared to the time in between collisions, see Chap. 2.

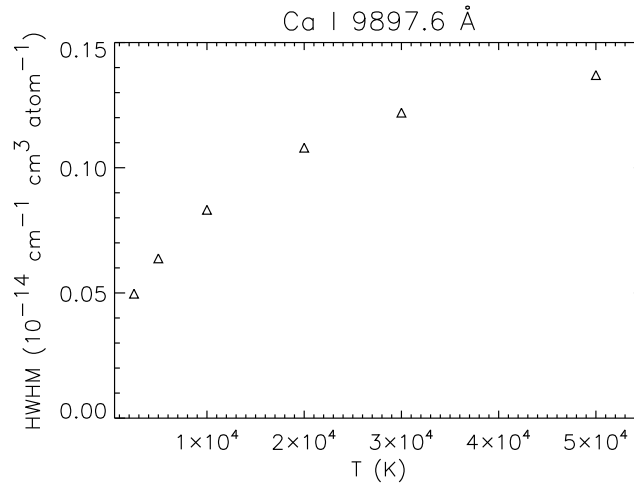


Fig. 9.1: Lorentzian HWHMs per perturbing electron of the Ca I absorption line at 9897.6 Å for $n_e = 10^{11} \text{ atom cm}^{-3}$.

Φ_p and Φ_q are phase shifts. The phase shift due to the polarization is $\Phi_p \propto r^{-4}$ and the phase shift due to the quadrupole potential is $\Phi_q \propto r^{-3}$, for details see Sahal-Bréchet (1969a) (Chap. 2, Sect. 3). The cut-off parameters R_1 , R_2 , and R_3 are determined in Sahal-Bréchet (1969b) (Chap. 3, Sect. 1). R_d is the Debye length taking into account Debye shielding which is one of the most important effects in plasmas in thermal equilibrium³.

M. S. Dimitrijević and S. Sahal-Bréchet (Dimitrijević & Sahal-Bréchet 1984) suggest to estimate the ion broadening contribution with the quasi-static ion broadening parameter (Griem 1974) introduced by Griem et al. (1962).

9.2 Non–Analytical Stark Profiles by M. S. Dimitrijević and S. Sahal-Bréchet

An overview of the new, non-analytical Stark profiles of the various species is given in Table 9.1. The data depends on the gas temperature and the electron density. In order to create the Stark profiles, the calculated multiplet transitions had to be matched with the transitions in the atomic databases with transitions known in PHOENIX. The transitions were either matched with the transitions of the “PHOENIX” database (it is the primary database and includes most atomic/ionic transitions by Kurucz & Bell (1995)) or the transitions of the “APED” database. The transition wavelengths provided in the tables by M. S. Dimitrijević and S. Sahal-Bréchet are given in Å with one decimal place. In PHOENIX, the transition wavelengths are derived by the energy difference of the transition. In order to identify uniquely the calculated multiplet lines, the agreement between the two sets of transition wavelengths had to be up to the first decimal place, otherwise an unambiguous assignment is impossible. Since the provided Lorentzian parameters, the FWHM and the shift, are given in Å, they must be converted into the units of the inverse wavelength per perturbing electron ($\text{cm}^{-1} \text{ cm}^3 \text{ atom}^{-1}$). For the FWHM the conversion into the HWHM is then $\gamma_S(1/\lambda_0) = 2\gamma_S(\lambda_0) \cdot 10^{-8} / (2 \cdot (\lambda_0 \cdot 10^{-8})^2 \cdot n_e)$ and analogue for the shift

³The Debye length is the “screening” distance, or the distance over which the usual Coulomb field is killed off exponentially by the polarization of the plasma.

Specie	Citation	Calc. Multiplets	Identified Lines	PHOENIX Database	T (K)	n_e (atom cm ⁻³)
Al XI	Dimitrijević & Sahal-Bréchet (1994)	7	7	APED	$5 \cdot 10^5 - 4 \cdot 10^6$	$10^{18} - 10^{23}$
Ba I	Dimitrijević & Sahal-Bréchet (1997)	14	3	PHOENIX	$2.5 \cdot 10^3 - 5 \cdot 10^4$	$10^{15} - 10^{18}$
C V	Dimitrijević & Sahal-Bréchet (1996)	25	59	APED	$5 \cdot 10^4 - 1 \cdot 10^6$	$10^{17} - 10^{22}$
Ca I	Dimitrijević & Sahal-Bréchet (1999)	189	63	PHOENIX	$2.5 \cdot 10^3 - 5 \cdot 10^5$	$10^{11} - 10^{19}$
Ca IX	Dimitrijević & Sahal-Bréchet (1998a)	4	3	APED	$2 \cdot 10^5 - 5 \cdot 10^6$	$10^{18} - 10^{22}$
Ca X	Dimitrijević & Sahal-Bréchet (1998a)	48	2	APED	$2 \cdot 10^5 - 5 \cdot 10^6$	$10^{17} - 10^{22}$
O IV	Dimitrijević & Sahal-Bréchet (1995)	5	2	PHOENIX	$2 \cdot 10^5 - 2 \cdot 10^6$	$10^{17} - 10^{22}$
O V	Dimitrijević & Sahal-Bréchet (1995)	19	21	PHOENIX	$2 \cdot 10^5 - 2 \cdot 10^6$	$10^{17} - 10^{22}$
P V	Dimitrijević & Sahal-Bréchet (1996)	51	21	PHOENIX	$5 \cdot 10^4 - 1 \cdot 10^6$	$10^{17} - 10^{22}$
Si XI	Dimitrijević & Sahal-Bréchet (1998b)	4	6	APED	$5 \cdot 10^5 - 4 \cdot 10^6$	$10^{18} - 10^{23}$
Si XIII	Dimitrijević & Sahal-Bréchet (1994)	9	9	APED	$5 \cdot 10^5 - 4 \cdot 10^6$	$10^{18} - 10^{23}$
Si XIII	Dimitrijević & Sahal-Bréchet (1998b)	61	41	APED	$5 \cdot 10^5 - 6 \cdot 10^6$	$10^{16} - 10^{23}$

Table 9.1: Overview of the new Stark profiles for PHOENIX.

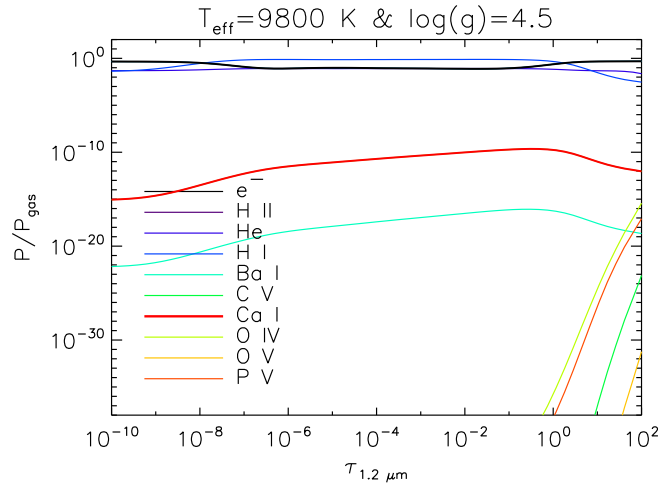


Fig. 9.2: Concentrations of the most important species in a model atmosphere of $T_{\text{eff}} = 9800$ K, $\log(g) = 4.5$, and solar composition.

$\eta(1/\lambda_0) = \eta(\lambda_0) \cdot 10^{-8} / ((\lambda_0 \cdot 10^{-8})^2 \cdot n_e)$. The HWHMs are increasing with increasing temperature (as the HWHMs in Chap. 9.2). In Fig. 9.1, the Lorentzian HWHMs per perturbing electron of the Ca I absorption line at 9897.6 \AA for an electron density of $n_e = 10^{11} \text{ atom cm}^{-3}$ are displayed. The information of the new Lorentzian Stark profiles, the HWHMs and the shifts, dependent on the temperature and electron density, is interpolated bilinearly in PHOENIX, for details see Appendix E.

9.3 The Influence of the Stark Profiles in Synthetic Spectra

As example of the application of Stark profiles, a model atmosphere with $T_{\text{eff}} = 9800$ K, $\log(g) = 4.5$, and solar composition has been chosen, representing a main sequence star of spectral type A.

The concentrations of the most important species are shown depth dependent in Fig. 9.2. Next to the concentration of the free electrons, the concentrations of H II (protons), He, and H I are plotted in order to underline the presence of the free electrons. The concentrations of most of the species listed in Table 9.1 are depicted also in Fig. 9.2. The species which do not appear in Fig. 9.2 but in Table 9.1 have a negligible concentration. Ca I is the species with the highest concentration in this model atmosphere for which there are new Stark profiles.

In Figs. 9.3, 9.5, and 9.7, as example three Ca I absorption lines at different wavelengths computed with the approximation by Kurucz (1979) and with the Lorentzian profiles by Dimitrijević & Sahal-Bréchet (1999) as well as the relative change of the flux are shown. A standard Ca I abundance of $\log(g) = 6.36$ has been assumed and the influence of any other atom or molecule has been neglected in order to point out just the effects in the Ca I absorption lines without any side effects of overlapping atomic lines. The influence of the new Stark profiles is only in the range of a few percent in the near line wings. The increased strength of the absorption lines due to the new Stark profiles is only hinted. A reason for the weakness of the effect is that although Ca I is the species with the highest concentration of the species listed in Table 9.1, its concentration is not very high over all. There are stronger Ca I absorption lines than those identified but no profiles are provided for them by M. S. Dimitrijević and S. Sahal-Bréchet. For other species with higher concentrations,

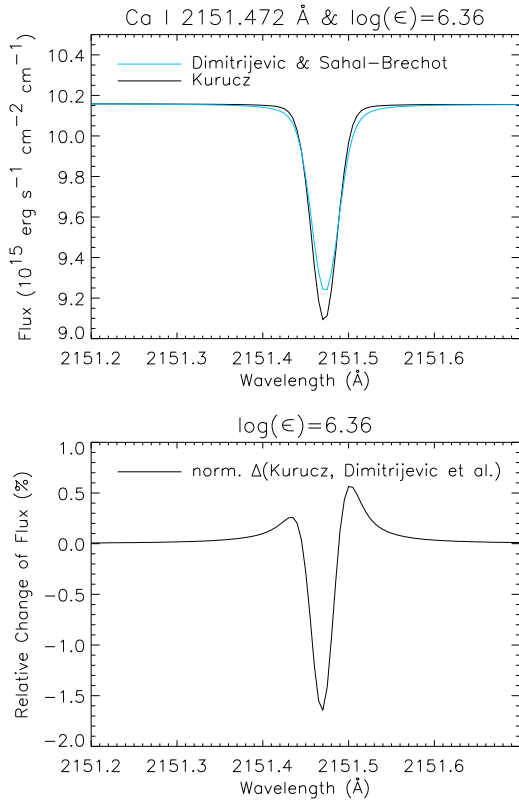


Fig. 9.3: Top panel: CaI absorption line at 2151.472 Å with an abundance of $\log(\epsilon) = 6.63$ at $T_{\text{eff}} = 9800$ K, $\log(g) = 4.5$, and solar composition. Bottom panel: relative change of the flux between the CaI absorption line computed with the approximation by Kurucz (1979) and the Lorentzian profiles by Dimitrijević & Sahal-Bréchet (1999).

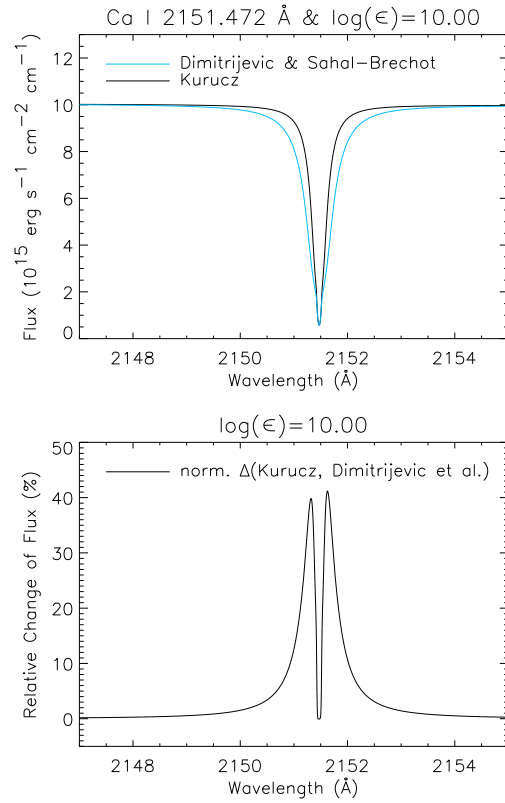


Fig. 9.4: Top panel: CaI absorption line at 2151.472 Å with an abundance of $\log(\epsilon) = 10.00$ at $T_{\text{eff}} = 9800$ K, $\log(g) = 4.5$, and solar composition. Bottom panel: relative change of the flux between the CaI absorption line computed with the approximation by Kurucz (1979) and the Lorentzian profiles by Dimitrijević & Sahal-Bréchet (1999).

no new Stark profiles are provided either.

For demonstration purposes, the logarithmic Ca I abundance has been increased to $\log(\epsilon) = 10.00$. The results with this higher Ca I abundance are displayed in Figs. 9.4, 9.6, and 9.8. Now, the influence of the new Stark profiles is easily visible. The absorption lines are stronger with the new Stark profiles than with the approximation by Kurucz (1979). The influence of the Lorentzian profiles covers the near line wings. It is noticeable that the two approximations are mostly alike in the Gaussian core (see Chap. 4).

Similar effects appear when studying the other species and comparing the Stark broadened absorption lines with the two different approximations.

9.4 Conclusion

The new Stark profiles by M. S. Dimitrijević and S. Sahal-Bréchet cause stronger absorption lines in synthetic spectra than the approximation by Kurucz (1979). The influence is visible in the near line wings. The new profiles can be used and tested on stars for which the provided lines are

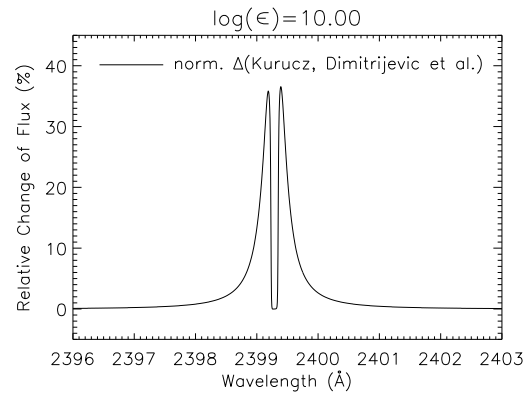
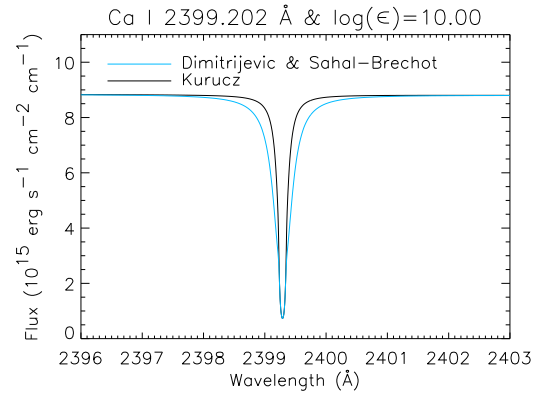
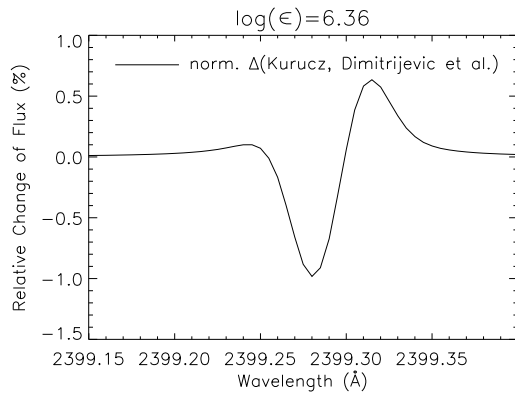
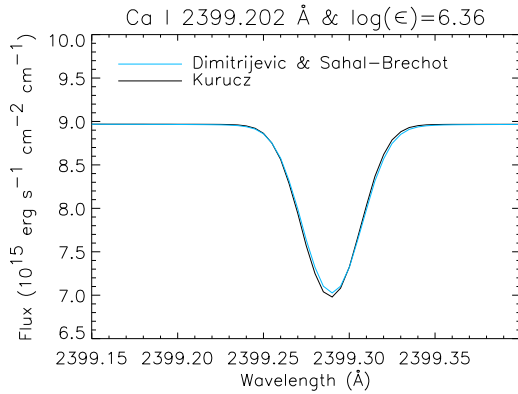


Fig. 9.5: Same as Fig. 9.3 with $\log(\epsilon) = 6.36$, but for the Ca I absorption line at 2399.202 \AA .

Fig. 9.6: Same as Fig. 9.4 with $\log(\epsilon) = 10.00$, but for the Ca I absorption line at 2399.202 \AA .

important, for example main sequence stars including planetary host stars. Furthermore, other Stark profiles, for example by Griem (1974), should be included and tested also considering the far line wings. The results have been obtained under the assumption that electrons are the most important perturber species. The availability of the data and the high density of protons in atmospheres for which Stark broadening is the most prominent pressure broadening mechanism, offers the opportunity to test the influence of Stark broadening by protons in future work.

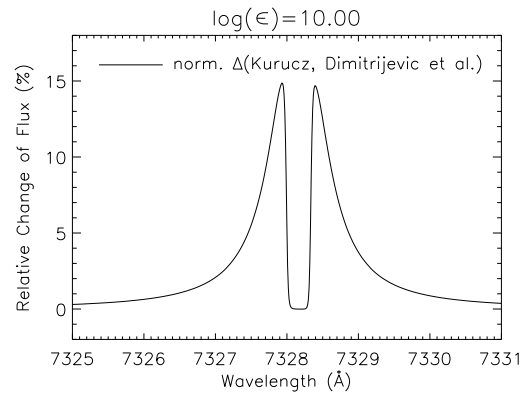
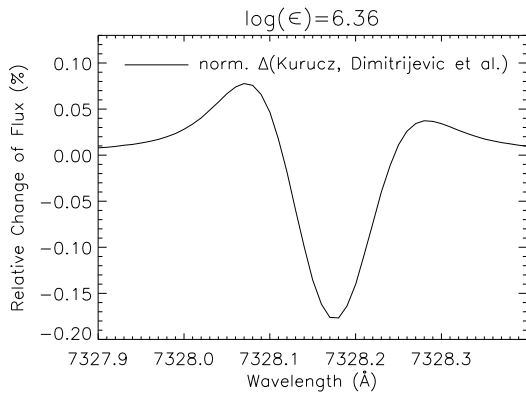
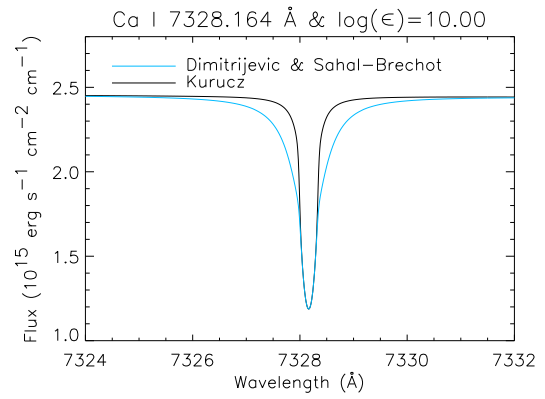
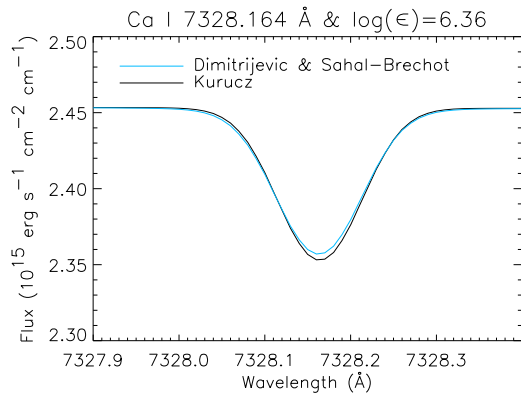


Fig. 9.7: Same as Fig. 9.3 with $\log(\epsilon) = 6.36$, but for the Ca I absorption line at 7328.164 \AA .

Fig. 9.8: Same as Fig. 9.4 with $\log(\epsilon) = 10.00$, but for the Ca I absorption line at 7328.164 \AA .

10 Summary and Outlook

10.1 Summary

Towards an improved description of observations, the goal of this work was to study the influence of line profiles in synthetic spectra. Throughout this work, the multi-purpose stellar atmosphere code PHOENIX has been used. For cool atmospheres, i.e., for atmospheres of late dwarfs, temperature dependent line profiles of the alkali resonance doublets Na I D, Li I, K I, and Rb I have been refined. The prevalent line broadening mechanism is van-der-Waals broadening with H₂, He, and H I as perturber species. Non-analytical alkali profiles for the far and near line wing with H₂ and He in the unified semi-classical theory have been added, as well as non-analytical He broadened Na I D, Li I, and K I near line wing profiles calculated in the fully quantum mechanical theory. It has been shown that the importance of H I broadened profiles increases towards $T_{\text{eff}} > 2000$ K. Therefore, non-analytical Na I D near line wing profiles perturbed by H I in the impact approximation have been included. The influence of these various alkali profiles in model atmospheres and synthetic spectra has been compared to the influence of the already existing analytical impact approximated van-der-Waals alkali profiles.

Stellar atmospheric structures and synthetic spectra for $1100 \text{ K} \leq T_{\text{eff}} \leq 3000 \text{ K}$, $\log(g) = 5.0$, and solar composition have been studied in respect of the various alkali profiles. In general, the T-p structures stay unchanged when including the new profiles. In the synthetic spectra, there are differences visible when considering the various alkali profiles. The size of the differences is dependent on the effective temperature, i.e., it is increasing towards lower effective temperatures. The new line profiles evoke stronger absorption lines in the synthetic spectra than the impact approximated profiles. This has been visualized in a study on the stellar parameters. The influence of the alkali profiles decreases towards $T_{\text{eff}} = 3000$ K and larger effective temperatures due to an decreasing gas density and molecular bands which are increasing in strength towards higher effective temperatures and masking the alkali absorption lines. Furthermore although the new alkali profiles become narrower towards lower effective temperatures, their influence increases in synthetic spectra towards lower effective temperatures because more broadening collisions occur due to an increasing gas density and the decreasing effect of the molecular bands due to condensation.

The strongest effect in the models and spectra is due to the far line wings of Na I D and K I whose profiles are calculated in the unified semi-classical theory. Next to the molecular bands of TiO and VO, they belong to the main contributors of the pseudo continuum.

Near line wings of Na I D broadened by H I have only a small influence on synthetic spectra. The two theoretical approaches for He broadened near line wing profiles provide very similar results so that they confirm each other. Larger differences in the synthetic spectra are expected if there would be a comparison including far line wing profiles calculated in each theoretical approach. Because of the small differences between the line profiles calculated in more sophisticated theories than the impact approximated van-der-Waals profiles, the following studies have been continued with the line profiles calculated in the unified semi-classical approximation, representing the all new non-analytical line profiles, hereafter called the new line profiles.

Another topic in this work has been the influence of different dust treatments on the alkali resonance absorption lines. Atmospheres in the DUSTY and DRIFT approximation have been studied as well as their synthetic spectra. The line shape of the alkali resonance lines is more dependent on the dust treatment than on the underlying line profiles. The alkali absorption doublets are generally stronger in the DRIFT spectra than in the DUSTY spectra, but there are no significant differences between the alkali lines computed with the impact approximated or new line profiles.

As application of the alkali line profiles, the Li I abundances of very low mass objects of Chamaeleon I have been determined for the first time. At the same time, it has been a test of the new profiles and the impact approximated van-der-Waals profiles. The very low mass Chamaeleon I objects are described satisfyingly by the synthetic spectra with both line profile setups.

Since the studied Cha I members are objects of spectral type late M, there have been more tests on selected observations, high and low resolution spectra, of objects of later spectral type (from M9 to T6). Other alkali resonance lines than the Li I lines have been inspected. As already noticed in Schweitzer et al. (2001), the fits of different spectral lines provide different stellar parameters. Another influence on the derived stellar parameters is found in the applied alkali line profiles. Generally, the derived stellar parameters differ for all studied objects so far when using the two different line profile setups. This has already been noticed in the fits of the Li I doublet of the Cha I objects. The fits with the new profiles result in higher effective temperatures and surface gravities. This effect must be studied further in future work, so that there might be an adjustment of the temperature scale necessary when describing observations of late spectral type with PHOENIX spectra.

In the observations of later spectral type, the alkalis with a lower concentration, i.e., Li I, and Rb I are described very well with the impact approximated profiles and the new line profiles. Because of the strong molecular bands and the overlap by the far line wings of the Na I D and K I doublets, only their line cores are visible. Thus, the far line wings of these alkalis are of minor importance. However, the description of details of these alkali doublets is often improved when fitting synthetic spectra computed with the new line profiles. The usage of the new line profiles becomes more important for the two doublets of the alkalis with the highest concentration, namely Na I and K I. The descriptions of the K I D₁ absorption line of these later objects with the synthetic spectra including the new profiles are improved, especially for the observations of later type. Altogether, the impact profiles are a good approximation, especially towards higher effective temperatures. But towards later spectral types, in the L and T dwarf regime, the application of the new line profiles, especially of the dominating K I (and Na I D) doublet, in synthetic spectra results very often in an improved description.

Up to this work, Stark broadening has been considered applying an analytical impact approximation for collisions with electrons by Kurucz (1979). A new set of non-analytical line profiles has been included with Lorentzian Stark profiles, which are calculated also under the assumption of the impact approximation and that collisions occur with electrons. The new Stark profiles for Al XI, Ba I, C V, Ca I, Ca IX, Ca X, O IV, O V, P V, Si XI, Si XII, and Si XIII have been provided by M. S. Dimitrijević and S. Sahal-Bréchet. Their Lorentzian constants, the HWHMs and the shift, are provided temperature and electron density dependent and interpolated accordingly. Compared to the already existing analytical approximation for Stark profiles by Kurucz (1979), the new Stark profiles cause stronger absorption lines in the synthetic spectra. Their application is in model atmospheres and synthetic spectra of those hot stars, which exhibit pressure broadening, e.g. main sequence stars and white dwarfs.

Summing up, spectral line profiles do make a difference in the description of the stellar spectra.

They are of fundamental importance when describing stellar objects.

It is still a challenge to observe spectra of objects of (very) late spectral type in the shorter, optical wavelength range. However, these observations are of significance for the tests of the line profiles of the two most important alkalis, Na I and K I, in order to deepen the understanding of line formation processes in these cool objects.

The detailed modelling of pressure broadened spectral lines can be applied for example when distinguishing between stellar and non-stellar, i.e., very low mass and planetary, components in a combined spectrum of a host star and its companions. For example, the measured line strength of Na I D could be an indicator for the components of the system.

10.2 Outlook

Cool Atmospheres

For an improved modelling of the alkali resonance lines, more line profiles need to be calculated. So far, the far line wing profiles perturbed by H₂ and He are only calculated in the unified semi-classical theory, but not in the fully quantum mechanical theory. A larger influence in synthetic spectra is expected if also alternative far line wing profiles are included.

Up to now, only two symmetries of the H₂ molecule are taken into account. Accordingly, the calculations should be done for more symmetries, since H₂ is the perturber species with the highest relative concentration in cool atmospheres.

The perturbations by HI should be also considered in the non-analytical line profile calculations. This includes the calculation of HI perturbed far line wing profiles which are missing so far.

Helium broadened far line wing profiles of Na I D, Li I, and K I have been calculated by (Zhu et al. 2005, 2006). Satellites are also visible in their line profiles which would lead to further studies on these absorption features. A future project is the collaboration with C. Zhu and his colleagues in order to include their profiles in the opacity calculation of PHOENIX (Babb 2007).

Of course, any other appropriate, new line profile should be also included, not only temperature dependent but also dependent on the perturber density.

Further studies on observations of late dwarfs (also with future telescopes) are necessary to test and improve the description of the Na I D and K I doublets. The application of the alkali line profiles should be considered when studying extrasolar planets. Alkalis could be an opacity source in these atmospheres, see for example the extrasolar planet HD 209458b. Charbonneau et al. (2002) reported first the sodium detection. However for this close-in extrasolar giant planet, irradiation and NLTE effects need to be taken into account (Barman et al. 2002; Barman 2007) so that alkali profiles with electrons as perturbing particles might be needed. The present alkali profiles might be useful for a planetary host star system with a large orbital distance.

Furthermore for improved synthetic spectra of very low mass objects and brown dwarfs (and extrasolar planets), the dust treatment and its influence on the alkali lines need to be studied in more detail.

Hot Atmospheres

The two approaches for Stark broadened spectral lines need to be tested on observations. Stark profiles of other species and obtained by other theoretical approaches, for example by Griem (1974), should be included in the opacity calculations of PHOENIX. Since the relative concentration of

protons is as high as the one of electrons and the Stark broadened profiles are supplied also for collisions by protons, it is an opportunity to test the influence of the Stark broadening by protons, too.

A Alkali Profile Data

In Sect. 3.5, the various Na I D profiles have been compared. Now, there is the comparison of the various profiles of Li I, K I and Rb I perturbed by H₂, see Figs. A.2–A.7.

In Figs. A.2–A.3, the far line wing profiles of K I, Li I, and Rb I perturbed by H₂ and He are shown. (Figure A.1 shows for completeness the far line wings of Na I D.) The discussion is similar as for the far line wing profiles of Na I D, see Sect. 3.5.

In Fig. A.6, the H₂ broadened HWHMs of K I and Li I are presented. The calculations for K I are done for temperatures up to 6000 K. The new data set describing the K I D₁ line (Allard et al. new) provides smaller HWHMs for both symmetries of H₂. For temperatures from 500 K to 3000 K, the HWHMs by Allard et al. new are between 24.9% and 7.7% smaller when considering H₂ C_{2v} as perturber compared to the data by Allard et al. 2003. The relative change with perturbations by H₂ C_{∞v} is even larger. The new HWHMs are between 36.4% (3000 K) and 42.2% (1000 K) smaller.

The HWHMs of K I D₂ perturbed by H₂ in both symmetries by Allard et al. new are always larger than the ones from 2003. The relative changes of the K I D₂ HWHMs are larger for H₂ C_{2v} as perturber than for H₂ C_{∞v}, namely between 37.9% (500 K) and 44.1% (2000 K). Relative changes between 7.3% (1000 K) and 11.8% (3000 K) exist for collisions with H₂ C_{∞v}.

The HWHMs of the Li I and Rb I doublets in Fig. A.6 are newly calculated by N. Allard so that there is no comparison possible.

As already mentioned in Sect. 3.2, the Li I and Rb I data perturbed by He exist only in the new version of N. Allard's calculations, see Figs. A.8 and A.9. There is also He broadened Li I data by Mullamphy et al. 2006. Their D₁ results are between 6.0% (500 K) and 9.6% (3000 K) larger than the new HWHMs by N. Allard whereas for the D₂ Li I line, their results are between 16.8% (3000 K) and 18.5% (1000 K) smaller.

When comparing the He broadened K I D₁ line damping constants by Allard et al. 2003 and Allard et al. new, again large changes between 32.3% (2000 K) and 46.8% (1000 K) are apparent (in favor of the data set from 2003). The relative change between the Allard et al. new data and the data by Mullamphy et al. 2006 amounts in only 2.0% for 500 K and up to 21.2% for 3000 K. Again the results of the Allard et al. new data are of smaller magnitude. For the K I D₂ line, the comparison between the Allard et al. new and the Allard et al. 2003 data shows a relative change between 1.8% (500 K) and 4.9% (2000 K) and respectively for the comparison between the new data and the results by Mullamphy et al. 2006, there are changes from 5.8% (1500 K) to 9.1% (1000 K).

H_2C_{2v}						$H_2C_{\infty v}$						He					
T_{gas}	NaID	KI	LiI	RbI	CsI	T_{gas}	NaID	KI	LiI	RbI	CsI	T_{gas}	NaID	KI	LiI	RbI	CsI
500 K	✓	✓	-	-	-	500 K	✓	✓	-	-	-	500 K	✓	✓ _{near}	✓ _{far}	✓ _{far}	✓ _{far}
1000 K	✓	✓	-	-	-	1000 K	✓	✓	-	-	-	1000 K	✓	✓	✓ _{far}	✓ _{far}	✓ _{far}
1500 K	✓	-	-	-	-	1500 K	✓	-	-	-	-	1500 K	-	-	✓ _{far}	✓ _{far}	✓ _{far}
2000 K	✓	✓	-	-	-	2000 K	✓	✓	-	-	-	2000 K	✓	✓ _{near}	✓ _{far}	✓ _{far}	✓ _{far}
2500 K	✓	-	-	-	-	2500 K	✓	-	-	-	-	2500 K	-	-	✓ _{far}	✓ _{far}	✓ _{far}
3000 K	✓	✓	-	-	-	3000 K	✓	✓	-	-	-	3000 K	✓	✓	✓ _{far}	✓ _{far}	✓ _{far}

Table A.1: Overview of the far and near line wing profiles of NaI D, KI, LiI, RbI and Cs I perturbed by H_2C_{2v} , $H_2C_{\infty v}$, and He for temperatures from 500 K to 3000 K by Allard et al. (2003). “✓” stands for existent profiles and “-” for the non-existent ones. A possible subscript states whether there is only a profile for the near or far line wing. For Rb I and Cs I, there are different far line wing profiles for the D₁ and D₂ line.

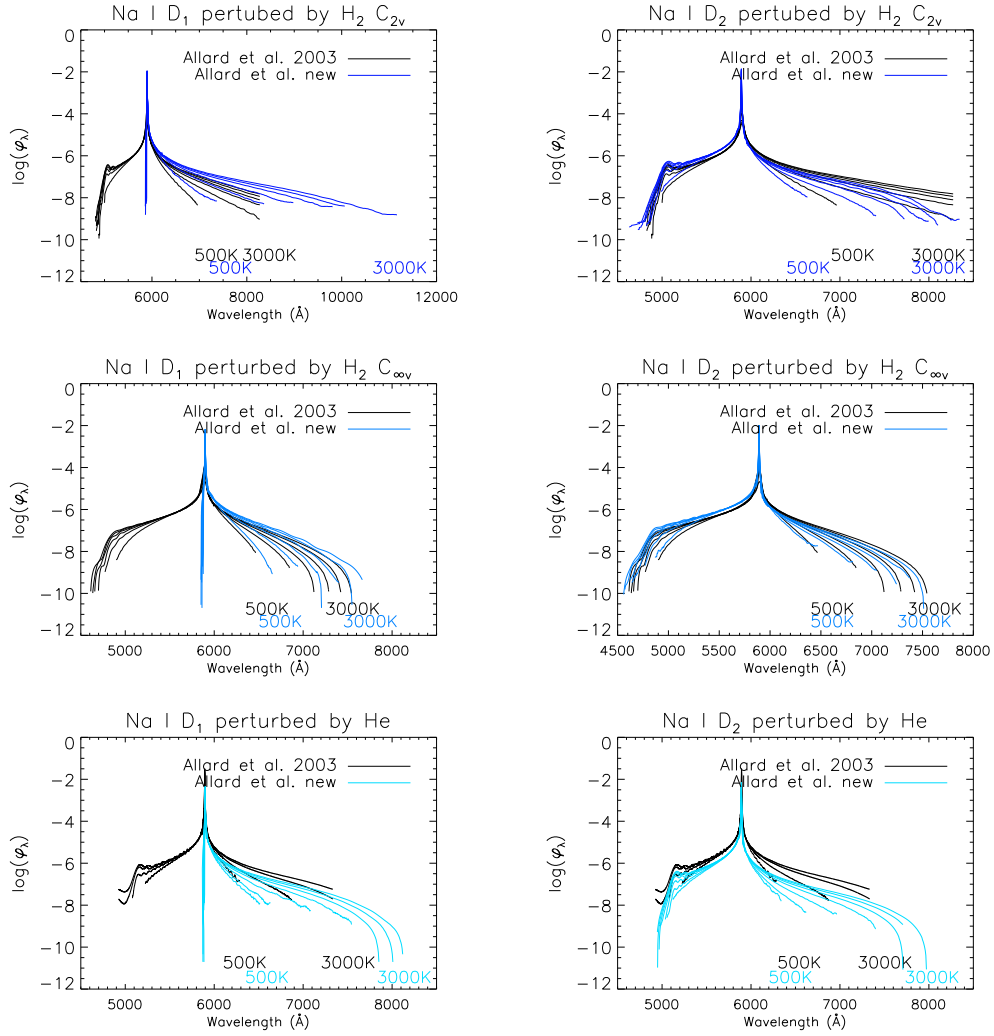


Fig. A.1: The far line wing profiles of Na I D₁ and D₂ perturbed by H₂ C_{2v}, H₂ C_{∞v}, and He by Allard et al. 2003 and Allard et al. new, see Chap. 3.2, with larger temperatures showing broader profiles. The profile function of the far line wing φ_λ per perturbing particle is displayed for a perturber density $n_p = 10^{19} \text{ cm}^3 \text{ atom}^{-1}$ in the units of $\text{cm}^{-1} \text{ cm}^3 \text{ atom}^{-1}$.

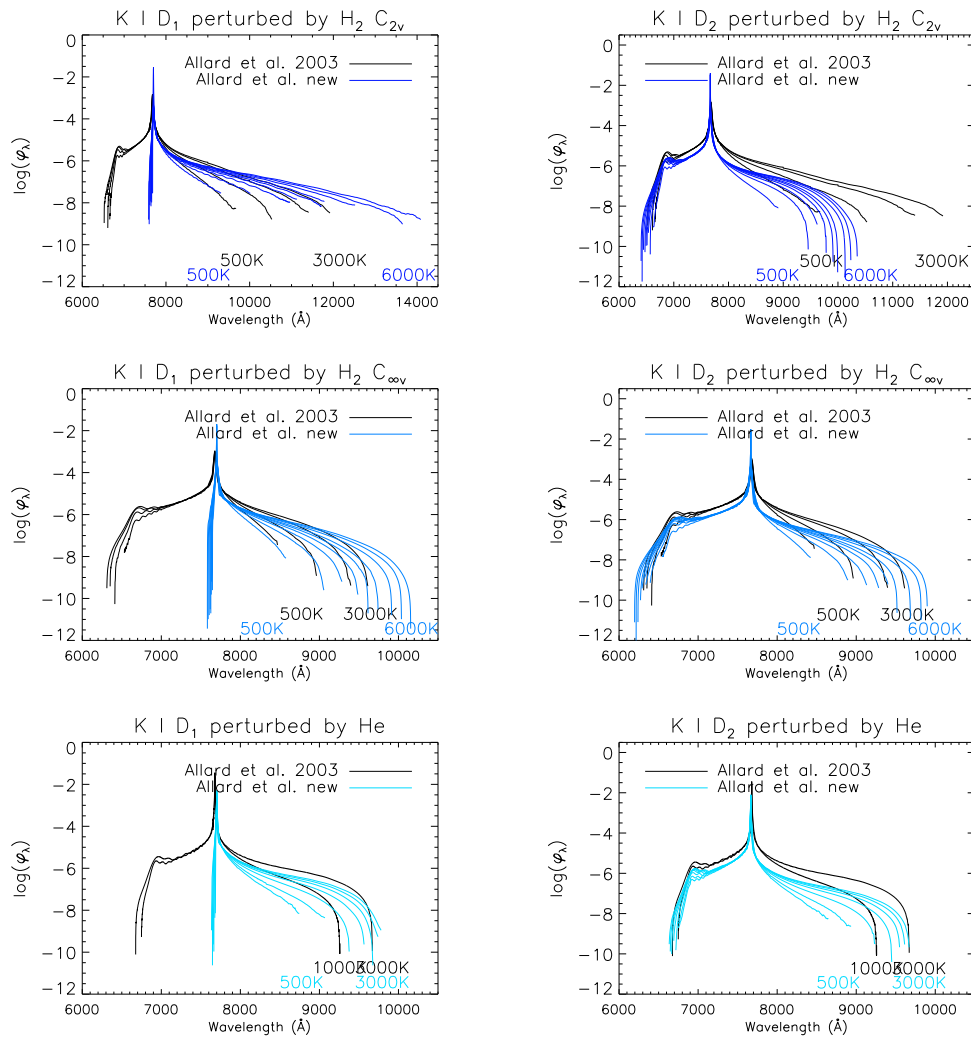


Fig. A.2: Same as Fig. A.1, but for the far line wing profiles of KID₁ and D₂ perturbed by H₂ C_{2v}, H₂ C_{∞v}, and He. The profile function of the far line wing φ_λ per perturbing particle is displayed for an perturber density $n_p = 10^{19} \text{ cm}^3 \text{ atom}^{-1}$ in the units of $\text{cm}^{-1} \text{ cm}^3 \text{ atom}^{-1}$.

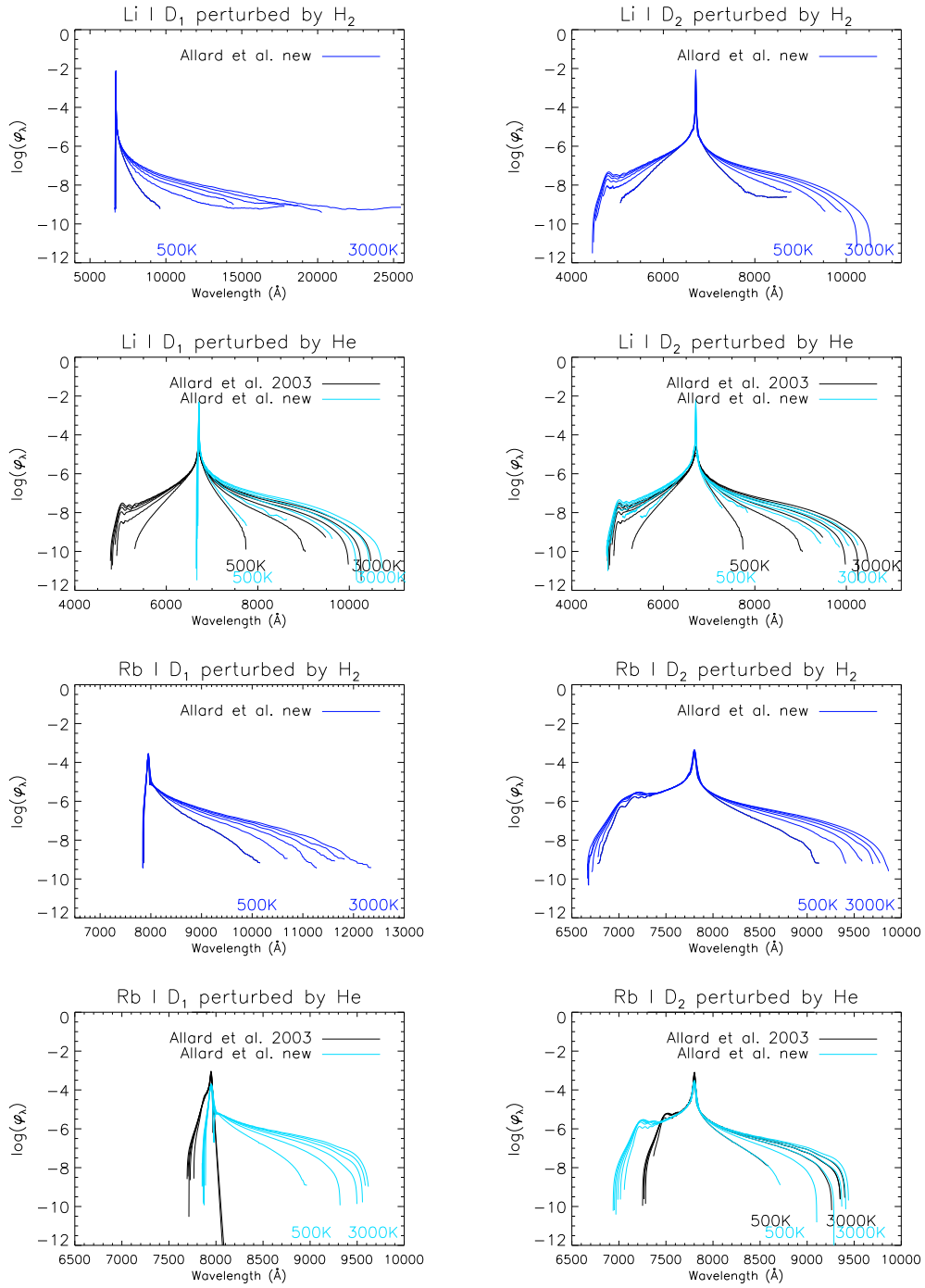


Fig. A.3: Same as Fig. A.1, but for the far line wing profiles of Li I and Rb I D₁ and D₂ perturbed by H₂ (Its two symmetries are already convoluted.) and He. The profile function of the far line wing φ_λ per perturbing particle is displayed for an perturber density $n_p = 10^{19} \text{ cm}^3 \text{ atom}^{-1}$ in the units of $\text{cm}^{-1} \text{ cm}^3 \text{ atom}^{-1}$.

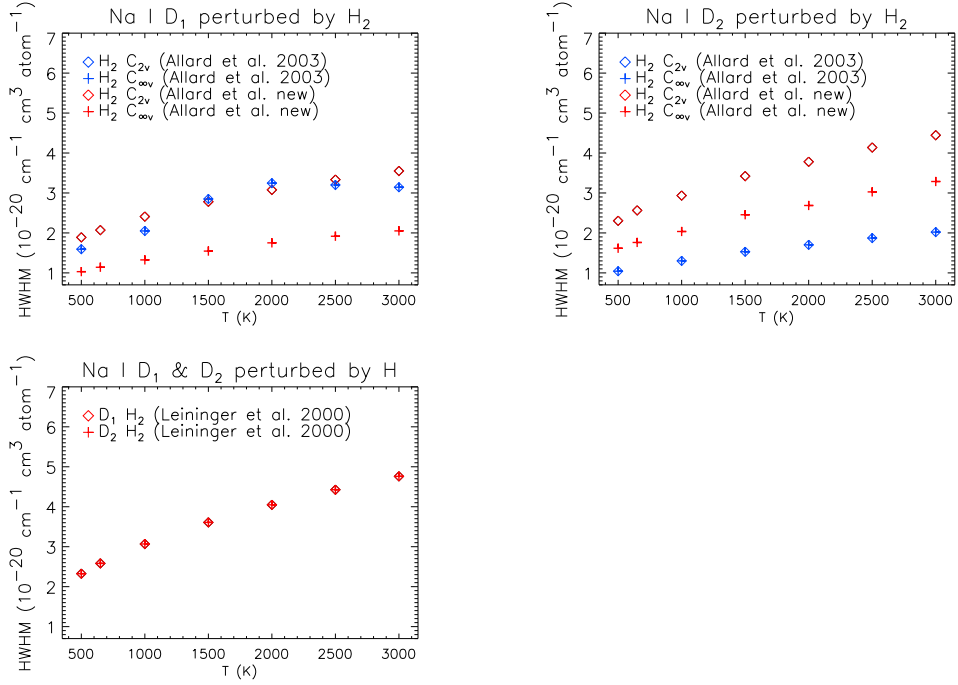


Fig. A.4: The Lorentzian damping constants for the Na I D doublet perturbed by H₂ in the two symmetries C_{2v} and C_{ooV} (top panels), introduced in Sect. 3.2, and by HI (lower panel) (Leininger et al. 2000), see Sect. 3.3.

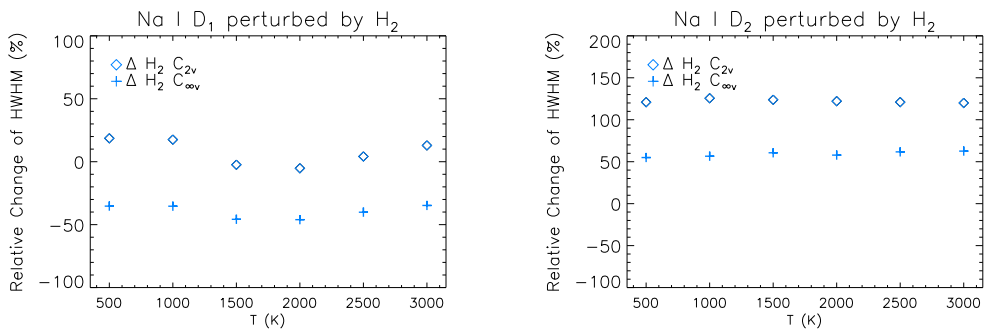


Fig. A.5: The relative change of the Lorentzian damping constants by Allard et al. new and Allard et al. 2003, shown in Fig. A.4, for the Na I D doublet perturbed by H₂ in the two symmetries C_{2v} and C_{ooV}.

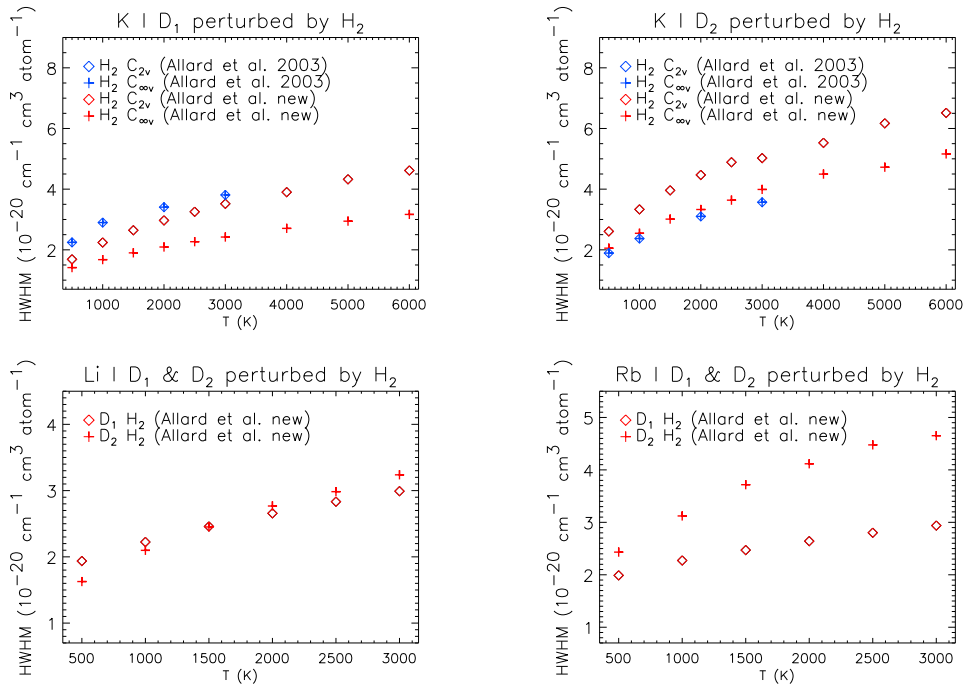


Fig. A.6: The Lorentzian damping constants for K I perturbed by H₂ in the two symmetries C_{2v} and C_{∞v} (top panels) and Li I (lower left panel) and Rb I (lower right panel) perturbed by H₂ for which the results of the two symmetries are already convolved. The labels are the same as in Fig. A.4.

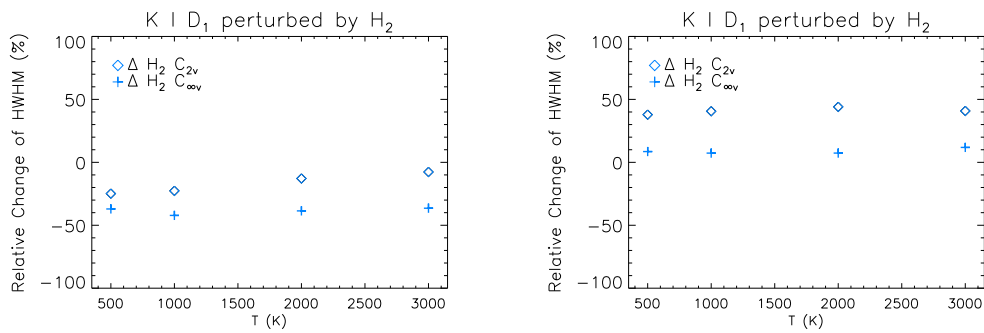


Fig. A.7: The relative change of the Lorentzian damping constants by Allard et al. new and Allard et al. 2003, shown in Fig. A.6, for the K I doublet perturbed by H₂ in the two symmetries C_{2v} and C_{∞v}.

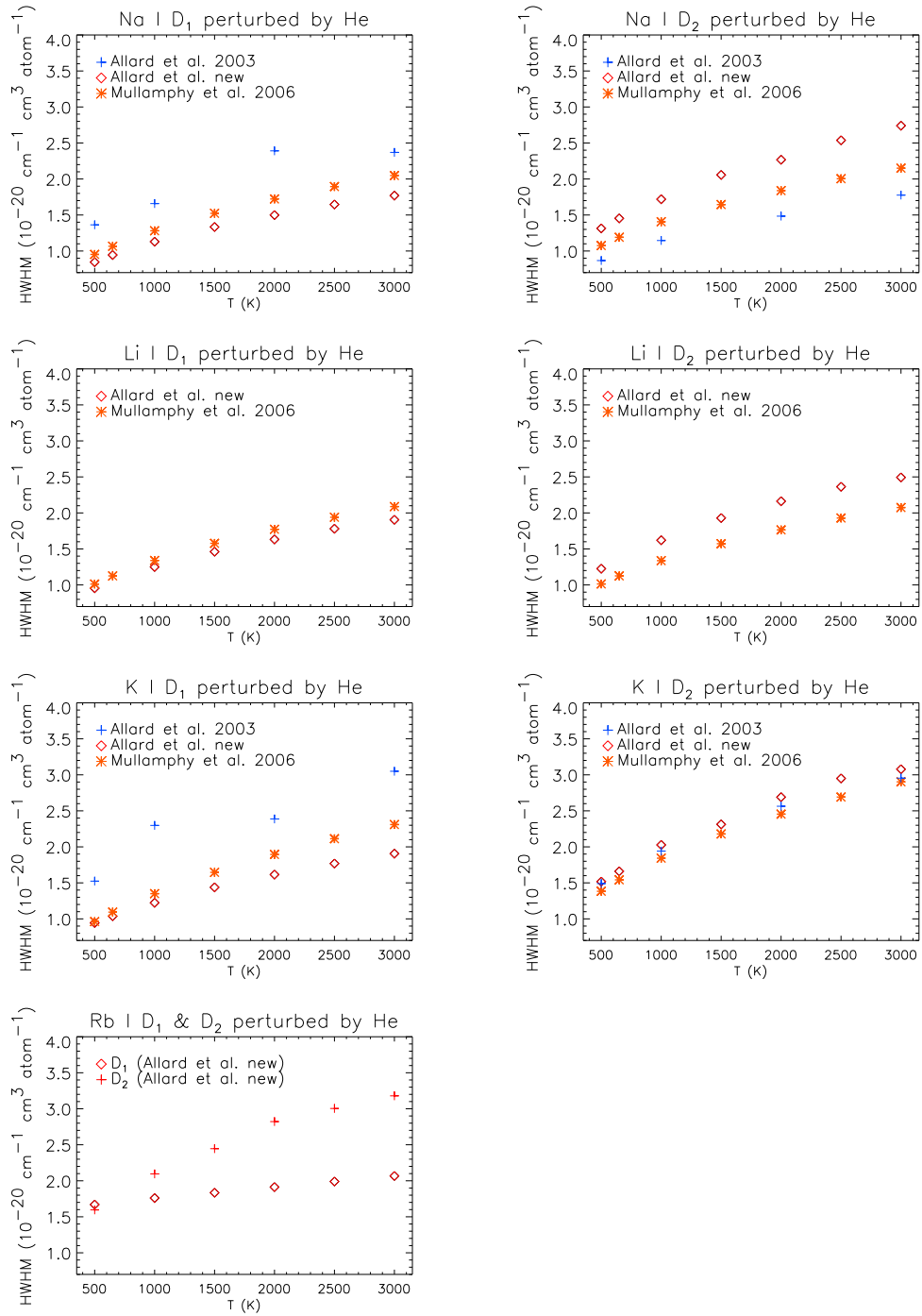


Fig. A.8: The Lorentzian damping constants for the Na I D (top panels), Li I (second panels from top), K I (third panels from top) and Rb I (lowest panel) doublets perturbed by He. For Na I D, Li I and K I, there is data by Allard et al. new, see Sect. 3.2, and by Mullamphy et al. 2006, see Sect. 3.4.

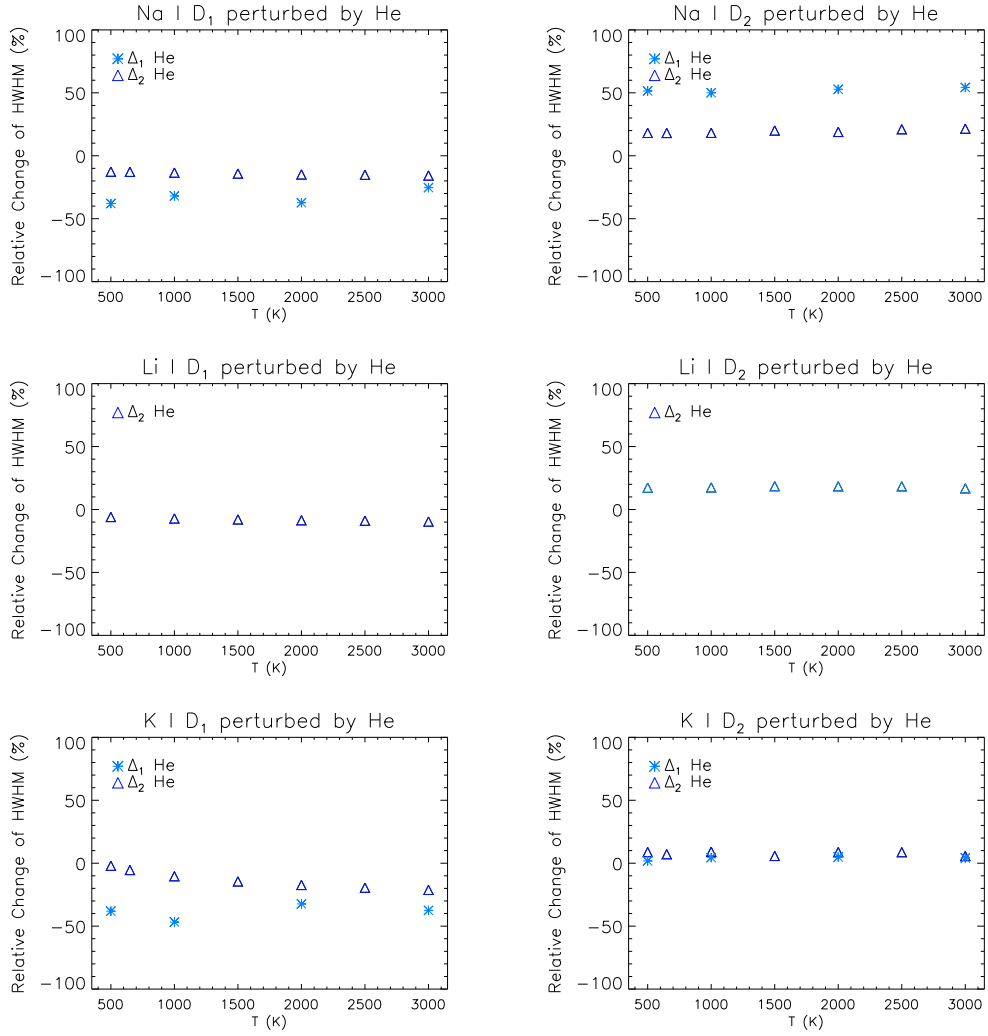


Fig. A.9: Δ_1 : The relative change of the Lorentzian damping constants by Allard et al. new and Allard et al. 2003, shown in Fig. A.8, for the Na I D, K I and Li I doublets perturbed by He. Δ_2 : The relative change of the Lorentzian damping constants by Allard et al. new and Mullanphy et al. 2006 for the Na I D, K I and Li I doublets perturbed by He, see also Fig. A.8.

B Numerical Implementation of the Total Line Profile Calculation

Each model atmosphere is discretized in radial layers. If not mentioned otherwise, the profile combination and opacity calculation is done in the subdirectory `Cassandra` of `PHOENIX`. Most of the subroutines can be found in `cas_profiles.f`, if not mentioned otherwise. For technical reasons, the line profile construction is only implemented in the NLTE code, but in this work, the code has been forced to use LTE populations. There are two methods for the combination of the far and near line wing. A first approach is the summation of the various profile parts, see `cas_profile_combine`. However, this first primitive approach is not outlined in detail in the following since it has been only a first approximation. Instead, the second approach in which the profile parts are convolved is described in detail. The hard coded value of the flag `prf_combine` in `casscom.f` (in the main directory) determines the method of combination: “0” first primitive summation approach, “1” second more sophisticated convolution approach. The routines are briefly introduced in the order as they are called by `PHOENIX`. Note, that `phoenix.f` coordinates the entire program and can be found in the main directory.

Subroutine `cas_profile_read`:

Called by `phoenix.f`.

Identification of the far and the near line wing profile, i.e., for which chemical element, transition, perturber species, temperatures and perturber densities the profile is provided. This information is found in the header of the profile and read in afterwards.

`cas_update_n.f`:

Called by `phoenix.f`.

The perturber density of each perturber type is attained from the classical ideal gas law.

Weighting of the perturber species.

Calls the subroutine `cas_profile_update` in `cas_profiles.f`.

Subroutine `cas_profile_update`:

Called by `cas_update_n.f`.

Provides the subroutines for the profile combination (for the primitive summation and more sophisticated convolution method).

Calls `cas_profile_make_wl2`.

Calls `cas_profile_convolve`.

Subroutine `cas_profile_make_wl2`:

Called by `cas_profile_update`.

An evenly distributed wavelength grid for the far line wing profiles from the blue end to the red end around the line center is created.

Subroutine cas_profile_convolve:

Called by `cas_profile_update`.

Input: data of all profiles of the treated alkali, its central wavelength (in Å in vacuum), wavelengths to interpolate to and the number of temperature and wavelength points.

Output: convolved alkali profile (either convolved pure far line wing profile or convolved far and near line wing profile), Voigt parameters for the further evaluation of the Voigt profile.

The far line wing profiles are treated separately from the near line wing and/or Gauss core profile. Calls `cas_profile_interp_all`: each far line wing profile, dependent on the temperature and perturber, is interpolated onto the wavelength grid from `cas_profile_make_wl2` and the temperature structure of the model atmosphere.

The interpolated far line wing profiles are multiplied with the perturber density, derived in `cas_update_n.f`, and converted from the logarithmic (to the base 10) representation (original input) into the plain representation.

Inter- and extrapolation of the near line wing profiles, i.e., the damping constants (HWHMs) and the shifts, onto the atmospheric layer temperature and multiplication with the perturber density for all atmospheric layers. Thereby, the damping constants are inter- and extrapolated with a $T^{0.3}$ law in order to match the van-der-Waals like $v^{3/5}$ behavior, see Eq. 2.16 with v from Eq. 2.9.

Evaluation of the total damping constant (`w2tot`) and shift (`d2tot`) by summing over all perturber types.

Unit conversion of the Lorentzian parameters: From cm^{-1} to cm (from $1/\lambda$ to λ).

The FWHM `dllrz`, which is the Lorentzian FWHM and additionally the natural FWHM (computed earlier in `cas_damp_const.f`, see Eq.2.2 in Chap. 2), and the shift `ddlrz` are obtained. Normalization of the new far line wing profiles and near line wing profile contributions.

Calls `convolve_profiles`: numerical convolution of the far line wing profiles over all possible combinations of perturber types.

Another check of the normalization: calls `cas_profile_getnorm`.

In case there is no Voigt core required, a Lorentzian profile is calculated (without considering natural line broadening), call `lorentz`.

Evaluation of the Voigt parameters: $\alpha = 0.5 \cdot \text{dllrz} \cdot \text{dgi}$, where `dgi` is the inverse Gauss width in cm^{-1} for the Doppler profile and calculated in `MISC/modcon.f`.

Merging of the partial convolutions over all wavelengths for the following cases: (a) only for the far line wing profiles and add the Voigt profile later, (b) for the far line wing profiles and Lorentzian near line wing profiles.

This case is split up into (a) the wavelength range of the far line wing regime ($\lambda \geq 116 \cdot \text{xlor} \cdot \text{dllrz}$), where `xlor` is a transition point to dampen out the Lorentzian near line wing for the transition to the far line wing and (b) the wavelength range for the transition region ($\lambda \geq \text{xlor} \cdot \text{dllrz}$), see Chapter 2.1.3, for which the final profile function is the sum of the summed far line wing convolution contributions plus the product of the Lorentzian profile and a decreasing exponential function dependent on the central wavelength which is weighted with `xlor · dllrz`; for wavelengths in the pure near line wing region, the final profile function is the sum of all far line wing convolution contributions and the Lorentzian profiles.

A final normalization is done.

cas_voigt_lines.f:

Called by `phoenix.f`.

Calculation of the opacity.

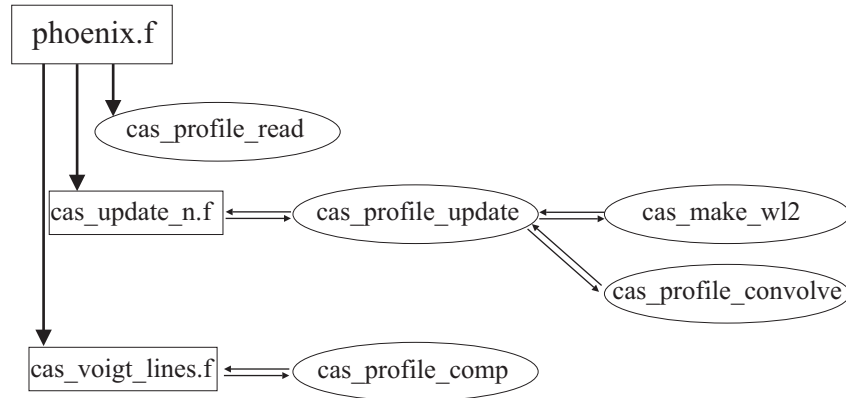


Fig. B.1: Schematic overview of the calling order for the evaluation of the total profile function. Ellipses stand for subroutines and rectangles for program files.

Calls `cas_profile_comp` in `cas_profiles.f`.

Subroutine `cas_profile_comp`:

Called by `cas_voigt_lines.f`.

Final evaluation of the Voigt profile.

Determination of the wavelength range of the Voigt profile in cm, $d\lambda = |\lambda - \lambda_0| + d\lambda_{\text{rz}}$.

Evaluation of the second Voigt parameter, $y = d\lambda \cdot dgi$.

Setting the Voigt function in the far line wing regime equal zero.

If $\alpha + y \geq 15$, then the approximation of the Voigt function for $\alpha \rightarrow \infty$ is valid, see Eq. 4.26; otherwise the Voigt function is approximated by Eq. 4.27, see Sect. 4.3.

Final computation of the extinction Voigt profile function φ , see Eq. 2.5 in Chap. 2,

$$\varphi(\Delta\lambda) = \frac{dgi}{\sqrt{\pi}} H(\alpha, y). \quad (\text{B.1})$$

If there are no far line wings provided, the total profile function is the Voigt function from Eq. B.1. If far line wings exist, there is the distinction between the two cases: (a) for the core region, the earlier convoluted total far line wing profile is merged with the normalized Voigt profile; (b) for the transition region, the profile function is the sum of the total far line wing profile and the product of the normalized Voigt function and a decreasing exponential function dependent on a cutoff parameter for the Voigt profile. This cutoff parameter is the transition point to dampen out the Voigt near line wing for the transition to the far line wing.

In Fig. B.1, a schematic overview of the order of calls needed for the evaluation of the total profile function, as described above, is shown.

Data Format Suggestion

For future work with profile data, one should change the far and near line wing profile data format into the Fourier space. This should simplify the further computations with the far and near line wing profiles, e.g., the convolution is simplified to a multiplication and also the interpolations should become easier. Therefore, it is necessary to provide the Fourier components directly.

C The Influence of Line Profiles on Models and Spectra II

C.1 T-p Structures: Impact, 1st Generation, and Modern1 Setup

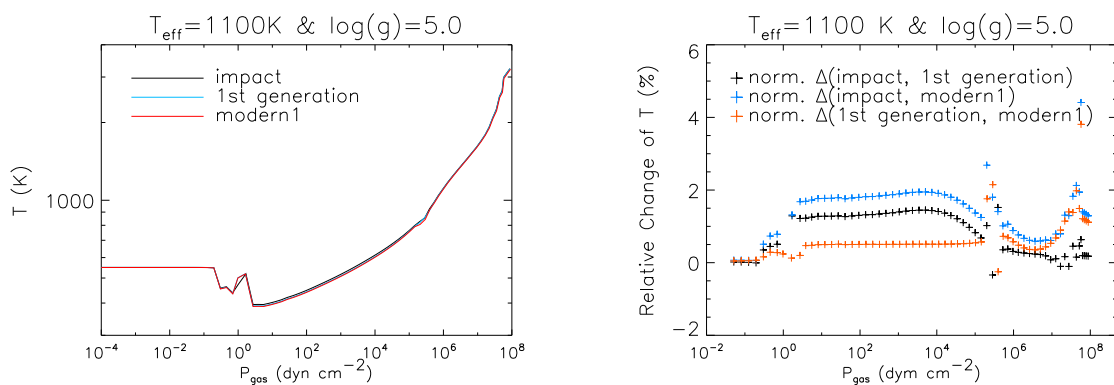


Fig. C.1: Left: T-p structures of the impact, 1st generation, and modern1 atmospheres. Right: relative changes of the temperature between the three setups.

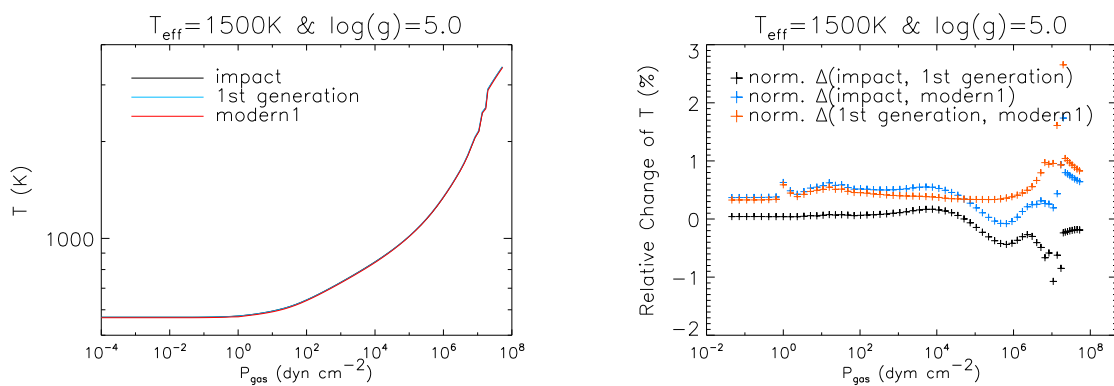


Fig. C.2: Same as Fig. C.1, but for $T_{\text{eff}} = 1500 \text{ K}$.

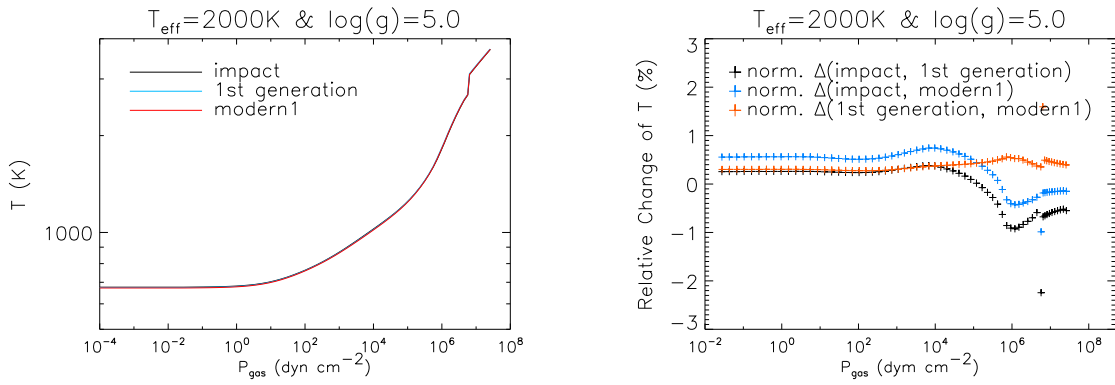


Fig. C.3: Same as Fig. C.1, but for $T_{\text{eff}} = 2000$ K.

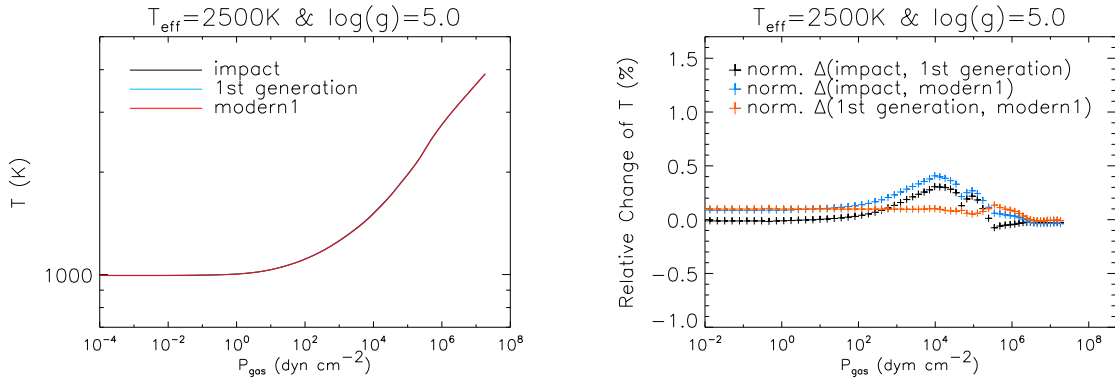


Fig. C.4: Same as Fig. C.1, but for $T_{\text{eff}} = 2500$ K.

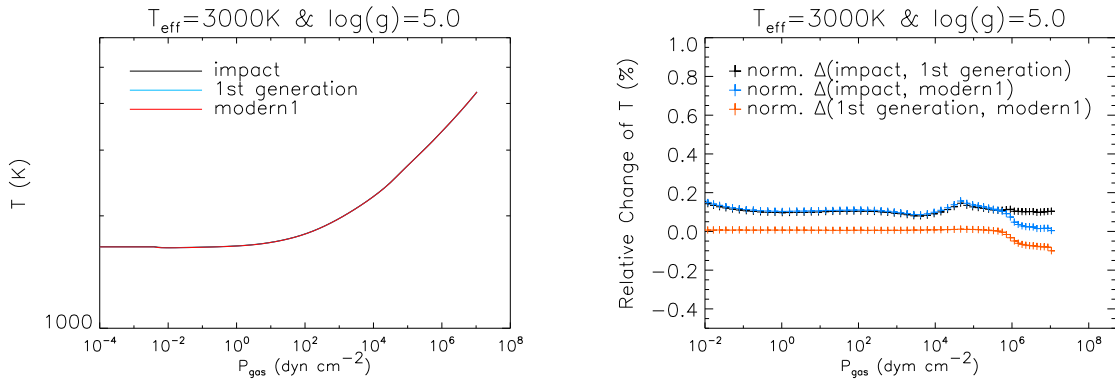


Fig. C.5: Same as Fig. C.1, but for $T_{\text{eff}} = 3000$ K.

C.2 Low Resolution Spectra

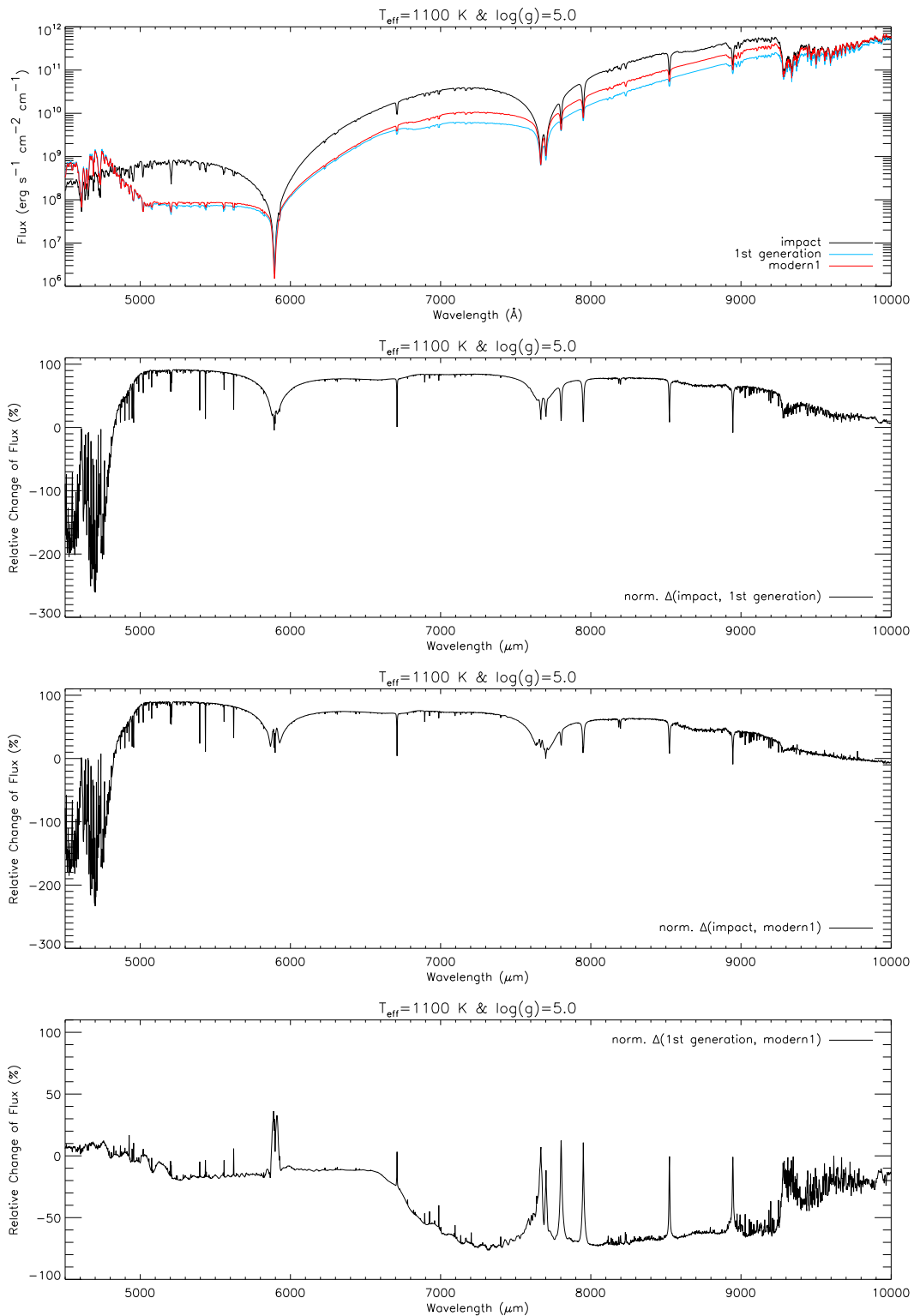


Fig. C.6: Upper panel: low resolution spectra ($\Delta\lambda = 2 \text{ \AA}$) with $T_{\text{eff}} = 1100 \text{ K}$, $\log(g) = 5.0$, and solar composition computed with the impact, 1st generation, and modern1 setup. In the three lower panels, the relative changes of the flux between the various setups are shown.

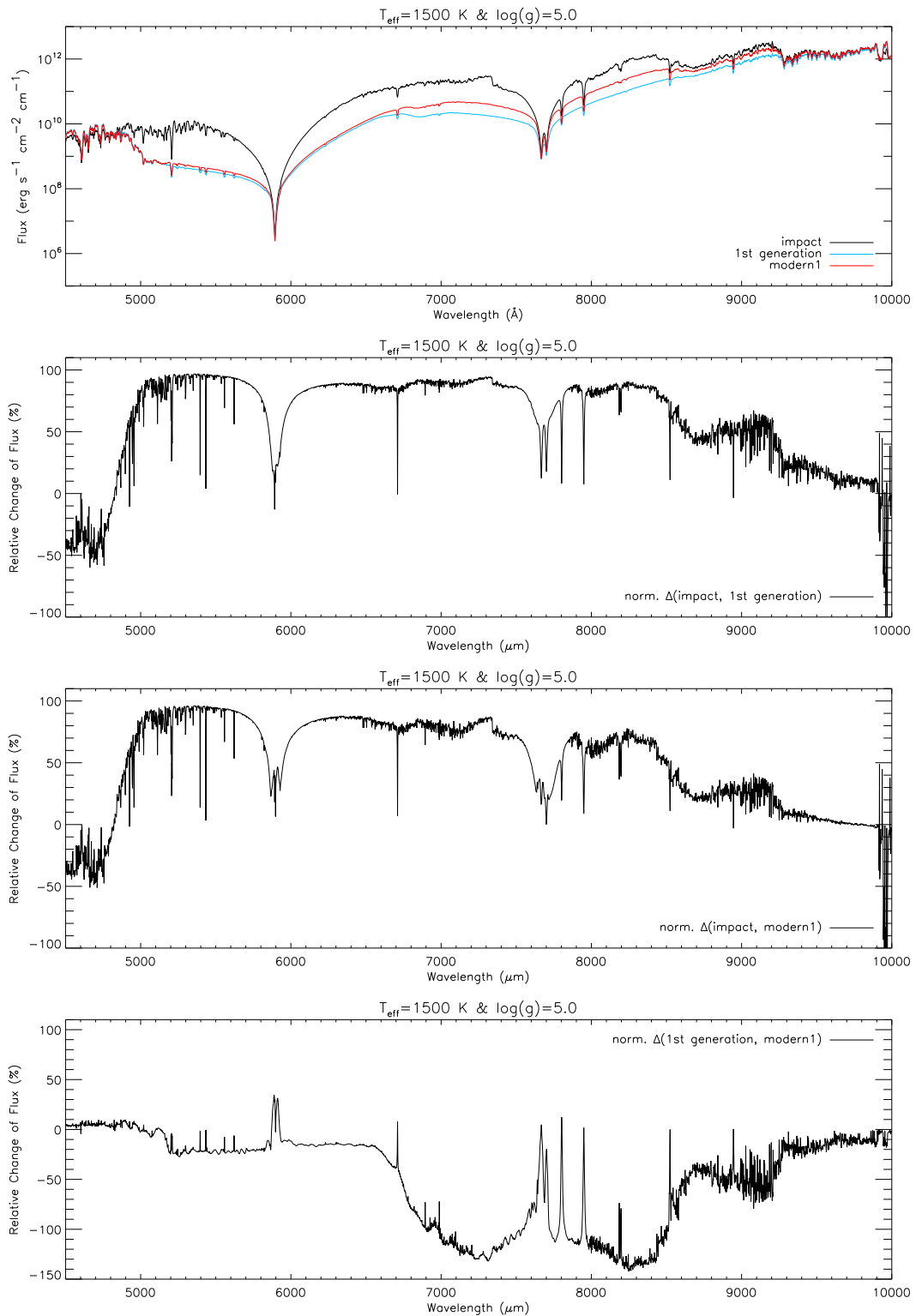


Fig. C.7: Same as Fig. C.6, but for $T_{\text{eff}} = 1500 \text{ K}$.

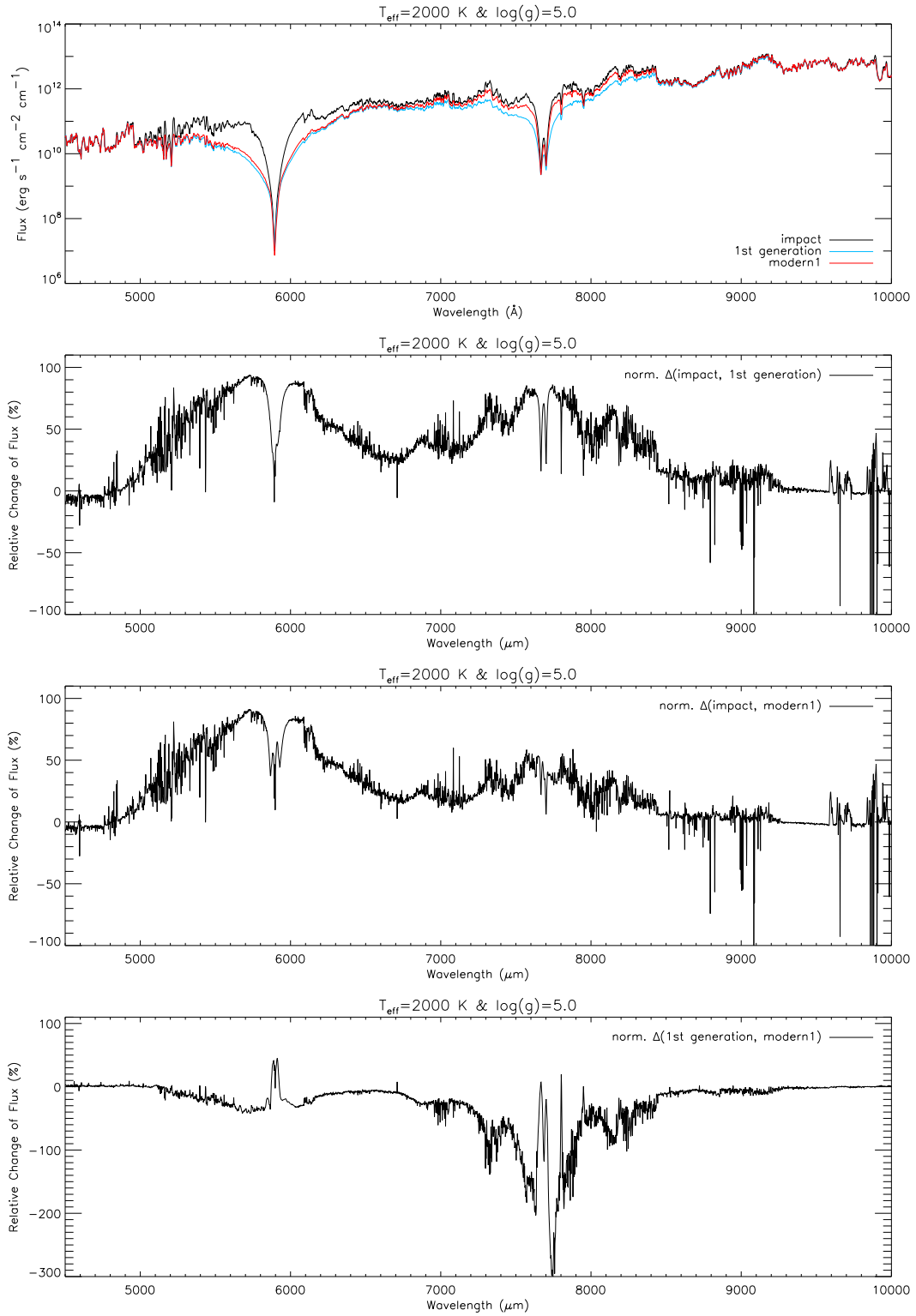


Fig. C.8: Same as Fig. C.6, but for $T_{\text{eff}} = 2000 \text{ K}$.

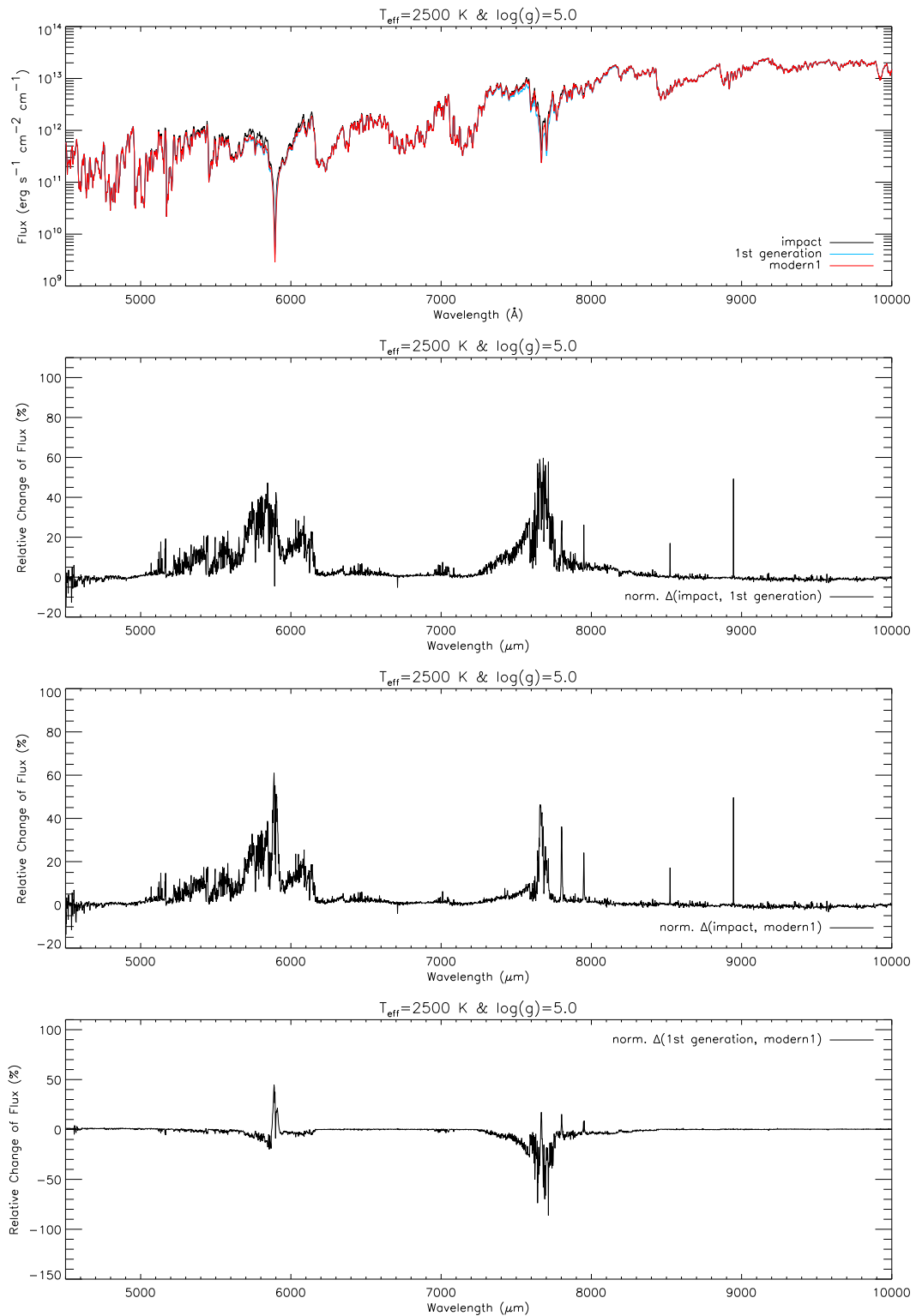


Fig. C.9: Same as Fig. C.6, but for $T_{\text{eff}} = 2500 \text{ K}$.

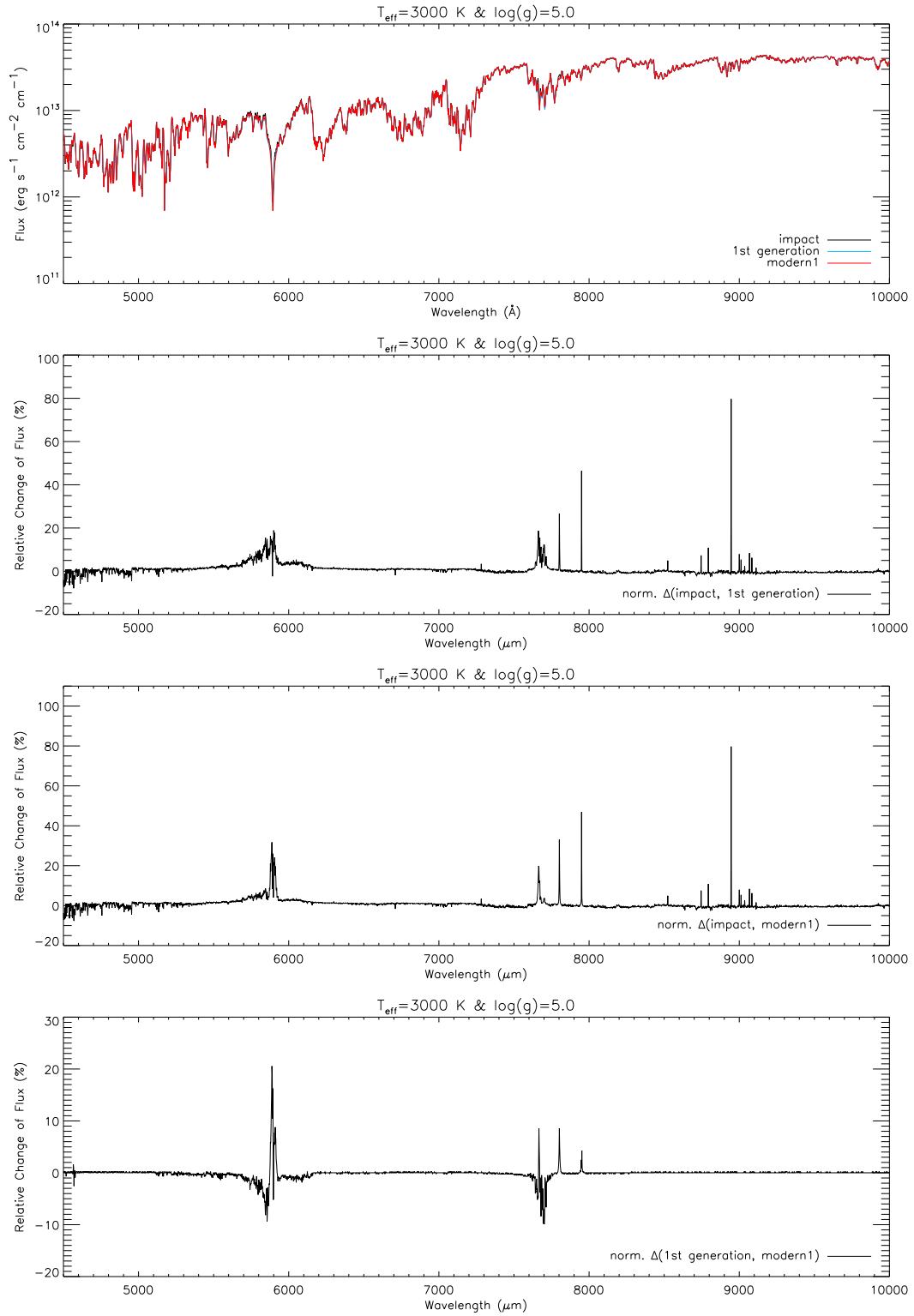


Fig. C.10: Same as Fig. C.6, but for $T_{\text{eff}} = 3000 \text{ K}$.

C.3 Close Up of the Alkali Doublets

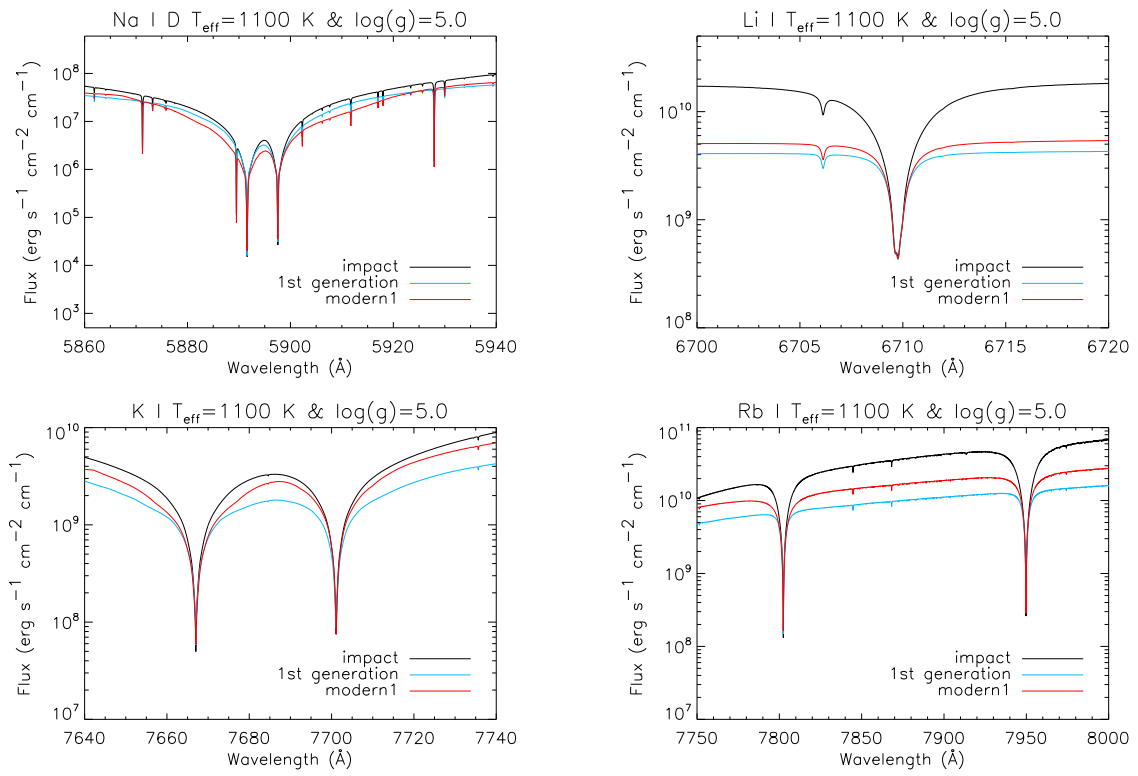


Fig. C.11: Close up of the high resolution spectra of Fig. C.6 stressing the description of the Na I D, Li I, K I, and Rb I doublets.

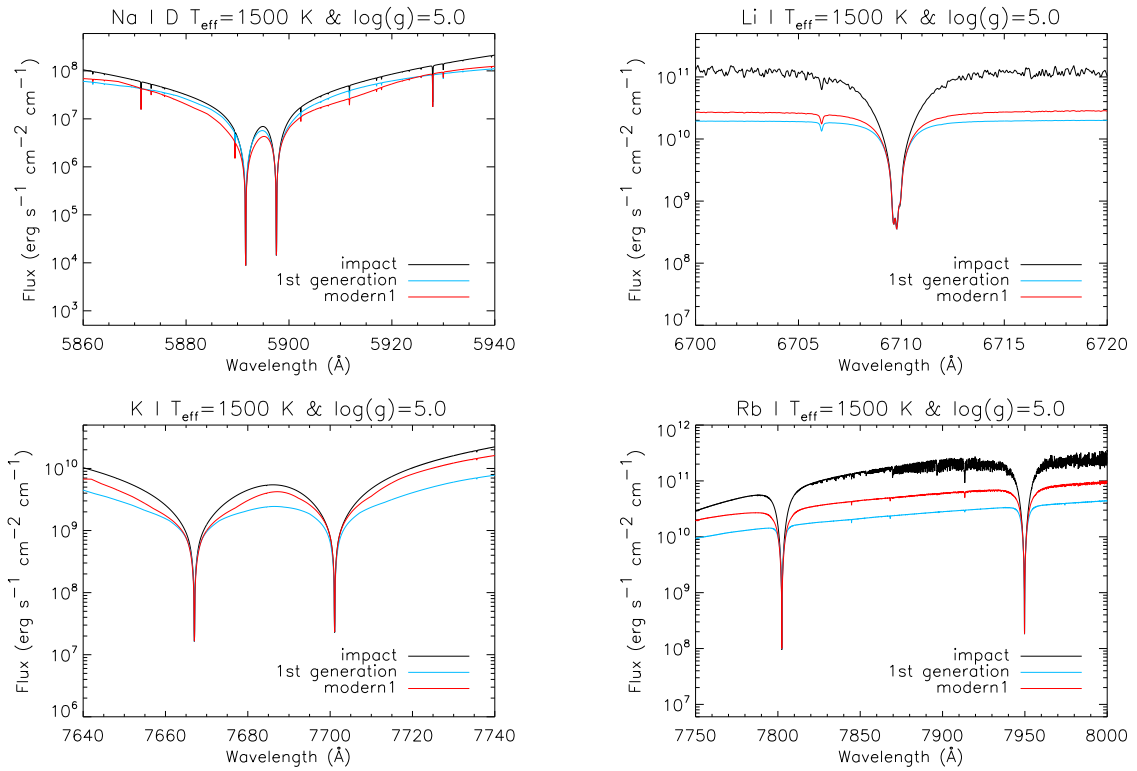


Fig. C.12: Same as Fig. C.11, but for $T_{\text{eff}} = 1500$ K.

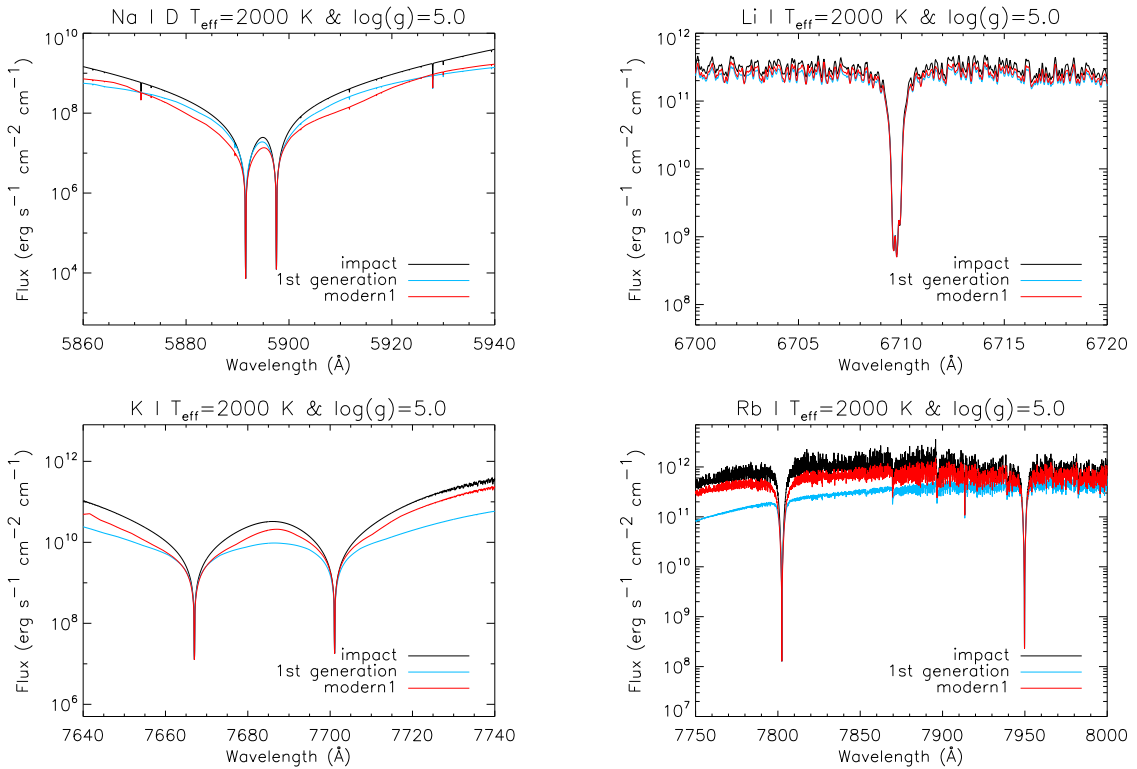


Fig. C.13: Same as Fig. C.11, but for $T_{\text{eff}} = 2000$ K.

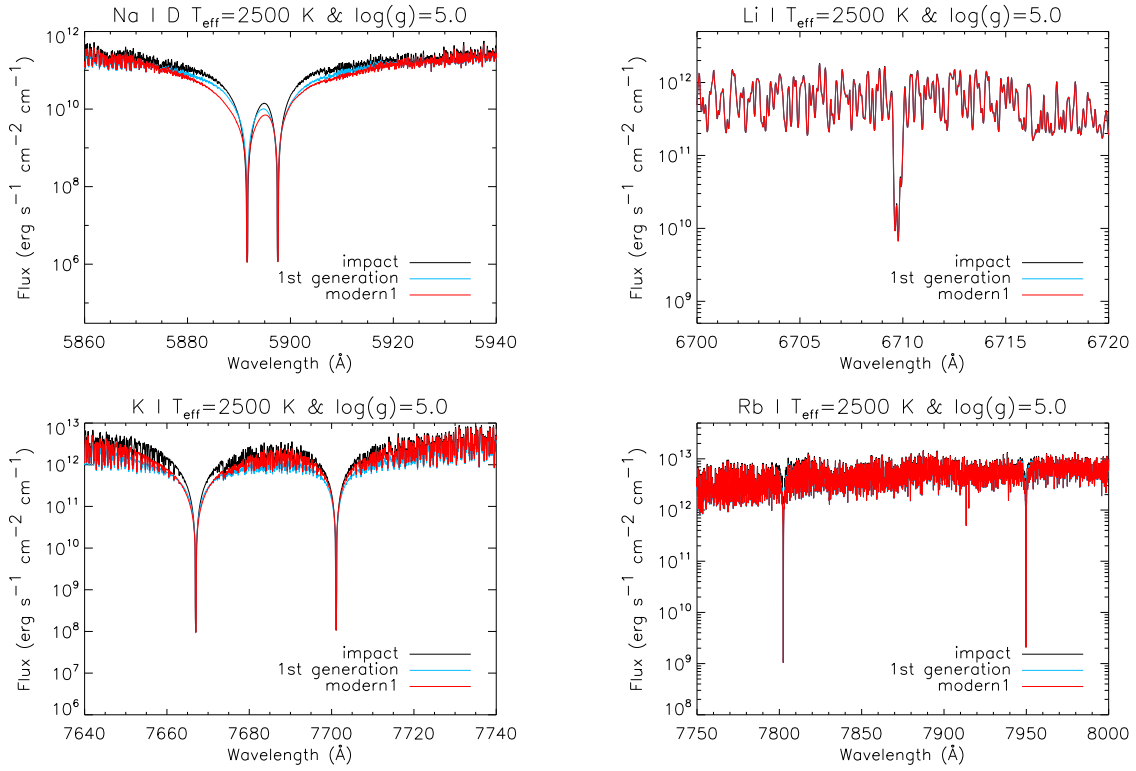


Fig. C.14: Same as Fig. C.11, but for $T_{\text{eff}} = 2500 \text{ K}$.

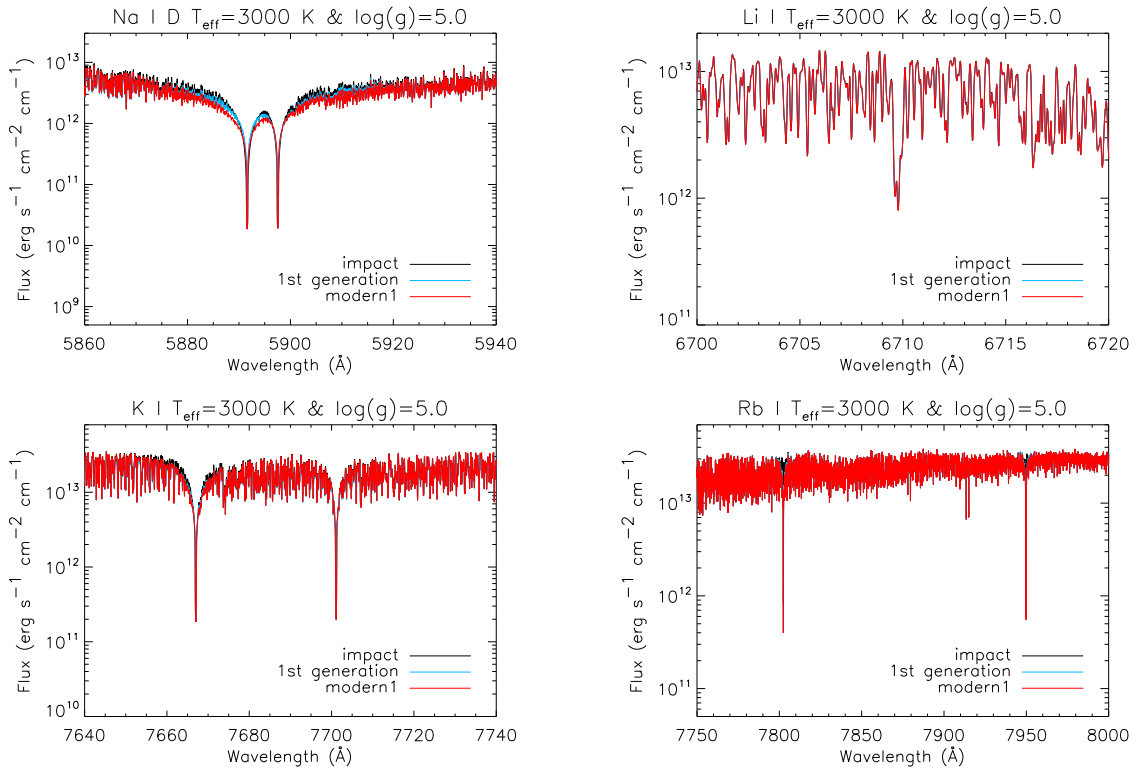


Fig. C.15: Same as Fig. C.11, but for $T_{\text{eff}} = 3000 \text{ K}$.

C.4 T-p Structures: Modern1, Modern2, and Modern3 Setup

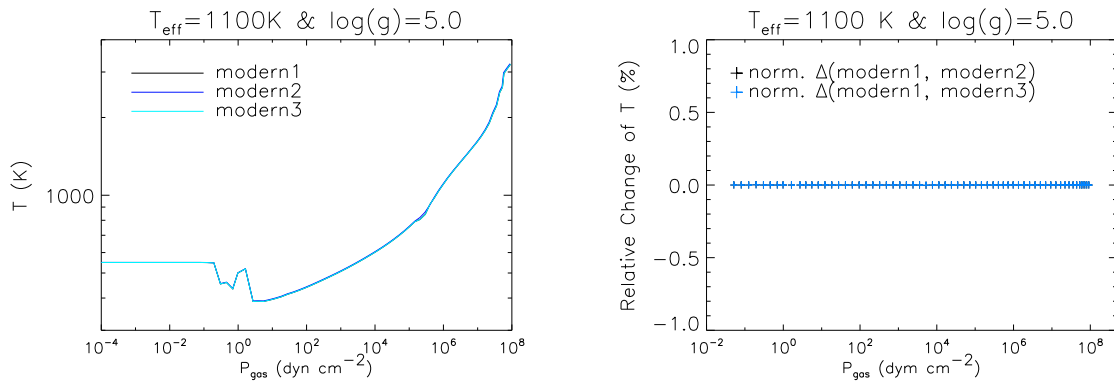


Fig. C.16: Left: T-p structures of the modern1–3 atmospheres for $T_{\text{eff}} = 1100 \text{ K}$, $\log(g) = 5.0$, and solar composition in Sect. 5.5. Right: relative change of the gas temperature between the three setups.

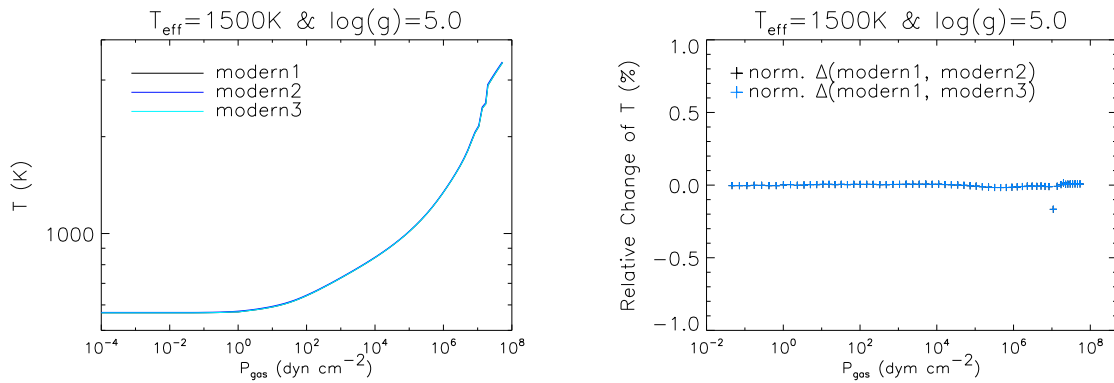


Fig. C.17: Same as Fig. C.16, but for $T_{\text{eff}} = 1500 \text{ K}$.

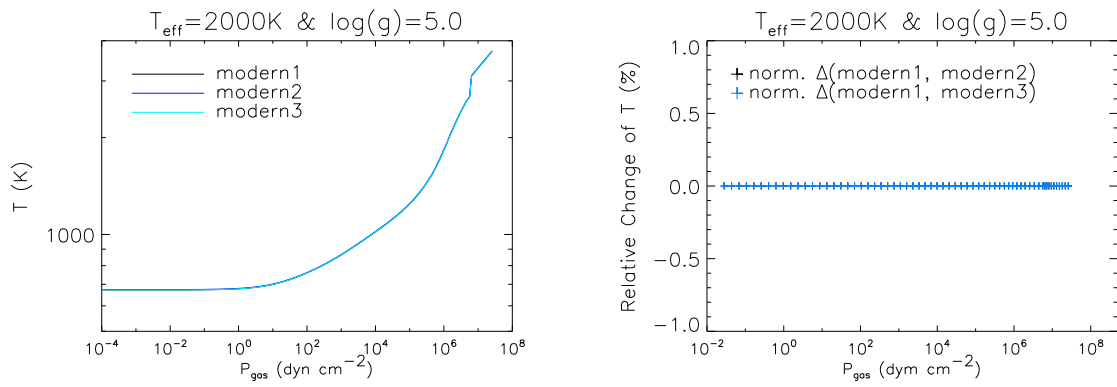


Fig. C.18: Same as Fig. C.16, but for $T_{\text{eff}} = 2000$ K.

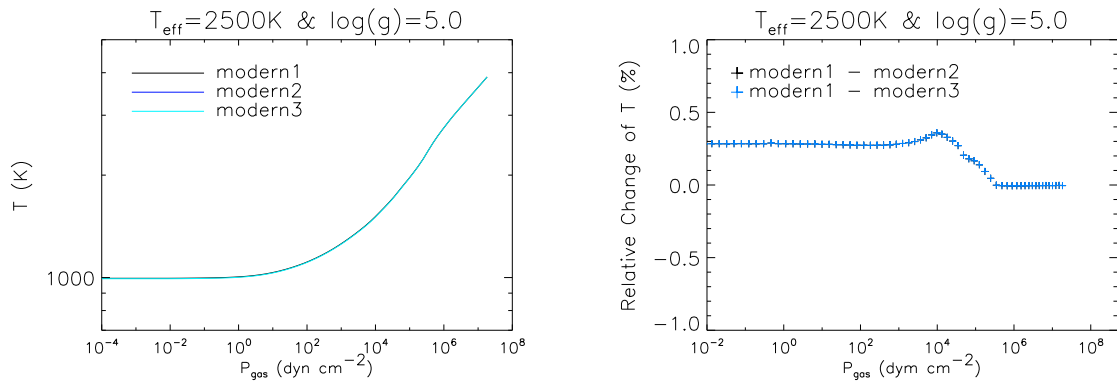


Fig. C.19: Same as Fig. C.16, but for $T_{\text{eff}} = 2500$ K.

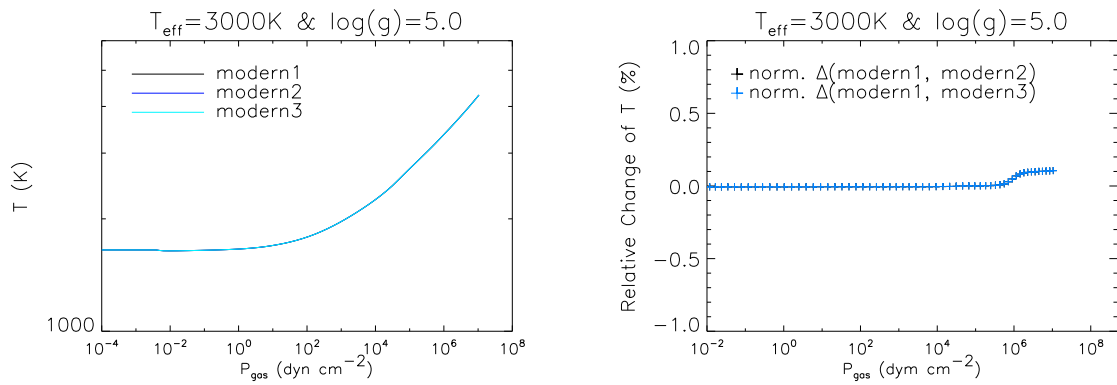


Fig. C.20: The same as in Fig. C.16 for $T_{\text{eff}} = 3000$ K.

D The Na I Doublet in the Impact and Modern1-3 Setup with $\log(g) = 4.5$

This appendix deals with the Na I D line profiles of the impact and the modern1-3 setups and their effects on synthetic spectra. In Sect. D.1, the analysis of the various Na I D profiles is presented. The content of Sect. D.1 has been published in Johnas et al. (2007a,b). A comparison with the results of Sect. 5.5, a similar study with $\log(g) = 5.0$, is given in Sect. D.2.

D.1 The Effects of New Na I D Line Profiles in Cool Atmospheres

In 1995, the first brown dwarf Gliese 229b was discovered (Nakajima et al. 1995). Since then there has been tremendous progress in the search for and identification of such cool objects. As a result of this work the spectral types L and T have been introduced by Kirkpatrick et al. (1999) and Burgasser et al. (2002) to classify the spectra of these substellar objects. Kirkpatrick et al. (1999) and Burrows et al. (2000) showed that in the spectra of brown dwarfs the wings of the alkali lines have widths of several 1000 Å.

The broadening of the alkali absorption lines in atmospheres of cool dwarfs is due to pressure broadening by the most important constituents of the atmospheres: molecular hydrogen, helium and (for M dwarfs) neutral hydrogen. Major improvements in the theoretical description of pressure broadening have been made compared to the commonly used van-der-Waals broadening in the impact approximation, see Allard et al. (2003) and Burrows & Volobuyev (2003). The discussion about the influence of different approximations for the line profiles in synthetic spectra for such cool stellar objects is resumed here, as introduced in Johnas et al. (2006). One of the main conclusions of Johnas et al. (2006) was that further studies of atomic hydrogen as a perturber are necessary, in particular for M dwarfs for which it is the species with the highest concentration in the atmospheric layers where the line wings of the alkalis form. Also profiles for Na I D broadened by atomic hydrogen (Leininger et al. 2000) are included. In addition, the new profiles of Na I, K I, and Li perturbed by helium from Mullamphy et al. (2007) have been added. The new profile data are damping constants for a Lorentzian line profile shape. Hence, they represent the physical conditions in the absorption near line wing and core regions. The profiles have been incorporated into the general model atmosphere code PHOENIX, version 15 (Hauschildt & Baron 1999). The model atmospheres and synthetic spectra presented here have been generated for effective temperatures from $T_{\text{eff}} = 1100$ K to 3000 K with a step size of 500 K and a gravity of $\log(g) = 4.5$. In the following, we concentrate on the Na I D resonance doublet since it is the alkali with the highest concentration in such cool atmospheres.

Profiles

In addition to the van–der–Waals profiles in the impact approximation (hereafter, impact) (Schweitzer et al. 1996) and modern and detailed calculations (hereafter, modern1), described in (Johnas et al. 2006) and references therein, in which molecular hydrogen in the symmetries C_{2v} and $C_{\infty v}$ as well as neutral helium have been considered as perturbers, we will discuss the following specific line profiles: line widths and shifts of a Lorentzian profile for atomic hydrogen perturbers of Na I in the impact approximation (Leininger et al. 2000) are added to modern1 resulting in the model type “modern2”. In “modern3” we have substituted the helium broadened Na I, K I, and Li I line profile data of modern2 with the results of Mullamphy et al. (2007). These have been obtained by using the fully quantum mechanical theory of Baranger (1958c). In this theory the perturbers are treated quantum mechanically. Thus inelastic collisions, degeneracy and overlapping lines are taken into account. Furthermore the impact approximation is used. Although concentrating on the Na I D doublet, the inclusion of the K I modern3 line profile is important for this work since Na I D and K I resonance lines form the pseudo continuum in the optical range. We present only synthetic spectra calculated using the “COND” model setup (Allard et al. 2001) in order to demonstrate the influence of the line profiles in the synthetic spectra. The “COND” approximations consider fully “rained-out” condensed dust in chemical equilibrium, see Allard et al. (2001) for details. For each line profile setup, a model atmosphere has been calculated and converged before generating the synthetic spectrum.

Analysis of the Different Line Profiles in the Synthetic Spectrum

Figure D.1 displays synthetic spectra for $T_{\text{eff}} = 1100 - 3000$ K and $\log(g) = 4.5$ at a reduced resolution of 10 000 around the Na I D resonance doublet. The original calculated resolution of the synthetic spectra is $3 \cdot 10^5$. All wavelengths are given in vacuum. In Fig. D.1, for effective temperatures of 1100 K, 1500 K, and 2000 K, large differences between the different model types are obvious, especially “impact” versus “modern1-3”. At $T_{\text{eff}} = 2500$ K and 3000 K, molecular bands, such as TiO, VO, CaH, and FeH, become predominant and overwhelm the effect of the different line profiles on the emitted spectrum. A close up of the Na I D doublet of Fig. D.1 is shown in Fig. D.2. It shows the differences in more detail at the full computed resolution.

The contribution of Na I D broadened by neutral hydrogen (modern2) is most visible in the near line wings at higher effective temperatures, $T_{\text{eff}} = 2000$ K–3000 K, as predicted by Johnas et al. (2006) and depicted in Fig. D.2. Under these atmospheric conditions, atomic hydrogen becomes the most prominent species at the optical depths where the line wing forms. There are differences¹ of up to 6.2 %, -7 %, and -3.4 % for $T_{\text{eff}} = 3000$ K, 2500 K, and 2000 K between the modern1 and modern2 spectra for the Na I D lines. At lower effective temperatures, the differences are smaller due to the decreasing concentration of atomic hydrogen: For $T_{\text{eff}} = 1500$ K the relative change in flux is at the most +0.35 % and for $T_{\text{eff}} = 1100$ K, in the near line wings the relative change decreases from +0.5 % to -2 %. Very close to each of the two central wavelengths, the relative change increases to 2.5 % at $T_{\text{eff}} = 1100$ K.

When comparing the impact spectra with modern2 spectra, the differences in the near line wing regions are between +25 % and -150 % at $T_{\text{eff}} = 3000$ K. The change is even stronger at $T_{\text{eff}} = 2500$ K, between +50 % and -290 % in the near wings. The strong decrease appears towards the line centers whereas at the line centers the relative change is only approximately 10 % and 20 % for

¹If not mentioned otherwise, the comparison refers to a wavelength range between 5850 Å and 5950 Å.

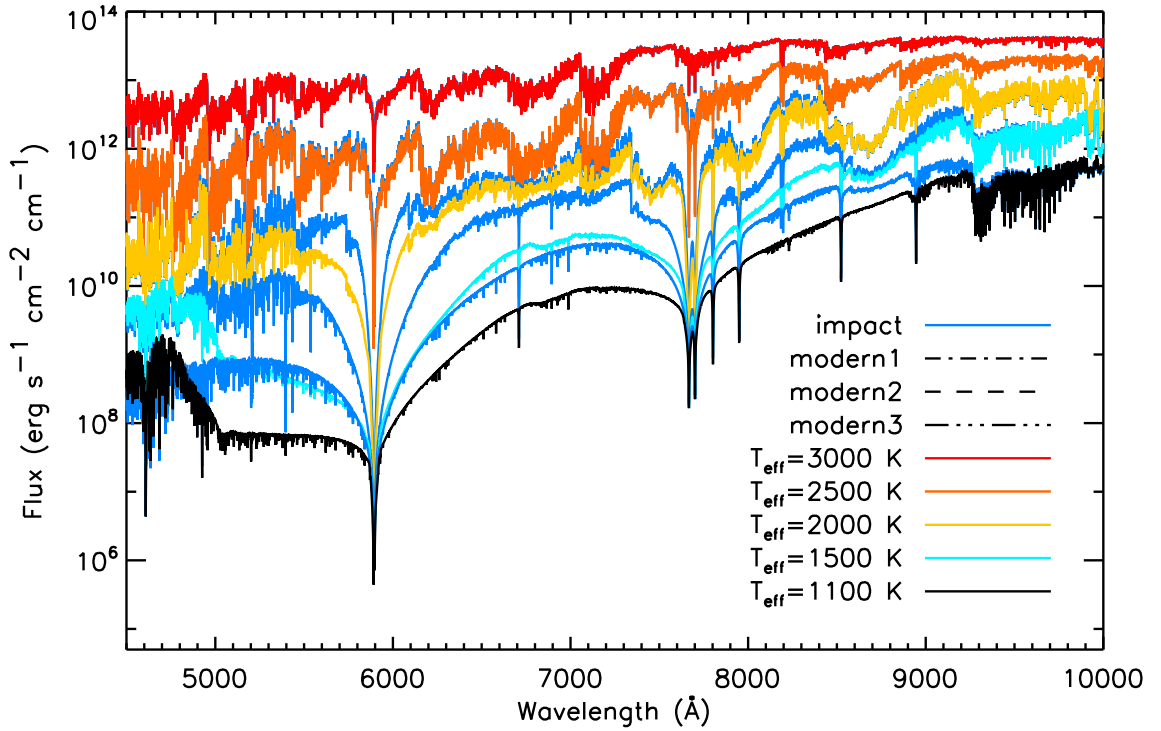


Fig. D.1: Smoothed synthetic spectra with a resolution of 10000 for models with $T_{\text{eff}} = 1100$ K to 3000 K displaying the differences between the four different line profile setups.

$T_{\text{eff}} = 3000$ K and 2500 K respectively. For lower effective temperatures starting at $T_{\text{eff}} = 2000$ K, the influence in the line wings (at 5800 \AA) is even greater, decreasing from 87 % to 76 % at $T_{\text{eff}} = 1500$ K and 63 % at $T_{\text{eff}} = 1100$ K. The near wing regions are affected by up to 70 %, 57 % and 45 % respectively for these effective temperatures. Towards the absorption cores the relative changes of the flux decreases from the differences in the near line wings to ≈ -15 %, 5 %, and 10 %. These strong differences are expected, however, as there are substantial differences between the impact and modern1–3 line profiles.

Due to the similar characteristics of the modern3 and modern2 spectra, the difference between the two is at the most between +1 % and -0.7 %, 0 % and -7 %, +0.9 % and -4.2 %, 1.35 % and -0.4 %, and +3.5 % and -2.7 % at effective temperatures from 3000 K to 1100 K. These changes describe the influence of the two different descriptions of the perturbations with helium. Differences between the modern1 and modern3 spectra are again noticeable in the entire effective temperature range. Their maximum values are +6.5 %, between +1.3 % and -1.7 %, between +0.7 % and -1 %, between +0.6 % and -0.9 % and +0.9 % and -1.3 % for the effective temperatures from 3000 K to 1100 K. Following the discussion above, comparing with the spectra of the impact setup, the differences between the impact and modern3 spectra are again of the same order of magnitude and the changes are increased in the line wings towards the lower effective temperatures as it can be seen in Fig. D.1.

With the flux contribution function \mathcal{C}_F as introduced in Magain (1986) and Fuhrmeister et al. (2006) and applied in Johnas et al. (2006), the differences around 5891 \AA seen in Fig. D.1 and D.2 between the different model types can be interpreted. The maximum of \mathcal{C}_F indicates the layers where the line forms in the atmosphere at a specific wavelength. The wavelength 5891 \AA has been

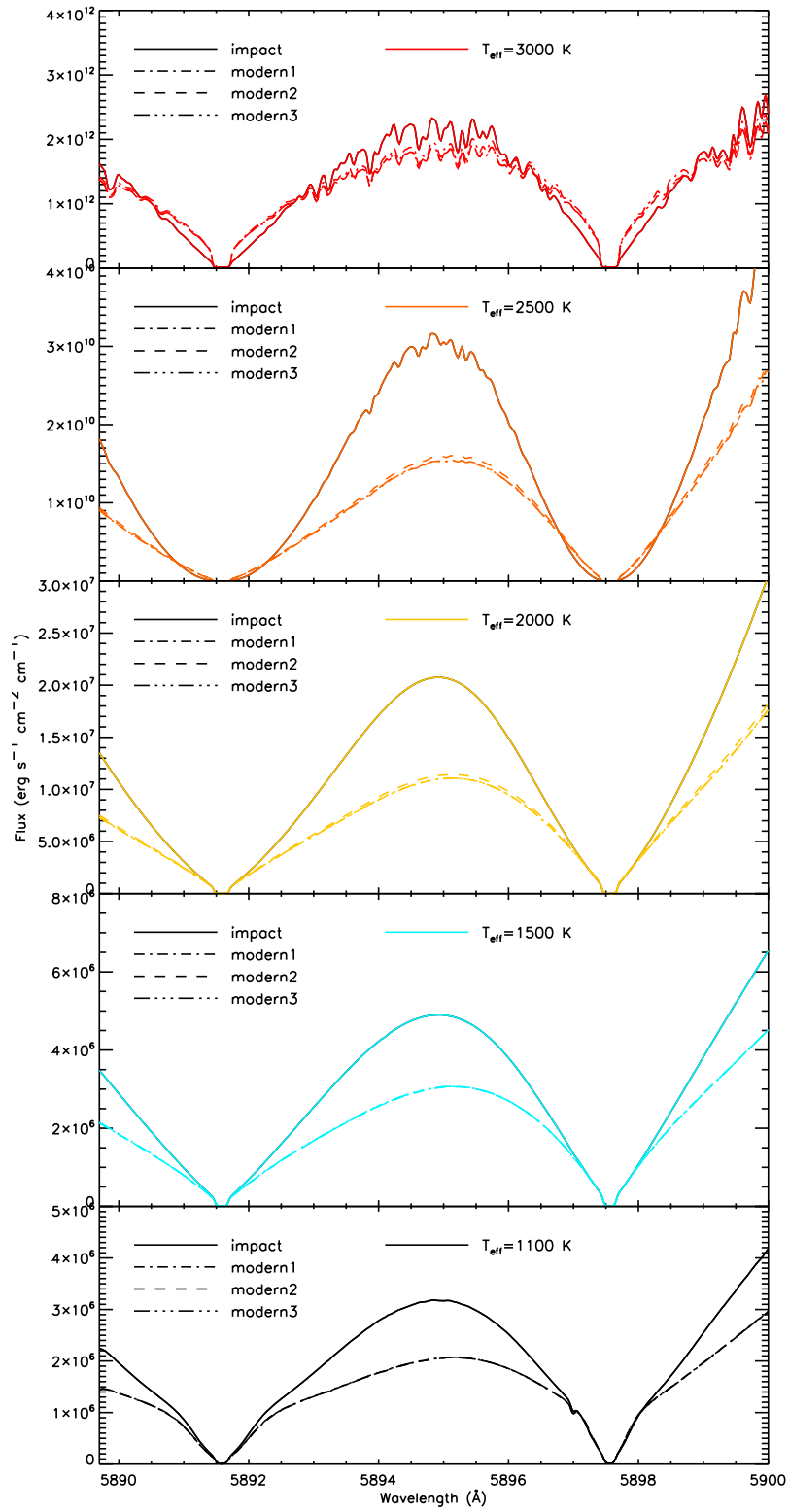


Fig. D.2: Zoom in of Fig. D.1 showing the Na I doublet at a resolution of $3 \cdot 10^5$.

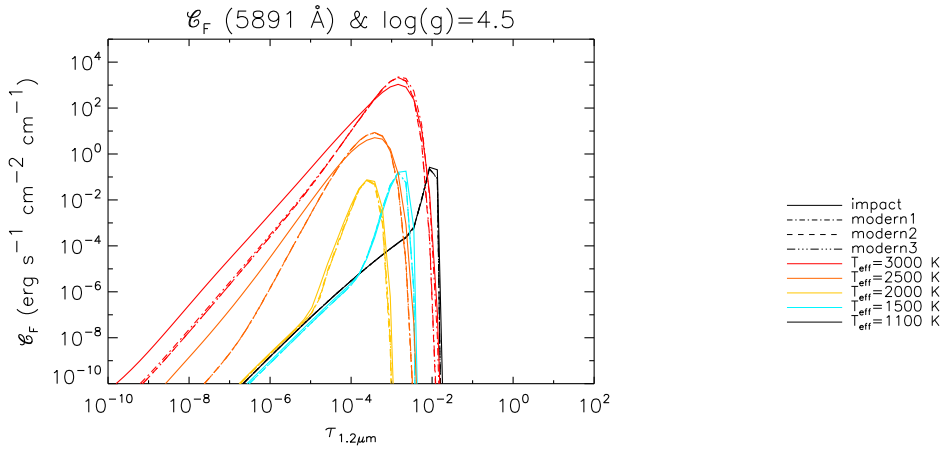


Fig. D.3: Contribution function at 5891 Å for effective temperatures from 3000 K to 1100 K for the four line profile setups.

chosen to represent the near line wing region in which the changes in the setups are significant. For each effective temperature slightly different locations of the line forming region in the atmosphere for each model type are found, as shown in Fig. D.3. This is one aspect for the differences in the emergent flux of the synthetic spectra.

Further analyses of the flux contribution function and the gas pressure of each model type for each effective temperature have shown that the locations of the maxima of the flux contribution functions are consistent with the theoretical predictions. Moving closer to the line core, the maxima are positioned at higher and hence cooler regions of the atmosphere. On the other hand, moving further into the line wings of the Na I D₂ absorption line, the flux contribution originates in deeper and hotter layers of the atmosphere.

Conclusions

We have demonstrated the effect of different line profiles of the Na I D lines on the emitted spectra. The changes made in the intrinsic line profiles of the modern2 and modern3 setups affects the data of the near wings. Their influence in the synthetic spectra depends on the effective temperature. Despite of the presence of strong molecular bands at higher effective temperatures, the inclusion of neutral hydrogen perturbers for the Na I D line profile data is significant for computing synthetic spectra.

There is an obvious need for extending the modern2 profiles especially to K I and Li I lines, due to their prominence in brown dwarf spectra. It is crucial to improve the Na I and K line profiles as they are also essential for the modelling of the other alkali doublets, i.e. Li I, Rb I, and Cs I. Furthermore, far line wing calculations for both modern2 and modern3 should be done in order to produce complete sets of line profiles, from the line core to the farthest wing. In a subsequent paper, the dependence of the equivalent widths on the different models will be discussed. Finally, it is very important to compare the results for the different profile types with low and high resolution observations of L and T dwarfs for conclusions of the quality of each profile type.

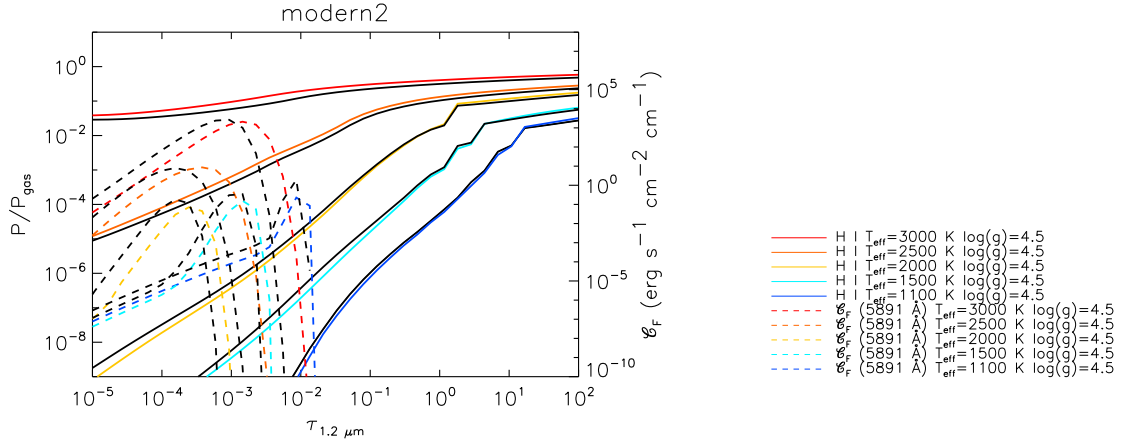


Fig. D.4: The concentrations (left ordinate) of HI for effective temperatures from 3000 K to 1100 K of modern2 models are depicted as well as the flux contribution functions at 5891 Å of the modern2 setup at each effective temperature. The results with $\log(g) = 4.5$ are plotted in color whereas the results with $\log(g) = 5.0$ are plotted in black.

D.2 Comparison to the Results of Sect. 5.5 with $\log(g) = 5.0$

The differences of the analysis of the Na I D line from Sect. D.1 to the one in Sect. 5.5 comprise other PHOENIX versions, slightly different line lists and also slightly different starting parameters. Towards higher values of $\log(g)$, one would expect larger effects of the setups in the synthetic spectra since the line broadening effect increases. Here, it is the opposite. The larger effects appear in the analysis with $\log(g) = 4.5$ instead of at $\log(g) = 5.0$. However, as shown in Fig. D.4, the effective temperature dependent concentrations of HI differ for the two $\log(g)$ values. In the innermost layers, the HI concentration of model atmospheres with $\log(g) = 4.5$ are higher. In the atmospheric region, where the line wings form, the HI concentration is increased compared to the one with $\log(g) = 5.0$ for $T_{\text{eff}} = 2500$ K and 3000 K.

Furthermore, all near line wings computed with $\log(g) = 4.5$, exemplarily shown for 5891 Å, form in deeper layers of the atmosphere for which the HI concentration is higher. Thus, here HI is the most important perturber, instead of being the second most important perturber in an atmosphere with $\log(g) = 5.0$, which influences the opacity calculation for the Na I D absorption lines.

Nevertheless, reasonably high HI concentrations appear above $T_{\text{eff}} = 2000$ K, so that the profile calculations of the modern2 setup should be focused on this effective temperature range.

E Numerical Implementation of the Stark Line Profile Calculation

The same computational background as described in Sect. 4.3 and Appendix B is assigned to the new non-analytical Stark profiles introduced above. In order to use the full provided information of the Stark profiles, a two dimensional, bilinear interpolation in terms of the temperature and perturber density for the Lorentzian HWHMs and shifts has been included in PHOENIX (in `cas_profiles.f`). This interpolation is done for each wavelength. For the internal profiles, the total Lorentzian damping constant is the sum of the natural, the van-der-Waals, and the Stark damping constant. For the new external profiles, the van-der-Waals component is neglected, since van-der-Waals damping constant has a diminishing influence in atmospheres, for which Stark broadening is prevalent. With the Lorentzian Stark parameters a Voigt profile including a Gaussian core is computed. Finally, a total Voigt profile is computed (in `cas_voigt_lines.f`). The results presented in Sect. 9.3 are obtained by considering only natural and Stark broadening for the near line wings (and Doppler broadening for the line core).

Bibliography

- Allard, F. & Hauschildt, P. H. 1995, *ApJ*, 445, 433
- Allard, F., Hauschildt, P. H., Alexander, D. R., Tamanai, A., & Schweitzer, A. 2001, *ApJ*, 556, 357
- Allard, N. F. 1978, *J. Phys. B*, 11, 1383
- Allard, N. F. 2004, private communication
- Allard, N. F. 2006, private communication
- Allard, N. F., Allard, F., Hauschildt, P. H., Kielkopf, J. F., & Machin, L. 2003, *A&A*, 411, L473
- Allard, N. F., Allard, F., Johnas, C. M. S., & Kielkopf, J. F. 2006, *A&A*, submitted
- Allard, N. F., Allard, F., & Kielkopf, J. F. 2005, *A&A*, 440, 1195
- Allard, N. F., Drira, I., Gerbaldi, M., Kielkopf, J., & Spielfiedl, A. 1998, *A&A*, 335, 1124
- Allard, N. F. & Kielkopf, J. 1982, *Rev. Mod. Phys.*, 54, 1103
- Allard, N. F., Koester, D., Feautrier, N., & Spielfiedel, A. 1994, *A&AS*, 108, 417
- Allard, N. F., Royer, A., Kielkopf, J. F., & Feautrier, N. 1999, *Phys. Rev. A*, 60, 1021
- Allard, N. F. & Spiegelman, F. 2006, *A&A*, 452, 351
- Allard, N. F., Spiegelman, F., & Kielkopf, J. F. 2007, *A&A*, 465, 1085
- Aller, L. H., Appenzeller, I., Baschek, B., et al. 1982, *Landolt-Börnstein: Numerical Data and Functional Relationships in Science and Technology - New Series "Gruppe/Group 6 Astronomy and Astrophysics" Volume 2 Schaifers/Voigt: Astronomy and Astrophysics / Astronomie und Astrophysik "Stars and Star Clusters / Sterne und Sternhaufen" (Landolt-Börnstein: Numerical Data and Functional Relationships in Science and Technology)*
- Anderson, P. W. 1952, *Phys. Rev.*, 86, 809
- Anderson, P. W. & Talman, J. D. 1956, *Bell System Technical Publication*, New Jersey, 3117
- Babb, J. F. 2007, private communication
- Baranger, M. 1958a, *Phys. Rev.*, 111, 481
- Baranger, M. 1958b, *Phys. Rev.*, 111, 494
- Baranger, M. 1958c, *Phys. Rev.*, 112, 855

- Baranger, M. 1962, Spectral Line Broadening in Plasmas (Atomic and Molecular Processes, Chapt. 13, ed. D. R. Bates, Academic Press, New York)
- Barman, T. 2007, *AJL*, 661, L191
- Barman, T. S., Hauschildt, P. H., Schweitzer, A., et al. 2002, *AJL*, 569, L51
- Basri, G. 2000, *ARA&A*, 38, 485
- Basri, G., Mohanty, S., Allard, F., et al. 2000, *ApJ*, 538, 363
- Burgasser, A. J., Geballe, T. R., Leggett, S. K., Kirkpatrick, J. D., & Golimowski, D. A. 2006, *ApJ*, 637, 1067
- Burgasser, A. J., Kirkpatrick, J. D., Brown, M. E., et al. 2002, *ApJ*, 564, 421
- Burgasser, A. J., Kirkpatrick, J. D., McElwain, M. W., et al. 2003, *AJ*, 125, 850
- Burrows, A., Marley, M. S., & Sharp, C. M. 2000, *ApJ*, 531, 438
- Burrows, A. & Volobuyev, M. 2003, *ApJ*, 583, 985
- Büscher, S. 2000, Dissertation
- Caballero, J. A., Martín, E. L., Dobbie, P. D., & Barrado Y Navascués, D. 2006, *A&A*, 460, 635
- Canon, C. J. 1973, *JQSRT*, 13, 627
- Carroll, B. W. & Ostlie, D. A. 1996, *An Introduction to Modern Astrophysics*, 1st edn. (Addison–Wesley Publishing Company, Inc.)
- Chabrier, G. & Baraffe, I. 2000, *ARA&A*, 38, 337
- Chabrier, G., Baraffe, I., Allard, F., & Hauschildt, P. H. 2005, *ArXiv Astrophysics e-prints*
- Charbonneau, D., Brown, T. M., Noyes, R. W., & Gilliland, R. L. 2002, *ApJ*, 568, 377
- Chauvin, G., Lagrange, A.-M., Dumas, C., et al. 2005, *A&A*, 438, L25
- Ch'en, S. Y. & Fountain, C. W. 1964, *J. Quant. Spectrosc. Radiat. Transfer.*, 4, 323
- Ch'en, S. Y. & Garrett, R. O. 1966, *Phys. Rev.*, 144, 59
- Ch'en, S. Y., Gilbert, D. E., & Tan, D. K. L. 1969, *Phys. Rev.*, 184, 51
- Ch'en, S. Y., Looi, E. C., & Garrett, R. O. 1967, *Phys. Rev.*, 155, 38
- Ch'en, S. Y. & Wilson, R. A. 1961, *Physica*, 27, 497
- Cohen, J. S. & Schneider, B. 1974, *J. Chem. Phys.*, 61, 3230
- Cooper, J. 1968, *University of Colorado: Lectures in Theoretical Physics*, 1st edn. (Gordon and Breach, New York)

- Cowley, C. R. 1970, *The Theory of Stellar Spectra*, 1st edn. (Gordon and Breach, New York)
- Dehn, M. 2007, Dissertation
- Demtröder, W. 2000, *Experimentalphysik 3*, 2nd edn. (Springer Verlag, Berlin Heidelberg New York)
- Dimitrijević, M. S. & Sahal-Bréchet, S. 1984, *A&A*, 136, 289
- Dimitrijević, M. S. & Sahal-Bréchet, S. 1994, *A&AS*, 105, 245
- Dimitrijević, M. S. & Sahal-Bréchet, S. 1995, *A&AS*, 109, 551
- Dimitrijević, M. S. & Sahal-Bréchet, S. 1996, *A&AS*, 115, 351
- Dimitrijević, M. S. & Sahal-Bréchet, S. 1997, *A&AS*, 122, 163
- Dimitrijević, M. S. & Sahal-Bréchet, S. 1998a, *A&AS*, 128, 359
- Dimitrijević, M. S. & Sahal-Bréchet, S. 1998b, *A&AS*, 129, 155
- Dimitrijević, M. S. & Sahal-Bréchet, S. 1999, *A&AS*, 140, 191
- Fuhrmeister, B., Short, C., & Hauschildt, P. H. 2006, *A&A*, 452, 1083
- Garrett, R. O. & Ch'en, S. Y. 1966, *Phys. Rev.*, 144, 66
- Garrett, R. O., Ch'en, S. Y., & Looi, E. C. 1967, *Phys. Rev.*, 156, 48
- Gillon, M., Pont, F., Demory, B.-O., et al. 2007, *A&A*, 472, L13
- Golimowski, D. A., Leggett, S. K., Marley, M. S., et al. 2004, *AJ*, 127, 3516
- Grevesse, N. & Noels, A. 1993, in *Origin and evolution of the elements: proceedings of a symposium in honour of H. Reeves, held in Paris, June 22-25, 1992*. Edited by N. Prantzos, E. Vangioni-Flam and M. Casse. Published by Cambridge University Press, Cambridge, England, 1993, p.14, ed. N. Prantzos, E. Vangioni-Flam, & M. Casse, 14–+
- Griem, H. R. 1974, *Spectral line broadening by plasmas* (Pure and Applied Physics, New York: Academic Press, 1974)
- Griem, H. R., Baranger, M., Kolb, A. C., & Oertel, G. 1962, *Phys. Rev.*, 125, 177
- Hauschildt, P. & Murdin, P. 2001, *Encyclopedia of Astronomy and Astrophysics*
- Hauschildt, P. H. 1992, *J. Quant. Spectrosc. Radiat. Transfer*, 47, 433
- Hauschildt, P. H. & Baron, E. 1999, *JCAM*, 109, 41
- Hauschildt, P. H. & Baron, E. 2005, *Mem. S.A.It.*, 7, 140
- Hayashi, C. & Nakano, T. 1963, *Progress of Theoretical Physics*, 30, 460
- Helling, C. & Woitke, P. 2006, *A&A*, 455, 325

- Helling, C., Woitke, P., & Thi, W.-F. 2007, A&A, submitted
- Holstein, T. 1950, Phys. Rev., 79, 744
- Holtzmark, J. 1919a, Ann. Physik, 58, 577
- Holtzmark, J. 1919b, Physik Z., 20, 162
- Holtzmark, J. 1924, Physik Z., 25, 73
- Jeong, K. S. 2000, Dissertation
- Johnas, C. M. S., Allard, N. F., Homeier, D., Allard, F., & Hauschildt, P. H. 2006, AIP Conf. Proc., 874, 354
- Johnas, C. M. S., Guenther, E. W., V., J., Schweitzer, A., & Hauschildt, P. H. 2007c, A&A, accepted
- Johnas, C. M. S., Hauschildt, P. H., Schweitzer, A., et al. 2007a, A&A, 466, 323
- Johnas, C. M. S., Hauschildt, P. H., Schweitzer, A., et al. 2007b, A&A, accepted
- Johnas, C. M. S., Helling, C., Witte, S., Dehn, M., & Woitke, P. and Hauschildt, P. H. 2007d, Proceeding to Extreme solar systems, ed. Rasio F.
- Kirkpatrick, J. D. 2005, ARA&A, 43, 195
- Kirkpatrick, J. D., Reid, I. N., Liebert, J., et al. 1999, ApJ, 519, 802
- Kuhn, H. & London, F. 1934, Philosophic. Mag., 18, 987
- Kumar, S. S. 1963a, ApJ, 137, 1126
- Kumar, S. S. 1963b, ApJ, 137, 1121
- Kurucz, R. L. 1979, AJS, 40, 1
- Kurucz, R. L. & Bell, B. 1995, Atomic line list, Kurucz CD-ROM No. 23
- Latham, D. W., Stefanik, R. P., Mazeh, T., Mayor, M., & Burki, G. 1989, Nature, 339, 38
- Leininger, T., Gadéa, F. X., & Dickinson, A. S. 2000, J. Phys. B, 33, 1805
- Lenz, W. 1924, Z: Physik, 25, 299
- Lenz, W. 1933, Z: Physik, 80, 423
- Leo, P. J., Peach, G., & Whittingham, I. B. 2000, J. Phys. B, 33, 4779
- Lewis, M. & Margenau, H. 1959, Phys. Rev., 109, 842
- Liebert, J., Reid, I. N., Burrows, A., et al. 2000, AJL, 533, L155
- Lodieu, N., Scholz, R.-D., McCaughrean, M. J., et al. 2005, A&A, 440, 1061

- Magain, P. 1986, *A&A*, 163, 135
- Margenau, H. 1932, *Phys. Rev.*, 40, 387
- Mayor, M. & Queloz, D. 1995, *Nature*, 378, 355
- Michelson, A. A. 1895, *Astrophys. J.*, 2, 251
- Mihalas, D. 1970, *Stellar Atmospheres*, 1st edn. (W. H. Freeman and Company, San Francisco)
- Mullamphy, D. F. T. 2002, Dissertation
- Mullamphy, D. F. T., Peach, G., Venturi, V., Whittingham, I. B., & Gibson, S. J. 2007, *J. Phys. B*, 40, 1141
- Nakajima, T., Oppenheimer, B. R., Kulkarni, S. R., et al. 1995, *Nature*, 378, 463
- Pascale, J. 1983, *Phys. Rev. A*, 28, 623
- Pavlenko, Y. V., Jones, H. R. A., Martín, E. L., et al. 2007, *MNRAS*, 725
- Peach, G. 1981, *Advances in Physics*, 30, 367
- Peach, G., Mullamphy, D. F. T., Venturi, V., & Wittingham, I. B. 2005, *Mem. S. A. It.*, 7, 147
- Phan–Bao, N., Bessell, M. S., Martín, E. L., et al. 2006, *MNRAS*, 366, L40
- Ralchenko, Y., Jou, F.-C., Kelleher, D. E., et al. 2007, NIST Atomic Spectra Database, <http://physics.nist.gov/asd3> (National Institute of Standards and Technology, Gaithersburg, MD)
- Rebolo, R., Martín, E. L., & Magazzu, A. 1992, *AJL*, 389, L83
- Reiners, A. 2006, private communication
- Rossi, F. & Pascale, J. 1985, *Phys. Rev. A*, 32, 2657
- Roueff, E. 1974, *J. Phys. B*, 7, 185
- Royer, A. 1971, *Phys. Rev. A*, 3, 2044
- Royer, A. 1978, *Acta Physica Polonia*, A54, 805
- Royer, A. 1980, *Phys. Rev. A*, 22, 1625
- Rutten, R. J. 2003, lecture notes Utrecht University, 8th WWW edition, <http://www.phys.uu.nl/rutten/>.
- Sahal-Bréchet, S. 1969a, *A&A*, 1, 91
- Sahal-Bréchet, S. 1969b, *A&A*, 2, 322
- Sahal-Bréchet, S. & Segre, E. R. A. 1971, *A&A*, 13, 161
- Scharmer, G. B. 1981, *ApJ*, 249, 720

- Schiff, L. 1955, *Quantum Mecanics*, 1st edn. (McGraw-Hill Book Company, Inc., New York Toronto London)
- Schweitzer, A. 1995, Diploma thesis
- Schweitzer, A., Gizis, J. E., Hauschildt, P. H., et al. 2002, *ApJ*, 566, 435
- Schweitzer, A., Gizis, J. E., Hauschildt, P. H., Allard, F., & Reid, I. N. 2001, *ApJ*, 555, 368
- Schweitzer, A., Hauschildt, P. H., Allard, F., & Basri, G. 1996, *MNRAS*, 283, 821
- Smith, D., Vidal, C. R., & Cooper, J. 1969, *J. Res. Nat. Bur. Stand.*, 73A, 389
- Spitzer, L. 1940, *Phys. Rev.*, 58, 348
- Stark, J. 1906a, *Verhandlungen der Deutschen Physik. Gesellschaft*, 8, 109
- Stark, J. 1906b, *Ann. Physik*, 21, 422
- Sudarsky, D., Burrows, A., & Hubeny, I. 2003, *ApJ*, 588, 1121
- Tinney, C. G. 1998, *MNRAS*, 296, L42
- Udry, S., Bonfils, X., Delfosse, X., et al. 2007, *A&A*, 469, L43
- Unsöld, A. 1968, *Physik der Sternatmosphären*, 2nd edn. (Springer Verlag, Heidelberg)
- Unsöld, A. & Baschek, B. 2005, *Der neue Kosmos*, 7th edn. (Springer Verlag Berlin Heidelberg New York)
- Weast, R. C. 1988, *Handbook of Chemistry and Physics*, 2nd edn. (CRC Press, Boca Raton)
- Wedler, G. 2005, *Lehrbuch der Physikalischen Chemie*, 5th edn. (WILEY-VCH Verlag GmbH & Co. KGaA)
- Weisskopf, V. 1932, *Z. Physik*, 75, 287
- Woitke, P. & Helling, C. 2003, *A&A*, 399, 297
- Woitke, P. & Helling, C. 2004, *A&A*, 414, 335
- Wolszczan, A. & Frail, D. A. 1992, *Nature*, 355, 145
- Zapatero Osorio, M. R., Béjar, V. J. S., Martín, E. L., et al. 2002, *ApJ*, 578, 536
- Zhu, C., Babb, J. F., & Dalgarno, A. 2005, *Phys. Rev. A*, 71, 527101
- Zhu, C., Babb, J. F., & Dalgarno, A. 2006, *Phys. Rev. A*, 73, 125061

Thank you!

“Adieu, dit le renard. Voici mon secret. Il est très simple: on ne voit bien qu’avec le cœur. L’essentiel est invisible pour les yeux.”

Antoine de Saint-Exupéry

I would never have been able to complete this thesis without the efforts of many people. I am very grateful for the assistance and support I received over the past three years. I wish to express my gratitude to all of the following:

- Prof. Dr. Peter H. Hauschildt for making this thesis possible as well as for his constant guidance and encouragement.
- Prof. Dr. Artie P. Hatzes for being the second referee of this thesis.
- Prof. Dr. Jürgen H. M. M. Schmitt for being the second referee of my disputation.
- Dr. Andreas Schweitzer for his continuous support, patience, and guidance and for many fruitful discussions.
- Dr. Nicole F. Allard, Dr. Gillian Peach, Dr. D’Arcy Mullanphy, and Prof. Dr. Ian B. Whittingham for providing their line profiles.
- Dr. Eike W. Guenther and Dr. Viki Joergens for providing their observations and their support.
- PD Dr. Christiane Helling and Dr. Peter Voitke for their insight in dust formation.
- All the current and former members of the stellar observatory. Without my colleagues, their friendliness and shared knowledge, I would not have enjoyed so much the time of my PhD thesis. Special thanks to Dr. Andreas Schweitzer, Dr. Sebastian Knop, and Dr. Suzanne Linder for proof-reading my thesis. Thanks to the staff of the “Hauptgebäude” who simplified the life next to science in the friendliest and most helpful way.
- The department Forschung und Wissenschaftsförderung for financial support via scholarships.
- The Deutsche Forschungsgemeinschaft for financial support via the research training group 1351 “Extrasolar Planets and Their Host Stars”.
- To all my friends for many pleasant and happy moments.
- To the most important people in my life, my parents and my sister, for their loving support at all times during my PhD thesis.